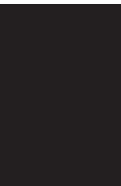


# ATMOSPHERIC AEROSOLS AND CLIMATE

GUEST EDITORS: HARRY D. KAMBEZIDIS, VICTORIA E. CACHORRO, STEFAN KINNE,  
KRISHNASWAMY KRISHNAMOORTHY, GERRIT DE LEEUW, AND VITO VITALE





---

# **Atmospheric Aerosols and Climate**

Advances in Meteorology

---

## **Atmospheric Aerosols and Climate**

Guest Editors: Harry D. Kambezidis, Victoria E. Cachorro,  
Stefan Kinne, Krishnaswamy Krishnamoorthy, Gerrit de Leeuw,  
and Vito Vitale



---

Copyright © 2010 Hindawi Publishing Corporation. All rights reserved.

This is a special issue published in volume 2010 of “Advances in Meteorology.” All articles are open access articles distributed under the Creative Commons Attribution License, which permits unrestricted use, distribution, and reproduction in any medium, provided the original work is properly cited.

## Editorial Board

Paulo Artaxo, Brazil  
Rebecca Barthelmie, USA  
Guy Brasseur, USA  
Mladjen Ćurić, Serbia  
Raymond Desjardins, Canada  
Klaus Dethloff, Germany  
Panuganti Devara, India  
Ellsworth Dutton, USA  
Shouting Gao, China  
Luis Gimeno, Spain  
C. S. B. Grimmond, UK

Branko Grisogono, Croatia  
Sven-Erik Gryning, Denmark  
Ismail Gultepe, Canada  
Hiroyuki Hashiguchi, Japan  
Didier Hauglustaine, France  
Qi Hu, USA  
I. S. A. Isaksen, Norway  
Yasunobu Iwasaka, Japan  
Hann-Ming Henry Juang, USA  
George Kallos, Greece  
Harry D. Kambezidis, Greece

Markku Kulmala, Finland  
Richard Leitch, Canada  
Monique Leclerc, USA  
Barry Lefer, USA  
Zhanqing Li, USA  
Edward Llewellyn, Canada  
Kyaw Tha Paw U, USA  
Sara C. Pryor, USA  
Eugene Rozanov, Switzerland

## Contents

**Atmospheric Aerosols and Climate**, Harry D. Kambezidis, Victoria E. Cachorro, Stefan Kinne, Krishnaswamy Krishnamoorthy, Gerrit de Leeuw, and Vito Vitale  
Volume 2010, Article ID 708782, 2 pages

**Diagnosis of the Relationship between Dust Storms over the Sahara Desert and Dust Deposit or Coloured Rain in the South Balkans**, N. G. Prezerakos, A. G. Paliatsos, and K. V. Koukouletsos  
Volume 2010, Article ID 760546, 14 pages

**An Assessment of the Efficiency of Dust Regional Modelling to Predict Saharan Dust Transport Episodes**, D. K. Papanastasiou, A. Poupkou, E. Katragkou, V. Amiridis, D. Melas, N. Mihalopoulos, S. Basart, C. Pérez, and J. M. Baldasano  
Volume 2010, Article ID 154368, 9 pages

**Identification of the Aerosol Types over Athens, Greece: The Influence of Air-Mass Transport**, D. G. Kaskaoutis, P. G. Kosmopoulos, H. D. Kambezidis, and P. T. Nastos  
Volume 2010, Article ID 168346, 15 pages

**Aerosol Monitoring over Athens Using Satellite and Ground-Based Measurements**, D. G. Kaskaoutis, N. Sifakis, A. Retalis, and H. D. Kambezidis  
Volume 2010, Article ID 147910, 12 pages

**Assessment of Aerosol Radiative Impact over Oceanic Regions Adjacent to Indian Subcontinent Using Multisatellite Analysis**, S. K. Satheesh, V. Vinoj, and K. Krishnamoorthy  
Volume 2010, Article ID 139186, 13 pages

**Vertical and Horizontal Gradients in Aerosol Black Carbon and Its Mass Fraction to Composite Aerosols over the East Coast of Peninsular India from Aircraft Measurements**, S. Suresh Babu, K. Krishna Moorthy, and S. K. Satheesh  
Volume 2010, Article ID 812075, 7 pages

**Urban Surface Temperature Reduction via the Urban Aerosol Direct Effect: A Remote Sensing and WRF Model Sensitivity Study**, Menglin Jin, J. Marshall Shepherd, and Weizhong Zheng  
Volume 2010, Article ID 681587, 14 pages

## Editorial

# Atmospheric Aerosols and Climate

**Harry D. Kambezidis,<sup>1</sup> Victoria E. Cachorro,<sup>2</sup> Stefan Kinne,<sup>3</sup>  
Krishnaswamy Krishnamoorthy,<sup>4</sup> Gerrit de Leeuw,<sup>5,6</sup> and Vito Vitale<sup>7</sup>**

<sup>1</sup> Atmospheric Research Team, National Observatory of Athens, 11810 Athens, Greece

<sup>2</sup> Group of Atmospheric Optics, University of Valladolid, 47011 Valladolid, Spain

<sup>3</sup> Max Planck Institute for Meteorology, 20146 Hamburg, Germany

<sup>4</sup> Space Physics Laboratory, Vikram Sarabhai Space Centre, Trivandrum 695022, India

<sup>5</sup> Climate Change Unit, Finnish Meteorological Institute, FI-00101 Helsinki, Finland

<sup>6</sup> Department of Physics, University of Helsinki, FI-00014 Helsinki, Finland

<sup>7</sup> Institute of Atmospheric Sciences and Climate, CNR, 40129 Bologna, Italy

Correspondence should be addressed to Harry D. Kambezidis, harry@noa.gr

Received 31 December 2010; Accepted 31 December 2010

Copyright © 2010 Harry D. Kambezidis et al. This is an open access article distributed under the Creative Commons Attribution License, which permits unrestricted use, distribution, and reproduction in any medium, provided the original work is properly cited.

Atmospheric aerosols affect the Earth's radiation budget directly by scattering and absorbing the solar and terrestrial radiation and indirectly by modifying the physical and radiative properties of clouds. Through their combined direct and indirect effects, anthropogenic aerosols have the potential to largely modify the albedo of the Earth-Atmosphere system. Globally, the aerosol radiative forcing (ARF) is believed to be comparable in magnitude, but opposite in sign, to that caused by anthropogenic emissions of greenhouse gases; regionally, however, the magnitude and sign of ARF is highly variable, with large uncertainties, especially due to inadequate representation of the physical and radiative properties of aerosols in models.

Aerosols in areas influenced by anthropogenic activities are physically and chemically different from those in remote regions. These differences influence the aerosol optical properties. Knowledge of the aerosol properties is important for modelling the aerosol radiative effects on climate and retrieving the aerosol optical properties using remote-sensing techniques. Besides, changes in the vertical structure of the atmosphere lead to formation of distinct layers of aerosols above the planetary boundary layer; under favourable conditions, these aerosols are transported over long distances. The radiative implications of such elevated aerosols have immense impact on regional weather and climate.

The aim of this special issue is to provide the scientific community with a compendium of recent advances in the understanding of atmospheric aerosols and their impacts on climate. The seven accepted papers cover a wide range of the above issues. More specifically, they refer to the following topics:

- (i) “*Diagnosis of the relationship between dust storms over the Sahara desert and dust deposit or coloured rain in the South Balkans,*”
- (ii) “*An assessment of the efficiency of dust regional modelling to predict Saharan dust transport episodes,*”
- (iii) “*Identification of the aerosol types over Athens, Greece: the influence of air-mass transport,*”
- (iv) “*Aerosol monitoring over Athens using satellite and ground-based measurements,*”
- (v) “*Assessment of aerosol radiative impact over oceanic regions adjacent to Indian Subcontinent using multi-satellite analysis,*”
- (vi) “*Vertical and horizontal gradients in aerosol black carbon and its mass fraction to composite aerosols over the east coast of Peninsular India from aircraft measurements,*”

- (vii) *“Urban surface temperature reduction via the urban aerosol direct effect—a remote sensing and WRF model sensitivity study.”*

*Harry D. Kambezidis  
Victoria E. Cachorro  
Stefan Kinne  
Krishnaswamy Krishnamoorthy  
Gerrit de Leeuw  
Vito Vitale*

## Research Article

# Diagnosis of the Relationship between Dust Storms over the Sahara Desert and Dust Deposit or Coloured Rain in the South Balkans

**N. G. Prezerakos, A. G. Paliatsos, and K. V. Koukouletsos**

*General Department of Mathematics, Technological Education Institute of Piraeus, 250 Thivon and P. Ralli, 12244 Athens, Greece*

Correspondence should be addressed to A. G. Paliatsos, [agpal@in.teipir.gr](mailto:agpal@in.teipir.gr)

Received 1 December 2009; Accepted 19 July 2010

Academic Editor: Harry D. Kambezidis

Copyright © 2010 N. G. Prezerakos et al. This is an open access article distributed under the Creative Commons Attribution License, which permits unrestricted use, distribution, and reproduction in any medium, provided the original work is properly cited.

The main objects of study in this paper are the synoptic scale atmospheric circulation systems associated with the rather frequent phenomenon of coloured rain and the very rare phenomenon of dust or sand deposits from a Saharan sandstorm triggered by a developing strong depression. Analysis of two such cases revealed that two days before the occurrence of the coloured rain or the dust deposits over Greece a sand storm appeared over the north-western Sahara desert. The flow in the entire troposphere is southerly/south-westerly with an upward vertical motion regime. If the atmospheric conditions over Greece favour rain then this rain contains a part of the dust cloud while the rest is drawn away downstream adopting a light yellow colour. In cases where the atmospheric circulation on the route of the dust cloud trajectories is not intensively anticyclonic dust deposits can occur on the surface long far from the region of the dust origin. Such was the case on 4th April, 1988, when significant synoptic-scale subsidence occurred over Italy and towards Greece. The upper air data, in the form of synoptic maps, illustrate in detail the synoptic-scale atmospheric circulations associated with the emission-transport-deposition and confirm the transportation of dust particles.

## 1. Introduction

The phenomenon of coloured rain over the South Balkans and, in particular, over Greece occurs rather frequently, being associated with the appearance of Sahara or Atlas Mountains depressions [1–3]. On the other hand a significant easily visible, dust deposit upon Greece, coming from North Africa, is a very rare phenomenon occurring only once within the last twenty years on 4 April 1988 in north Greece. Also on 17 April 2005 the city of Athens was enveloped in a thick dust cloud. The dust cloud was not a localised event over Athens, but it was part of a synoptic-scale dust transport from Africa [4]. This event over Athens seems to be a little bit different from the other one, on 4th April 1988 in Thessalonica, studied here, because the dust was concentrated in the boundary layer with very little dry deposit on surface reducing dramatically the visibility. Of course coloured rain and/or dust deposits occur also in other European countries which are further north than Greece, for

example, United Kingdom [5, 6], Spain [7], and generally Europe [8]. Also the transport and deposition of African dust is known to affect distant regions in the North Atlantic as far away as the Caribbean Islands [9, 10]. Something similar occurs for the East Asian dust that is transported and deposited to a long distance towards the East as far as Hawaii [11–13]. Also Danielsen [14] investigated the development of severe storms above Texas as a dust source in the early 1970s. Finally, an intense dust storm over Greece has recently been studied by Kaskaoutis et al. [15].

Although many papers that deal with monitoring and predicting Saharan dust transporting northwards appeared after mid-90s when dispersion models were developed and very advanced sensors were put on meteorological satellites [4, 13, 16–23], few papers before mid-90s that deal with case studies of the coloured rain phenomenon [1, 3, 24, 25] and one paper which deals with the phenomenon of dust or sand dry deposit on north Greece [26] have revealed the type of synoptic-scale atmospheric circulation which

is associated with coloured rain or dry dust deposit over Greece. The dominant feature of this type of atmospheric circulation is a southerly to south-westerly flow through the entire troposphere extending from the North Sahara as far as the Balkans.

The whole process starts with the development of a North African depression resulting in a dust storm. This African depression is initiated by an upper-level trough or PV anomaly which occurs on the polar front jet (PFJ), when it overlies a heat low. Alternatively it is initiated by low-level baroclinicity southeast of the Atlas Mountains just north or beneath the Subtropical jet stream (STJ) [27] when there is an interaction between the PFJ and the STJ because the PFJ has moved south as far as North Africa to approach the STJ closely. The suggestion that the interaction of the two jets can initiate and develop the depression due to the increase of hydrodynamic instability which needs more research as Karein [28] based on Defant's theory [29] has studied only one case in the eastern Mediterranean. Also Prezerakos et al. [30] have revealed the role of the interaction of these two jets on the rejuvenation of depression over the eastern Mediterranean. The option that these North African depressions can be treated as normal baroclinic waves [27, 31, 32] associated with the PFJ PV anomalies typically occurring in the winter and the spring due to the approaching of the PFJ over North Africa seems to be more satisfactory.

The rising dust embedded in the south-westerly and upward synoptic-scale vertical motion tropospheric flow drifts over large distances together with significant warm air advection reaching Greece and the South Balkans. This dust is responsible for hazy weather conditions for several days over Greece.

Sometimes the rising dust forms a dust cloud stirring up to a few tens or hundreds of meters with the thinner dust grains ascending to greater heights, for example, 3-4 km or more [2, 6, 25]. This dust cloud and the Sahara depression move together, being steered by the polar or subtropical jet stream but mainly in the lower half of the tropospheric flow. Some of the dust grains, being in an atmospheric environment of increased humidity, become condensation nuclei falling on the ground as raindrops, when ascending air motions dominate the region. Also, the rest of the dust grains are mixed into the raindrops which thus appear coloured. This is shown clearly when the rain droplets evaporate. In such a case numerous spots cover every surface, especially cars, in the open air. These spots are approximately round, with a diameter of about 0.1-0.2 cm and with a light yellow colour consisting of extremely fine-grained dust [25]. When the drifting dust cloud is embedded in an intense but dry upper tropospheric anticyclonic flow leading to strong synoptic-scale descending motion or in an ordinary (not small scale) synoptic-scale upward motion, then it is accelerated due to gravity to fall out as a thick deposit on the earth surface looking like desert sand (particles < 20  $\mu\text{m}$ ).

It follows from the previous paragraphs that the dust transport toward the South Balkans occurs when intensive cyclogenesis develops in Northwest Africa (the source region) and at the same time the dominant feature of the

regional atmospheric circulation is a southerly to south-westerly flow throughout the entire troposphere from the Northwest Sahara as far as the Balkans. This combination is a frequent event in winter and especially in spring [2, 3, 18, 33, 34]. As a result spring is the most likely season for the occurrence of coloured rain or dust deposit over the South Balkans [18, 33, 34].

Previous attempts have been made by other Greek scientists [1, 24-26] to study the synoptic-scale atmospheric circulation using early satellite images associated with cases of coloured rain or/and dust deposit upon the South Balkans. This work will focus on the study of the correlation between sand storms over North Africa and coloured rain and/or dust deposit upon Greece. We will base our study mainly on high resolution satellite images but not so advanced as the nowadays ones and air trajectories. These are effective tools to diagnose and forecast the course of drifting airborne particles and pollutants within the atmosphere. This paper can then be used as a standard for verifying the results of physical models of dust emission [19, 35] or forecast numerical models of dust suspension, transport, and deposition. Such forecast numerical models are already in operation [16-18, 21-23, 36-38] with reliable results in a number of tests.

A part of the data used in this paper constituted a presentation delivered in an international symposium held in Damascus, Syrian Arab Republic in November 1997 [39]. At that presentation, the justification of the dry dust deposit in the morning of 4th April 1988 on surface in Thessalonica a place with upward synoptic-scale vertical air motion, that time, appeared highly questionable. Then this justification has been under continuing consideration with more data added intending a more reasonable explanation to be formatted.

The publication of this paper in a worldwide circulated journal, as the "Advances in Meteorology", provides the trigger effect to other researchers to investigate more in depth this case for an absolutely clear justification.

This paper is organized as follows. Section 2 describes the dataset and methodology employed in this study. In Section 3 there is an analysis and discussion of the 27th March 1992 case of coloured rain upon Greece. Section 4 consists of a further brief analysis and discussion of the 4th April 1988 case of significant dust deposit upon Thessalonica, north Greece. The conclusions are summarized and discussed in Section 5.

## 2. Data and Methodology

The majority of data used in this investigation comes from the ECMWF archived operational initialized analyses using a resolution of  $1.5^\circ \times 1.5^\circ$  along latitude and longitude circles. More specifically, these data are geopotential height, temperature, and horizontal winds at 900, 850, 700, 500, and 300 hpa isobaric levels, which depict the course of the drifting dust toward the South Balkans. Also, data of mean sea level atmospheric pressure and vertical velocities at 900, 850, 700, and 500 hpa isobaric levels was obtained from the same source in order to show the dust source and deposit places.

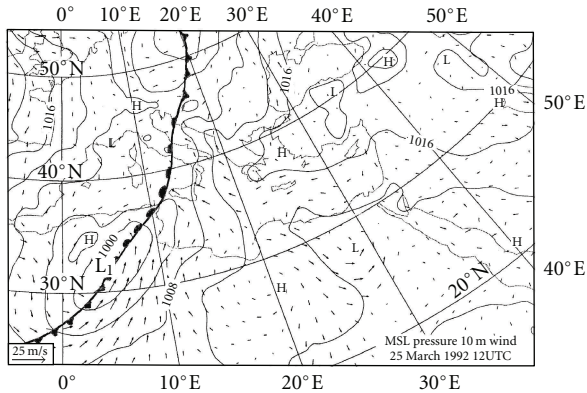


FIGURE 1: Mean sea level objective pressure analysis at 12:00 UTC on 25 March 1992. Isobars: every 4 hpa. The fronts are denoted by the conventional symbols and are transferred from the Hellenic National Meteorological Center respective subjective analysis. The scale of the wind velocity is at the lower left corner.

To facilitate the study and understand the course of the drifting dust in the atmosphere and its final arrival, 5-day backward air trajectories were calculated for Athens and Thessalonica which arrived at 12:00 UTC on 27 March 1992 (the day on which coloured rain occurred) for four different heights (below 900, 850, 700, and 500 hpa). The trajectories were calculated using the trajectory model of the Deutscher Wetterdienst (DWD) based on the results of the DWD global model (here 6 hourly analyses of the spectral parameters of divergence and potential vorticity were transformed to give horizontal winds and surface pressure on a global Gaussian grid). Additional information on the DWD trajectory model can be found in the paper by Kottmeier and Fay [40].

As there was no archive before 1990 it was not possible to run the DWD global model for calculating trajectories for the case of dust deposit upon the Thessalonica region in the morning on 4 April 1988. To compute trajectories for this case we used Seijo Kruizinga's program, which is the operational one in ECMWF, and the ECMWF Reanalysis (ERA 40) as input. Nowadays this program can be used freely for research purposes and internal purposes of all the ECMWF member states. The program can be used for computing three-dimensional forward as well as backward trajectories using wind analyses and wind forecasts from the ECMWF model. In order to have three-dimensional trajectories all three wind components are used.

The computed trajectories are 5-day backward air-parcel trajectories originating in Thessalonica on 4th April 1988 at 00:00 UTC in 900, 850, 700, 500, and 300 hpa heights. For these studies only the first 2 days of the back trajectories are used. Also images from NOAA AVHRR (Advanced Very High Resolution Radiometer) being adopted from météo-France archives are used for the case on 25–27 March 1992 to confirm the origin and tracking of the dust cloud. The satellite images for the 1988 case are coming from University of Dundee archives.

According to the annual international WMO (World Meteorological Organization) verification of numerical

weather prediction model results, the ECMWF model and the GM of DWD on average show a similar performance and rank amongst the best NWP models worldwide [41]. As the quality of the wind fields determined by the two models is not different, the trajectories produced by both models appear to have the same efficacy since they depend on the quality of the wind fields. The main trajectory error sources come from the wind errors, which are caused directly by incorrect observations, model forecasts, and analyses and also by spatial and temporal interpolation of the wind fields to the trajectory positions.

However, the use of trajectories based on analyses associated with AVHRR images and synoptic atmospheric circulation patterns is the best way to describe the path of infinitesimal air parcels through the atmosphere, and they are widely used for evaluating measurements and verifying forecast trajectory models.

### 3. Analysis and Discussion of the 27th March 1992 Case of Coloured Rain over Greece

**3.1. Synoptic-Scale Atmospheric Patterns.** At about 12:00 UTC on 27 March 1992, a significant amount of coloured rain (about 30 mm from 06:00 to 18:00 UTC), occurred in Athens (Athens Observatory, 37.97°N, 23.72°E and Helleniko WM016716). Two days earlier, that is, at 12:00 UTC on 25 March 1992 two depressions were developing over North Africa. One vigorous depression was centred south of the Atlas Mountains extending north-eastwards as far as Sicily and eastwards as far as the borders between Tunisia and Libya. The other one, much weaker, was centred over Egypt (Figure 1). These two depressions were separated by a weakening high-pressure system. Strong winds up to 30 kn accompanied the depressions in the rear and ahead of the cold front associated with the depression. These increased due to the unstable thermal stratification and associated intense vertical mixing producing downward transport of high momentum to the surface, and this resulted in the Sahara sand rising into suspension causing dust storms. It is worthwhile recalling that only dust particles smaller than 20  $\mu\text{m}$  can be lifted up into the atmosphere for days and experience long range transport whereas sand particles greater than 20  $\mu\text{m}$  result in sandblasting and creeping sand dunes.

Synoptic-scale ascending motion can be seen over the region of the Atlas depression (Figures 2(a), 2(b), and 2(c)) at 850, 700, and 500 hpa isobaric levels especially along the front. The maximum values are  $-0.6$ ,  $-0.5$ , and  $-0.6 \text{ Pas}^{-1}$  at 850, 700, and 500 hpa correspondingly, thus helping the vertical mixing for transferring dust upwards. The airflow near the surface, being between the Atlas Mountains depression and the high over Libya, is from the south (Figure 1).

Also the tropospheric flow at 850, 700, and 500 hpa (Figures 3(a), 3(b), and 3(c)) in the vicinity of the Atlas Mountains depression is south-westerly carrying the dust north-eastwards. This low level warm air is moving polewards and gradually rising to reach the level of 700 hpa or

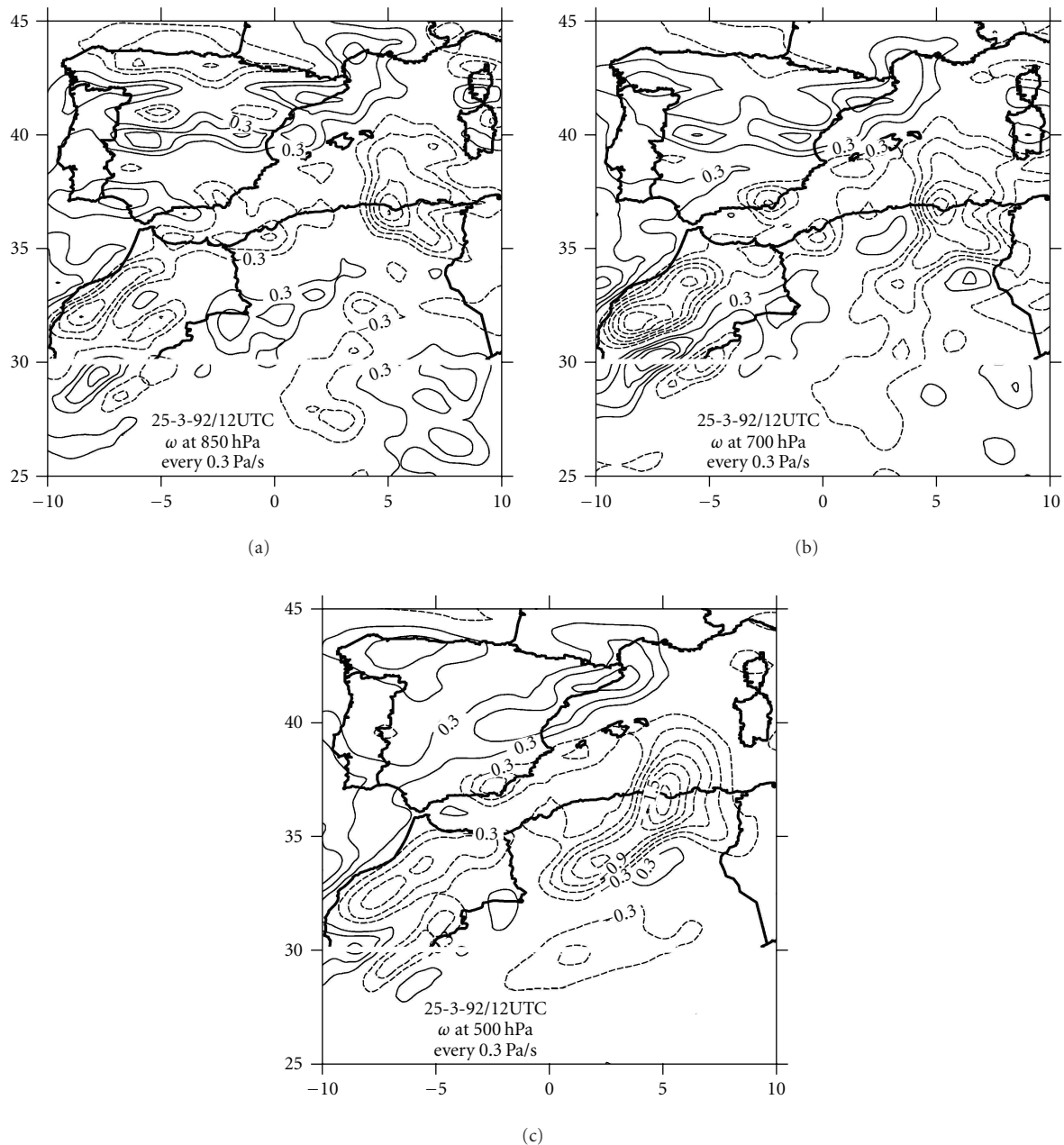


FIGURE 2: Vertical velocity fields at 12:00 UTC on 25 March 1992 at, (a) 850 hPa, (b) 700 hPa, and (c) 500 hPa. Isopleths of vertical velocity: every  $0.3 \text{ Pa s}^{-1}$  (dash: upward; continuous: downward).

higher over Greece 48 h later. The flow at the same levels over Egypt is westerly/south-westerly steering the Egyptian depression eastwards. A quantitative approach regarding the location and activity of dust sources in the Sahara can be found in the literature, for example, [19, 35, 38, 42–44].

At 300 hPa (Figure 4) at the same time there is an interaction between the polar and subtropical jet streams southwest of the Atlas Mountains. It may be hypothesised that this interaction causes an increase in the hydrodynamic instability [28] over this region or strengthens the synoptic-scale upward motion [30], which itself may lead to the development of the vigorous depression  $L_1$  as shown in

Figure 1. These views are in need of more research. Indeed, following Petterssen's [45] ideas, we can suggest that the Atlas depression  $L_1$  was initiated when the region of positive absolute vorticity advection ahead of the 500 or 300 hPa trough  $T_1$  (Figure 4) became superimposed over the shallow frontal surface shown in Figure 1. This suggestion is backed up by the narrow zone of potential temperature isopleths in this region (Figure 3(a)). At 12:00 UTC on March 25 1992 depression  $L_1$  was developing, while the head of the region of positive absolute vorticity advection ahead of trough  $T_2$  (Figure 4) results in barometric tendencies becoming negative at the surface and a well-developed depression  $L_2$

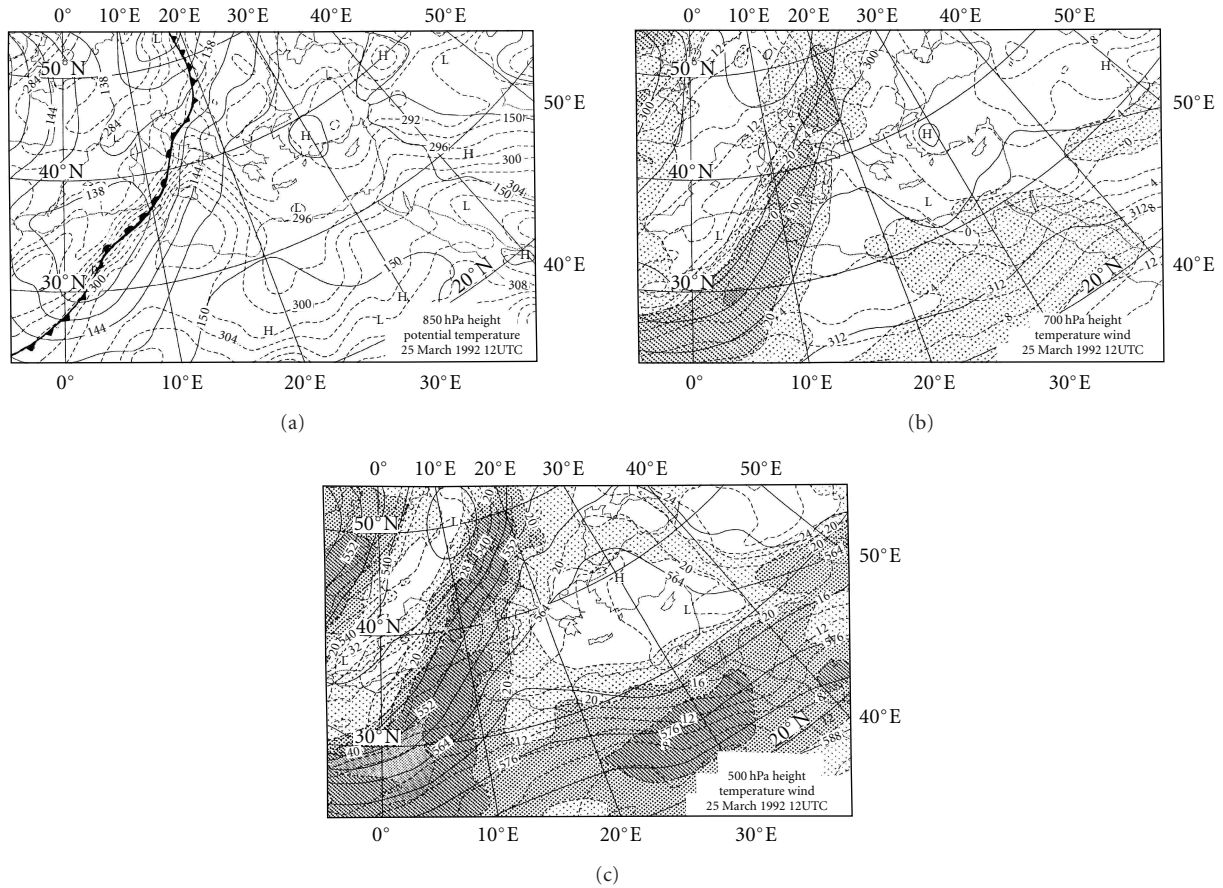


FIGURE 3: (a) Objective analysis of geopotential height and potential temperature at 850 hpa at 12:00 UTC on 25 March 1992. Geopotential contours: every 30 gpm, isentropes: every 2 K, (b) 700 hpa and (c) 500 hpa at the same time and date. Contours are drawn every 60 gpm and isotherms every 2°C. Wind speed above 30 ms<sup>-1</sup> is stippled and more than this is shaded with shading increasing every 5 ms<sup>-1</sup>.

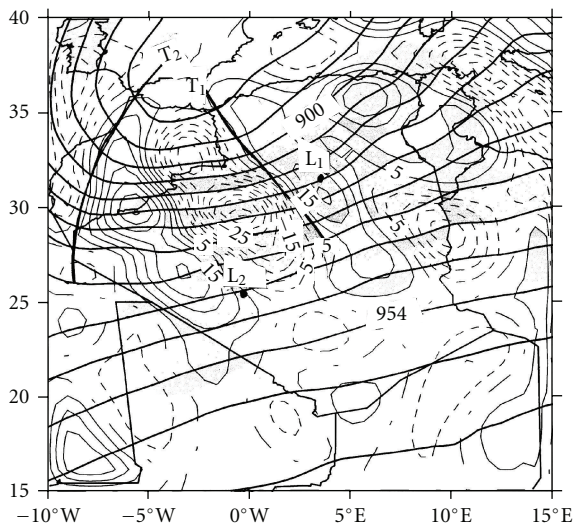


FIGURE 4: Objective analysis of geopotential height (thick continuous every 60 gpm) and absolute vorticity advection every  $5 \times 10^{-10} \text{ s}^{-2}$  at 300 hpa at 12:00 UTC on 25 March 1992. Negative advection isopleths are dotted, and the zero one is dot-dashed. Positive advection isopleths are thin continuous. L<sub>1</sub> and L<sub>2</sub> denote the centres of the surface depressions, and T<sub>1</sub> and T<sub>2</sub> are the corresponding trough lines.

appearing 12 h later (not shown). At this time the area of positive absolute vorticity advection is lying over an area of maximum thermal advection at the 850 hpa surface. This cyclogenesis belongs to type B cyclogenesis of Petterssen and Smebye [46], since there is significant warm advection in the region of surface cyclogenesis while the earlier development resulting in depression L<sub>1</sub> belongs to type A cyclogenesis.

Following Hoskins et al. [47] we can describe almost the same process for the above cyclogenesis replacing the positive absolute vorticity advection with a potential vorticity anomaly at the upper levels and the shallow frontal surface with a low level baroclinic zone or with a low level potential vorticity anomaly [48]. These two approaches to the surface cyclogenesis process are advocated by Prezerakos [31], Prezerakos et al. [32], and Thorncroft and Flocas [27] in their findings about the baroclinic character of the Atlas depressions.

During the next 48 h the direction of the tropospheric flow at all the isobaric levels remains almost constant making the atmospheric circulation systems, surface depressions, and upper air troughs move north-eastwards (Figures 5 and 6). Thus, depression L<sub>1</sub> (Figure 5), being associated with trough T<sub>1</sub> in the south of Atlas Mountains at 12:00 UTC on 25 March 1992 (Figure 4), moves to a position with

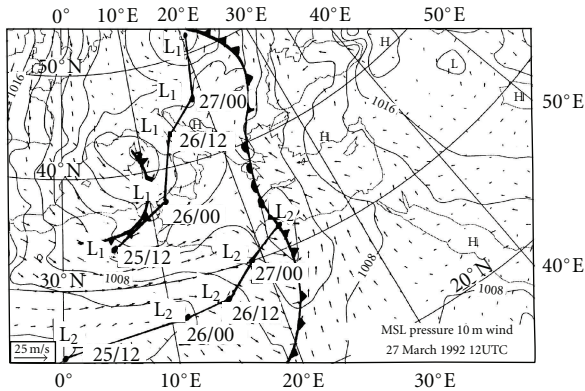


FIGURE 5: Same as Figure 1, but for 27 March 1992/12:00 UTC. Dots and straight segments show the successive 12-hour positions and tracks of the surface depressions  $L_1$  and  $L_2$ . The numbers dd/hh denote day and hour.

its centre located at  $50^\circ\text{N}$ ,  $21^\circ\text{E}$  at 12:00 UTC on 27 March 1992 (Figure 5) ahead of trough  $T_1$  (Figure 6) which followed almost the same path. Trough  $T_2$ , lying behind  $T_1$  at 12:00 UTC on 25 March 1992 (Figure 4) is within an asymmetrical wind field with much stronger winds on its western side plus cold advection and an SW-NE orientation of its axis. Thus it intensified within the next 24 h. Trough  $T_2$ , following a path almost parallel to that of trough  $T_1$  but more southerly, arrives at a position just southwest of Greece at 12:00 UTC on 27 March 1992 (Figure 6) making the advection of absolute vorticity toward Greece positive enough to create strong upward vertical motion over the Athens region at 700 and 500 hpa levels.

Figure 7 shows that the maximum values of the upward synoptic-scale velocities at 700 and 500 hpa levels are 2.8 and  $3.0 \text{ Pas}^{-1}$ .

The combination of the warm air advection—caused by depression  $L_1$  at lower levels—and cold air advection at upper levels (the lowest temperatures in the vicinity of trough  $T_2$  are  $-27^\circ\text{C}$  at 500 hpa level and  $-48^\circ\text{C}$  at 300 hpa level) contributes significantly to this upward motion regime over Athens, leading to destabilization of the air mass. As the air mass ascends, the water vapour contained cools due to adiabatic expansion and clouds are formed using as condensation nuclei a part of the dust grains at higher levels, while the remaining dust grains and those drifting at lower levels are drawn away down by the rain.

**3.2. Trajectories.** The best way to diagnose and identify the sources of the air at various levels up to 500 hpa above Athens and Thessaloniki regions at the time of the appearance of coloured rain is to calculate backward trajectories arriving at the point and time under consideration (here Athens and Thessaloniki at 12:00 UTC on 27 March 1992). Figure 8(a) shows such trajectories. It can be seen that the air at 850 and 700 hpa at 12:00 UTC on 27 March 1992 above Athens was, 48 h previously (25 March/12:00 UTC), over Libya (Figure 8(a) left) behind a surface high at the south-eastern

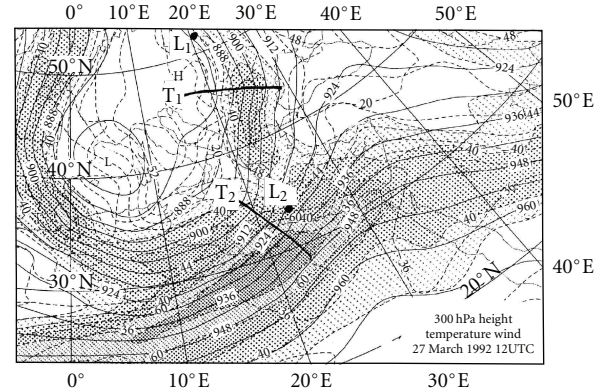


FIGURE 6: Objective analysis of geopotential height, temperature, and jet stream axes for 300 hpa on 27 March 1992/12:00 UTC. Geopotential contours: every 60 gpm, isotherms: every  $2^\circ\text{C}$ , and jet stream axes denote wind speed more or equal to  $30 \text{ ms}^{-1}$ ;  $T_1$  and  $T_2$  are trough lines and  $L_1$  and  $L_2$  the surface depression centres.

most flank of depression  $L_2$  (Figure 1) at a height of about 1000 m (air reaching 850 hpa above Athens was at 910 hpa and air reaching 700 hpa above Athens was at 890 hpa as Figure 8(a) right shows).

The air at these levels came from the region where depression  $L_1$  initiated. Also, the air at 500 hpa over Athens at 12:00 UTC on 27 March 1992 was, 48 h earlier (25 March/12:00 UTC), at a level of 800 hpa to the south of the Atlas Mountains, where the depression  $L_1$  was developing. This air at 800 hpa level is likely to contain dust grains and to carry them for a long distance over Greece. On the other hand, the air near the surface has come to Athens following a path passing through southwest Turkey and north Crete toward Athens with little likelihood of containing dust.

Figure 8(b) shows the same trajectories for Thessalonica, in northern Greece, where the coloured rain appeared in smaller amounts of 6 mm/12 h, almost all trajectories come from the region where depression  $L_1$  developed 48 h earlier. The trajectory which brings the air to the arrival point at 850 hpa is the most important one, since 60 h before it is at the region, where depression  $L_1$  was developing (Figure 8(b) left and Figure 1), it was at a height of 930 hpa (about 700 m) (Figure 8(b) right) and likely to have acquired significant quantities of dust and to convey it for a very long distance. The lowest trajectory comes from the eastern Mediterranean Sea. It brings moisture due to its path being tracked over the sea but does not carry dust or sand particles.

From the above discussion it can be claimed that the calculation of trajectories by a global or regional sophisticated numerical model using initialized analyses every 6 h is the best way to detect the source and the course of the dust or the sand which is responsible for the creation of coloured rain falling over Greece and generally over the South Balkans.

**3.3. Satellite Images.** Satellite images are a useful tool to detect sand clouds. During the initial process of the dust cloud formation and the depression development over the north Sahara it is very difficult to identify the dust cloud

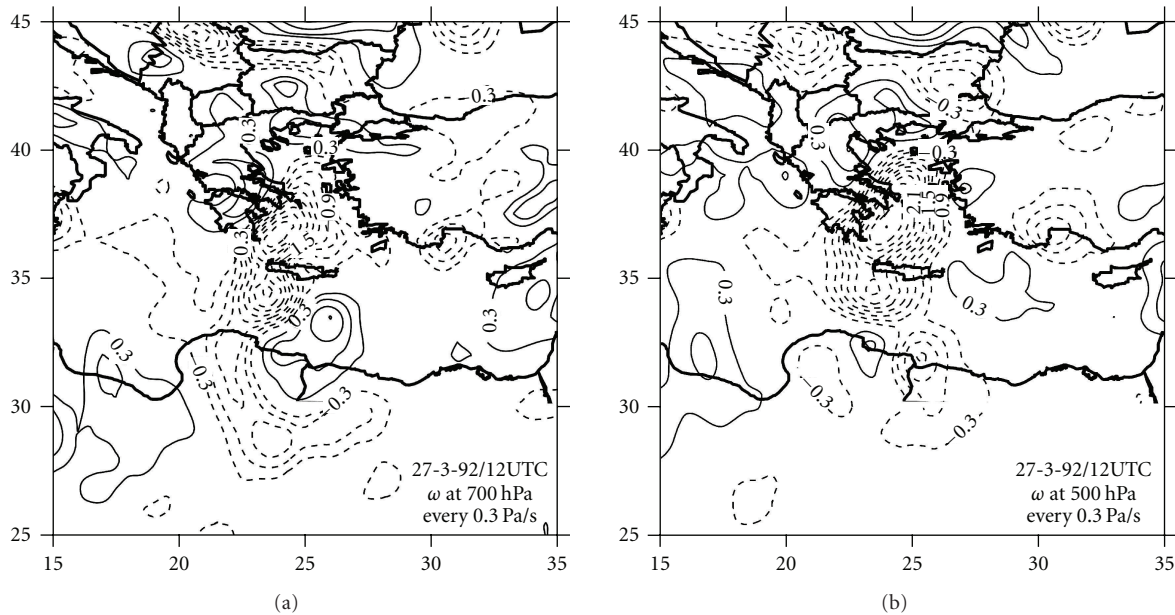


FIGURE 7: Same as Figure 2, but for (a) 700 hpa and (b) 500 hpa for 27 March 1992/12:00 UTC.

in the visible band since, being still near the ground, the dust cloud exhibits almost the same reflectivity as the ground below. Infrared imagery should overcome this difficulty because, during daytime, measurements by Ackerman and Inoue [49], Ackerman [50], and Wald [51] show that the thermal gradient is so strong near the overheated arid surfaces that 10–20 K [52] are typical values of the difference between the “skin” surface temperature and the air temperature at 2 m. Therefore a dust layer is colder than the surface by at least this value and can be detected by the satellite radiometer NOAA 11. Unfortunately infrared imagery at 12:00 UTC on 25 March 1992 over the source of the dust cloud in NW Sahara was not available. However, when the sand cloud moved on to a position over the Mediterranean Sea, then the necessary differences in reflectivity existed and there was a better temperature contrast between the dust cloud and the sea surface below, especially where the sea was rough. In this case, the dust cloud can be easily identified from the sea surface below, because it appears in the imagery as white or light grey and the sea surface as black in both visible and infrared images.

Combining the visible imagery of NOAA 11 received at 12:24 UTC on 26 March 1992 (Figure 9(a)) and Figure 8 showing the trajectories coming to Greece, we can detect (Figure 9(a), where the arrow points) a dust cloud at low levels between Libya and Greece moving towards Greece. Twelve hours later the sand cloud has reached Greece, while in twelve hours more two clouds of dust particles have entered the Mediterranean Sea coming from Tunisia and Libya (Figure 9(b), where the arrows point).

By making use of satellite pictures in association with forecasting trajectories, it is possible to forecast the time of coloured rain appearance in the South Balkans.

#### 4. Analysis and Discussion of the 4th April 1988 Case of Dust Deposit in North Greece

During the morning on 4th April 1988 fine sand deposits occurred in north-eastern Greece and especially upon Thessalonica. As this phenomenon has already been investigated synoptically by Makrogiannis et al. [26], we will give only a brief description of the synoptic-scale atmospheric circulation associated with it and focus on the NOAA AVHRR images and the 2-day backward trajectories, which are parts of the computed 5-day backward ones, using the methodology described in Section 2. Although the chemical and aeromicrobiological nature of the dust deposit was investigated by many scientists in the last years [53–56], there is no data available for this case. Makrogiannis et al. [26] noted that “the National Commission of Environmental Protection announced that this was not a case of common Greek dust and hence did not cause any change in the concentration of sulphur dioxide, carbon dioxide and nitrogen oxides in air. The Laboratory of Nuclear Physics of the University of Thessalonica also announced that the dust in question was relatively more radioactive than the common Greek dust or sand found in the area.”

Two days earlier at 00:00 UTC on 2 April 1988 an intensive depression developed covering almost all the northwest Sahara (Figure 10) accompanied by strong winds.

The main depression is moving north-eastwards so that, 24 h later, it is found over the coast of Tunisia in the Mediterranean Sea (not shown). The atmospheric conditions for a deep turbulent kinetic energy (TKE) field and a very deep mixing layer, which over the desert, reaches up to a depth of over 5 km during the hours of daylight, are thus favourable for fluxes of dust from the land to the atmosphere, which increase during the less stable daytime

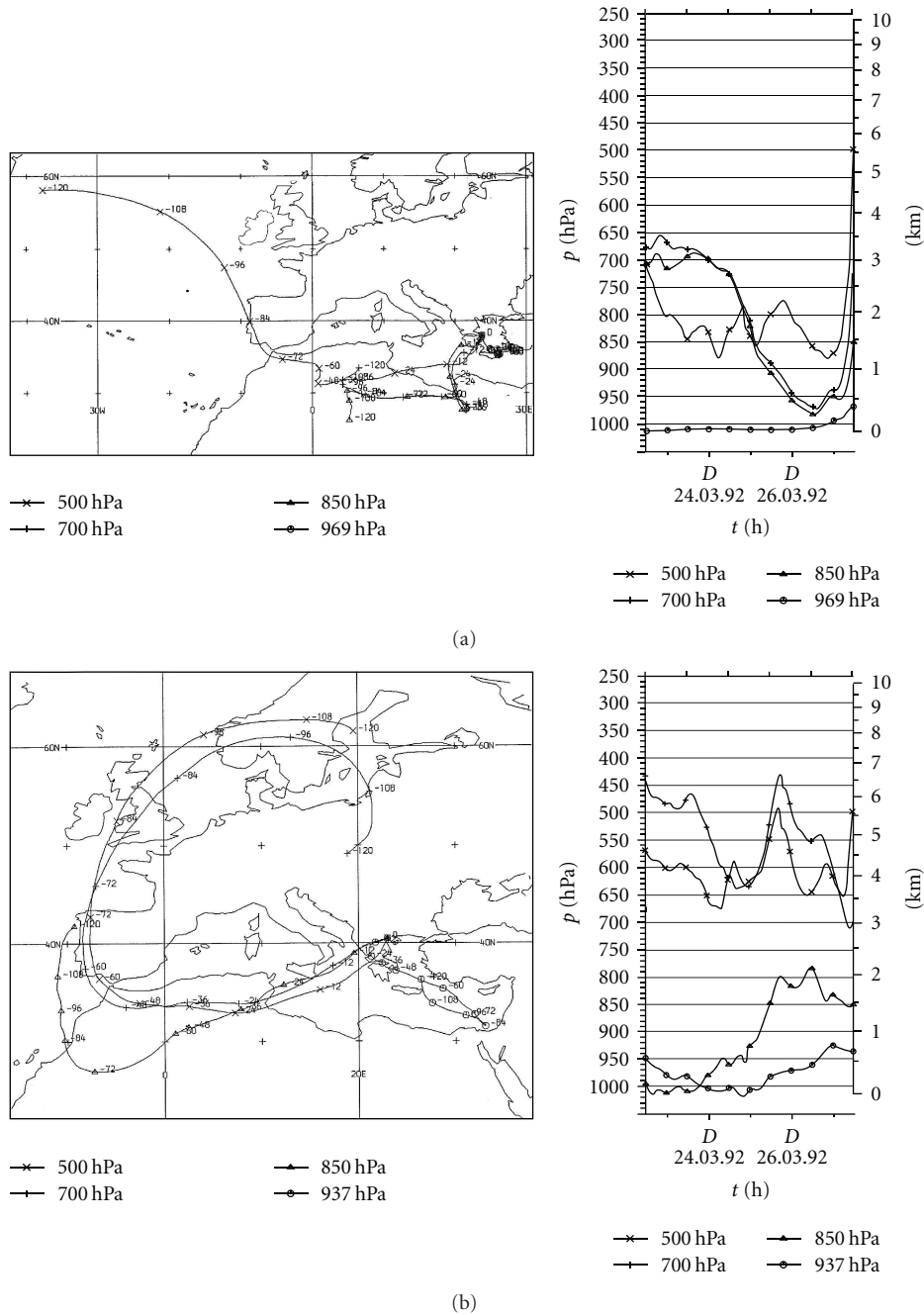


FIGURE 8: Backward trajectories with arrival (starting) point of (a) Athens ( $23.72^{\circ}\text{E}$ ,  $37.97^{\circ}\text{N}$ ) and (b) Thessalonica at 12:00 UTC on 27 March 1992. Left part shows geographical positions and time (hours from the arrival time), and the right part shows vertical positions and time.

boundary layer conditions and reach a peak in the early afternoon. As a result, large amounts of fine sand grains smaller than  $20\ \mu\text{m}$  (dust) were stirred up in the form of a dust cloud with vertical velocities very much greater than the synoptic-scale ones. The synoptic-scale velocity values are about  $-0.6\ \text{Pas}^{-1}$  at 850 hpa and  $-0.5\ \text{Pas}^{-1}$  at 700 hpa level, especially at the vicinity of the depression's centre (not shown). As the atmospheric flow in the entire troposphere was south-westerly (Figures 11(a) and 11(b)), the dust cloud was conveyed north-eastwards.

This movement is fully supported by the two-day parts of the computed 5-day backwards trajectories depicted by Figure 12 and the NOAA AVHRR images (Figures 13(a) and 13(b)). Three of the trajectories calculated to arrive over Thessalonica at 00:00 UTC on 4 April 1988 (namely at 300, 500, 700, hpa heights) came from the southwest. The air parcels associated with the 300 hpa and 500 hpa trajectories are found over the region of the strong pressure gradients, thus where the sandstorms were 48 h previously. The calculated air parcels heights at 00:00 UTC/2 April 1988

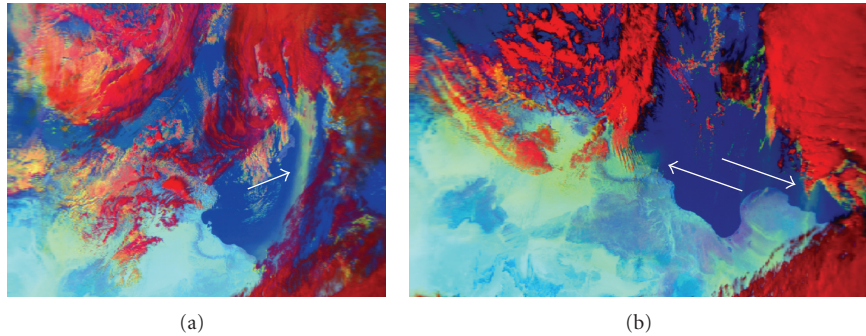


FIGURE 9: NOAA11 AVHRR satellite visible images received at (a) 12:24 UTC on 26 March and (b) 12:12 UTC on 27 March 1992.

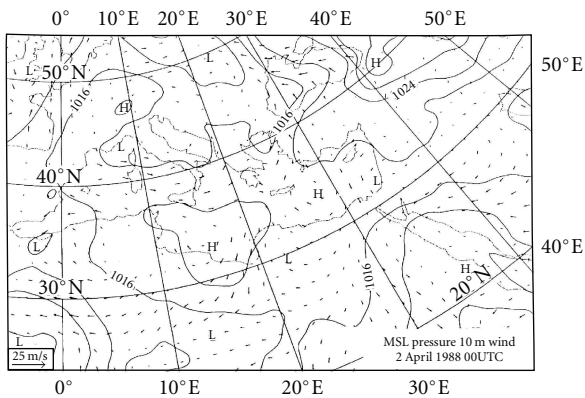


FIGURE 10: Same as Figure 1, but for 00:00 UTC on 2 April 1988.

are 835 hpa for the 300 hpa trajectory and 804 hpa for the 500 hpa trajectory, that is, they were fully inside the mixing layer. The forming dust cloud will have extended up to the mixing layer top, that is, over 5 km, and it will travel together with the air parcels between 500 hpa and 300 hpa trajectories rising continuously in the beginning of the period. But later the dust cloud moves far from the source region and the deep mixing layer. Thus it diffuses, becoming sparse and independent whether being in a synoptic-scale downward or ordinary upward vertical motion field, and it slightly subsides due to the force of gravitation.

At the same time the air parcels associated with the 700 hpa trajectory can be found 48 hours before their arrival over Thessalonica at the south borders of Tunisia and Libya (16°E, 26°N) at a height of 757 hpa (Figure 13) where a secondary depression is developing in the neighbourhood of a surface anticyclone. Strong pressure gradients are produced in this region causing dust storms. This trajectory, waving up and down slightly, is directed towards south Italy being at 830 hpa level over the Mediterranean Sea. Almost all trajectories converge at the atmospheric layer between about 850 and 700 hpa levels over southeast Italy as they approach North Greece.

Examining a coloured NOAA satellite image on 2 April 1988 at 14:17 UTC produced by AVHRR channels 4, 5, and 4 inverted after processing, we are able to observe the dust cloud. On this image yellowish pixels represent large areas

of the dust clouds coming from northern Africa and are mostly to be found over the Mediterranean close to the Tunisia coastline. A secondary dust maximum shown in the Adriatic sea seems not to be associated with the dust settled at Thessalonica 36 h later because it is much northern than Thessalonica, and the lower tropospheric circulation, west of northern Greece, is intensively southern. Also on this image clouds are blue or dark blue and land gets an orange or reddish colour. The main dust cloud is shown clearly in the coloured version of the abovementioned image where the letter S is (Figure 13(a)).

On the next day (14:17 UTC on 3 April 1988) all the area of Italy, Greece, and Algeria is covered by clouds as shown in another coloured image (Figure 13(b)) and it is difficult to recognize the dust, which is embedded in them. However, where the clouds are broken, we are able to see the yellow pixels of the dust close to south Italy extending towards the coasts of Algeria and Tunisia where a dust cloud is depicted clearly. On this coloured image, a different image processing approach has been applied than that on the previous one. On this image clouds are white, sea is blue, and land is green. Dust remains yellow. These pieces of evidence lead us to the estimation that the region between letters C and S (Figure 13(b)) is covered by the dust cloud (the colour AVHRR images were received from University of Dundee). It is evident that the dust plume observed more west, where the letter C is, would rather be associated to a Sahelian source as 500 and 300 hpa back trajectories indicate (Figures 13(b) and 12).

During the 12-hour interval, (that is, between 00:00 and 1200 UTC on 3 April 1988) the atmospheric circulation remains anticyclonic over West and North Greece (Figures 14(a) and 14(b)) with a distinct synoptic scale surface anticyclone at 12:00 UTC on 3 April 1988 (Figure 15).

In the next hours the surface anticyclone advances north-eastwards while an intensive field of upward synoptic scale motion dominates over Greece, especially west of Thessalonica. At the same time over the sea south of Italy a field of downward vertical synoptic scale of atmospheric motion is established (Figure 16). At that region the 700, 500, and 300 hpa trajectories converge facilitating the transport of dust to Thessalonica ground following often the isentropes, keeping the falling even at 00:00 UTC on 4 April 1988, although upward synoptic-scale vertical motion

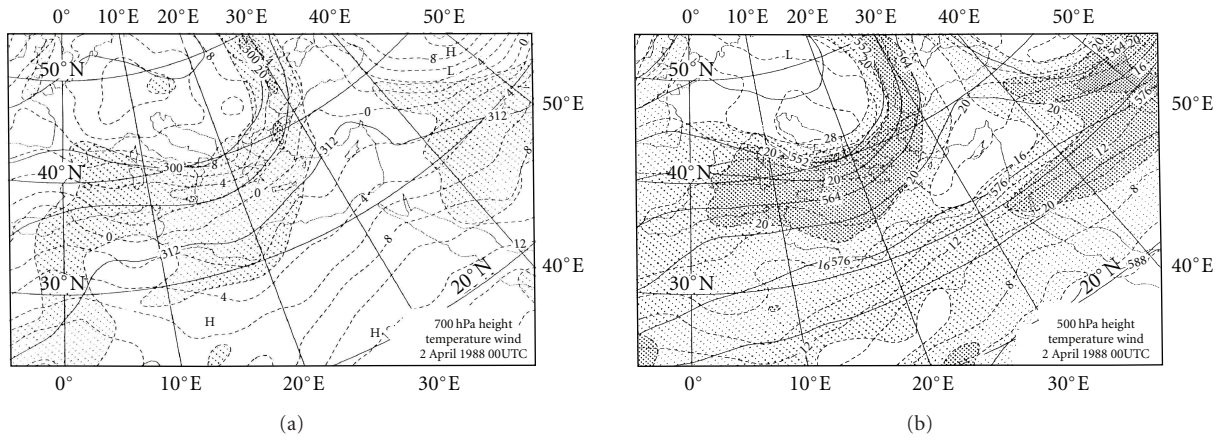


FIGURE 11: Same as Figures 3(b) and 3(c), but for 00:00 UTC on 2 April 1988, (a) 700 hPa and (b) 500 hPa.

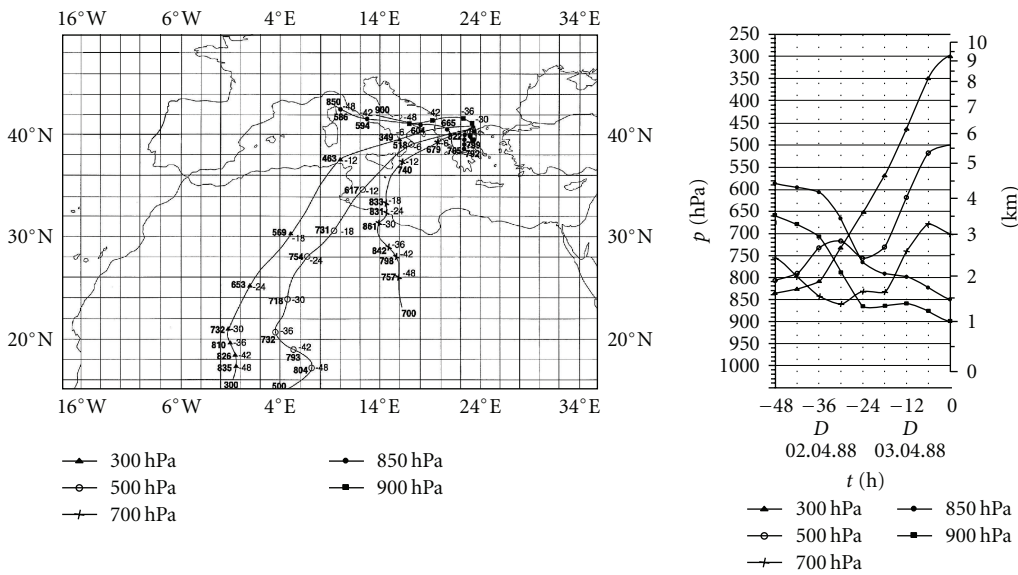


FIGURE 12: Same as Figure 8(b), but for 00:00 UTC on 4 April 1988.

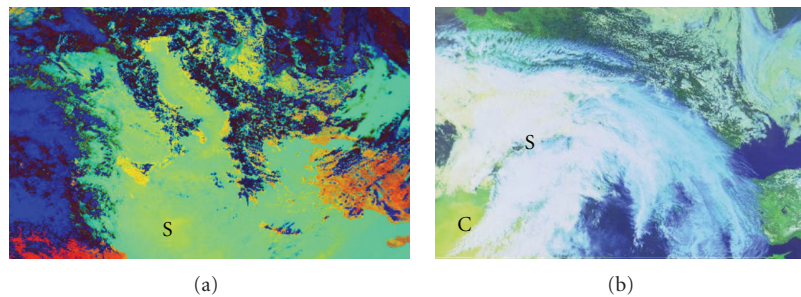


FIGURE 13: NOAA AVHRR images coloured versions (a) of channels 4, 5, and 4 inverted at 14:17 UTC on 2 April 1988 and (b) of channel 4 at 14:17 UTC on 3 April 1988.

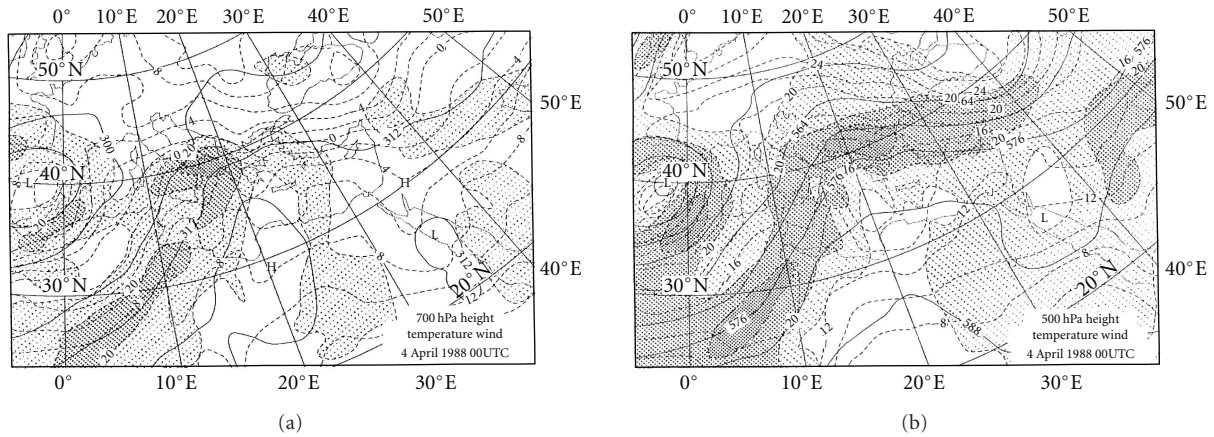


FIGURE 14: Same as Figures 3(b) and 3(c), but for 00:00 UTC on 4 April 1988, (a) 700 hpa and (b) 500 hpa.

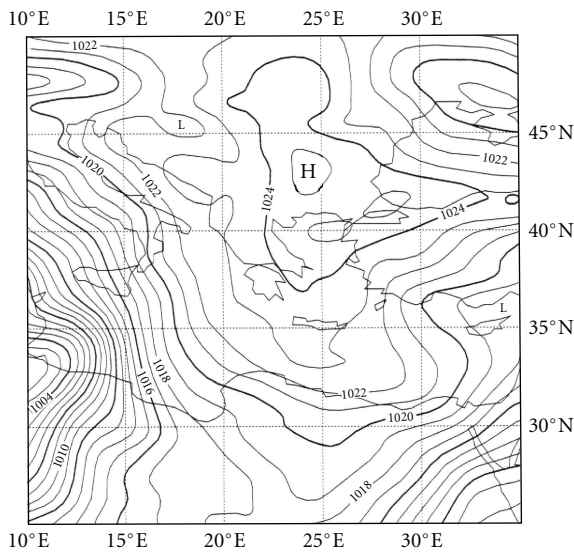


FIGURE 15: Same as Figure 1, but for 12:00 UTC on 3 April 1988. Isobars: every 1 hpa.

was maintaining over Thessalonica (Figure 16(b)). The final result was deposits of fine sand being left visible on the roofs of the cars. This last one is an irrefutable fact coming from the observation.

The above analysis showed that the dust has come from the region where the dust storms appeared two days earlier. The trajectories arriving at Thessalonica came from the area of interest starting from inside a very deep mixing layer. This fact and the irrefutable fact of dry dust deposit upon Thessalonica ground lead us to the conclusion that (i) a dust cloud after being stirred up to the top of mixing layer in this case at a height of five km as mentioned above can travel over a large distance if it is in an atmospheric environment of strong upward vertical motion resisting the gravity, and (ii) when a dust cloud, which has already been diffused and moved out of its source area, is found in an environment of downward vertical motion or in ordinary synoptic-scale upward motion, the dust will start to fall out

under the force of gravity after reaching a critical downward velocity. Figure 12 right shows that this occurred for the 700, 500, and 300 hpa trajectories 30 h to 24 h before arriving at Thessalonica. They then moved into a subsiding region and converged over South Italy and north Ionian Sea in the layer 800–700 hpa. The dust cloud in this layer is forced at this time by the subsiding motion of the trajectories, and the particles, accelerated by gravity, continually fall out into lower levels forwarding at the same time following the wind direction. Thus, eventually, the south-westerly air flow with its load of sand grains lands at North Greece and reaches Thessalonica. This dust layer 800–700 hpa having a gravitational settling velocity of  $\sim 10 \text{ cm s}^{-1}$  should take about 10 h to reach the ground, but the dust cloud moving eastwards to Thessalonica enters a field of strong upward synoptic scale atmospheric motion contrasting the gravity fall reducing very much the gravitational settling velocity, thus justifying the length of time of approximately 24 h for the particulate to finally settle down in Thessalonica. To better clarify the dry deposition mechanism, the presentation of time series of PM concentrations in Thessalonica would be very useful, but such data is not available. During that period only gas pollutants were being observed.

### 5. Concluding Remarks

In this study we have attempted to examine the phenomenon of significant dust deposits over Greece through the analysis of two case studies. The first case study is relevant to the coloured rain which occurs frequently over Greece and the second case study to the very rare cases of dust deposit. This second phenomenon, consisting of a large amount of dust deposit which is visible on the streets, the car, and house roofs, has occurred only once in the last twenty years, on 4 April 1988 over northern Greece. On the other hand throughout the year, and especially during spring, there are often very light, barely visible dust deposits over the South Balkans. Both phenomena are associated with the appearance of depressions that are generated in northwest

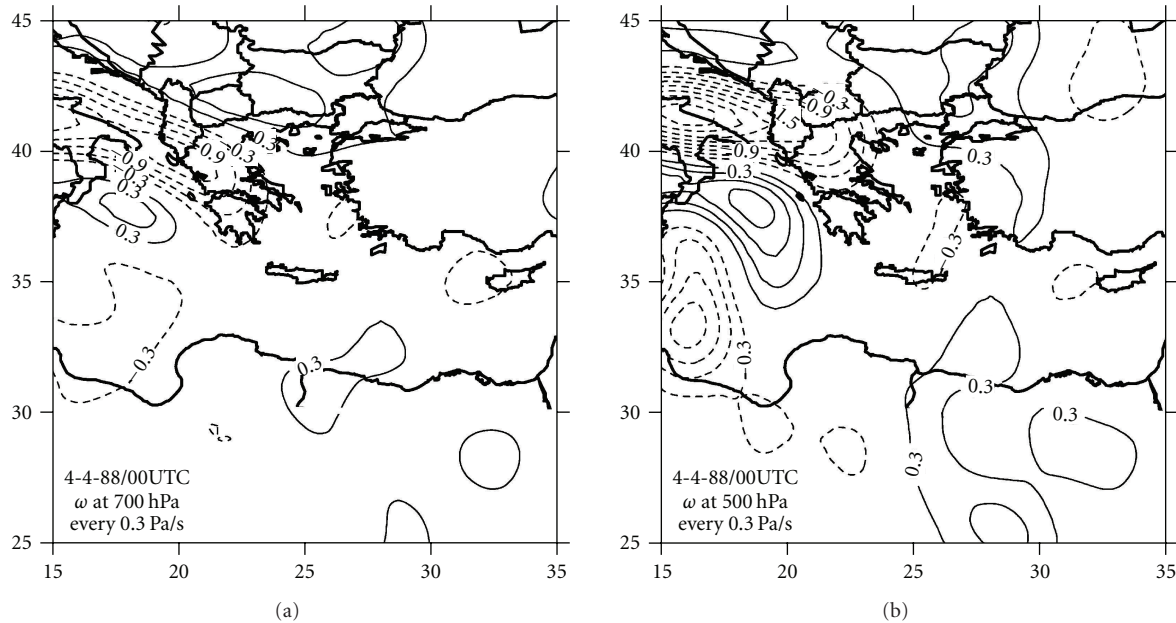


FIGURE 16: As Figure 2, but for 00:00 UTC on 4 April 1988, (a) 700 hPa and (b) 500 hPa.

Sahara, to the south of the Atlas Mountains especially during spring [3, 18, 33, 34].

It was found that, two days before the occurrence of the dust deposit over Greece, a sand storm appeared over the northwest part of the Sahara desert due to a vigorous Atlas mountain depression. The flow in the entire troposphere, and especially in its lower half where the dust grains in the form of a dust cloud could be stirred up, was S-SW carrying the dust cloud for a long distance reaching Greece and the South Balkans.

In the case of coloured rain, the dust cloud arrived over Greece with warm air advection and upward synoptic-scale vertical motion resulting in the cooling of the water vapour contained due to adiabatic expansion and clouds were formed using as condensation nuclei a part of the dust grains at higher levels while the remaining dust grains and those drifting at lower levels were drawn away down by the rain.

In the case of the dry dust deposit upon Thessalonica the atmospheric circulation at the start of the route of the dust cloud was intensively cyclonic while over the route about 30 h to 24 h before the dust appearance it was intensively anti-cyclonic resulting in the initiation of large-scale subsidence. This together with the contributing downward gravitational motion resulted in the occurrence of widespread dust deposit on the surface although upward large-scale synoptic motion regime dominated over Thessalonica.

Air backward trajectories starting from the time and the point under consideration confirm the origin of the dust cloud but the justification given of the dry dust deposit over Thessalonica ground is rather complicated and not absolutely clear. Also, AVHRR satellite images were able to give information on the base height and the depth of the dust cloud, when this was positioned away from the Sahara, over the Mediterranean Sea.

It should be noted that the process followed, leading to the development of the Atlas depression necessary for the occurrence of a dust storm, is the usual one characterizing the baroclinic waves and starting when the PFJ migrates southwards enough to reach the Atlas Mountains of north-west Africa. Good example cases could be found on the EUMETSAT web page: <http://www.eumetsat.int/> (satellite images of the month).

Finally it would be mentioned that special attempt has been done for the physical justification of the fact that deposits of fine sand are left visible especially on the roofs of the cars in Thessalonica in the morning on 4th April 1988. The inclusion of time series of PM concentration would strengthen the analysis, but unfortunately such data is not available. For those readers who are not satisfied with the justification given, the road is open for complementary research using more advanced scientific tools. We may continue our attempt for a future second paper including in our scientific tools the Athens University Eta model (Professor G. Kallos research group). This sophisticated model [17, 22] that has been under continuous upgrading proved very effective in predicting the dust cycle (suspension, transport, concentration, and deposition) in every day weather forecasts.

## Acknowledgments

The authors wish to thank Dr. David Axford, former deputy Secretary General of World Meteorological Organization (WMO) for his constructive comments, ECMWF, DWD, associate Professor H. Feidas, and Dr. A. Anthis, for the provided data. Also, the authors would like to thank the reviewers for their very constructive and detailed comments.

## References

- [1] V. E. Angouridakis, *A Case of Coloured Rain in the Area of Thessaloniki*, Meteorologika, no. 14, University of Thessaloniki, 1971.
- [2] S. Karoulias, *The Saharian Depressions*, Meteorologika, no. 57, University of Thessaloniki, 1971.
- [3] N. G. Prezerakos, "The northwest African depressions affecting the south Balkans," *Journal of Climatology*, vol. 5, no. 6, pp. 643–654, 1985.
- [4] M. Athanassiadou, H. Flocas, M. A. J. Harrison, M. C. Hort, C. S. Witham, and S. Millington, "The dust event of 17 April 2005 over Athens, Greece," *Weather*, vol. 61, no. 5, pp. 125–131, 2006.
- [5] M. T. Tullet, "A dust fall on 6 March 1977," *Weather*, vol. 33, pp. 48–52, 1978.
- [6] R. F. File, "Dust deposit in England on 9 November 1984," *Weather*, vol. 41, pp. 191–195, 1986.
- [7] S. Rodríguez, X. Querol, A. Alastuey, G. Kallos, and O. Kakaliagou, "Saharan dust contributions to PM10 and TSP levels in Southern and Eastern Spain," *Atmospheric Environment*, vol. 35, no. 14, pp. 2433–2447, 2001.
- [8] J.-B. Stuut, I. Smalley, and K. O'Hara-Dhand, "Aeolian dust in Europe: African sources and European deposits," *Quaternary International*, vol. 198, no. 1-2, pp. 234–245, 2009.
- [9] J. M. Prospero, E. Bonatti, C. Schubert, and T. N. Carlson, "Dust in the Caribbean atmosphere traced to an African dust storm," *Earth and Planetary Science Letters*, vol. 9, no. 3, pp. 287–293, 1970.
- [10] J. M. Prospero and T. N. Carlson, "Vertical and areal distribution of Saharan dust over the western equatorial North Atlantic Ocean," *Journal of Geophysical Research*, vol. 77, pp. 5255–5265, 1972.
- [11] G. E. Shaw, "Transport of Asian desert aerosol to the Hawaiian Islands," *Journal of Applied Meteorology*, vol. 19, no. 11, pp. 1254–1259, 1980.
- [12] Y. Iwasaka, H. Minoura, and K. Nagaya, "The transport and spacial scale of Asian dust-storm clouds: a case study of the dust-storm event of April 1979," *Tellus*, vol. 35B, no. 3, pp. 189–196, 1983.
- [13] M. Uematsu, R. A. Duce, J. M. Prospero, L. Chen, J. T. Merrill, and R. L. McDonald, "Transport of mineral aerosol from Asia over the North Pacific ocean," *Journal of Geophysical Research*, vol. 88, no. C9, pp. 5342–5352, 1983.
- [14] E. F. Danielsen, "The relationship between severe weather, major dust storms and rapid large-scale cyclogenesis, Parts I and II," in *Subsynchronous Extratropical Weather Systems: Observations, Analysis, Modeling, and Prediction; Notes from a Colloquium: Summer 1974*, vol. 2, National Center for Atmospheric Research, Boulder, Colo, USA, 1975.
- [15] D. G. Kaskaoutis, H. D. Kambezidis, P. T. Nastos, and P. G. Kosmopoulos, "Study on an intense dust storm over Greece," *Atmospheric Environment*, vol. 42, no. 29, pp. 6884–6896, 2008.
- [16] R. Jones, "Atmospheric dispersion modelling at the Met. Office," *Weather*, vol. 59, no. 11, pp. 311–316, 2004.
- [17] G. Kallos, A. Papadopoulos, P. Katsafados, and S. Nickovic, "Transatlantic Saharan dust transport: model simulation and results," *Journal of Geophysical Research*, vol. 111, no. 9, Article ID D09204, 2006.
- [18] N. Kubilay, S. Nickovic, C. Moulin, and F. Dulac, "An illustration of the transport and deposition of mineral dust onto the eastern Mediterranean," *Atmospheric Environment*, vol. 34, no. 8, pp. 1293–1303, 2000.
- [19] B. Marticorena, G. Bergametti, B. Aumont, Y. Callot, C. N'Doumé, and M. Legrand, "Modeling the atmospheric dust cycle 2. Simulation of Saharan dust sources," *Journal of Geophysical Research*, vol. 102, no. 4, pp. 4387–4404, 1997.
- [20] S. Michaelides, P. Evripidou, and G. Kallos, "Monitoring and predicting Saharan Désert dust events in the eastern Mediterranean," *Weather*, vol. 54, pp. 311–316, 1999.
- [21] S. Ničković and S. Dobričić, "A model for long-range transport of desert dust," *Monthly Weather Review*, vol. 124, no. 11, pp. 2537–2544, 1996.
- [22] S. Nickovic, O. Kakaliagou, G. Kallos, D. Jovic, and A. Papadopoulos, "Eta/dust model: sensitivity to model resolution and desert source specification," in *Proceedings of the 1st LAS/WMO International Symposium on Sand and Dust Storms*, WMO Programme on Weather Prediction Research Report Series Project no. 10, WMO Technical Document no. 864, pp. 187–196, Damascus, Syria, November 1997.
- [23] S. Nickovic, G. Kallos, A. Papadopoulos, and O. Kakaliagou, "A model for prediction of desert dust cycle in the atmosphere," *Journal of Geophysical Research*, vol. 106, no. 16, pp. 18113–18129, 2001.
- [24] L. Carapiperis and A. Tataris, "Coloured rain during the 15 and 22 March of 1962," in *Proceedings of the Academy of Athens*, vol. 38, pp. 300–308, 1963.
- [25] T. A. Charadonis, T. J. Makrogiannis, and A. A. Flocas, "The possibility of identification of sand clouds and prediction of coloured rain over Greece by mean of satellite imagery," *Bulletin of the Geological Society of Greece*, vol. 25, no. 4, pp. 303–314, 1991.
- [26] T. Makrogiannis, A. Flocas, N. Ramos, and A. Karipidis, "A case of dust fall and coloured rain in the Greek area," *Rivista di Meteorologia Aeronautica*, vol. 50, no. 1-2, pp. 65–74, 1990.
- [27] C. D. Thorncroft and H. A. Flocas, "A case study of Saharan cyclogenesis," *Monthly Weather Review*, vol. 125, no. 6, pp. 1147–1165, 1997.
- [28] Karein D., *The forecasting of cyclogenesis in the Mediterranean region*, Ph.D. thesis, University of Edinburgh, Edinburgh, Scotland, 1975.
- [29] F. Defant, "On the hydrodynamic instability caused by approach of subtropical and polar front jet stream in northern latitudes before the onset of strong cyclogenesis," in *Rossby Memorial Volume: The Atmosphere and Sea in Motion*, B. Bolin, Ed., pp. 305–325, Rockefeller Institute, New York, NY, USA, 1959.
- [30] N. G. Prezerakos, H. A. Flocas, and D. Brikas, "The role of the interaction between polar and subtropical jet in a case of depression rejuvenation over the Eastern Mediterranean," *Meteorology and Atmospheric Physics*, vol. 92, no. 1-2, pp. 139–151, 2006.
- [31] N. G. Prezerakos, "Synoptic flow patterns leading to the generation of north-west African depressions," *International Journal of Climatology*, vol. 10, no. 1, pp. 33–48, 1990.
- [32] N. G. Prezerakos, S. C. Michaelides, and A. S. Vlasi, "Atmospheric synoptic conditions associated with the initiation of north-west African depressions," *International Journal of Climatology*, vol. 10, no. 7, pp. 711–729, 1990.
- [33] U. Dayan, J. Heffter, J. Miller, and G. Gutman, "Dust intrusion events into the Mediterranean basin," *Journal of Applied Meteorology*, vol. 30, no. 8, pp. 1185–1199, 1991.
- [34] C. Moulin, C. E. Lambert, U. Dayan et al., "Satellite climatology of African dust transport in the Mediterranean atmosphere," *Journal of Geophysical Research*, vol. 103, no. D11, pp. 13137–13144, 1998.

- [35] B. Marticorena and G. Bergammetti, "Modelling the atmosphere dust cycle: 1-Design of a soil-derived dust production scheme," *Journal of Geophysical Research Atmospheres*, vol. 100, pp. 16415–16430, 1995.
- [36] D. Soderman and F. Dulac, "Monitoring and prediction of the atmospheric transport and deposition of desert dust in the Mediterranean region," in *Programme on Weather Prediction Research (PWPR)*, vol. 10 of *Report Series Project*, pp. 181–186, World Meteorological Organization, Geneva, Switzerland, 1998.
- [37] I. Tegen and I. Fung, "Modeling of mineral dust in the atmosphere: sources, transport, and optical thickness," *Journal of Geophysical Research*, vol. 99, no. D11, pp. 22897–22914, 1994.
- [38] S. A. Grigoryan and M. A. Sofiev, "Numerical modeling of dust elevation during storm episodes and its long-range atmospheric transport," in *Proceedings of the 1st LAS/WMO International Symposium on Sand and Dust Storms*, WMO Programme on Weather Prediction Research Report Series Project no. 10, WMO Technical Document no. 864, pp. 88–98, Damascus, Syria, November 1997.
- [39] N. G. Prezerakos, "Dust storms over Sahara Desert leading to dust deposit or coloured rain in the South Balkans," in *Proceedings of the 1st LAS/WMO International Symposium on Sand and Dust Storms*, WMO Programme on Weather Prediction Research Report Series Project no. 10, WMO Technical Document no. 864, pp. 21–38, Damascus, Syria, November 1997.
- [40] C. Kottmeier and B. Fay, "Trajectories in the Antarctic lower troposphere," *Journal of Geophysical Research*, vol. 103, no. D9, pp. 10947–10959, 1998.
- [41] World Meteorological Organization, World Weather Watch (WWW) Program, "Technical Progress Report on the Global Data-Processing System (GDPS)," Report Series 2, WMO, Geneva, Switzerland, 1995.
- [42] N. Brooks and M. Legrand, "Dust variability over northern Africa and rainfall in the Sahel," in *Linking Climate Change to Land Surface*, S. J. McLaren and D. R. Kniveton, Eds., Springer, New York, NY, USA, 2000.
- [43] P. Ginoux, M. Chin, I. Tegen, et al., "Global simulation of dust in the troposphere: model description and assessment," *Journal of Geophysical Research Atmospheres*, vol. 106, no. D17, pp. 20255–20273, 2001.
- [44] J. M. Prospero, P. Ginoux, O. Torres, S. E. Nicholson, and T. E. Gill, "Environmental characterization of global sources of atmospheric soil dust identified with the Nimbus 7 Total Ozone Mapping Spectrometer (TOMS) absorbing aerosol product," *Reviews of Geophysics*, vol. 40, no. 1, p. 1002, 2002.
- [45] S. Petterssen, *Weather Analysis and Forecasting*, vol. 1, McGraw-Hill, New York, NY, USA, 2nd edition, 1956.
- [46] S. Petterssen and S. J. Smebye, "On the development of extratropical cyclones," *The Quarterly Journal of the Royal Meteorological Society*, vol. 97, no. 414, pp. 457–482, 1956.
- [47] B. J. Hoskins, M. E. McIntyre, and A. W. Robertson, "On the use and significance of isentropic potential vorticity maps," *The Quarterly Journal of the Royal Meteorological Society*, vol. 111, no. 470, pp. 877–946, 1985.
- [48] N. G. Prezerakos, H. A. Flocas, and S. C. Michaelides, "Absolute vorticity advection and potential vorticity of the free troposphere as synthetic tools for the diagnosis and forecasting of cyclogenesis," *Atmosphere-Ocean*, vol. 35, no. 1, pp. 65–91, 1997.
- [49] S. A. Ackerman and T. Inoue, "Radiation energy budget studies using collocated AVHRR and ERBE observations," *Journal of Applied Meteorology*, vol. 33, no. 3, pp. 370–378, 1994.
- [50] S. A. Ackerman, "Remote sensing aerosols using satellite infrared observations," *Journal of Geophysical Research*, vol. 102, no. D14, pp. 17069–17079, 1997.
- [51] L. Wald, "Some terms of reference in data fusion," *IEEE Transactions on Geoscience and Remote Sensing*, vol. 37, no. 3, pp. 1190–1193, 1999.
- [52] J. P. Frangi, A. Druilhet, P. Durand, H. Ide, J. P. Pages, and A. Tinga, "Energy budget of the Sahelian surface layer," *Annales Geophysicae*, vol. 10, no. 1-2, pp. 25–33, 1992.
- [53] E. Katragkou, S. Kazadzis, V. Amiridis, V. Papaioannou, S. Karathanasis, and D. Melas, "PM10 regional transport pathways in Thessaloniki, Greece," *Atmospheric Environment*, vol. 43, no. 5, pp. 1079–1085, 2009.
- [54] A. Papayannis, D. Balis, V. Amiridis et al., "Measurements of Saharan dust aerosols over the eastern Mediterranean using elastic backscatter-Raman lidar, spectrophotometric and satellite observations in the frame of the EARLINET project," *Atmospheric Chemistry and Physics*, vol. 5, no. 8, pp. 2065–2079, 2005.
- [55] A. Poupkou, D. Melas, I. Ziomas et al., "Simulated summer-time regional ground-level ozone concentrations over Greece," *Water, Air, & Soil Pollution*, vol. 196, no. 1–4, pp. 169–181, 2009.
- [56] K. Markakis, A. Poupkou, D. Melas, and C. Zerefos, "A GIS based anthropogenic PM10 emission inventory for Greece," *Atmospheric Pollution Research*, vol. 1, no. 2, pp. 71–81, 2009.

## Research Article

# An Assessment of the Efficiency of Dust Regional Modelling to Predict Saharan Dust Transport Episodes

**D. K. Papanastasiou,<sup>1</sup> A. Poupkou,<sup>2</sup> E. Katragkou,<sup>2</sup> V. Amiridis,<sup>3</sup> D. Melas,<sup>2</sup> N. Mihalopoulos,<sup>4</sup> S. Basart,<sup>5</sup> C. Pérez,<sup>6</sup> and J. M. Baldasano<sup>5</sup>**

<sup>1</sup>Laboratory of Agricultural Engineering and Environment, Institute of Technology and Management of Agricultural Ecosystems, Centre for Research and Technology—Thessaly, Technology Park of Thessaly, 1st Industrial Area of Volos, 38500 Volos, Greece

<sup>2</sup>Laboratory of Atmospheric Physics, Aristotle University of Thessaloniki, Campus Box 149, 54124 Thessaloniki, Greece

<sup>3</sup>Institute for Space Applications & Remote Sensing, National Observatory of Athens, Metaxa and Vas. Paulou street, 15236 Penteli, Greece

<sup>4</sup>Environmental Chemical Processes Laboratory, Department of Chemistry, University of Crete, P.O.Box 2208, Voutes, 71003 Heraklion, Greece

<sup>5</sup>Earth Sciences Division, Barcelona Supercomputing Center, Nexus II Building, c/ Jordi Girona 29, 08034 Barcelona, Spain

<sup>6</sup>Earth Institute at Columbia University, NASA Goddard Institute for Space Studies and International Research Institute for Climate and Society, 405 Low Library, MC 4335, 535 West 116th Street, NY 10027, USA

Correspondence should be addressed to D. K. Papanastasiou, dkpapan@auth.gr

Received 17 May 2010; Accepted 19 July 2010

Academic Editor: Harry D. Kambezidis

Copyright © 2010 D. K. Papanastasiou et al. This is an open access article distributed under the Creative Commons Attribution License, which permits unrestricted use, distribution, and reproduction in any medium, provided the original work is properly cited.

Aerosol levels at Mediterranean Basin are significantly affected by desert dust that is eroded in North Africa and is transported northwards. This study aims to assess the performance of the Dust REgional Atmospheric Model (BSC-DREAM8b) in the prediction of dust outbreaks near the surface in Eastern Mediterranean. For this purpose, model PM10 predictions covering a 7-year period and PM10 observations at five surface monitoring sites in Greece are used. A quantitative criterion is set to select the significant dust outbreaks defined as those when the predicted PM10 surface concentration exceeds  $12 \mu\text{g}/\text{m}^3$ . The analysis reveals that significant dust transport is usually observed for 1–3 consecutive days. Dust outbreak seasons are spring and summer, while some events are also forecasted in autumn. The seasonal variability of dust transport events is different at Finokalia, where the majority of events are observed in spring and winter. Dust contributes by 19–25% to the near surface observed PM10 levels, which can be increased to more than  $50 \mu\text{g}/\text{m}^3$  during dust outbreaks, inducing violations of the air quality standards. Dust regional modeling can be regarded as a useful tool for air quality managers when assessing compliance with air quality limit values.

## 1. Introduction

A large portion of atmospheric Particulate Matter (PM) is derived from arid regions of the Earth (North Africa, Arabian Peninsula, central Asia, Australia, etc.) and is distributed all over the globe. Saharan desert is responsible for up to half of the global mineral dust emissions, thus it is considered as the most important dust source worldwide [1]. Once in the atmosphere, dust aerosols induce serious environmental and health effects [2]. They influence the Earth's radiation balance as they interact with solar and thermal radiation, causing large uncertainties in assessing climate forcing by

atmospheric aerosols [3], they impact on photolysis rates and ozone chemistry by modifying UV radiation [4], and they contribute to the increase of PM levels over populated areas. Therefore, the estimation of the dust load over an area as well as its contribution to aerosols surface concentration is crucial for the implementation of air quality and generally environmental management policies.

The North African desert dust cycle depends on the synoptic circulations, which control the frequency and extent of transport and on the washout by precipitation which influences the residences time of dust particles in the atmosphere. The bulk of the dust is transported

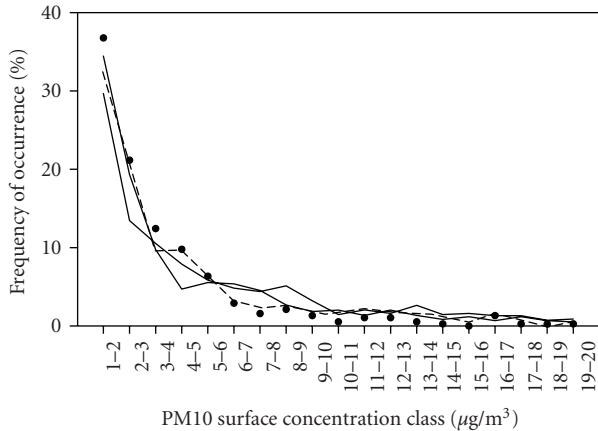


FIGURE 1: Frequency distribution of modelled PM10 surface concentrations. Finokalia: solid line; Thrakomakedones: bold solid line; Volos: dashed line; Panorama: dots.

westward into the Atlantic Ocean and an unnegligible part is transported northward across the Mediterranean basin to southern and even central Europe [5–7]. The dust cycle presents a marked seasonal variation and the more intense outbreaks are observed in summer [5, 8]. The Mediterranean dust is found to be multilayered within a wide range of altitudes, penetrating rather higher in the troposphere [9]. During strong perturbations, dust can reach up to 10 km in altitude and may last there for several days [10]. A detailed description of the synoptics that control the dust transport over the Mediterranean is given by Barkan et al. [7].

Regional modelling is considered as a useful tool to simulate and predict the dust cycle in the atmosphere. The Dust REgional Atmospheric Model (DREAM) [11] has reached a level of delivering reliable operational dust forecasts capable to predict all the major dust events over Mediterranean. It solves the Euler-type partial differential nonlinear equation for dust mass continuity. During model integration, calculation of the surface dust injection fluxes is made over the model grid points declared as deserts. The concentration equation simulates all major processes of the atmospheric dust cycle, namely, production, diffusion, advection, and removal. DREAM is already exploited in several studies. Viana et al. [12] applied it in combination with the MM5 meteorological model to interpret the levels and composition of particulate matter at the greater Barcelona area. Pérez et al. [13] report that the simulated dust horizontal and vertical structure shows very good qualitative agreement when compared to satellite images and lidar observations over Barcelona. Balis et al. [14] also found that there is a good agreement on the thickness and location of the dust layer between the model simulation and the lidar measurements recorded in Thessaloniki. However, Gerasopoulos et al. [15] state that the model shows a tendency to underpredict the atmospheric optical depth values and the surface PM10 concentrations in Athens urban area, where local anthropogenic emissions are significant. As the model undergoes significant revisions in order to improve the forecasting ability, there is a need for continuous validation by comparison of model

results with observations. The model could be validated using PM surface concentrations monitored in rural and/or urban areas, as well as remote sensing observations.

The aim of this study is to examine the capability of the updated version of DREAM at the Barcelona Supercomputer Center (BSC-DREAM8b, [13]) to predict the occurrence of Saharan dust transport episodes in the Eastern Mediterranean. Data recorded at five Greek sites (two urban, two suburban and one rural) are analyzed. The study is focused on the days when a dust outbreak is clearly predicted by the model. Therefore, a critical concentration value is firstly defined so as to select the dust transport events. The analysis covers the period 2001–2007.

## 2. Materials and Methods

**2.1. Near Surface PM10 Data.** PM10 data recorded automatically at five monitoring sites in Greece are exploited in this study (Table 1). Finokalia monitoring station is a member of the EMEP measurement network, while the rest four stations are members of the national network of air pollution monitoring that is developed by the Hellenic Ministry for the Environment, Physical Planning & Public Works (current title since 2009: Hellenic Ministry for the Environment, Energy & Climate Change). The stations have been selected in order to represent all geographic parts of Greece, for example, south (Finokalia, Heraklion), central (Thrakomakedones, Volos), and north (Panorama) parts of the country.

**2.2. Model Outputs.** The updated version of DREAM model, BSC-DREAM8b [13, 16], has been delivering operational dust forecasts over the North Africa-Mediterranean-Middle East and over Asia regions in the last years in the BSC (currently at <http://www.bsc.es/projects/earthscience/DREAM/>). The partial differential nonlinear equation for dust mass continuity is resolved in the Eulerian mode. BSC-DREAM8b is forced by the NCEP/Eta meteorological driver [17–21]. In this latest version of the model, the aerosol description is improved from 4 to 8 bins and dust-radiation interactions are included. As shown by Haustein et al. [22] for the SAMUM-I field campaign, BSC-DREAM8b (with increased number of dust size bins) transports the dust more efficient since the small particle size range ( $<10 \mu\text{m}$  effective radius) is better described. Furthermore, as shown in the annual evaluation of the model against AERONET data [23] for southern Europe, also good agreement is found with correct temporal representation of AOD peaks. BSC-DREAM8b distinguishes well between events and no-events, although the amplitude of the dusty events is generally underestimated. Finally, BSC-DREAM8b shows better results during the wet episodes due to the modified wet deposition scheme that it includes.

For the present study, simulation is initialized with 24-hourly (at 00UTC) updated NCEP (National Centers for Environmental Prediction)  $0.5^\circ \times 0.5^\circ$  analysis data and the initial state of dust concentration in the model is defined by the 24-hour forecast from the previous-day model run because there are not yet satisfactory three-dimensional dust

TABLE 1: PM10 monitoring sites<sup>1</sup>.

Monitoring site	Latitude (N)	Longitude (E)	Altitude (m)	Type	Data availability (%)
Heraklion	35.30°	25.13°	10	Urban	71
Finokalia	35.33°	25.67°	150	Background	70
Thrakomakedones	38.14°	23.76°	550	Suburban	82
Volos	39.37°	22.94°	31	Urban	82
Panorama	40.59°	23.03°	330	Suburban	81

<sup>1</sup>Data from Heraklion and Finokalia stations are available for the periods 2001–2005 and 2004–2007, respectively, while the rest refer to the whole study period (2001–2007).

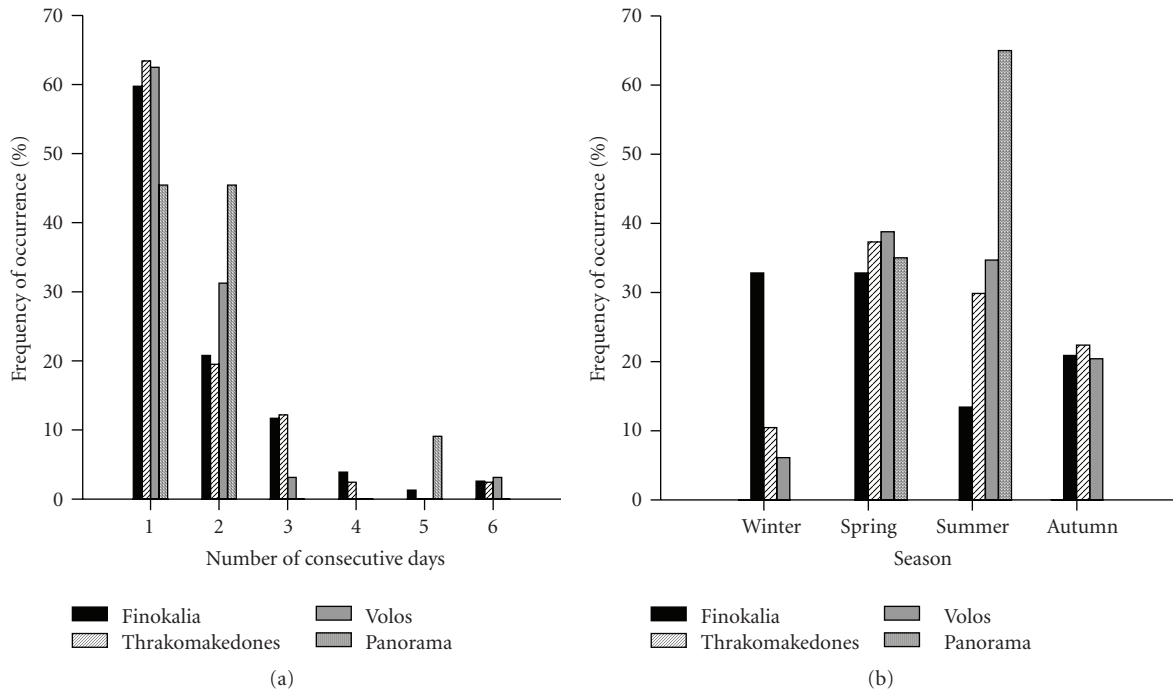


FIGURE 2: (a) Duration and (b) seasonality of the most significant dust outbreaks according to BSC-DREAM8b.

concentration observations to be assimilated. Only in the “cold start” of the model, concentration is set to zero. The cold start of the model was initiated on 21 December 2003. The resolution is set to  $1/3^\circ$  ( $\sim 50$  km) in the horizontal and to 24 layers extending up to approximately 15 km in the vertical.

BSC-DREAM8b’s simulations regarding the contribution of transported dust to surface PM10 concentration at Finokalia, Thrakomakedones, Volos, and Panorama are exploited in this study. As Finokalia station is situated 70 km northeast of Heraklion, and although Heraklion is included in an adjacent model’s grid point, it is assumed that the contribution of transported dust to surface PM10 concentration at Heraklion is the same as at Finokalia.

### 3. Results and Discussion

**3.1. Selection of Dust Transport Events.** In this study, the capability of the BSC-DREAM8b to simulate the desert dust

transported in the Eastern Mediterranean especially during dust outbreaks is examined. Therefore, model outputs have to be filtered so as to select the most important dust transport events that significantly influence surface PM10 levels. It was decided to define one threshold for all monitoring stations, based on the modelled PM10 surface concentrations. For this purpose, modelled PM10 surface concentrations are classified and the critical part of their distribution is presented in Figure 1. Studying the tail of the distribution, it is revealed that the frequency of occurrence becomes rather constant when the concentration exceeds the value of  $10 \mu\text{g}/\text{m}^3$ . Additionally, modelled values are well converged when concentration becomes  $12 \mu\text{g}/\text{m}^3$ . So, it could be assumed that significant dust transport and deposition occurs when BSC-DREAM8b simulates surface concentration over  $12 \mu\text{g}/\text{m}^3$ . Consequently, it is decided to set this value as the selection threshold. This limit value corresponds to the 5th, 3rd, 2nd, and 1st upper percentile of the predicted PM10 surface concentrations at Finokalia, Thrakomakedones, Volos, and Panorama, respectively. These

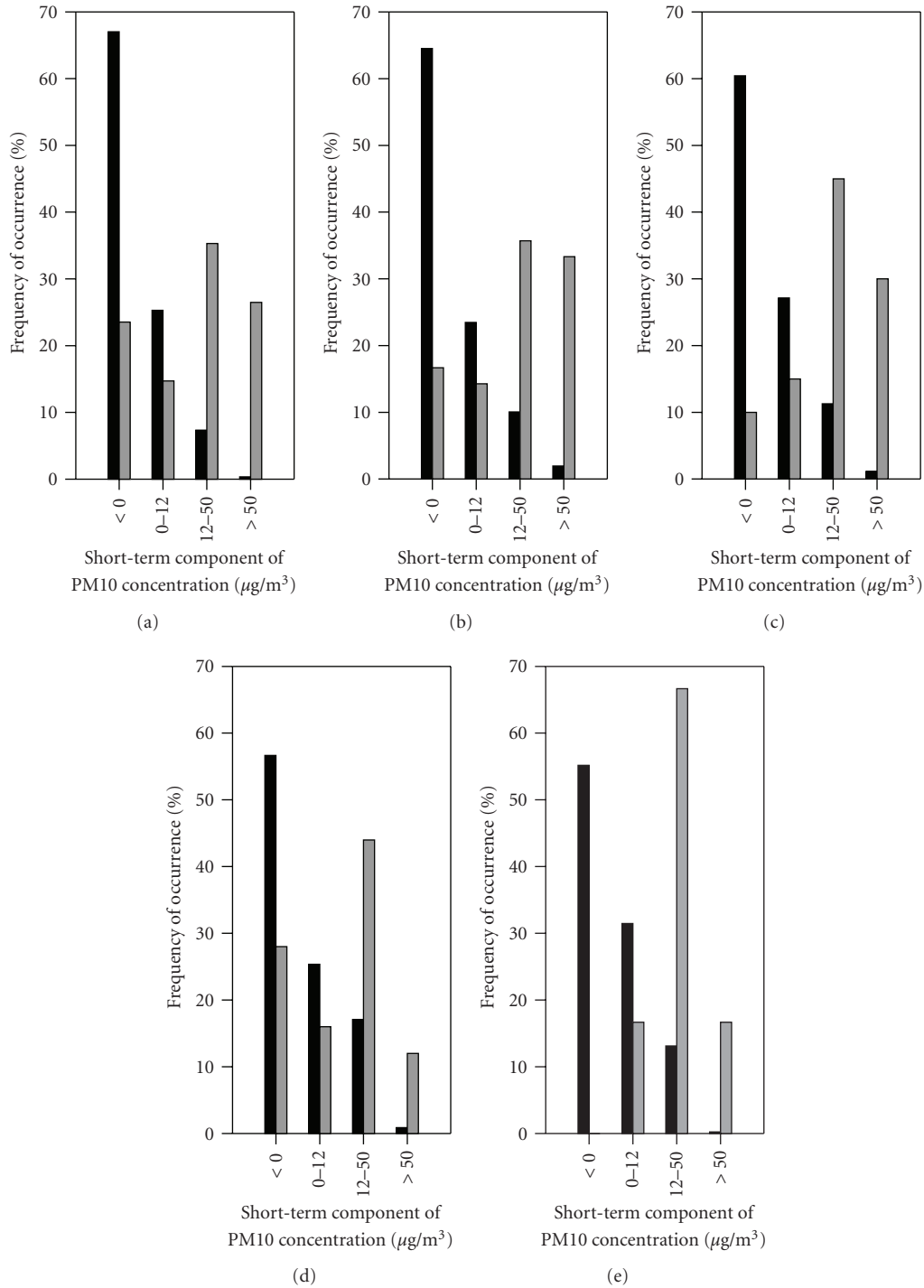


FIGURE 3: Frequency distribution of the short-term component of the observed PM10 concentrations at (a) Finokalia, (b) Heraklion, (c) Thrakomakedones, (d) Volos, and (e) Panorama; Grey bars correspond to the days when a dust outbreak is identified, while black bars correspond to the rest of the days.

percentiles verify that only significant dust outbreaks are selected.

**3.2. Application of the Selection Criterion.** The criterion that is defined above is applied to the time series predicted by BSC-DREAM8b. Quantitative information about the

selected events is provided in Table 2. Table 2 reveals that the defined threshold is very restrictive for sites located mainly to the northern part of Greece (e.g., Panorama). This fact indicates that the definition of an overall European or national threshold is not very useful for planning control strategies on a regional level. In this case, it would be better if

TABLE 2: Statistics for the selected dust outbreaks during the examined 7-year period.

	Site			
	Finokalia	Thrakomakedones	Volos	Panorama
Number of days when predicted PM10 surface concentration exceeds the threshold value ( $12 \mu\text{g}/\text{m}^3$ )	134	67	49	20
Number of events identified	78	41	32	11

different thresholds are regionally defined, taking also into account local emissions and meteorological conditions, in order to assess the impact of transported dust on surface PM levels. It is also worth mentioning that the results referring to Panorama, that are reported in this study, should be treated with caution, as just a few dust outbreaks are identified.

The duration of the selected events is presented in Figure 2(a). The duration of the dust events is similar at Finokalia and Thrakomakedones, while episodes of shorter duration are identified at Volos and Panorama. As far as the longer events identified, two 6-day and one 5-day events are detected at Finokalia. One of the two 6-day events that are predicted at Finokalia coincides with the 6-day event that is detected at Thrakomakedones and Volos and the 5-day event that is detected at Panorama. This dust outbreak could be regarded as the most significant during the examined period not only due to its long duration but also due to its large spatial extent. This event coincided with the heat wave episode that influenced the Eastern Mediterranean during the last days of June 2007. Therefore, it contributed not only to the aggravation of air quality in Greece but also to the deterioration of discomfort conditions that were prevailing due to the extremely high air temperatures [24].

The seasonal distribution of the selected events is presented in Figure 2(b), which shows that the dust transport exhibits an annual cycle. Most of the outbreaks are observed during spring and summer, some outbreaks are observed during autumn and a very limited number during winter. This result is in accordance to the conclusions drawn by Moulin et al. [5] who analyzed satellite observations and found that the dust transport from North Africa to the Mediterranean Basin is favoured from March to August, while during autumn and winter dust transport is less pronounced. Papayannis et al. [8] analyzed lidar data in Athens and Thessaloniki obtained during an almost 3-year period and reported that the period when the more important Saharan dust transport occurred over the Eastern Mediterranean is summer followed by autumn. The present study suggests that autumn could also be considered as a period with important dust outbreaks over the Eastern Mediterranean, as  $\sim 20\%$  of the selected events are predicted during autumn months. Dust transport over Greece is favoured during the warmer months of the year, when the prevailing meteorological situation is characterized by western-south-western synoptic flows, a condition that favours the transport of dust from North Africa [25]. However, the seasonal pattern of the southernmost station of Finokalia exhibits some differences and is discussed in detail by Kalivitis et al. [26]. Koulouri et al. [27] report that according to measurements conducted at

Finokalia station during the period July 2004–July 2006, the seasonal variability of the masses of coarse particles, which are defined as those that have aerodynamic diameter between 1.3 and  $10 \mu\text{m}$ , presents a prominent peak in spring (April) and a secondary one in February, both due to dust transport from North Africa. This is in agreement with the results of BSC-DREAM8b for the seasonality of serious dust events at Finokalia as shown in Figure 2(b).

*3.3. Evaluation of BSC-DREAM8b.* BSC-DREAM8b's outputs are compared to surface PM10 observations. The efficiency of the model to predict dust transport episodes is discussed and the contribution of transported desert dust to the determination of surface PM10 concentrations at the areas studied is presented. Predicting PM concentrations in time and space is important for air quality and health concerns, weather prediction, and climate studies. As dust transport events influence surface levels for relatively short time periods, it is preferred to compare the model's results to the short-term component of measured PM10 concentration. Short-term variations are attributed to weather processes. They could be separated from the original time series by using the Kolmogorov-Zurbenko (KZ<sub>m,p</sub>) filter [28]. The KZ filter is a low-pass filter produced through  $p$  repeated iterations of a moving average calculated over an  $m$  time window that can provide time series that does not include short-term periodicities. Then, by subtracting the filtered time series from the original one, the time series of the short-term component of measured PM10 concentration is generated. According to Rao et al. [29], the application of a KZ<sub>15,5</sub> filter is the best choice to remove the short-term part of the time series. This technique has widely been applied in ozone studies [30, 31] in order to separate a time series into different temporal components, while its application has also been extended in PM studies [32].

In this study, the KZ<sub>15,5</sub> filter is applied to the time series of the observed daily average PM10 concentration. Days are separated in two groups. One group includes the days when a dust outbreak is identified by the application of the selection criterion that is presented above, while the other group includes the rest of the days. The short-term component is classified and the frequency of occurrence of each class for every group is presented in Figure 3. Figure 3 reveals that during the majority of the days selected as dust episodes according to the results of BSC-DREAM8b, the values of the short-term component are positive, indicating an increase in PM10 levels that could be partially attributed to the transport of desert dust. However, for several days that are included in the first group, the values of the short-term component

TABLE 3: Contribution of transported dust to near surface PM10 levels<sup>1</sup>.

Site	Case a			Case b			Case c			Case d		
	S	R <sup>2</sup>	N									
Finokalia	1.48	0.44	33	3.69	0.64	45	2.61	0.74	17	5.32	0.82	18
Thrakomakedones	2.06	0.49	40	3.96	0.68	59	2.58	0.86	29	5.04	0.80	30
Volos	1.19	0.42	25	3.55	0.83	36	1.92	0.71	13	4.08	0.83	13
Panorama	1.80	0.85	12	3.77	0.95	12	1.99	0.92	10	3.94	0.97	10

<sup>1</sup>S: Slope of the regression line; R<sup>2</sup>: Squared Correlation Coefficient regarding the regression procedure; N: Number of Days included in the regression analysis.

are lower than the selection threshold ( $12 \mu\text{g}/\text{m}^3$ ) or are even negative. Negative values indicate that the simulation of BSC-DREAM8b concerning the occurrence of a dust episode might be false. However, negative values of the short-term component can also be caused by local effects (e.g., related to the weekly variation of PM10 levels), especially at urban or suburban sites. Positive values lower than  $12 \mu\text{g}/\text{m}^3$  indicate that the BSC-DREAM8b model might be successful in the prediction of the occurrence of a dust outbreak; however, it fails to estimate the magnitude of the dust being transported. More specifically, negative values are calculated for the 24, 17, 10, 28, and 0% of the days at Finokalia, Heraklion, Thrakomakedones, Volos, and Panorama, respectively, while positive values lower than  $12 \mu\text{g}/\text{m}^3$  are calculated for the 15, 14, 15, 16, and 17% of the days, respectively. The short-term component of the daily average value of PM10 concentration raises more than  $12 \mu\text{g}/\text{m}^3$  during the 61, 69, 75, 56, and 83% of the days at Finokalia, Heraklion, Thrakomakedones, Volos, and Panorama, respectively. Violations of the Air Quality Standard (AQS) are observed during all of these days at Heraklion (29 days), Volos (14 days), and Panorama (10 days) and during the 86 and 93% of these days at Finokalia (18 days) and Thrakomakedones (28 days), respectively, as the daily average value of PM10 concentration exceeds  $50 \mu\text{g}/\text{m}^3$ . The limit value is established by the European Union's Directive 1999/30 and is kept by the Directive 2008/50, which recently replaced the former Directive. This fact indicates that when BSC-DREAM8b achieves to predict a significant dust outbreak, an AQS exceedance will most probably be observed. Additionally, the number of exceedances at Heraklion and Thrakomakedones is close to the allowed number of exceedances, which is set equal to 35 according to the above-mentioned Directives. However, it should be pointed out that Directive 2008/50 states that where natural contributions to pollutants in ambient air can be determined with sufficient certainty, and where exceedances are due in whole or in part to these natural contributions, these may be subtracted when assessing compliance with air quality limit values. The results of the present study and dust regional modelling in general can be useful in the development of air pollution control strategies.

It should be noted though that the increase in PM10 levels, observed during the days when dust events take place according to BSC-DREAM8b, could be attributed not only to the transported dust but also to the local meteorological conditions that are prevailing during dust outbreaks. It is well known that specific meteorological

conditions could favour the accumulation of dust as well as the accumulation of pollutants that are locally emitted due to anthropogenic activities. Moreover, anthropogenic as well as natural emissions of PM10 undergo a significant temporal variation that could mask the influence of the transported Saharan dust.

The analysis of the data that refer to the selected events is extended in order to quantify the contribution of the transported dust to the observed near surface PM10 levels. For this reason, model predictions are compared to PM10 observations, as well as to their short-term component. Four cases are examined. Case (a): model predictions are compared to the short-term component of the PM10 observations. Case (b): model predictions are compared to the PM10 observations. Case (c): model predictions are compared to the short-term component of PM10 observations, only when the short-term component of PM10 concentrations is higher than the value forecasted by the model. Case (d): model predictions are compared to the PM10 observations, only when the short-term component of PM10 concentrations is higher than the value forecasted by the model. The results of the cases (a) and (b) include uncertainties as model's possible mispredictions are not excluded from the analysis. The results of cases (c) and (d) are more indicative as the introduction of the criterion regarding the short-term component cuts off the possible mispredicted events and allows the inclusion in the analysis of only those days when dust transport could have contributed to the increase of the observed PM10 levels.

A regression line is calculated for every site for each of the cases examined, considering the model's prediction as the independent variable and the PM10 concentration or its short-term component as the dependent one. Additionally, intercept is forced to zero. The results of all regressions are presented in Table 3. Table 3 shows that model's predictions are better correlated to the PM10 observations than to their short-term component, with just one exception (Thrakomakedones, cases (c) and (d)). This fact could be attributed to the variability of the anthropogenic emissions that have diurnal and weekly cycles and moreover to meteorological phenomena that also present variations of one or more days, such as the sea breeze circulation and synoptic winds. The influence of the above factors and phenomena is probably masked by the application of the KZ<sub>15,5</sub> filter, since their variability is much shorter than the 15-day window of the filter applied. The slope values when model predictions are regressed to PM10 observations are higher than when

regressed to their short-term component indicating the contribution of additional sources other than desert to the determination of surface PM10 levels in the areas studied.

According to the analysis of case (c), dust contribution accounts for the 38, 39, 52, and 50% of the increase in PM10 concentrations at Finokalia, Thrakomakedones, Volos, and Panorama, respectively, while according to the results of case (d), the 19, 20, 25, and 25% of the measured PM10 concentrations is attributed to dust transport. The percentage differences support the conclusion drawn above regarding the drawback of the application of the KZ filter.

As Finokalia is a background site, it was expected that dust contribution to surface PM10 levels would be relatively higher. This fact indicates that BSC-DREAM8b probably underestimates the dust transported at Finokalia station during the dust outbreaks and that the background PM10 levels at this site could be influenced not only by the transported desert dust but also by particles emitted by other natural sources. Gerasopoulos et al. [33] state that ions and particulate carbonaceous matter could also contribute to PM10 mass, although they report that PM10 levels at Crete are mainly influenced by desert dust during dust outbreaks. According to the previous analysis, the desert dust contribution accounts for the 39% of the increase in PM10 concentrations at Thrakomakedones. Thrakomakedones station is located to the north of the Athens Basin and PM10 levels there are affected also by anthropogenic emissions. This fact is closely linked to the sea breeze circulation that frequently develops in Athens Basin during the warm period of the year [34, 35]. Most of the cases that are involved in the regression analysis correspond to spring and summer days. Sea breeze is associated to winds blowing from southeast directions that advect pollutants that are released at the heavily industrialized south-western part of the urban agglomeration, as well as at the city centre, to the north part of the Athens Basin where Thrakomakedones are located. The estimated dust contribution to the PM10 levels at Volos and Panorama could be regarded as reasonable. Volos is a medium-sized coastal city where anthropogenic emissions are high during the cold period of the year [36]. Local emissions are less intense during the warm period. The vast majority of the dust transport events that are included in the regression analysis correspond to spring and summer days. Therefore, it can be supported that although Volos is an urban site, PM10 levels could be significantly influenced by dust transport during the selected outbreaks. As far as Panorama is concerned, it is considered as a suburb that is not significantly affected by anthropogenic emissions [25]. The results presented and the conclusions drawn above should be further verified by future studies including even longer timeseries than the 7-year timeseries used in the present analysis.

#### 4. Conclusions

The objective of this study is to assess the efficiency of BSC-DREAM8b model to predict Saharan dust transport episodes in the Eastern Mediterranean. For this reason, model outputs

that cover the period 2001–2007 are compared to PM10 data recorded by five automatic monitoring stations in Greece. A quantitative criterion is established in order to select the most important dust outbreaks. When modelled surface concentration becomes higher than  $12 \mu\text{g}/\text{m}^3$ , significant dust transport and deposition is assumed to occur.

The duration of the selected events is longer at the monitoring sites located to south Greece (namely, Finokalia and Thrakomakedones). A significant dust outbreak that lasted more than 5 days is detected at all sites in June 2007. This event coincided with the heat wave episode that influenced the Eastern Mediterranean, contributing to the aggravation of air quality and discomfort conditions.

Dust transport is more favoured during summer and spring at Thrakomakedones, Volos, and Panorama and during winter and spring at Finokalia. Additionally, ~20% of the selected dust outbreaks at Finokalia, Thrakomakedones, and Volos are observed during autumn, therefore autumn could also be considered as a season when important dust transport events occur over the Eastern Mediterranean.

In order to evaluate BSC-DREAM8b outputs, the modelled values are compared to the daily average values of surface PM10 concentration, as well as to their short-term component. Short-term variations are attributed to weather processes and do not include seasonal or long term variations. The short-term component is separated by applying a  $\text{KZ}_{15,5}$  filter to the original time series and then by subtracting the filtered time series from the original one. The values of the short-term component are positive (indicating an increase in PM10 levels) and higher than  $12 \mu\text{g}/\text{m}^3$  (indicating contribution of transported dust to PM10 levels reliably) during the 61, 69, 75, 56, and 83% of the days identified as dust outbreaks at Finokalia, Heraklion, Thrakomakedones, Volos, and Panorama, respectively. During the rest of these days, the model fails either to simulate the occurrence of a dust episode or to estimate its magnitude. However, it is found that modelled values correlate better with PM10 observations than with their short-term component, as the application of the  $\text{KZ}_{15,5}$  filter probably masks the influence of some factors and meteorological phenomena that have periodicities much shorter than the 15-day window of the applied filter (e.g., anthropogenic emissions with diurnal and weekly cycles, sea breeze circulation). The comparison between the model's predictions and the short-term component of PM10 observations reveals that dust contribution accounts for the 38, 39, 52, and 50% of the increase in PM10 concentrations at Finokalia, Thrakomakedones, Volos, and Panorama, respectively, while the comparison between the model's predictions and PM10 observations shows that the 19, 20, 25, and 25% of the measured PM10 concentrations at Finokalia, Thrakomakedones, Volos, and Panorama, respectively, is attributed to dust transport.

#### Acknowledgment

The work has been financed by the MED-APICE project in co financed by the European Regional Development Fund in the framework of the MED Programme.

## References

- [1] C. S. Zender, R. L. Miller, and I. Tegen, "Quantifying mineral dust mass budgets: terminology, constraints, and current estimates," *Eos*, vol. 85, no. 48, pp. 509–512, 2004.
- [2] WHO, *WHO Air Quality Guidelines Global Update 2005*, World Health Organization, Bonn, Germany, 2005.
- [3] IPCC, W. G. I.: Climate change 2007: the physical science basis, Summary for Policy Makers, Contribution of Working Group I to the 4th Assessment Report of the Intergovernmental Panel on Climate Change, 2007.
- [4] H. Liao, J. H. Seinfeld, P. J. Adams, and L. J. Mickley, "Global radiative forcing of coupled tropospheric ozone and aerosols in a unified general circulation model," *Journal of Geophysical Research D*, vol. 109, no. 16, 33 pages, 2004.
- [5] C. Moulin, C. E. Lambert, U. Dayan et al., "Satellite climatology of African dust transport in the Mediterranean atmosphere," *Journal of Geophysical Research D*, vol. 103, no. 11, pp. 13137–13144, 1998.
- [6] J. Barkan, H. Kutiel, P. Alpert, and P. Kishcha, "Synoptics of dust intrusion days from the African continent into the Atlantic Ocean," *Journal of Geophysical Research D*, vol. 109, no. 8, article no. D08201, 9 pages, 2004.
- [7] J. Barkan, P. Alpert, H. Kutiel, and P. Kishcha, "Synoptics of dust transportation days from Africa toward Italy and central Europe," *Journal of Geophysical Research D*, vol. 110, no. 7, article no. D07208, pp. 1–14, 2005.
- [8] A. Papayannis, D. Balis, V. Amiridis et al., "Measurements of Saharan dust aerosols over the eastern Mediterranean using elastic backscatter-Raman lidar, spectrophotometric and satellite observations in the frame of the EARLINET project," *Atmospheric Chemistry and Physics*, vol. 5, no. 8, pp. 2065–2079, 2005.
- [9] A. Di Sarra, T. Di Iorio, M. Cacciani, G. Fiocco, and D. Fuà, "Saharan dust profiles measured by lidar at Lampedusa," *Journal of Geophysical Research D*, vol. 106, no. 10, pp. 10335–10347, 2001.
- [10] G. P. Gobbi, F. Barnaba, R. Giorgi, and A. Santacasa, "Altitude-resolved properties of a Saharan dust event over the Mediterranean," *Atmospheric Environment*, vol. 34, no. 29-30, pp. 5119–5127, 2000.
- [11] S. Nickovic, G. Kallos, A. Papadopoulos, and O. Kakaliagou, "A model for prediction of desert dust cycle in the atmosphere," *Journal of Geophysical Research D*, vol. 106, no. 16, pp. 18113–18129, 2001.
- [12] M. Viana, C. Pérez, X. Querol, A. Alastuey, S. Nickovic, and J. M. Baldasano, "Spatial and temporal variability of PM levels and composition in a complex summer atmospheric scenario in Barcelona (NE Spain)," *Atmospheric Environment*, vol. 39, no. 29, pp. 5343–5361, 2005.
- [13] C. Pérez, S. Nickovic, J. M. Baldasano, M. Sicard, F. Rocadenbosch, and V. E. Cachorro, "A long Saharan dust event over the western Mediterranean: Lidar, Sun photometer observations, and regional dust modeling," *Journal of Geophysical Research D*, vol. 111, no. 15, article no. D15214, 2006.
- [14] D. Balis, V. Amiridis, S. Kazadzis et al., "Optical characteristics of desert dust over the east Mediterranean during summer: a case study," *Annales Geophysicae*, vol. 24, no. 3, pp. 807–821, 2006.
- [15] E. Gerasopoulos, P. Kokkalis, V. Amiridis et al., "Dust specific extinction cross-sections over the Eastern Mediterranean using the BSC-DREAM model and sun photometer data: the case of urban environments," *Annales Geophysicae*, vol. 27, no. 7, pp. 2903–2912, 2009.
- [16] C. Pérez, S. Nickovic, G. Pejanovic, J. M. Baldasano, and E. Özsoy, "Interactive dust-radiation modeling: a step to improve weather forecasts," *Journal of Geophysical Research D*, vol. 111, no. 16, article no. D16206, 2006.
- [17] Z. I. Janjic, "Pressure gradient force and advection scheme used for forecasting with steep and small scale topography," *Contributions to Atmospheric Physics*, vol. 50, pp. 186–199, 1977.
- [18] Z. I. Janjic, "Forward-backward scheme modified to prevent twogrid-interval noise and its application in sigma coordinate models," *Contributions to Atmospheric Physics*, vol. 52, pp. 69–84, 1979.
- [19] Z. I. Janjic, "Nonlinear advection schemes and energy cascade on semi-staggered grids," *Monthly Weather Review*, vol. 112, no. 6, pp. 1234–1245, 1984.
- [20] Z. I. Janjic, "The step-mountain coordinate: physical package," *Monthly Weather Review*, vol. 118, no. 7, pp. 1429–1443, 1990.
- [21] Z. I. Janjic, "The step-mountain eta coordinate model: further developments of the convection, viscous sublayer, and turbulence closure schemes," *Monthly Weather Review*, vol. 122, no. 5, pp. 927–945, 1994.
- [22] K. Haustein, C. Pérez, J. M. Baldasano et al., "Regional dust model performance during SAMUM 2006," *Geophysical Research Letters*, vol. 36, no. 3, article no. L03812, 2009.
- [23] S. Basart, C. Pérez, E. Cuevas, and J. M. Baldasano, "Evaluation of a regional mineral dust model over Northern Africa, Southern Europe and Middle East with AERONET data," in *Proceedings of the EGU General Assembly*, vol. 11 of *Geophysical Research Abstracts*, Vienna, Austria, 2009, EGU2009-10799.
- [24] D. K. Papanastasiou, D. Melas, T. Bartzanas, and C. Kittas, "Temperature, comfort and pollution levels during heat waves and the role of sea breeze," *International Journal of Biometeorology*, vol. 54, no. 3, pp. 307–317, 2010.
- [25] E. Katragkou, S. Kazadzis, V. Amiridis, V. Papaioannou, S. Karathanasis, and D. Melas, "PM10 regional transport pathways in Thessaloniki, Greece," *Atmospheric Environment*, vol. 43, no. 5, pp. 1079–1085, 2009.
- [26] N. Kalivitis, E. Gerasopoulos, M. Vrekoussis et al., "Dust transport over the eastern mediterranean derived from total ozone mapping spectrometer, aerosol robotic network, and surface measurements," *Journal of Geophysical Research D*, vol. 112, no. 3, article no. D03202, 2007.
- [27] E. Koulouri, S. Saarikoski, C. Theodosi et al., "Chemical composition and sources of fine and coarse aerosol particles in the Eastern Mediterranean," *Atmospheric Environment*, vol. 42, no. 26, pp. 6542–6550, 2008.
- [28] I. G. Zurbenko, *The Spectral Analysis of Time Series*, North Holland, New York, NY, USA, 1986.
- [29] S. T. Rao, I. G. Zurbenko, R. Neagu, P. S. Porter, J. Y. Ku, and R. F. Henry, "Space and time scales in ambient ozone data," *Bulletin of the American Meteorological Society*, vol. 78, no. 10, pp. 2153–2166, 1997.
- [30] M. L. Milanchus, S. T. Rao, and I. G. Zurbenko, "Evaluating the effectiveness of ozone management efforts in the presence of meteorological variability," *Journal of the Air and Waste Management Association*, vol. 48, pp. 201–215, 1998.
- [31] J. Yang and D. R. Miller, "Trends and variability of ground-level O<sub>3</sub> in Connecticut over the period 1981–1997," *Journal of the Air and Waste Management Association*, vol. 52, no. 12, pp. 1354–1361, 2002.
- [32] E. K. Wise and A. C. Comrie, "Extending the Kolmogorov-Zurbenko filter: application to ozone, particulate matter, and meteorological trends," *Journal of the Air and Waste Management Association*, vol. 55, no. 8, pp. 1208–1216, 2005.

- [33] E. Gerasopoulos, G. Kouvarakis, P. Babasakalis, M. Vrekoussis, J.-P. Putaud, and N. Mihalopoulos, "Origin and variability of particulate matter (PM<sub>10</sub>) mass concentrations over the Eastern Mediterranean," *Atmospheric Environment*, vol. 40, no. 25, pp. 4679–4690, 2006.
- [34] D. Melas, I. Ziomas, O. Klemm, and C. S. Zerefos, "Anatomy of the sea-breeze circulation in Athens area under weak large-scale ambient winds," *Atmospheric Environment*, vol. 32, no. 12, pp. 2223–2237, 1998.
- [35] D. Melas, I. Ziomas, O. Klemm, and C. S. Zerefos, "Flow dynamics in Athens area under moderate large-scale winds," *Atmospheric Environment*, vol. 32, no. 12, pp. 2209–2222, 1998.
- [36] D. K. Papanastasiou and D. Melas, "Application of PM<sub>10</sub>'s statistical distribution to air quality management—a case study in central Greece," *Water, Air, and Soil Pollution*, vol. 207, no. 1–4, pp. 115–122, 2010.

## Research Article

# Identification of the Aerosol Types over Athens, Greece: The Influence of Air-Mass Transport

D. G. Kaskaoutis,<sup>1</sup> P. G. Kosmopoulos,<sup>2</sup> H. D. Kambezidis,<sup>1</sup> and P. T. Nastos<sup>2</sup>

<sup>1</sup> Atmospheric Research Team, Institute for Environmental Research and Sustainable Development, National Observatory of Athens, Lofos Nymphon, P.O. Box 20048, 11810 Athens, Greece

<sup>2</sup> Department of Geology and Geo-Environment, University of Athens, University Campus, 15784 Zografou, Greece

Correspondence should be addressed to H. D. Kambezidis, [harry@meteo.noa.gr](mailto:harry@meteo.noa.gr)

Received 27 June 2009; Revised 4 September 2009; Accepted 3 October 2009

Academic Editor: Krishnaswamy Krishnamoorthy

Copyright © 2010 D. G. Kaskaoutis et al. This is an open access article distributed under the Creative Commons Attribution License, which permits unrestricted use, distribution, and reproduction in any medium, provided the original work is properly cited.

Aerosol optical depth at 550 nm (AOD<sub>550</sub>) and fine-mode (FM) fraction data from Terra-MODIS were obtained over the Greater Athens Area covering the period February 2000–December 2005. Based on both AOD<sub>550</sub> and FM values three main aerosol types have been discriminated corresponding to urban/industrial aerosols, clean maritime conditions, and coarse-mode, probably desert dust, particles. Five main sectors were identified for the classification of the air-mass trajectories, which were further used in the analysis of the (AOD<sub>550</sub> and FM data for the three aerosol types). The HYSPLIT model was used to compute back trajectories at three altitudes to investigate the relation between AOD<sub>550</sub>-FM and wind sector depending on the altitude. The accumulation of local pollution is favored in spring and corresponds to air masses at lower altitudes originating from Eastern Europe and the Balkan. Clean maritime conditions are rare over Athens, limited in the winter season and associated with air masses from the Western or Northwestern sector. The coarse-mode particles origin seems to be more complicated proportionally to the season. Thus, in summer the Northern sector dominates, while in the other seasons, and especially in spring, the air masses belong to the Southern sector enriched with Saharan dust aerosols.

## 1. Introduction

Atmospheric aerosols play a crucial role in the Earth's climate through scattering and absorption both solar and thermal radiation (direct effect), thus influencing the radiative and energy balance and/or acting as cloud condensation nuclei (indirect effect), affecting cloud albedo and lifetime, precipitation rate, and hydrology cycle [1]. The great effort spent over the last decades by the scientific community focusing on aerosol climatology and optical properties reflects the importance attributed to aerosols in controlling the Earth's climate [2]. Major advancements in this field have been achieved by the new generation of space borne instruments (e.g., Along Track Scanning Radiometer (ATSR-2) on board the European Space Agency (ESA-ERS2), Moderate Resolution Imaging Spectroradiometer (MODIS), and Multiangle Imaging Spectroradiometer (MISR) on board the NASA Terra, POLarization and Directionality of the Earth's Reflectances (POLDER) on board the ADEOS), specifically designed

to provide detection and characterization of atmospheric aerosols [3].

The Mediterranean Sea is one of the most affected areas regarding aerosol load in the world [4]. Due to the variety of the regions surrounding the Mediterranean basin, different aerosol types can be found within the basin, having both strong temporal and spatial distribution [4, 5]; desert dust, originated from the Sahara desert, polluted aerosols produced mainly in urban and industrial centers of Continental and Eastern Europe, marine aerosols, formed over Mediterranean itself or transported from the North Atlantic, and biomass smoke often produced by seasonal forest fires.

Transport of Saharan dust from the North African arid regions towards Mediterranean and coastal Europe has been widely investigated, either in the form of statistical analyses or as "case studies" using ground-based instrumentation, sun photometers, lidar and satellite observations [6–10]. In contrast, studies for the particle transport from the

European continent to the Mediterranean Sea are still limited. However, a growing scientific interest in this topic is now developed, and in this way an international effort to quantify the impact of anthropogenic emissions on the Eastern Mediterranean is represented by the Mediterranean Intensive Oxidant Study (MINOS) campaign. That campaign highlighted the important role of pollutants in the Mediterranean atmosphere during summer [11]. Pollution transfer models have also been successfully utilized to investigate the export pathways of air pollution from Europe [12, 13]. Nevertheless, the investigation of the export of pollutants from the industrialized areas surrounding the Eastern Mediterranean and Aegean Sea is not an easy task due to the fact that a large number of aerosols and gas precursors (including organic and inorganic compounds) contribute to it. Model calculations also indicate that pollutants emitted from Central and Eastern Europe are transported towards the Eastern Mediterranean [14], and hence, anthropogenic aerosols and their direct radiative effects are considered to be significant. In addition to long-range transport, this region is affected from pollution caused by local metropolitan areas, such as Athens. The identification of clean marine conditions over Eastern Mediterranean is particularly rare, due to the influence of continental aerosols (natural and anthropogenic). Prospero et al. [15] investigated aerosols over different oceanic areas and reported that the Mediterranean ones were heavily contaminated by dust and anthropogenic pollutants. Moreover, Heintzenberg et al. [16] excluded Mediterranean and other closed seas (Baltic, Yellow Sea) as not representative for the investigation of chemical composition of marine aerosols.

The MODIS products of aerosol optical depth at (550 nm) ( $AOD_{550}$ ) and fine-mode (FM) fraction were obtained over Athens covering the period February 2000–December 2005. These observations, in combination with the air-mass trajectories, aim to identify the aerosol types originating from different sectors and determine their seasonal optical properties. A recent work by Kaskaoutis et al. [17] investigated the optical properties of specific aerosol types over Athens, while Kosmopoulos et al. [18] analyzed the seasonal variation of three different aerosol types; both studies used the same data set. The main contribution of the present study, though, is the investigation of the prime pathways favoring the presence of specific aerosol types over Athens. Such a long-term (~6 years) analysis associating the aerosol types and properties with air-mass trajectories constitutes the first study conducted over Athens. It is also highlighted that different aerosol types can occur simultaneously in the atmosphere transported by air masses of different origins. In addition, the major role of the vertical transport is underlined favoring the domination of different aerosol types in relation to the season and the synoptic meteorological patterns.

## 2. Data Collection

**2.1. MODIS Retrievals.** The Moderate Resolution Imaging Spectroradiometer (MODIS) was launched in December

1999 on the polar orbiting NASA-EOS Terra spacecraft with a dayside equatorial 10:30 AM local crossing time. Aerosol retrievals from MODIS data are performed over land and ocean surfaces by means of two separate algorithms thoroughly described in Kaufman and Tanré [19]. The two aerosol products employed in this study are (1) the optical thickness at 550 nm ( $AOD_{550}$ ) and (2) the fine-mode fraction (FM). The latter is derived as the ratio of optical depth of small mode versus effective optical depth at 550 nm. The MODIS aerosol products are only created for cloud-free regions, although Levy et al. [20] showed that MODIS can retrieve optical properties even in case that a  $10 \times 10$  km pixel (Level 2) is about 90% cloudy. Both  $AOD_{550}$  and FM data used in the present study were retrieved by MODIS and correspond to Collection 5 (C005) data. The FM fraction was initially given over ocean. Nevertheless, Chu et al. [21] showed that the separation of fine- and coarse-mode particles is also possible over land by comparing the path radiances at 660 and 470 nm. Therefore, FM can also be obtained over land and coastal areas.

The validation of MODIS aerosol products is usually achieved by comparing them with the AERONET AOD data [22]. The retrieval accuracy is ( $\pm 0.05 \pm 0.2$  AOD) over land [23] and ( $\pm 0.03 \pm 0.05$  AOD) over ocean [24]. Over land, even larger errors can be found in coastal zones due to subpixel water contamination. This effect tends to produce AOD overestimation [21]. Similarly, a significant water-color contribution can reduce the ocean AOD retrieval quality in coastal areas. At higher AOD values accompanied with desert aerosols larger uncertainty is caused in their retrieval due to the complexity of the dust nonsphericity problem [24, 25]. Analyzing numerous Mediterranean sites, Remer et al. [24] indicated that the particle size-dependent parameters (such as FM) are retrieved with an accuracy of  $\pm 25\%$ . Even though both  $AOD_{550}$  and FM values corresponding to new Collection 5 datasets [20, 26] are more accurate than the previous version, Collection 4 [27], shows an overestimation for low  $AOD_{550}$  values and underestimation for high  $AOD_{550}$  values compared to AERONET retrievals. Unfortunately, such an intercomparison cannot be performed over Athens during the study period because of lack of ground-based data.

The MODIS aerosol products ( $AOD_{550}$  and FM) provided over Athens in a spatial resolution of  $1^\circ \times 1^\circ$  (Level 3). A total of 1804 daily data were collected from 26 February 2000 to 31 December 2005 [17, 18]. The winter, spring, summer, and autumn days represent the 20.8%, 25.7%, 28.4%, and 25.1% of the whole dataset, respectively. Thanks to the long-term period (2000–2005) the MODIS data are employed to evaluate the seasonal variability of the aerosol types over the region.

**2.2. HYSPLIT Retrievals.** The HYSPLIT model [28] is used for the identification of the main sectors, which favors the presence of specific aerosol types over Athens. Three different altitudes are used for the sector discrimination since the various aerosol types over Mediterranean coming from different directions are mainly transported in different

altitudes. Air mass back-trajectories ending at Athens at three altitudes, 500, 1000, and 4000 m a.s.l., are calculated by the HYSPLIT model including model vertical wind. The National Center for Environmental Prediction (NCEP) reanalysis is used as model input. The HYSPLIT back trajectories refer to 11:00 UTC close to the Terra-MODIS overpass, on a daily basis. Previous investigations on Saharan dust outbreaks in Athens [29] and Northern Greece [30] showed that the dust outflow from the Sahara to the Eastern Mediterranean occurs mainly in the first 4-5 km. Therefore, the selection of the 4000 m altitude for the identification of the Saharan dust particles is appropriate. The trajectory ending at 1000 m is associated with cases of dust transported in the lower atmospheric layers, or when the mixed layer is low as in winter [31], conversely, when air masses originate from other regions (e.g., continental Europe) are generally observed within the lowest 2-3 km [11].

### 3. Methodology

*3.1. Identification of the Aerosol Types.* In order to reduce the complexity of the aerosol field, some general types can be determined depending on the aerosol origin and optical properties. Over Athens, three main aerosol types are expected to be dominant in the atmospheric load: (1) continental aerosols produced by local industries, anthropogenic activities, or seasonal forest fires, (2) maritime aerosols produced at the sea surface by the winds, and (3) desert dust originating from the North African arid regions. Due to their different origins, these aerosol types generally show remarkably different optical and physicochemical characteristics [32]. More specifically, in urban environments aerosol optical properties are dominated by fine-mode particles [33], while desert dust is strongly contaminated by coarse particles [34]. In marine environments, the relative contribution of coarse particles, although variable [35], is general higher than in urban atmospheres and lower than for desert dust. A method originally proposed by Barnaba and Gobbi [4] was implemented to distinguish three main aerosol types over Athens, urban/industrial (UI), clean maritime (CM), and desert dust (DD). Based on the combination of  $AOD_{550}$  and FM values, the presence of the three aerosol types was separated over Athens on seasonal basis [17]. The method was based on the sensitivity of the two parameters to different, somewhat independent, microphysical aerosol properties: the fine-mode fraction depends on the size of the particles, while  $AOD_{550}$  depends both on the aerosol column density and, secondarily, on size. For the identification of UI aerosols the  $AOD_{550}$  values above 0.2 associated with significant FM contribution to the total AOD (above 80%) were obtained, while the threshold values for the DD aerosols were  $AOD_{550} > 0.3$  and  $FM < 0.6$ . The CM conditions occurred for  $AOD_{550} < 0.2$  and  $FM < 0.7$ . The cases not belonging in any of these groups are characterized as “undetermined” (mixed) aerosols and have been excluded from the present analysis. It was found [17] that these cases constitute

the 46.6% of the whole dataset (842 out of 1804). The remaining 442 cases (24.5%) belong to the UI type, 183 (10.2%) correspond to CM conditions, while 337 (18.7%) to DD. Because of its simplicity, the discrimination method used is associated with some arbitrariness (e.g., incorrect aerosol-type interpretation), particularly at the threshold values between the aerosol types. However, the inclusion of the “undetermined” aerosol type takes provision for overestimating the presence of UI, CM, or DD aerosols. Despite its simplicity, this scheme seems to be appropriate for the aerosol discrimination over Athens as previous studies proved [17, 18]. Moreover, it was found that the UI aerosols are associated with air masses from the European sector, the CM conditions with fast moving Atlantic air masses, while the coarse-mode aerosols, probably DD, were related with air masses from the African continent. All the above give credit to the validity of the discrimination scheme and the relationship between the different aerosol types with air masses from their favorable sector. All these are quite important especially in the absence of ground-based measurements for justification of the satellite retrievals. However, the present results are in close agreement with previous studies over Eastern Mediterranean and Greece, which used ground-based measurements.

*3.2. Identification of the Aerosol Origin.* Four-day back trajectories ending at Athens were calculated by means of the HYSPLIT dispersion model to identify the origin of the air masses. The 4-day analysis seems to be appropriate for the scope of the study, since the air masses can be transported over long distances, such as North Atlantic and Europe before reaching over Athens. Furthermore, it was found that the use of 4 or 6 days does not significantly deviate the results. Each computed trajectory is associated with the corresponding aerosol optical characteristics. However, relating column-integrated quantities to trajectories at specific altitudes maybe problematic and does not give a clear view of the dominant aerosol type. It was found that the definition of the sector might be different proportionally to the air mass altitude used. Therefore, great differences in the aerosol origin may be revealed if the analysis is based on back trajectories in the free troposphere (4000 m) or in the boundary layer (1000 and 500 m). This investigation constitutes the main goal of the present study. Nevertheless, back trajectories have been widely used in connection with aerosol optical depth and Ångström exponent [36–38] in order to identify various aerosol types. For the investigation of the main pathways favoring the presence of each aerosol type over Athens, five geographical sectors are defined (Figure 1) in relation to different aerosol sources. The selected sectors are the following:

- (a) a Southern sector, associated with the African region; the main source is the Sahara desert;
- (b) a Western sector, which includes the Western Mediterranean basin, the Atlantic Ocean, the Iberian Peninsula, and Western France; the main aerosol type is of marine origin;

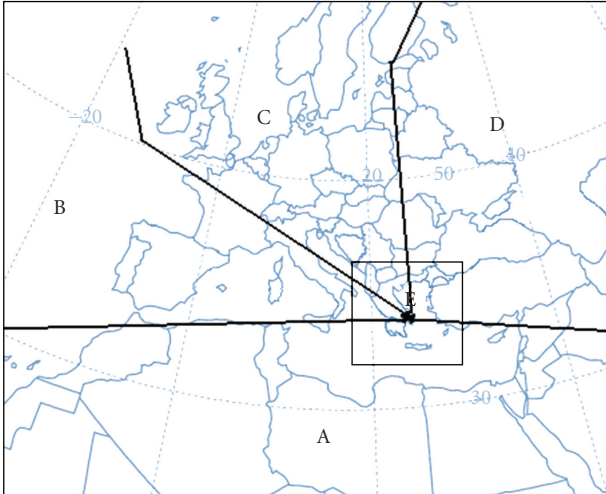


FIGURE 1: Separation of the regions acting as origins for the air masses ending at GAA. The location of GAA is indicated by an asterisk.

- (c) a North, Northwestern sector, including Central-Western Europe; the dominant aerosols are of anthropogenic origin;
- (d) a North, Northeastern sector, including Eastern Europe and former Soviet Union counties; the aerosols are expected to be of anthropogenic origin or seasonal forest fires;
- (e) a local sector including continental Greece and neighboring Balkan countries, Aegean Sea, and the Libyan Sea; the dominant aerosol type is of local emissions (mainly anthropogenic) and in some cases dust transported from Libya.

However, a degree of arbitrariness in the definition of the sectors exists, due to the effective distribution of the sources. Nevertheless, Pace et al. [36] showed that a little change in the borders of the sectors does not significantly affect the results on climatological basis. Also, they found that the use of different back-trajectories with varying duration (3 or 7 days) does not significantly modify the average optical properties in each sector. Therefore, the simple trajectory classification scheme (Figure 1) appears sufficiently robust to allow the identification of the main aerosol types. Previous studies (e.g., [39]) identified the air-mass origin sector by considering the time spent along the trajectory or using more sophisticated correlation methodologies [39] or cluster analysis [30]. Furthermore, previous results showed that dust could be detected even after a quick passage over the African continent [40]. Therefore, the time spent in each sector or the start of the air mass 4 days before reaching over Athens does not always provide reliable information about the aerosol origin. For this reason a different method was used to identify the air mass sector, taking into account the altitude of the air trajectories and possible interactions with the boundary layer. The same method has been developed and used by Pace et al. [36] and Meloni et al. [31], while an extensive

description is given there. Nevertheless, a briefly overview is provided here.

It is assumed that the aerosol origin is confined to the mixed layer at the source location, when the air mass is inside the mixed layer at the source location. When this is not the case, the source of the trajectory is defined in the sector where the air mass interacts with the mixed layer. This criterion is satisfied when the air mass altitude is lower or close to the altitude of the mixed layer. The mixed layer is defined by the HYSPLIT model as the height where the potential temperature first exceeds the surface value by 2 K, while a minimum value of 250 m is assumed [36]. If this condition is met more than once and at different sectors along the trajectory path, the sector is defined as the one where the air mass spends most of the time inside the boundary layer. In almost all the cases (95%) this criterion was satisfied for the air masses ending at 1000 m, while for 70% of the air masses ending at 4000 m this criterion was not met. Nevertheless, the majority of the air masses at 4000 m coming from North Africa satisfy this criterion, since the mixed-layer altitude is much larger over the African continent [31]. In the cases where the above criterion is not satisfied, the sector is defined as the one where the air mass spends more time. In order to include an air mass to B sector, it must spend more than ~75% of the 4 days above sea surface (Atlantic Ocean and/or Mediterranean Sea).

## 4. Results and Discussion

In the present study the aerosol properties ( $AOD_{550}$  and FM) are computed over Athens for each sector and trajectory altitude, separately. It is obvious (see Tables 1, 2, 3, and 4) that the number of occurrences in each sector and the mean  $AOD_{550}$  and FM values differentiate proportionally to the air-mass altitude used for the sector definition. Therefore, the choice of the air-mass altitude constitutes the most complicated parameter for the sector identification and, as a consequence, the investigation on the computed differences constitutes a real challenge.

*4.1. Seasonal Distribution of the Back Trajectories.* Table 1 summarizes the number of occurrences in each sector based on the three altitudes selected. Regarding the whole dataset (Table 1) it is concluded that the choice of the air-trajectory altitude for the sector identification plays a very crucial role, since large variations can emerge for the air masses traveling within the boundary layer and in the free troposphere. Regarding the lower altitude (500 m) it is seen that the majority of the air masses correspond to Northwestern (33%) and Northern (30%) directions, while these originating from the Atlantic Ocean are very few (only 9%). A rather significant fraction (16%) corresponds to air masses of Saharan origin, thus leading to vertical dust transport [41]. It is also worth noticing that the majority of the cases belonging to local emissions (sector E) correspond to air masses in the lower atmospheric layers. As the altitude increases, the air mass changes sector with preference to western directions due to the dominant western flow in the

TABLE 1: Mean values of AOD<sub>550</sub> and FM fraction for all aerosol types over GAA. These values correspond to the whole dataset. The number and the relative frequency of the trajectories from each sector are also given for the three altitude levels: 500 m, 1000 m, and 4000 m.

Trajectory altitude		AOD <sub>550</sub>	FM	Year	Winter	Spring	Summer	Autumn
500 m	A	0.38 ± 0.13	0.61 ± 0.10	155 (16%)	16%	25%	25%	34%
	B	0.34 ± 0.10	0.58 ± 0.12	87 (9%)	33%	18%	20%	29%
	C	0.36 ± 0.16	0.59 ± 0.12	317 (33%)	16%	21%	39%	24%
	D	0.39 ± 0.11	0.65 ± 0.10	285 (30%)	8%	33%	35%	24%
	E	0.37 ± 0.10	0.64 ± 0.09	118 (12%)	8%	34%	26%	31%
1000 m	A	0.38 ± 0.12	0.61 ± 0.10	196 (20%)	15%	26%	24%	36%
	B	0.34 ± 0.09	0.58 ± 0.12	108 (11%)	28%	15%	25%	32%
	C	0.36 ± 0.17	0.60 ± 0.12	333 (35%)	15%	24%	39%	23%
	D	0.39 ± 0.12	0.65 ± 0.10	228 (24%)	8%	32%	36%	23%
	E	0.37 ± 0.11	0.65 ± 0.11	97 (10%)	10%	32%	26%	32%
4000 m	A	0.39 ± 0.13	0.60 ± 0.12	233 (24%)	16%	31%	25%	27%
	B	0.34 ± 0.10	0.60 ± 0.12	477 (50%)	16%	23%	32%	29%
	C	0.35 ± 0.09	0.63 ± 0.10	166 (17%)	10%	25%	40%	25%
	D	0.37 ± 0.11	0.63 ± 0.12	51 (5%)	8%	41%	31%	20%
	E	0.40 ± 0.16	0.65 ± 0.11	35 (4%)	0%	23%	49%	29%

TABLE 2: As in Table 1, but for the UI aerosols.

Trajectory altitude		AOD <sub>550</sub>	FM	Year	Winter	Spring	Summer	Autumn
500 m	A	0.45 ± 0.12	0.88 ± 0.06	40 (9%)	5%	48%	23%	25%
	B	0.45 ± 0.29	0.89 ± 0.08	14 (3%)	14%	64%	14%	7%
	C	0.42 ± 0.13	0.89 ± 0.07	120 (27%)	8%	42%	34%	17%
	D	0.46 ± 0.13	0.89 ± 0.08	198 (45%)	8%	44%	25%	24%
	E	0.44 ± 0.13	0.89 ± 0.07	70 (16%)	7%	37%	21%	34%
1000 m	A	0.44 ± 0.12	0.88 ± 0.06	65 (14%)	6%	45%	14%	35%
	B	0.45 ± 0.32	0.87 ± 0.08	12 (3%)	17%	67%	17%	0%
	C	0.43 ± 0.12	0.89 ± 0.08	145 (33%)	6%	41%	38%	14%
	D	0.46 ± 0.13	0.90 ± 0.07	159 (37%)	8%	45%	23%	25%
	E	0.46 ± 0.14	0.88 ± 0.07	62 (13%)	10%	40%	23%	27%
4000 m	A	0.47 ± 0.14	0.88 ± 0.09	93 (21%)	16%	45%	15%	24%
	B	0.44 ± 0.14	0.89 ± 0.07	209 (47%)	4%	43%	33%	20%
	C	0.44 ± 0.11	0.90 ± 0.06	86 (19%)	8%	41%	26%	26%
	D	0.46 ± 0.14	0.89 ± 0.07	34 (8%)	6%	59%	21%	15%
	E	0.48 ± 0.14	0.89 ± 0.09	21 (5%)	0%	33%	29%	38%

free troposphere occurring in the temperate zone. Thus, the Atlantic air masses (sector B) represent 50% of the air masses over Athens in the free troposphere (4000 m). Furthermore, a large fraction (24%) corresponds to African air masses, suggesting that the Saharan outflow over Eastern Mediterranean occurs mainly in the free troposphere. On the other hand, only few cases correspond to air masses from Northeast or local origin at 4000 m.

Very interesting findings can be revealed when the above analysis is performed for each season. In Figure 2 the seasonal frequency distribution (%) of the air masses is given for any altitude and sector together with the number of available cases, N. In winter, the majority of the air

masses, specifically at 4000 m, belong to Sector B, further verifying the clean atmospheric conditions occurred in this season [18]. This distribution is essentially produced by the annual evolution of the meteorological synoptic patterns over the Eastern Mediterranean, with strong Northwestern and Western winds in winter as a consequence of the cyclonic circulation patterns. The Saharan air masses exhibit almost the same frequency with the C sector while that of the other two directions is very low. In spring and summer the above situation is clearly reversed since the majority of the air masses influencing Athens belong to the Northwestern and Northeastern directions, especially for air masses within the boundary layer. In summer, a strong North pressure gradient

TABLE 3: As in Table 1, but for the CM aerosols.

Trajectory altitude	AOD <sub>550</sub>	FM	Year	Winter	Spring	Summer	Autumn	
500 m	A	0.15 ± 0.04	0.51 ± 0.09	27 (15%)	48%	4%	0%	48%
	B	0.13 ± 0.04	0.46 ± 0.14	47 (26%)	55%	11%	0%	34%
	C	0.14 ± 0.04	0.47 ± 0.16	77 (43%)	52%	10%	13%	25%
	D	0.16 ± 0.03	0.60 ± 0.09	17 (9%)	35%	12%	18%	35%
	E	0.15 ± 0.03	0.58 ± 0.10	14 (7%)	29%	64%	7%	0%
1000 m	A	0.15 ± 0.03	0.51 ± 0.10	30 (17%)	53%	7%	0%	40%
	B	0.12 ± 0.04	0.46 ± 0.14	50 (27%)	54%	6%	2%	38%
	C	0.14 ± 0.04	0.49 ± 0.16	81 (45%)	47%	14%	14%	26%
	D	0.15 ± 0.03	0.59 ± 0.10	13 (7%)	46%	0%	8%	46%
	E	0.15 ± 0.04	0.58 ± 0.13	8 (4%)	25%	0%	13%	63%
4000 m	A	0.14 ± 0.03	0.47 ± 0.15	22 (12%)	59%	9%	0%	32%
	B	0.13 ± 0.04	0.49 ± 0.15	127 (70%)	50%	8%	5%	37%
	C	0.16 ± 0.04	0.54 ± 0.12	26 (14%)	38%	15%	23%	23%
	D	0.15 ± 0.04	0.55 ± 0.17	5 (3%)	40%	0%	40%	20%
	E	0.13 ± 0.09	0.62 ± 0.10	2 (1%)	0%	0%	0%	100%

TABLE 4: As in Table 1, but for the DD aerosols.

Trajectory altitude	AOD <sub>550</sub>	FM	Year	Winter	Spring	Summer	Autumn	
500 m	A	0.53 ± 0.22	0.43 ± 0.15	88 (26%)	11%	22%	33%	34%
	B	0.45 ± 0.15	0.40 ± 0.13	26 (8%)	4%	8%	58%	31%
	C	0.45 ± 0.14	0.41 ± 0.14	120 (36%)	1%	8%	61%	30%
	D	0.54 ± 0.17	0.46 ± 0.12	69 (20%)	1%	7%	70%	22%
	E	0.51 ± 0.13	0.46 ± 0.10	34 (10%)	3%	15%	44%	38%
1000 m	A	0.54 ± 0.21	0.43 ± 0.14	101 (30%)	9%	19%	38%	35%
	B	0.44 ± 0.14	0.40 ± 0.13	46 (14%)	2%	11%	52%	35%
	C	0.46 ± 0.12	0.42 ± 0.14	107 (32%)	2%	7%	59%	32%
	D	0.55 ± 0.19	0.46 ± 0.12	56 (16%)	0%	5%	80%	14%
	E	0.50 ± 0.16	0.48 ± 0.13	27 (8%)	7%	22%	37%	33%
4000 m	A	0.57 ± 0.21	0.45 ± 0.13	118 (35%)	8%	25%	38%	29%
	B	0.44 ± 0.12	0.41 ± 0.14	141 (42%)	3%	6%	56%	35%
	C	0.45 ± 0.12	0.46 ± 0.13	54 (17%)	0%	4%	70%	26%
	D	0.49 ± 0.15	0.46 ± 0.13	12 (3%)	0%	8%	58%	33%
	E	0.59 ± 0.24	0.45 ± 0.15	12 (3%)	0%	8%	92%	0%

is developed over the Aegean Sea as a consequence of the combined effects of the North Balkan high-pressure system with the low-pressure one developed in Eastern Levantine Basin. This pressure pattern is associated with air masses from the Northern Balkan countries, whilst the Etesians are quite strong in many cases. These winds carry either pollution and biomass-burning aerosols, affecting mainly Northern Greece [42, 43], or sea-spray particles from the Aegean Sea before reaching Athens. This is the reason for the dominance of the D sector in late spring and summer. Our results are in agreement with those of Stohl et al. [12] and Duncan and Bey [13], who show that the main continental outflow at the lower atmospheric levels towards the Eastern Mediterranean occurs during summer; this flow is greatly

reduced during the other seasons. Also, a significant fraction (18%–28%) corresponds to air masses from Saharan desert especially at the 4000-m altitude. A recent work by Sciare et al. [44] investigated the contribution of different aerosol sources in the Eastern Mediterranean basin, showing that this region is influenced by a wide range of air masses originating mainly from Europe and Africa during summertime. In autumn all the sectors contribute almost in the same way to the air masses reaching Athens, with a shift towards West as the altitude increases. For a more detailed analysis in the followings, the air-mass classification is given for each aerosol type separately aiming at investigating about the main pathways favoring the presence of specific aerosol types over Athens.

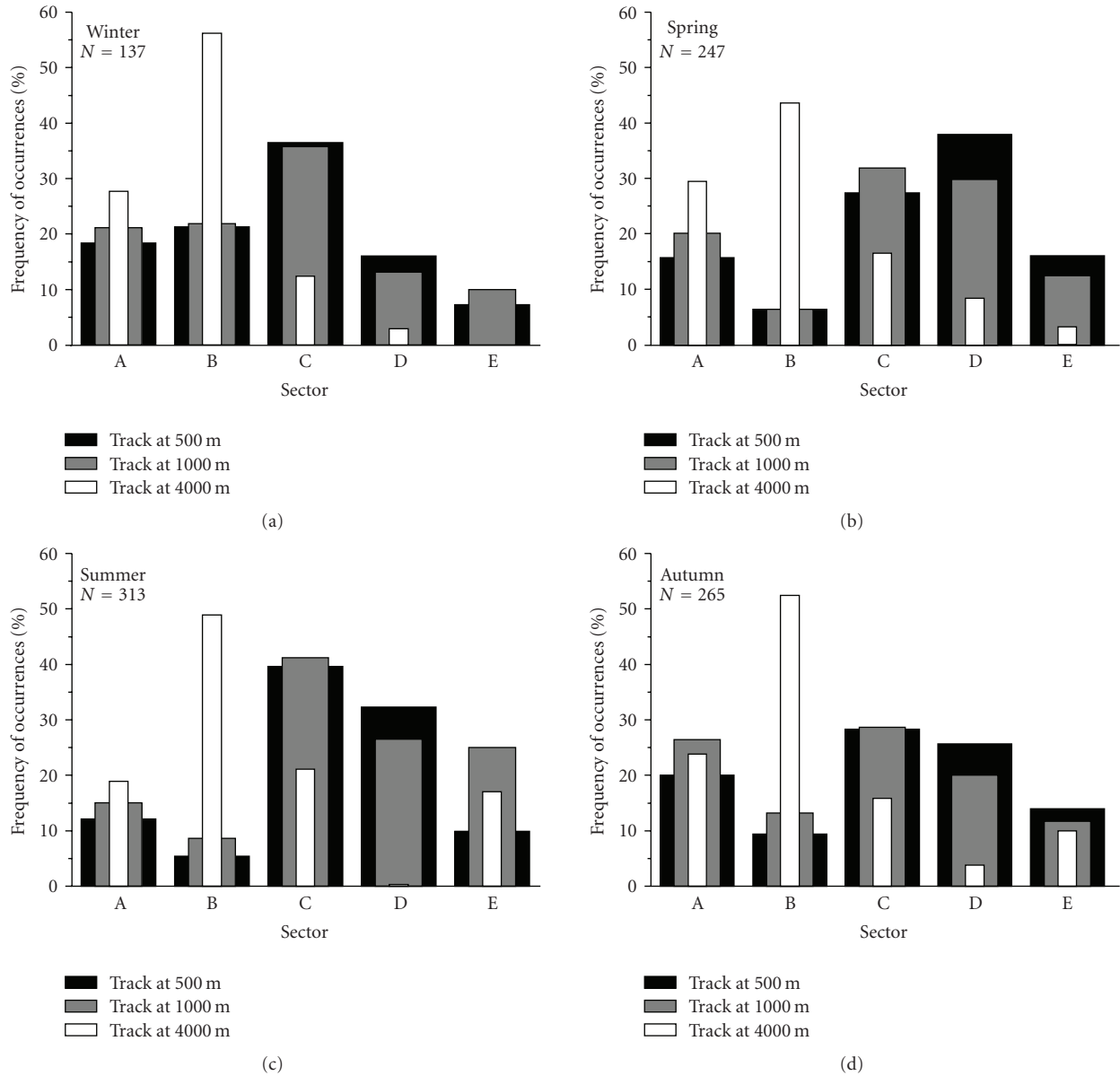


FIGURE 2: Seasonal frequency (%) distribution of the air-mass trajectories at three atmospheric levels over GAA for the whole dataset. The number of data, N, in each season is also given.

4.2. Main Sectors for the Occurrence of Each Aerosol Type. In this Section the above analysis is divided into three classes according to the dominant aerosol type over Athens and the criteria described in Section 3. For cases corresponding to the UI type, the majority of the trajectories belong to the Northeastern Sector (see Figure 3 and Table 2). The main finding regarding the favorable direction for UI type over Athens leads to a Northern flow, mainly from Eastern Europe, within the boundary layer (500 and 1000 m). In contrast, the use of the air masses at 4000 m shows a preferable western and south direction in agreement with the western circulation patterns occurring in the free atmosphere at Northern mid latitudes. Note that a significant number of African air masses (9%–21%) can be characterized as

UI aerosols in the Athens urban environment. In these cases the Saharan outflow is weak and the boundary layer anthropogenic aerosols dominate. Therefore, the necessity of using vertical aerosol profiles in order to distinguish different aerosol types in an urban environment is obvious [29]. Air masses belonging to Sector A can have high FM values (such as 0.93) indicative of anthropogenic rather than Saharan dust aerosols. This fact was also obvious in Lampedusa [36] where in some cases dust-loading air masses were mixed with smoke aerosols from forest fires in the coastal areas of Algeria. Moreover, the occurrence of UI conditions is not favored by Atlantic air masses at the lower altitudes, since they strongly interact with the marine boundary layer. Inversely, a significant contribution

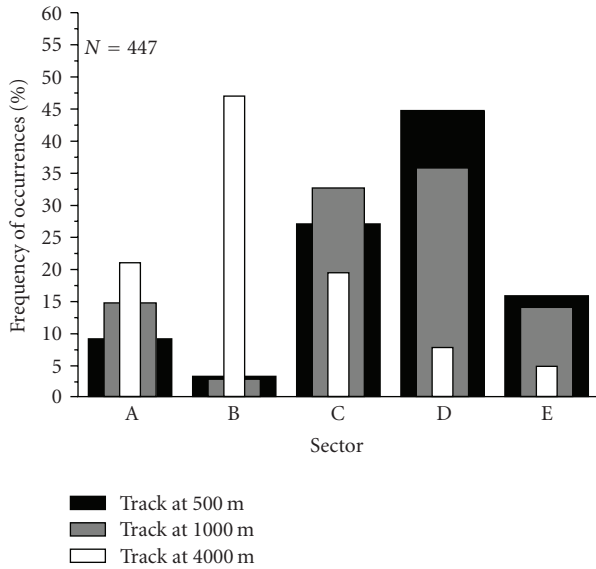


FIGURE 3: Frequency (%) distribution of the air-mass trajectories at three atmospheric levels over GAA for the UI aerosol type. The number of data,  $N$ , is also given.

to these conditions (13%–16%) is provided by the local air masses within the boundary layer favored under stagnant atmospheric conditions. The air-trajectory pattern suggests a prevalent northerly flow at the lower altitudes, where transport of pollutants mainly occurs [42]. In addition, Lelieveld et al. [11] revealed a dominant northerly flow below 4 km in Crete, further confirming our results and those of Stohl et al. [12] and Duncan and Bey [13]. Conversely, in the middle and upper troposphere, Lelieveld et al. [11] found westerly/southerly winds to prevail over Crete. Similarly to the latter, the present analysis for the UI aerosol type over Athens reveals considerable influence from westerly air masses (47%) at 4000 m compared to only 3% in the boundary layer (Table 2). The close agreement of the present results with those of previous studies supports the validity of the identification scheme for the aerosol type discrimination [17] and, in general, the satellite retrievals and the methodology used despite the lack of intercomparison with ground-based measurements.

Regarding the air masses favoring the presence of CM conditions over Athens (Figure 4, Table 3) it is obvious that the B and C Sectors dominate. The majority of the air masses from Sector B belong to the free troposphere (4000 m) for the reasons mentioned above. These results are in agreement with relevant studies in Northern Greece [30] who found more transparent atmospheric conditions associated with air masses from the Atlantic Ocean and Western Europe. Pay attention also to the very low frequencies related to the D and E Sectors, both favoring the trans-boundary pollution transport or the accumulation of aerosols. It is also worth mentioning the significant fraction of air masses from the African continent (12%–17%) that, in general, do not favor the presence of clean atmospheres over Mediterranean. It was found that in these cases either is the dust outflow very weak or wet scavenging via precipitation occurs during its

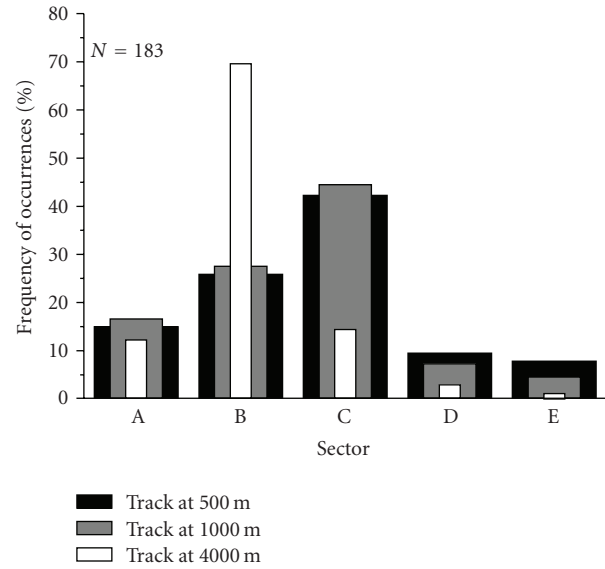


FIGURE 4: Same as in Figure 3, but for the CM aerosol type.

transport over Mediterranean before reaching Athens. It was also found that 70% of these cases include precipitation over Athens, while the majority of the air masses belonging to Sector C have initial Atlantic origin.

As expected, the DD aerosol type occurs mainly from air masses originating from the Sahara desert, especially for air trajectories at 4000 m (35%, see Table 4). Thus, it is concluded that the 4000 m level for the identification of Saharan outflows is reliable as has also been suggested from a variety of studies [40, 45]. The most unexpected feature is the high occurrence of air masses from C (32%–36%) and D (16%–20%) Sectors within the boundary layer (1000 m and 500 m), which favor the presence of DD type over Athens. As clearly mentioned above, only a fraction of the DD type corresponds to dust particles and the occurrence of such aerosols associated with a northern flow maybe related to sea-spray or soil coarse-mode particles lifted from the Aegean Sea and transported above Athens. There should be noticed the great differences in the occurrence of DD type revealed from the trajectory analysis (Figure 5). Thus, the Saharan dust aerosols originating from the Sector A are mainly identified by the trajectories at 4000 m, while the coarse-mode particles from northern directions (mainly soil materials and sea spray) seem to travel within the boundary layer. As also expected, the presence of DD type associated with Atlantic air masses is low, mainly occurring in cases that these air masses (specifically at 4000 m) pass near the African continent. It was also found (not presented) that nearly the whole of the air masses originating from Sector E, and associated with DD aerosols over Athens, come from the south direction (North Libyan Sea) enriched with desert particles.

The above fractions are strongly modified proportionally to the season, and this will be further analyzed. This seasonal variation is mainly driven by the meteorological and

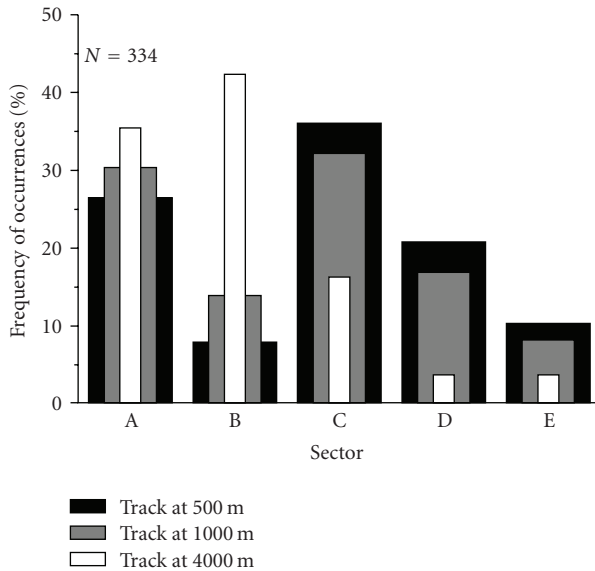


FIGURE 5: Same as in Figure 3, but for the DD aerosol type.

synoptic circulation patterns over Eastern Mediterranean, the local emissions, the meteorological fields favoring the dust outbreaks, the wind speed and direction, and the removal processes. The above analysis is repeated for each individual season in order to establish the differences in the frequency of occurrence for each Sector.

The dominance of UI type in spring is apparent in Figure 6 ( $N = 195$ ). The back trajectory distribution of UI type in spring is closely related to the whole dataset (Figure 2). In winter, despite the low occurrence of the UI type ( $N = 34$ ), its presence is favored by air masses from the D Sector for air masses within the boundary layer. The large occurrence of air masses from the B Sector at 4000 m is not associated with local pollution, which is mainly attributed to air masses in the boundary layer. Furthermore, significant contribution to the UI type is provided by the local stagnant air masses (Sector E) mainly in the warm period of the year.

Clean maritime conditions are rare over Athens, occurring mainly in winter, and are generally associated with air masses originating from North Atlantic and to a lesser extent from Western and Central Europe (Figure 7, Table 3). The CM cases belonging to Sector C are associated with fast-moving air masses exhibiting a descent trajectory when reaching Athens, thus not carrying air pollutants from Continental Europe. Note also that these air masses are very few in spring and summer, when they contribute to the trans-boundary air pollution (Figure 6). It is also worth noticing that in all seasons the CM conditions over Athens associated with Sectors D and E are nearly absent at any level. CM conditions can also be found from air masses originating from the African region. Note that nearly all of them occur in winter and autumn and none in summer. The majority of them are associated with wet removal processes before reaching Athens.

The most interesting features regarding the seasonal distribution of the trajectories are depicted for the DD type

(Figure 8, Table 4). Figure 8 gives support to our previous statements regarding different origins of the coarse-mode particles (referred to as DD) proportionally to the season. Thus, in winter nearly the whole of the DD cases are associated with air masses from Saharan origin (sector A). It is also worth noticing that the African air masses carry desert-dust aerosols at all altitudes favoring the vertical dust transport this season, a feature which is in close agreement with Kalivitis et al. [41] results. In spring, the Saharan contribution to the coarse particles remains the dominant process, with the only difference being the higher number of air masses at 4000 m (70%) enhancing the dust transport in the free troposphere. In further contrast, in summer the above situation is reversed and the coarse-mode particles are most associated with air masses from northern directions, Sectors C and D. The lower  $AOD_{550}$  values of the DD type in summer compared to the spring ones also verify our assumptions, as only part of these DD cases is associated with Saharan desert-dust particles. In early autumn, a similar situation seems to exist, while in late autumn the conditions approach those of winter. Therefore, in autumn similar percentages of the C and A Sectors take place. Regarding the Saharan outflow, the upper troposphere transport dominates in summer and the vertical in autumn, in agreement with the transport observed over Crete [41]. All the above findings are presented in Figure 9, where the differences in the occurrences of each aerosol type proportionally to the transport altitude are clearly depicted.

**4.3. Back Trajectories and Aerosol Properties.** In this section the  $AOD_{550}$  and FM values for each aerosol type are studied with respect to the back trajectories at the three altitudes selected. The mean and the standard deviations of the  $AOD_{550}$  and FM values are given in Tables 1, 2, 3 and 4 for the whole dataset, UI, CM, and DD aerosol types, respectively. The number of the available data is also given for each sector and air-mass altitude.

Values of  $AOD_{550}$  and FM averaged over the whole experimental period are about 0.38 and 0.61 for Sector A, while the lowest values ( $\sim 0.34$  and  $\sim 0.58$ ) are associated with air masses from Sector B. The lowest  $AOD_{550}$  and FM from this sector are expected because of the dominance of marine aerosols. On the other hand, the highest  $AOD_{550}$  ( $\sim 0.37$ – $0.40$ ) in conjunction with the highest FM values (0.63–0.65) are associated with pollution air masses from Eastern Europe and local emissions (Sectors D and E, resp.). Zerefos et al. [43] showed enhanced columnar  $SO_2$  values over northern Greece that correspond to northeastern directions mainly during summertime, providing further evidence for the pollution transport. In addition, this sector has been also affected by severe biomass burning episodes [46]. Sector E is representative mostly for local circulation patterns, and therefore, the enhanced  $AOD_{550}$  and FM values should be attributed to local pollution with some enhancement at the higher altitudes by Saharan dust from Libya (see the higher  $AOD_{550}$  values at 4000 m). Finally, a great part of the measurements at all altitudes (17%–35%) corresponds to Sector C, which is representative at northwestern flow from

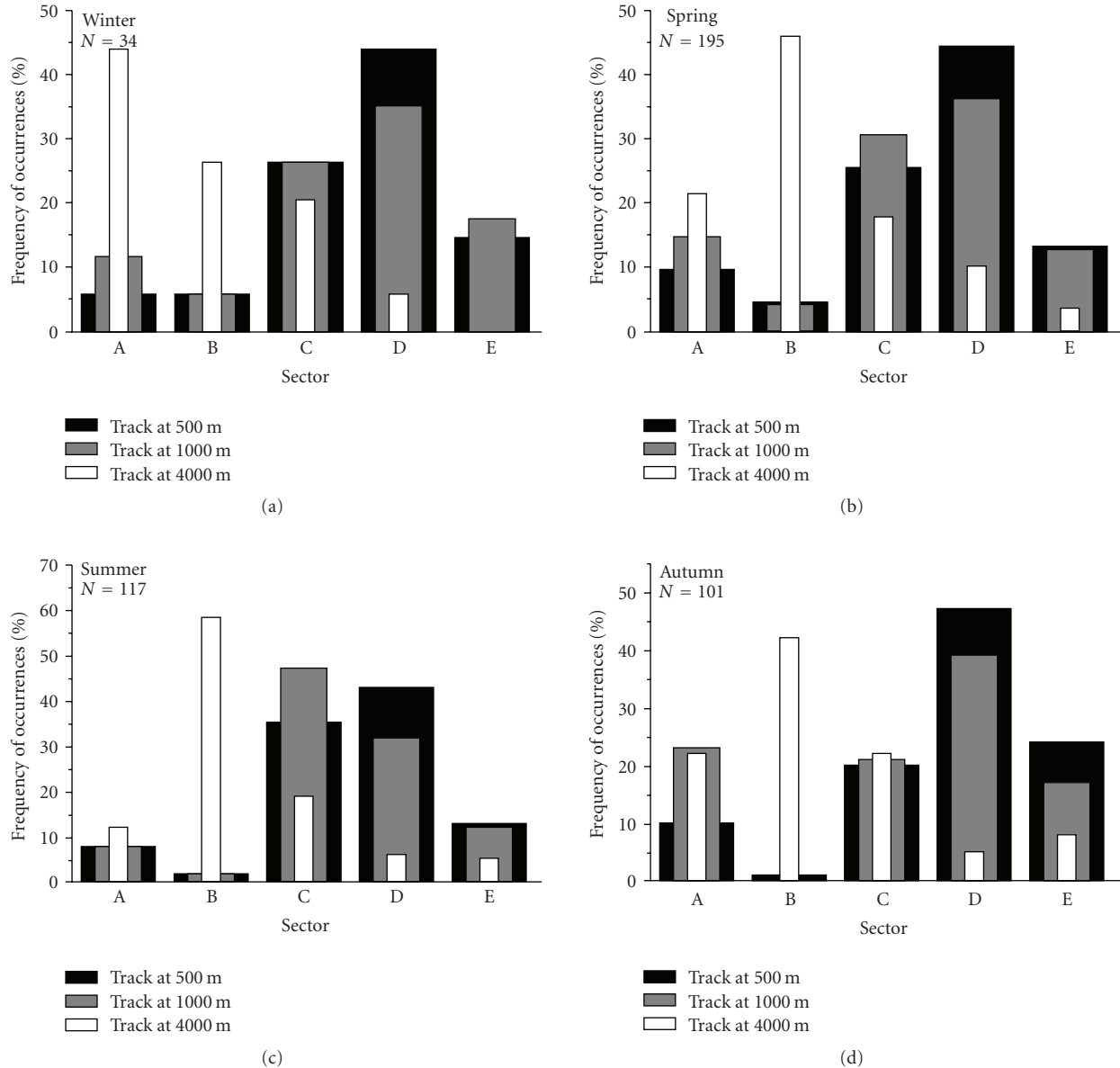


FIGURE 6: Seasonal frequency (%) distribution of the air-mass trajectories at three atmospheric levels over GAA for the UI aerosol type. The number of data, N, in each season is also given.

Central Europe. The lower  $AOD_{550}$  compared to Sector D could be a consequence of the control in emissions and air pollution in the countries of Western and Central Europe.

It is obvious that for the whole dataset the differences in the air-mass altitudes and in the number of trajectory occurrences do not affect the aerosol properties in the vertical. Nevertheless, larger differences are computed for the FM values rather than  $AOD_{550}$ . These results are in agreement with those presented by Pace et al. [36] who prepared a similar sensitivity study changing the border of the sectors and the duration of the back-trajectories. They also found higher differences in  $\alpha$ -Ångström rather than AOD. The mean  $AOD_{550}$  and FM values computed in our analysis are in close agreement with the results obtained for Northern Greece by Amiridis et al. [30],

who found higher AODs to correspond to eastern, local, and southern sectors and lower for the western. These also agree with the results conducted by Formenti et al. [39] at Mount Athos (North Greece) in June–September 1998. They found that the largest values of  $\alpha$  correspond to air masses coming from Eastern Europe and former Soviet Union. Furthermore, Pace et al. [36] found that low values of  $\alpha$ -Ångström at Lampedusa were measured for air masses coming from North Africa, while air masses originating from Europe showed progressively increasing values.

Table 2 summarizes the mean and standard deviations of  $AOD_{550}$  and FM values proportionally to the Sector and air-mass altitude for the UI type. Due to the limited range of FM values corresponding to the UI type (0.8–1.0) the differences

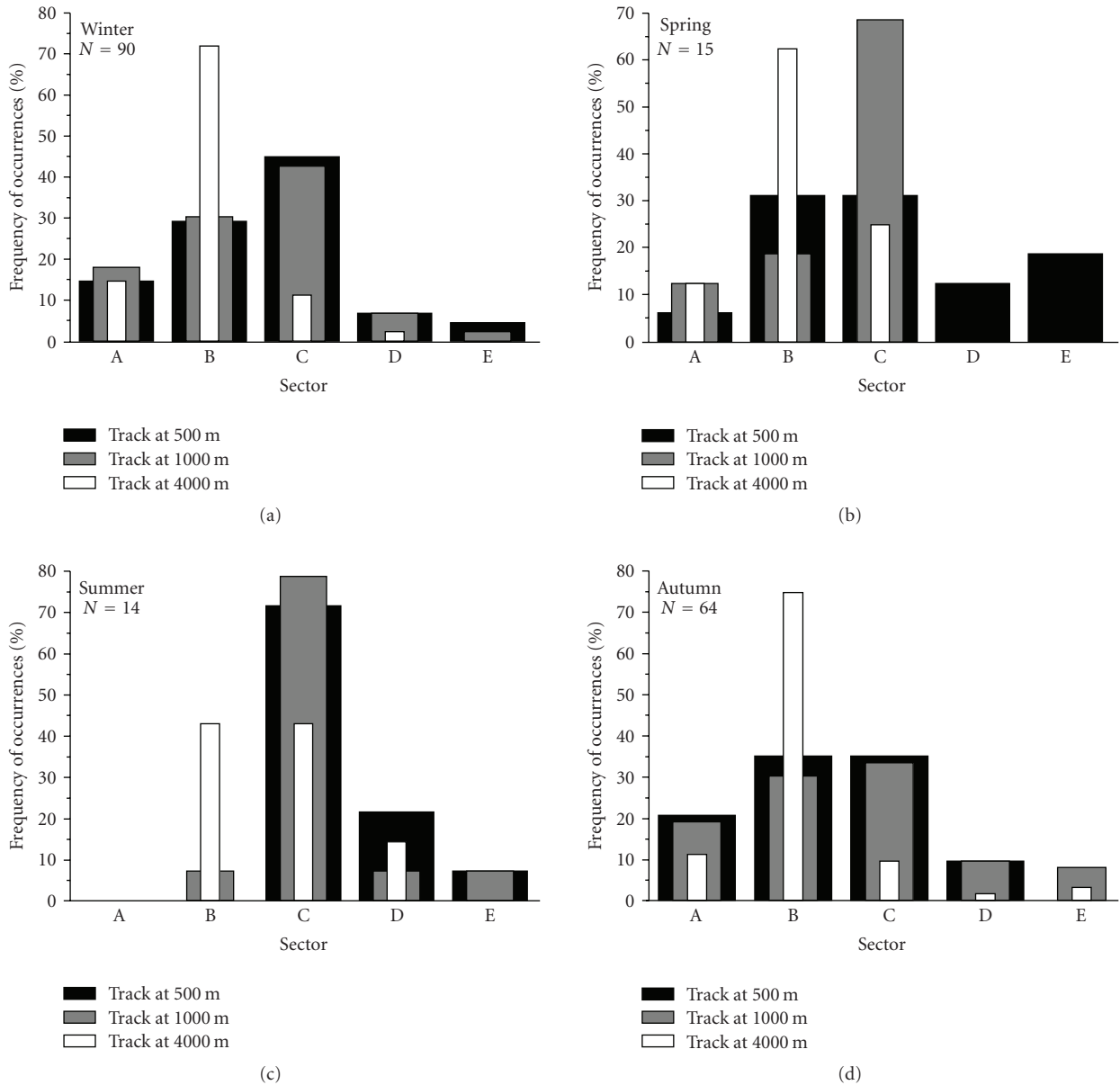


FIGURE 7: Same as in Figure 6, but for the CM aerosol type.

in this parameter are negligible. Also, very high  $AOD_{550}$  values, varying from 0.42 to 0.48, are computed almost independently from the sector and the air-mass altitude. As previously mentioned, the UI type is favored by air masses within the boundary layer and the aerosol properties can more safely be studied for trajectories at 500 and 1000 m. Therefore, the higher  $AOD_{550}$  is associated with air masses from the Sectors D and E, further confirming the transport or the accumulation of pollutants. The high mean  $AOD_{550}$  values corresponding to the Sector B (0.45) are referred to a limited number of data (3%) and are attributed to three days when the Athens environment can be characterized as “pollution smog.” The large standard deviations also confirm that these values are not representative for the whole dataset. An additional interesting finding is the highest mean  $AOD_{550}$

values (0.47 and 0.48) corresponding to air masses at 4000 m from Sectors A and E. It was found that 18 out of 21 cases from the Sector E correspond to air masses from south directions (Libyan Sea) enriched with dust aerosols at the upper levels. Therefore, under such conditions, that is, heavy anthropogenic aerosols in the boundary layer associated with uplifted layer of Saharan dust enhance the aerosol load over Athens.

As regards the CM aerosol type, the lowest  $AOD_{550}$  (~0.13) corresponds to Sector B (Table 3). Since the  $AOD_{550}$  range is limited (0–0.2) for this type, no large variations between the sectors and air-mass altitudes in the  $AOD_{550}$  values are observed. Nevertheless, air masses probably carrying desert particles from Sector A or pollution from Sector D exhibit little higher  $AOD_{550}$  values (0.15–0.16).

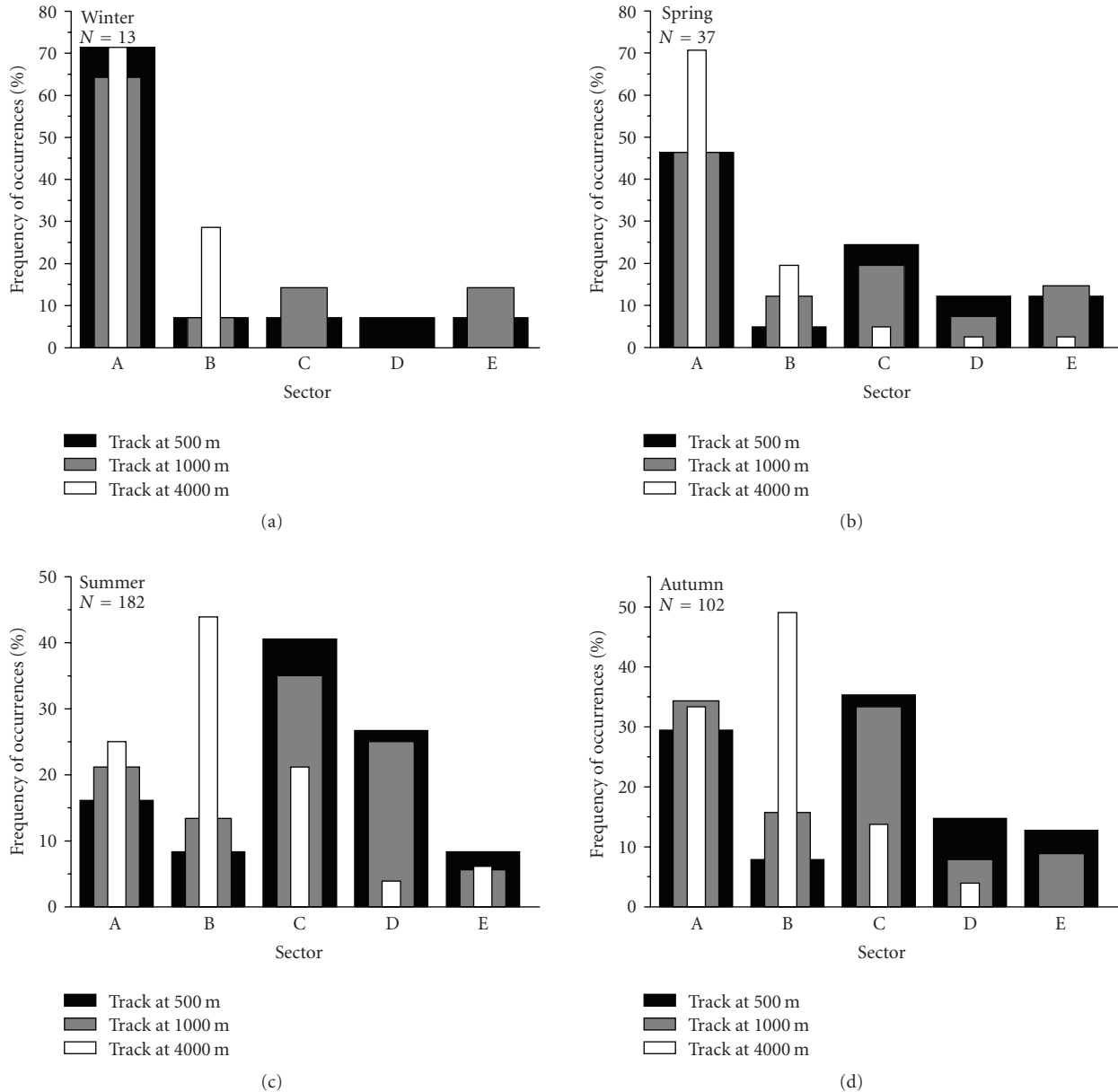


FIGURE 8: Same as in Figure 6, but for the DD aerosol type.

On the other hand, higher variations are observed regarding the FM values. Therefore, the higher contribution of the coarse-mode particles (desert dust or sea spray) as well as the contribution of the fine-mode aerosols (local or transported pollution) to the total AOD<sub>550</sub> is more intense for the Sectors A, B (0.46–0.51) and D, E (0.55–0.62), respectively.

As regards the DD type, it was established that this type can be divided into two groups: (a) desert-dust aerosols of Saharan origin and (b) coarse-mode particles (sea-spray or soil dust) from northern directions. The AOD<sub>550</sub> and FM values at the three altitudes presented in Table 4 further confirm the previous assumptions. An increase in AOD<sub>550</sub> values (from 0.53 to 0.57) from Sector A is

observed as the air-mass altitude increases; this suggests that the dust transport over GAA occurs mainly in the free troposphere. Inversely, lower AOD<sub>550</sub> values (0.49 to 0.54) correspond to Sector D, exhibiting a decreasing trend with the air-mass altitude. As expected, the lowest AOD<sub>550</sub> values (0.44) are associated with air masses from the Atlantic Ocean. Another interesting feature is the very high AOD<sub>550</sub> value ( $0.59 \pm 0.24$ ), despite the limited number of cases (12), corresponding to air masses at 4000 m from Sector E. Additionally, even in cases when DD is the dominant aerosol type in the vertical, the local emissions and the anthropogenic aerosols associated with Sectors D and E increase the FM values, which are the lowest for air masses originating in Sector B.

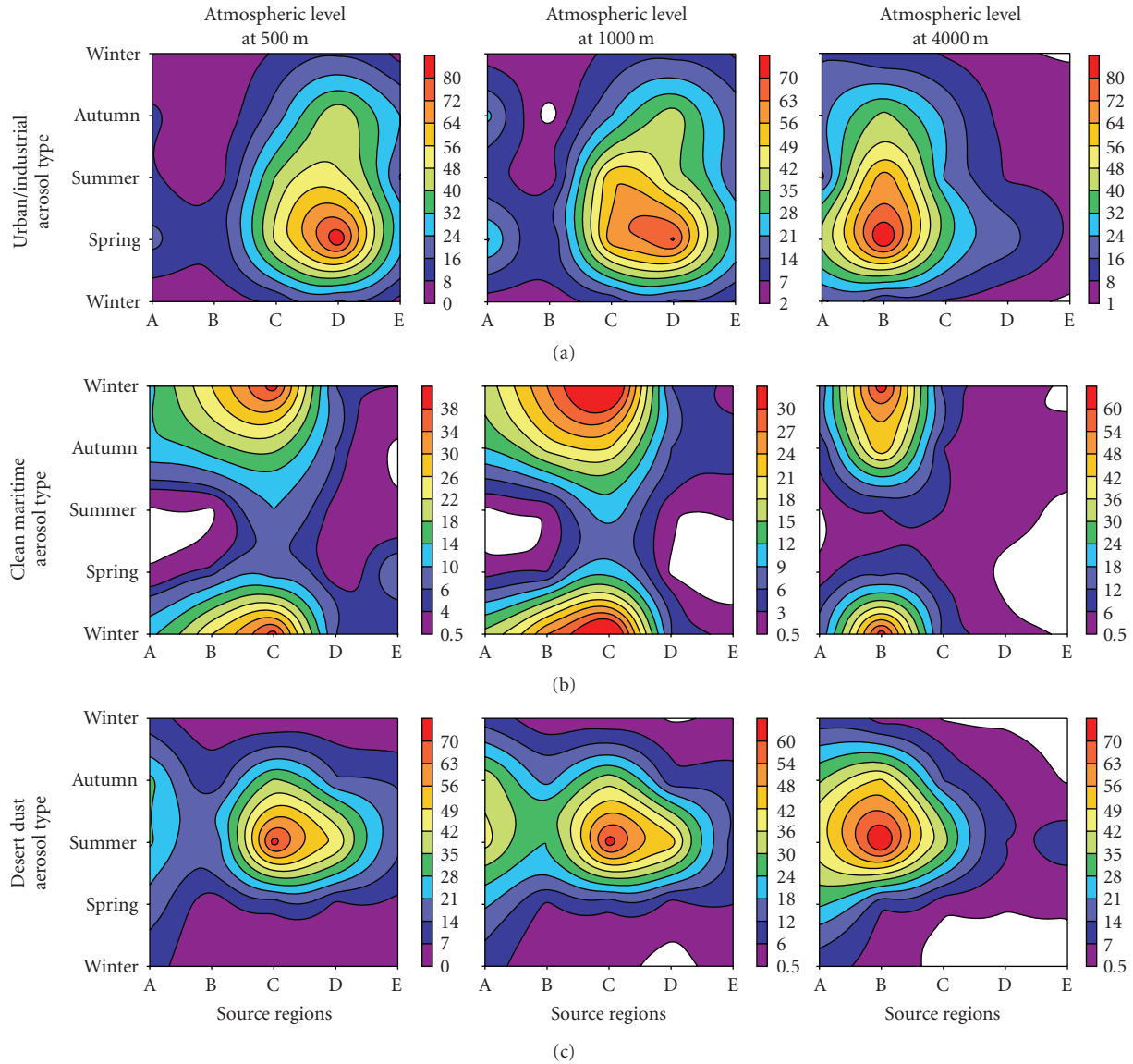


FIGURE 9: Contour plot of the seasonal frequency distribution of the air-mass trajectories at three atmospheric levels over GAA for all aerosol types. The white gaps correspond to lack of data.

### 5. Conclusions

Terra-MODIS aerosol products (AOD<sub>550</sub> and FM) obtained over Athens, Greece, have been analyzed in order to provide information about the climatological characteristics of the aerosol optical properties. The data cover the period February 2000–December 2005. Based on AOD<sub>550</sub> and FM values three main aerosol types corresponding to urban/industrial (UI) aerosols, clean maritime (CM) conditions, and coarse-mode desert dust (DD) particles were discriminated. The investigation of the source regions, via 4-day air-mass back-trajectory analysis at three altitudes, showed that the UI type is favored by air masses within the boundary layer originating from Eastern Europe or due to local emissions. In contrast, the desert-dust conditions are associated with African air masses mainly at the upper atmospheric levels, while clean

maritime conditions, although rare, are associated with fast-moving air masses from the Atlantic Ocean. In almost all cases, African aerosols display high values of AOD<sub>550</sub> and low values of FM, typical of Saharan dust (mean values of AOD<sub>550</sub> and FM are ~0.39 and ~0.60, resp.). Particles originating from Eastern Europe show relatively large average values of AOD<sub>550</sub> and FM (0.38 and 0.65) respectively, while particles from North Atlantic show the lowest AOD<sub>550</sub> values (0.34) and relatively small values of FM (0.60), which are consistent with those of maritime aerosols. However, the identification of the aerosol type and properties based on air-mass trajectories is a rather difficult thing due to fast changes in the aerosol vertical distribution, which is caused by air masses of different origins in the vertical column. Many variations in the observed patterns of the aerosol types were attributed to the transport origins and meteorological

conditions. Overall, this may overemphasize the importance of the processes relative to chemistry, emissions source strengths, and local influences on the observed variability of the aerosol type and properties. The close agreement of our results with other studies and chemical transport models gives credit to the analysis used in order to identify the transport mechanisms of different aerosol types over Athens. Therefore, the present methodology seems to be sufficient in monitoring the long-range transport of aerosols and pollutants at different atmospheric levels and can also be applicable for air-quality studies. However, despite the consistency of the present results with those of chemical transport models, the long-range transport may not always be the most importance factor in determining the observed aerosol properties over Athens. Therefore, some open issues still exist. How does the strong seasonal variability in the aerosol sources, such as secondary organic aerosols or photochemical pollution, affect the variability in the observed aerosol types? How does the effectiveness of sulfate aerosol formation in cloud processing impact the results? How does the mass of aerosols transported along any given trajectory vary or weigh the importance of that trajectory in the overall analysis? The approach taken in this manuscript cannot really address such issues, which would require chemical transport modeling to understand.

## Acknowledgments

The authors would like to thank the MODIS science data support team (past and present) for processing data via Giovanni website. The HYSPLIT scientific team for providing the back-trajectory plots is also gratefully acknowledged.

## References

- [1] J. Haywood and O. Boucher, "Estimates of the direct and indirect radiative forcing due to tropospheric aerosols: a review," *Reviews of Geophysics*, vol. 38, no. 4, pp. 513–543, 2000.
- [2] IPCC, "Summary for policymakers," in *Climate Change 2007: The Physical Science Basis. Contribution of Working Group I to the Fourth Assessment Report of the Intergovernmental Panel on Climate Change*, S. Solomon, D. Qin, M. Manning, et al., Eds., Cambridge University Press, Cambridge, UK, 2007.
- [3] M. D. King, Y. J. Kaufman, D. Tanré, and T. Nakajima, "Remote sensing of tropospheric aerosols from space: past, present, and future," *Bulletin of the American Meteorological Society*, vol. 80, no. 11, pp. 2229–2259, 1999.
- [4] F. Barnaba and G. P. Gobbi, "Aerosol seasonal variability over the Mediterranean region and relative impact of maritime, continental and Saharan dust particles over the basin from MODIS data in the year 2001," *Atmospheric Chemistry and Physics*, vol. 4, no. 9–10, pp. 2367–2391, 2004.
- [5] C. D. Papadimas, N. Hatzianastassiou, N. Mihalopoulos, X. Querol, and I. Vardavas, "Spatial and temporal variability in aerosol properties over the Mediterranean basin based on 6-year (2000–2006) MODIS data," *Journal of Geophysical Research D*, vol. 113, no. 11, Article ID D11205, 2008.
- [6] C. Moulin, C. E. Lambert, U. Dayan, et al., "Satellite climatology of African dust transport in the Mediterranean atmosphere," *Journal of Geophysical Research D*, vol. 103, no. D11, pp. 13137–13144, 1998.
- [7] D. Antoine and D. Nobileau, "Recent increase of Saharan dust transport over the Mediterranean Sea, as revealed from ocean color satellite (SeaWiFS) observations," *Journal of Geophysical Research D*, vol. 111, no. 12, Article ID D12214, 2006.
- [8] A. M. Tafuro, F. Barnaba, F. De Tomasi, M. R. Perrone, and G. P. Gobbi, "Saharan dust particle properties over the central Mediterranean," *Atmospheric Research*, vol. 81, no. 1, pp. 67–93, 2006.
- [9] D. G. Kaskaoutis, H. D. Kambezidis, P. T. Nastos, and P. G. Kosmopoulos, "Study on an intense dust storm over Greece," *Atmospheric Environment*, vol. 42, no. 29, pp. 6884–6896, 2008.
- [10] D. Meloni, A. di Sarra, F. Monteleone, G. Pace, S. Piacentino, and D. M. Sferlazzo, "Seasonal transport patterns of intense Saharan dust events at the Mediterranean island of Lampedusa," *Atmospheric Research*, vol. 88, no. 2, pp. 134–148, 2008.
- [11] J. Lelieveld, H. Berresheim, S. Borrmann, et al., "Global air pollution crossroads over the Mediterranean," *Science*, vol. 298, no. 5594, pp. 794–799, 2002.
- [12] A. Stohl, S. Eckhardt, C. Forster, P. James, and N. Spichtinger, "On the pathways and timescales of intercontinental air pollution transport," *Journal of Geophysical Research*, vol. 107, Article ID D4684, 2002.
- [13] B. N. Duncan and I. Bey, "A modeling study of the export pathways of pollution from Europe: seasonal and interannual variations (1987–1997)," *Journal of Geophysical Research D*, vol. 109, no. 8, Article ID D08301, pp. 1–19, 2004.
- [14] J. Feichter, E. Kjellström, H. Rodhe, F. Dentener, J. Lelieveld, and G.-J. Roelofs, "Simulation of the tropospheric sulfur cycle in a global climate model," *Atmospheric Environment*, vol. 30, no. 10–11, pp. 1693–1707, 1996.
- [15] J. M. Prospero, "Mineral and sea salt aerosol concentration in various ocean regions," *Journal of Geophysical Research*, vol. 84, no. C2, pp. 725–731, 1979.
- [16] J. Heintzenberg, D. C. Covert, and R. Van Dingenen, "Size distribution and chemical composition of marine aerosols: a compilation and review," *Tellus, Series B*, vol. 52, no. 4, pp. 1104–1122, 2000.
- [17] D. G. Kaskaoutis, P. Kosmopoulos, H. D. Kambezidis, and P. T. Nastos, "Aerosol climatology and discrimination of different types over Athens, Greece, based on MODIS data," *Atmospheric Environment*, vol. 41, no. 34, pp. 7315–7329, 2007.
- [18] P. G. Kosmopoulos, D. G. Kaskaoutis, P. T. Nastos, and H. D. Kambezidis, "Seasonal variation of columnar aerosol optical properties over Athens, Greece, based on MODIS data," *Remote Sensing of Environment*, vol. 112, no. 5, pp. 2354–2366, 2008.
- [19] Y. J. Kaufman and D. Tanré, "Algorithm for remote sensing of tropospheric aerosol from MODIS," Algorithm Theoretical Basis Documents (ATBD-MOD-02), p. 85, 1998.
- [20] R. C. Levy, L. A. Remer, S. Mattoo, E. F. Vermote, and Y. J. Kaufman, "Second-generation operational algorithm: retrieval of aerosol properties over land from inversion of moderate resolution imaging spectroradiometer spectral reflectance," *Journal of Geophysical Research D*, vol. 112, no. 13, Article ID D13211, 2007.
- [21] D. A. Chu, Y. J. Kaufman, G. Zibordi, et al., "Global monitoring of air pollution over land from the Earth observing system-terra moderate resolution imaging spectroradiometer (MODIS)," *Journal of Geophysical Research D*, vol. 108, no. 21, article 4661, pp. ACH4.1–ACH4.18, 2003.

- [22] C. Ichoku, D. A. Chu, S. Mattoo, et al., "A spatio-temporal approach for global validation and analysis of MODIS aerosol products," *Geophysical Research Letters*, vol. 29, no. 12, pp. 1.1–1.14, 2002.
- [23] D. A. Chu, Y. J. Kaufman, C. Ichoku, L. A. Remer, D. Tanré, and B. N. Holben, "Validation of MODIS aerosol optical depth retrieval over land," *Geophysical Research Letters*, vol. 29, no. 12, pp. 2.1–2.4, 2002.
- [24] L. A. Remer, D. Tanré, Y. J. Kaufman, et al., "Validation of MODIS aerosol retrieval over ocean," *Geophysical Research Letters*, vol. 29, no. 12, pp. 3.1–3.4, 2002.
- [25] R. C. Levy, L. A. Remer, D. Tanré, et al., "Evaluation of the moderate-resolution imaging spectroradiometer (MODIS) retrievals of dust aerosol over the ocean during PRIDE," *Journal of Geophysical Research D*, vol. 108, no. 19, pp. 10.1–10.13, 2003.
- [26] R. C. Levy, L. A. Remer, and O. Dubovik, "Global aerosol optical properties and application to moderate resolution imaging spectroradiometer aerosol retrieval over land," *Journal of Geophysical Research D*, vol. 112, no. 13, Article ID D13210, 2007.
- [27] L. A. Remer, Y. J. Kaufman, D. Tanré, et al., "The MODIS aerosol algorithm, products, and validation," *Journal of the Atmospheric Sciences*, vol. 62, no. 4, pp. 947–973, 2005.
- [28] R. R. Draxler and G. D. Rolph, "HYSPLIT (Hybrid single-particle Lagrangian Integrated Trajectory) model," NOAA Air Resources Laboratory, Silver, Spring, Md, USA, 2003, <http://www.arl.noaa.gov/ready/hysplit4.html>.
- [29] A. Papayannis, D. Balis, V. Amiridis, et al., "Measurements of Saharan dust aerosols over the Eastern Mediterranean using elastic backscatter-Raman lidar, spectrophotometric and satellite observations in the frame of the EARLINET project," *Atmospheric Chemistry and Physics*, vol. 5, no. 8, pp. 2065–2079, 2005.
- [30] V. Amiridis, D. S. Balis, S. Kazadzis, et al., "Four-year aerosol observations with a Raman lidar at Thessaloniki, Greece, in the framework of European Aerosol Research Lidar Network (EARLINET)," *Journal of Geophysical Research D*, vol. 110, no. 21, Article ID D21203, pp. 1–12, 2005.
- [31] D. Meloni, A. di Sarra, G. Biavati, et al., "Seasonal behavior of Saharan dust events at the Mediterranean island of Lampedusa in the period 1999–2005," *Atmospheric Environment*, vol. 41, no. 14, pp. 3041–3056, 2007.
- [32] Y. J. Kaufman, D. Tanré, and O. Boucher, "A satellite view of aerosols in the climate system," *Nature*, vol. 419, no. 6903, pp. 215–223, 2002.
- [33] L. A. Remer and Y. J. Kaufman, "Dynamic aerosol model: urban/industrial aerosol," *Journal of Geophysical Research D*, vol. 103, no. D12, pp. 13859–13871, 1998.
- [34] K. O. Ogunjobi, Z. He, and C. Simmer, "Spectral aerosol optical properties from AERONET Sun-photometric measurements over West Africa," *Atmospheric Research*, vol. 88, no. 2, pp. 89–107, 2008.
- [35] A. Smirnov, B. N. Holben, O. Dubovik, R. Frouin, T. F. Eck, and I. Slutsker, "Maritime component in aerosol optical models derived from aerosol robotic network data," *Journal of Geophysical Research D*, vol. 108, no. 1, pp. AAC14.1–AAC14.11, 2003.
- [36] G. Pace, A. di Sarra, D. Meloni, S. Piacentino, and P. Chamard, "Aerosol optical properties at Lampedusa (Central Mediterranean). 1. Influence of transport and identification of different aerosol types," *Atmospheric Chemistry and Physics*, vol. 6, no. 3, pp. 697–713, 2006.
- [37] K. K. Moorthy, S. S. Babu, and S. K. Satheesh, "Aerosol characteristics and radiative impacts over the Arabian Sea during the intermonsoon season: results from ARMEX field campaign," *Journal of the Atmospheric Sciences*, vol. 62, no. 1, pp. 192–206, 2005.
- [38] K. K. Moorthy, S. S. Babu, and S. K. Satheesh, "Aerosol spectral optical depths over the Bay of Bengal: role of transport," *Geophysical Research Letters*, vol. 30, no. 5, pp. 53.1–53.4, 2003.
- [39] P. Formenti, M. O. Andreae, T. W. Andreae, et al., "Aerosol optical properties and large-scale transport of air masses: observations at a coastal and a semiarid site in the Eastern Mediterranean during summer 1998," *Journal of Geophysical Research D*, vol. 106, no. D9, pp. 9807–9826, 2001.
- [40] A. di Sarra, T. Di Iorio, M. Cacciani, G. Fiocco, and D. Fuà, "Saharan dust profiles measured by lidar at Lampedusa," *Journal of Geophysical Research D*, vol. 106, no. D10, pp. 10335–10348, 2001.
- [41] N. Kalivitis, E. Gerasopoulos, M. Vrekoussis, et al., "Dust transport over the Eastern Mediterranean derived from total ozone mapping spectrometer, aerosol robotic network, and surface measurements," *Journal of Geophysical Research D*, vol. 112, no. 3, Article ID D03202, 2007.
- [42] D. Melas, H. D. Kambezidis, J. L. Walmsley, et al., "Summary of meeting: NATO/CCMS pilot study workshop on air pollution transport and diffusion over coastal urban areas," *Atmospheric Environment*, vol. 29, no. 24, pp. 3713–3718, 1995.
- [43] C. Zerefos, K. Ganev, K. Kourtidis, M. Tzortziou, A. Vasaras, and E. Syrakov, "On the origin of SO<sub>2</sub> above Northern Greece," *Geophysical Research Letters*, vol. 27, no. 3, pp. 365–368, 2000.
- [44] J. Sciare, H. Bardouki, C. Moulin, and N. Mihalopoulos, "Aerosol sources and their contribution to the chemical composition of aerosols in the Eastern Mediterranean Sea during summertime," *Atmospheric Chemistry and Physics*, vol. 3, pp. 291–302, 2003.
- [45] P. Alpert, P. Kishcha, A. Shtivelman, S. O. Krichak, and J. H. Joseph, "Vertical distribution of Saharan dust based on 2.5-year model predictions," *Atmospheric Research*, vol. 70, no. 2, pp. 109–130, 2004.
- [46] D. S. Balis, V. Amiridis, C. Zerefos, et al., "Raman lidar and sunphotometric measurements of aerosol optical properties over Thessaloniki, Greece during a biomass burning episode," *Atmospheric Environment*, vol. 37, no. 32, pp. 4529–4538, 2003.

## Research Article

# Aerosol Monitoring over Athens Using Satellite and Ground-Based Measurements

D. G. Kaskaoutis,<sup>1</sup> N. Sifakis,<sup>2</sup> A. Retalis,<sup>1</sup> and H. D. Kambezidis<sup>1</sup>

<sup>1</sup> Atmospheric Research Team, Institute for Environmental Research and Sustainable Development, National Observatory of Athens, Lofos Nymphon, P.O. Box 20048, 11810 Athens, Greece

<sup>2</sup> Institute for Space Applications and Remote Sensing, National Observatory of Athens, Metaxa & Vas. Pavlou, Pendeli, 15236 Athens, Greece

Correspondence should be addressed to H. D. Kambezidis, [harry@meteo.noa.gr](mailto:harry@meteo.noa.gr)

Received 27 June 2009; Revised 25 October 2009; Accepted 2 December 2009

Academic Editor: Krishnaswamy Krishnamoorthy

Copyright © 2010 D. G. Kaskaoutis et al. This is an open access article distributed under the Creative Commons Attribution License, which permits unrestricted use, distribution, and reproduction in any medium, provided the original work is properly cited.

Satellite data of moderate spatial resolution (MODIS and MERIS) were used to retrieve the aerosol optical depth (AOD) over the urban area of Athens. MODIS products were obtained at a horizontal resolution of 10 by 10 km<sup>2</sup> centered over Athens, while the differential textural analysis (DTA) code was applied to MERIS images to retrieve relative-to-reference AOD with a resolution of 260 m by 290 m. The possibility of exploiting the full resolution of MERIS data in retrieving AOD over a grid of a few hundreds metres was thereby investigated for the first time. MERIS-based AOD, centred at 560 nm, showed strong positive correlation to ground-based PM<sub>10</sub> data ( $R^2 = 0.85$ ), while MODIS AOD products were in agreement with both MERIS and PM<sub>10</sub>. Back trajectories were used to study the impact of atmospheric conditions prevailing during the examined days. Days associated with Saharan air masses corresponded to enhanced AOD and predominance of coarse-mode particles. The results suggest that, at least for the case of Athens, AOD retrieved by MERIS images using the DTA code over cloud-free areas can be related to PM<sub>10</sub>. The accuracy of retrieval mainly depends on the successful selection of the reference satellite data, namely, an image being least contaminated by tropospheric aerosols.

## 1. Introduction

Various types of aerosol can be found in the Mediterranean, namely, desert dust, originated from the Saharan desert, pollution particles, emitted mainly by urban and industrial activities, marine aerosol, formed continuously over the Mediterranean, and biomass-burning smoke, produced by seasonal forest fires during summer. PM<sub>10</sub> and PM<sub>2.5</sub> have been accounted for health impairment of citizens in urban areas [1, 2], and high levels of such particulate pollutants, along with gaseous pollutants (nitrogen oxides, carbon monoxide, and ozone) have been reported in Athens (Greece) over the last two decades [3]. Therefore, air quality improvement and monitoring in the capital of Greece is of great concern to the government since reduction of air pollutant exposures will have both short- and long-term public health benefits. Furthermore, Greece has to comply with the related directives of the European Union.

Aerosol parameters can be measured in-situ or remotely sensed from ground, aircraft, or satellite. In particular, satellite remote sensing has been increasingly used to map aerosols in the atmosphere [4]. It constitutes a recent but powerful tool for assessing aerosol spatial distribution and properties due to its major benefit of providing complete and synoptic views of large areas in single snapshots. The data from satellite sensors can be used to improve current understanding and to give a boost to the effort in future climate predictions caused by aerosols. A variety of techniques have been applied to different datasets with spatial resolutions varying from moderate and low (using Meteosat, AVHRR, or SeaWiFS data) [5–9] to high (using SPOT and Landsat data) [10–12]. Because satellite-based information on tropospheric aerosols is relatively recent, its reliability must still be checked against ground-based measurements [13].

The derivation of aerosol parameters from the Moderate Resolution Imaging Spectroradiometer (MODIS) ushers in

a new era in aerosol remote sensing from space [14] since their launch in 1999 and 2002 onboard the Terra and Aqua polar-orbiting satellites, respectively. MODIS aerosol data have demonstrated their utility in studies at regional and at global level as well as in radiative forcing calculations [14–17]. Moreover, Hutchison [18] has shown that MODIS data and products can detect and track the migration of pollutants; he analyzed some cases to show the usefulness of remote sensing in monitoring air quality in urban areas. The Medium Resolution Imaging Spectrometer (MERIS) is also a moderate-to-high spatial resolution Earth observing system on-board ENVISAT, launched in 2002.

The present study attempts to retrieve the aerosol load in terms of aerosol optical depth (AOD) related to air quality in the Athens urban area. For the purpose of this study, both satellite remote sensing and ground-based measurements were used in conjunction with model applications. The goal of this research is to investigate whether MERIS can provide information on the spatial distribution of aerosols over urban areas, with horizontal resolution as high as its inherent ground sampling distance, that is, of the order of a few hundreds of metres. MERIS 5th band, centred at 560 nm, has a spatial advantage over the spectrally equivalent MODIS 4th band (555 nm); less than 300 metres versus 500 metres. Such information could be best associated to urban aerosol distribution and could also be used to link local pollution emissions to their regional and global effects in climatology.

## 2. Description of the Area

Athens is located in an oblong basin that is characterized by a complex topography and covers an area of approximately 450 km<sup>2</sup> with a population of about 3.5 million inhabitants (census 2001). The basin is surrounded by mountains at the three sides and by the sea (Saronikos Gulf) in the south. This complex topography gives a result of poor air-mass mixing within the basin [19]. The main sources of pollution are industrial activities, concentrated in the southwest edge, and the increasing number of vehicles.

During summer there are two opposite wind regimes; calms or sea-breeze circulation that appear when the synoptic flow is weak, and are frequently associated with high levels of air pollution [20], and the strong northeasterly winds called “Etesian”. Different aerosol loading and properties have been monitored in the basin proportionally to the wind pattern [20]. The sea breeze and calms favor the accumulation of pollutants in the Athens atmosphere and the formation of a yellowish-brown cloud of optically effective particles over Athens due to photochemical reactions (e.g., [19]).

## 3. Datasets

**3.1. MERIS Data.** MERIS data are currently available in 15 spectral bands, in the nominal spectral range 400–900 nm, in two modes; at full spatial resolution (260 m by 290 m), and at reduced resolution (1200 m), with a swath of 1150 km around nadir. MERIS provides a global coverage of the

Earth every 3 days [21]. A series of MERIS Level 2 Full Resolution images acquired over the Prefecture of Attica including the Greater Athens Area (GAA), were pre-selected. Their selection was based on the criterion of identical orbit over the study area in order to avoid geometrical distortions that would affect the radiometry of the images. The images selected corresponded to six dates (Table 1) with minimum cloud cover and high acquisition quality. MERIS Level 2 images had already been corrected for gaseous absorption and Rayleigh contributions and represented “top-of-atmosphere reflectance values”. All images were acquired at approximately 11:30 a.m. local time. The pre-selected images were visually inspected in order to detect, and eventually delineate, thin clouds or dense dust cloud transportation (e.g., from Sahara). MERIS images were classified with respect to pollution levels on the basis of ground-based pollutant concentration measurements in order to designate a “reference image” that is, the image with the lowest pollution load, that was required to apply the DTA method.

**3.2. MODIS Data.** MODIS acquires daily imagery in 36 spectral bands from the visible to the thermal infrared (29 spectral bands with 1-km resolution, 5 spectral bands with 500 m resolution, and 2 with 250 m resolution, nadir pixel dimensions). The data used in this study are MODIS aerosol retrieval products based on distinguished algorithms over land and ocean to obtain AOD at 550 nm (AOD<sub>550</sub>) and the proportion of AOD contributed by fine-mode aerosols (fine-mode fraction: FM), which are only created over cloud-free regions. Both AOD<sub>550</sub> and FM data correspond to Collection 5 (c005) data, where much of the high bias is removed [22]. However, in dust-aerosol regimes, retrieved AOD<sub>550</sub> will have greater error due to their non-spherical effects [23, 24]. The FM fraction was initially given over ocean but it can now be obtained also over coastal areas. The retrieval algorithms are fully described by Remer et al. [25] and Levy et al. [22].

The MODIS study area included GAA centered at 37.5°N latitude and 23.4°E longitude with 10 km × 10 km (Level 2) spatial resolution. Since Athens is a coastal urban area the previous pixel is probably affected by the differences between land and sea. An additional uncertainty in both AOD and FM retrievals over coastal areas is caused by the land-ocean sub-pixel contamination. Even with improved formulation of FM, retrievals of both parameters still have large uncertainties because the assumption of the empirical surface reflectance ratios seems too simple to account for complexities of land-surface reflectance [17].

**3.3. PM<sub>10</sub> and Gaseous Pollutant Measurements.** The Ministry of Environment (MINENV) provided the necessary air-pollutant concentration data. MINENV operates an organized monitoring network covering GAA with eighteen stations on hourly basis. The examined data refer to hourly concentration measurements of NO<sub>2</sub>, NO, SO<sub>2</sub>, O<sub>3</sub>, and PM<sub>10</sub> (Table 1). PM<sub>10</sub> concentrations were monitored at four air-pollution monitoring stations within GAA representative of different environments. “Aristotelous” station is established in the city center near a road with heavy traffic. High

TABLE 1: Mean daily NO<sub>2</sub>, NO, SO<sub>2</sub>, O<sub>3</sub>, and PM<sub>10</sub> concentrations at each air-pollution monitoring station for all examined days (source: Ministry of Environment, Physical Planning and Public Works, 2004).

	Aristotelous					Zografou				
	NO <sub>2</sub> [ $\mu\text{g}/\text{m}^3$ ]	NO	SO <sub>2</sub>	O <sub>3</sub>	PM <sub>10</sub>	NO <sub>2</sub>	NO	SO <sub>2</sub>	O <sub>3</sub>	PM <sub>10</sub>
22/6/03	59.85	13.55	4.45		37.71	11.46	1.12			27.83
25/6/03	103.12	54.91	8.32		71.45	31.13	3.22			45.46
4/7/03	97.36	47.54	9.5		98.37	29.75	1.75			54.12
14/7/03	80.31	44.35	4.08		68.58	24.96	2.62			41.08
15/8/03	72.15	34.15	3.8		48.25					33.71
31/8/03	87.5	65.25	5.75		96.17					62.46
	Agia Paraskevi					Likovrisi				
	NO <sub>2</sub>	NO	SO <sub>2</sub>	O <sub>3</sub>	PM <sub>10</sub>	NO <sub>2</sub>	NO	SO <sub>2</sub>	O <sub>3</sub>	PM <sub>10</sub>
22/6/03	10.37	1.00	4.41	125.2	29.12	17.62	4.51		82.37	
25/6/03	19.82	1.41	9.57	141.5	54.79	52.51	19.54		74.71	
4/7/03	29.62	1.37	9.12	158.8	53.86	63.42	24.92		74.08	
14/7/03	24.33	2.33	10.71	121.1	48.25	50.83	14.62		60.12	
15/8/03	5.50	1.00	15.02	153.0	37.71	25.58	5.83		69.46	54.75
31/8/03	29.75	2.1	18.83	130.8	71.17	66.67	19		54.83	85.37

levels of primary air pollutants (e.g., NO<sub>2</sub>, SO<sub>2</sub>) are still measured at this station. “Zografou” station is located in the University of Athens campus in a suburban region with low traffic and far from inhabited areas. This location is at the east edge of the basin, at the foothills of mountain Hymettos. It should be noted that these two stations were used by Chaloulakou et al. [3] as representing urban and suburban environments from the PM monitoring point of view. “Agia Paraskevi” is a suburb of Athens located in the northeast edge of the basin. Last, “Likovrisi” station is situated in a north suburb with low population density and close to open areas near the Parnitha mountain. It should be noted that, despite the distance from the city center, air-pollution and PM concentrations at this station are significant due to the city circulation patterns, which carry the pollutants to the north.

PM<sub>10</sub> filter samples were collected using low-volume samplers. The sampling flow rate was  $16.71 \text{ l min}^{-1}$ . The particles were collected on 47-mm Pallflex TX40  $\text{lm}^{-1}$  filters (Teflon-coated glass fiber filters), which were mounted in plastic filter holders. Each filter was inspected for its integrity prior to its use. Particle concentrations were determined gravimetrically using an electronic microbalance (Mettler Toledo AT201), with 0.01-mg resolution. Air pollutants, such as nitrogen dioxide (NO<sub>2</sub>), nitrogen oxide (NO), sulfur dioxide (SO<sub>2</sub>), and tropospheric ozone (O<sub>3</sub>), are concurrently measured by the MINENV network. NO<sub>2</sub> and NO, O<sub>3</sub>, and SO<sub>2</sub> concentrations are determined using chemiluminescence, UV, and fluorescence techniques, respectively.

Analysis of PM<sub>10</sub> and gaseous pollutant data was initially performed for classifying the available images into highly, moderately, slightly polluted and pollution-free. According to the examined ground-based pollution information, the selected images acquired on 25/6/2003, 4/7/2003, 14/7/2003, 15/8/2003 and 31/8/2003 were considered as “pollution

images” compared to that of 22/6/2003. In particular, among these dates the 4/7/2003 and the 31/8/2003 indicated rather high levels of pollution and AOD (i.e., PM<sub>10</sub> exceeded the upper limit of the mean daily value of  $50 \mu\text{g m}^{-3}$ ), the 15/8/2003 shows light pollution, and the other two days present moderate pollution levels. Finally, the 22/6/2003 was identified as “reference image” (pollution-free) according to its low PM<sub>10</sub> values.

#### 4. Methodology

The method used for AOD retrieval from MERIS data is the differential textural analysis (DTA) based on the “contrast reduction” principle. The DTA code is part of the SMA code developed by Sifakis et al. [11], and has already been tested on high-spatial resolution data, such as SPOT [10] and Landsat [12], and moderate-spatial resolution data, such as AVHRR [8]. The code quantifies contrast-reduction as the local “textural degradation” on geometrically and radiometrically corrected satellite datasets composed by a “pollution” image and a “reference” image (pollution-free). Contrast reduction is then attributed to the presence of aerosols assuming that the surface reflectance is invariable between the two images, which requires their proximity in acquisition time. Retrieved AOD values are then relative to the reference image. More specifically, the following stages were implemented for the application of the DTA code.

The first step was the selection of appropriate reference and polluted images. This stage was critical because the accuracy in the AOD retrieval depends on the quality of the reference image. More specifically, the reference image should present minimum AOD values with a homogeneous spatial distribution. The selection of a reference image can be arduous requiring the examination of long time-series of

satellite data. The reference image was selected on the basis of the following criteria:

- (i) low PM and other pollutant concentrations as measured by ground-based stations,
- (ii) available meteorological information, and
- (iii) availability of cloud-free image.

In case of lack of actual pollution data (e.g.,  $PM_{10}$ ,  $NO_2$ ) the selection of the reference image could be based on a statistical comparison applied to the available images: lower pollution levels on an image would be revealed by higher values of standard deviation (expressing the apparent texture or local contrast). In our case study,  $PM_{10}$  concentration data measured at ground level by the organized network of MINENV (see Section 3.3) were used for the selection of “pollution” images so that significant tropospheric aerosol concentrations be captured.

In the second step, the selected images underwent geometric correction (georeferencing). At this stage re-sampling was carried out according to the “nearest neighborhood” code in order to avoid altering the initial radiometric values of the pixels.

In the third step the DTA code was applied. The code calculates the local textural degradation in order to derive the spatial distribution of AOD values. This calculation was carried out inside an adjustable moving window. The size of the window was optimized according to the resolution of the sensor as a compromise between

- (a) a large window including sufficient apparent ground texture, directly linked to the local contrast, and
- (b) a small window allowing to consider a homogeneous atmospheric correction.

The structure-function performance suggested by Paronis and Sifakis [26] allowed to determine the window size. The application of the structure-function performance showed that the optimal window size was 13 pixels by 13 pixels. The use of this moving window allowed the final results to maintain the spatial resolution of MERIS pixel, namely  $260\text{ m} \times 290\text{ m}$ , thus perceiving aerosol inhomogeneities at this scale. For the case of GAA, covering approximately  $450\text{ km}^2$ , AOD information was derived at 3000 points versus only four ground air-pollution monitoring stations. The DTA code was applied to the selected series of MERIS images over GAA, considering, in total, five “polluted” and one “reference” images. All images underwent geo-referencing according to the UTM WGS 84 (zone 34N) projection system using Ground Control Points (GCPs) included in the header file of each of the images with the use of BEAM software (BEAM 2004). Subsequently, the images were reported to the ERDAS imaging software (ERDAS 2003) in order to be processed for AOD retrieval over land in the vicinity of GAA by applying the DTA code, which has been developed in the MODELLER module of ERDAS Imaging software.

Using the previous methodology we obtained the AOD values at the fourteen MERIS spectral channels with  $260\text{ m} \times 290\text{ m}$  spatial resolution, centered over each ground-based

monitoring station. AOD values were subsequently averaged to cover the entire GAA for the five days considered. In all cases a reduction of the retrieved spectral AOD values with wavelength according to a power law was observed as foreseen by Mie theory.

The knowledge of spectral dependence of AOD is important for the modeling of the radiative effects of aerosols on the land-atmosphere system, as well as for the retrieval of the aerosol optical parameters from satellite-remote sensors [27]. The wavelength dependence of AOD depends on the aerosol type, that is, the physical and chemical characteristics of the particles. Wavelength dependence is expressed by the Ångström exponent ( $\alpha$ ), which is the slope of the logarithm of AOD versus the logarithm of wavelength ( $\ln\lambda$ ), and is commonly used to characterize the spectral dependence of AOD and to provide information on the aerosol-size distribution. For the whole dataset the  $\alpha$ -Ångström was derived using the least-squares method, which is the least imprecise and wavelength dependent [28], covering the spectral region 412.5–885 nm of the MERIS-based AOD. Errors and uncertainties in its derivation are attributed to the dispersion of AOD values from the linear fit and are more biased than those produced using ground-based radiometers [29]. The DTA method assumes the proximity of the pollution and reference dates. We have not assessed the impact of extended surface changes to the AOD, since such changes do not exist in a two-month period. Usually, areas suspected for major surface-reflective changes are avoided (masked). Therefore, the error in the estimated AOD due to changes in the surface reflectivity is negligible. Typical errors in  $\alpha$  derivation applying the least-squares method on MERIS AODs were found to range from 0.05 to 0.24, which is much higher than those obtained via radiometers  $0.032 \pm 0.001$  [29]. Kaskaoutis et al. [29] also found that a 0.03 error in AOD can introduce a 7–10% error in the Ångström exponent.

## 5. Results and Discussion

**5.1. Satellite Images.** Figures 1(a)–1(e) show true color Terra-MODIS images covering the whole Eastern Mediterranean and corresponding to the five examined days. These images, due to their larger spatial coverage, are capable of detecting Saharan dust outbreaks above the Eastern Mediterranean basin. The MODIS pictures referring to 25/6/2003 (Figure 1(a)), 14/7/2003 (Figure 1(c)) and 15/8/2003 (Figure 1(d)) seem to be rather clear over the whole Greek territory, while the sea glint effect is quite intense. A clearly different pattern was obvious on 4/7/2003 (Figure 1(b)) when a thin dust plume was blown north of Libya affecting the Aegean Sea and continental Greece intensifying the aerosol load above Athens. However, even on this day the sea glint is obvious above the seas adjoining the Greek subcontinent. Figure 1(d), referring to 15/8/2003, represents the clearest day over Athens in accordance to the minimum air-pollutant and  $PM_{10}$  concentrations (Table 1). In contrast, 31/8/2003 is a dusty day with a dust plume blowing northeastward of the Tunisian/Libyan coasts. The

MODIS image clearly reveals the geographical extension of this dust plume moving northeast through the Central Mediterranean, Aegean Sea and continental Greece.

**5.2. Back Trajectories.** Analytical air-mass back trajectories for the five dates, obtained by the Hybrid Single-Particle Langrangian Integrated Trajectory (HYSPLIT) Model [30], were used to identify the pathway of air masses over Athens. The back trajectories were computed for 3 distinct arrival levels, namely 100 m, to give representative origin of air masses near the surface, 1500 m, which could serve as a representative height for the boundary layer, in which the majority of the aerosol particles was present, and 4000 m for the presence of Sahara dust layers to be captured. The 4-day back trajectory analysis, presented in Figures 2(a)–2(e), clearly verifies the two dusty days (Figures 2(b) and 2(e)), where the trajectories at both 4000 m and 1500 m show a Sahara origin. Particularly, they originated from areas in Northwestern Africa (Algeria and Morocco) under the influence of intense surface winds. In their trip over the Sahara desert they were both within the boundary layer as was also established via the HYSPLIT model. It should be noted that this direction is the main pathway for the dust plumes influencing both the Central [31, 32] and Eastern Mediterranean [33]. On the other three days the air masses influencing Athens came at all altitudes from the northern sector traversing Central Europe and the Balkan countries. It was established that these air masses usually carry anthropogenic or biomass-smoke aerosols over Greece [34]. From MODIS fire-mapping website <http://maps.geog.umd.edu/firms/> it was found (not shown) that on 12–15 August a large number of fire events occurred in the Balkan counties probably influencing the air mass on 15/8/2003; therefore, an increase in  $\alpha$  values was derived from MERIS (see Section 5.4).

**5.3. DREAM Model Applications.** The dusty days (4/7/2003 and 31/8/2003) were also successfully forecasted by the Dust Regional Atmospheric Modelling (DREAM) model [35], which has been extensively used for the identification of dust events in the Mediterranean [33, 36, 37]. The 0-hr forecast presented in both figures is the safest prediction and represents the real situation. Typical output results for 12 UTC (0-h forecast) are given in Figures 3(a) and 3(b) indicating the dust loading affecting the whole Greek territory on these days. In these figures the wind speed and direction at 3000 m are also shown, and they are consistent with air-mass trajectories reaching Athens (Figures 2(b) and 2(e)). From the wind pattern at 3000 m it can be revealed that an anticyclone was established in North Libya (Figure 3(a)) and North Algeria (Figure 3(b)) carrying dust particles over Greece. These anticyclones were also observed (not shown) on the preceding days to those selected. An important finding using the DREAM model is the dry deposition of dust particles occurring over Greece on both dusty days (not presented), thus leading to significant enhancement of  $PM_{10}$  concentrations on the surface. This is very important to be mentioned since, in numerous cases, the air masses transport dust over Greece in the free troposphere without any signal

in  $PM_{10}$  measurements [38]. On the other three days, no dust load was found over Greece and for this reason the respective figures are not presented.

**5.4. Comparison between Satellite and Ground-Based Measurements.** MERIS AOD values retrieved with the proposed method (DTA) precisely over the locations of the MINENV stations were compared to  $PM_{10}$  measurements at the respective stations. The data sets for all days were correlated through linear regression and the correlation coefficients for each one of the 14 MERIS spectral bands are presented in Table 2. The correlations between satellite-based AODs and ground-based  $PM_{10}$  concentrations are higher than 70% ( $R^2 > 0.50$ ) when using any of the spectral bands in the visible region. The highest correlation ( $R^2 = 0.83$ ) was found when using the MERIS AOD at 560 nm for all days combined. On the other hand, the correlation coefficients drop significantly in the NIR band ( $R^2 < 0.3$ ). The correlations between AOD and  $PM_{10}$  for individual days varied from  $R^2 = 0.63$  to  $R^2 = 0.88$ ; they are strong enough, especially in the visible spectrum but not in the infrared ( $>770$  nm), to justify the above error levels. The slope values in Table 2 are small since the  $X$  axis corresponds to  $AOD(\times 10^3)$ . From all MERIS channels, channel 5 (560 nm) is considered the best correlated, where the slope is the highest and the intercept the lowest. In this channel the strong correlation justifies the dependency of  $PM_{10}$  on AOD and, in general, the above correlation is statistically significant at the 95% confidence level for the visible spectrum. The revealed linearity and the low scatter at 560 nm allow a first-order prediction of the  $PM_{10}$  levels near the surface based on the AOD values. The strong positive correlation between the AOD-derived from satellites and ground-based  $PM_{10}$  concentrations suggests that the majority of the aerosol particles are within the boundary layer; their influence on the aerosol load increases with the slope of their correlation. Papayannis et al. [33] also proved via lidar signals that even during the dust events, the majority of the aerosols are within the boundary layer, below 1500 m. The relation between  $PM_{10}$  and AOD also indicates to what extent and in which cases and columnar data reflect surface characteristics.

Figure 4 presents mean AOD,  $PM_{10}$  and Aerosol Index (AI) values, averaged over GAA for each individual day. In the same figure AOD values from MERIS correspond to 560 nm and constitute the average values for all available AODs above all MINENV stations, retrieved at a spatial grid of 260 m by 290 m; while the vertical bars express one standard deviation from the mean value. The  $AOD_{550}$  from both Terra-MODIS and Aqua-MODIS have been retrieved from the pixel centered above Athens city center ( $37.5^\circ N$   $23.4^\circ E$ ) with a spatial resolution of  $10 \text{ km} \times 10 \text{ km}$ . AI data using version “8” algorithm were obtained from the TOMS sensor onboard Earth-Probe platform. AI is available on a daily basis, at a  $1^\circ \times 1.25^\circ$  resolution. Finally,  $PM_{10}$  concentrations constitute the mean values in the time interval between 11:00 and 12:00 a.m. (local time) thus best corresponding to MERIS (11:30 a.m.) and to Terra-MODIS (10:30 a.m.) passes. Such a comparison between “MERIS retrievals” and “MODIS products” may include some arbitrariness,

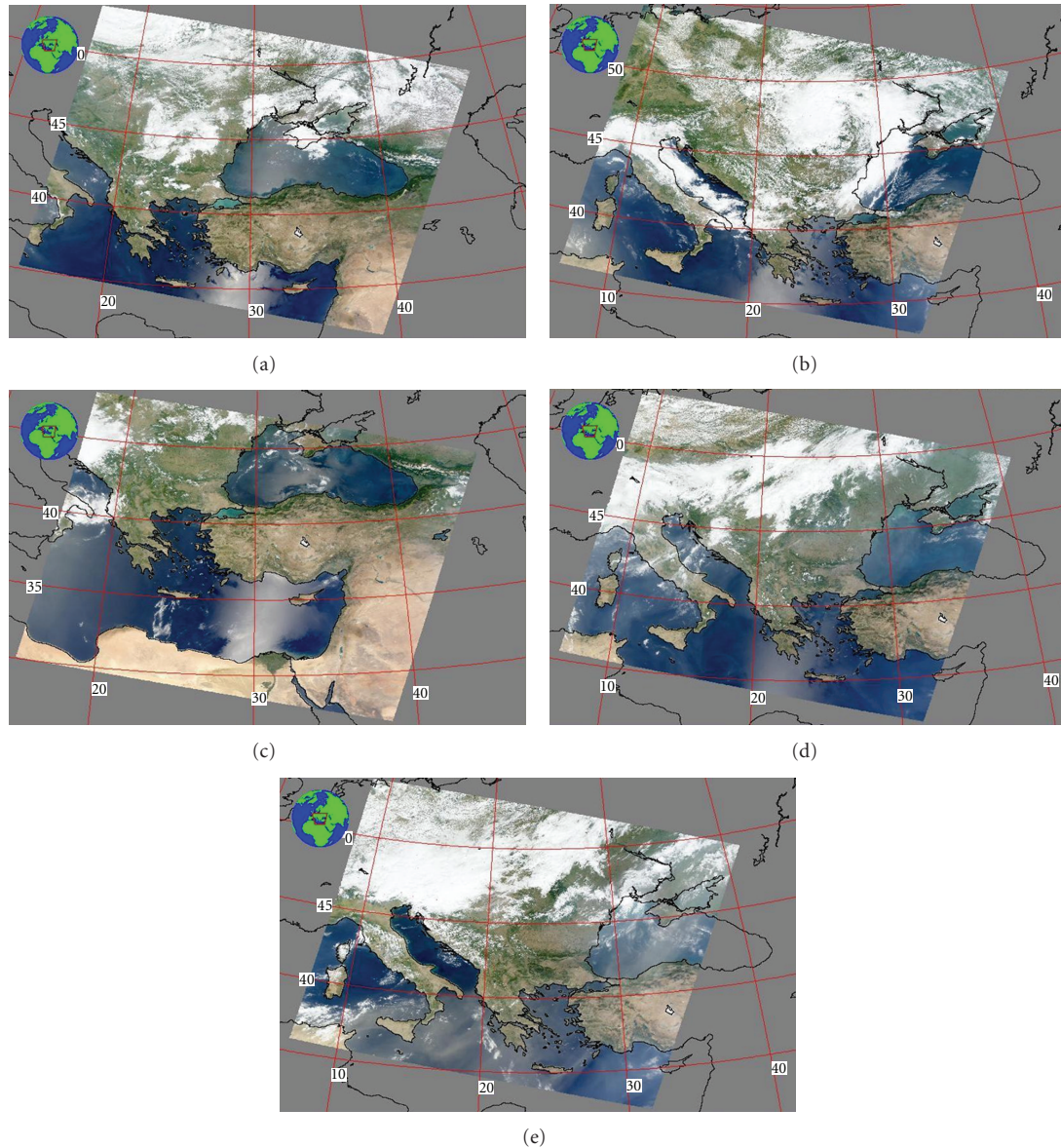
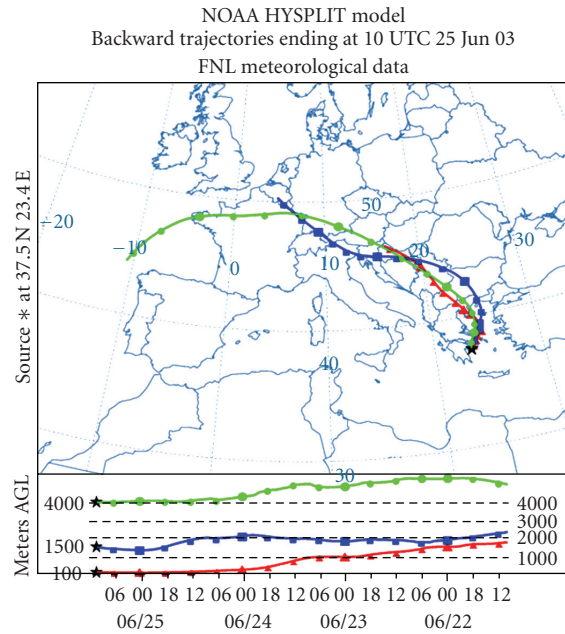


FIGURE 1: True color images from Terra-MODIS sensor on five days in summer 2003, (a) on 22/6/03, (b) on 4/7/03, (c) on 14/7/03, (d) on 15/8/03, and (e) on 31/8/03.

mainly due to the different AOD-retrieval codes and different spatial resolutions. It is, however, noteworthy that all satellite sensors and ground-based measurements were in agreement regarding the aerosol-load variation over GAA between the different days examined. It was found that the spatially-averaged AOD values from MERIS are highly correlated with the respective AOD product from Terra-MODIS ( $R^2 = 0.85$ ) or Aqua-MODIS ( $R^2 = 0.83$ ). Furthermore, the MERIS spatially-averaged AOD at 560 nm was correlated with ground-based  $PM_{10}$  concentration measurements with  $R^2$  to be as high as 0.82. The strong correlations between  $PM_{10}$  and columnar AOD are mainly affected by dust events on two of the days, which significantly enhanced dust deposition on the surface and  $PM_{10}$ . Similar strong correlation between  $PM_{10}$ , sun-photometer based AOD and

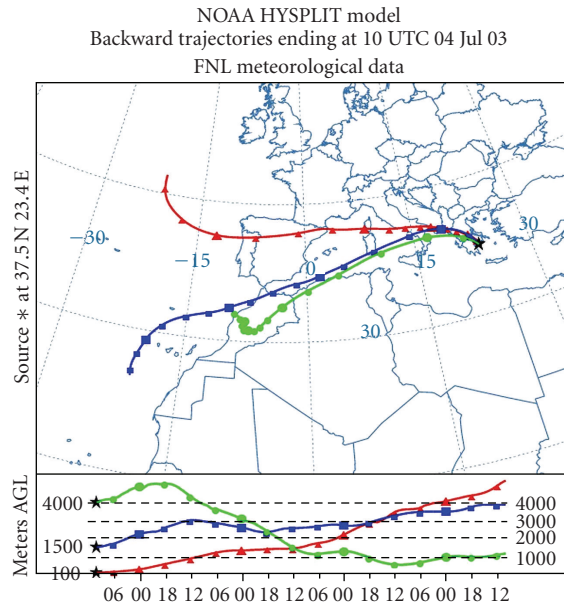
TOMS AI was found in Crete during Sahara dust events [38].

From Figure 4, the 25th of June and the 14th of July can be characterized as days with moderate air pollution levels; the 15th of August as day with low pollution levels, and the 4th of July and particularly the 31st of August as days with high or severe air pollution. Mean MERIS AOD at 560 nm was found to range from 0.13 to 0.33 when days are examined individually (Figure 4). The lower MERIS-AOD values, compared to those obtained by MODIS, are attributed to the “relative” method used to derive AOD including the use of a “reference” day, which was assumed to be pollution-free. The examination of this “reference” day in view to  $PM_{10}$  showed low but not negligible pollution in the Athens atmosphere (Table 1), while Terra and Aqua MODIS



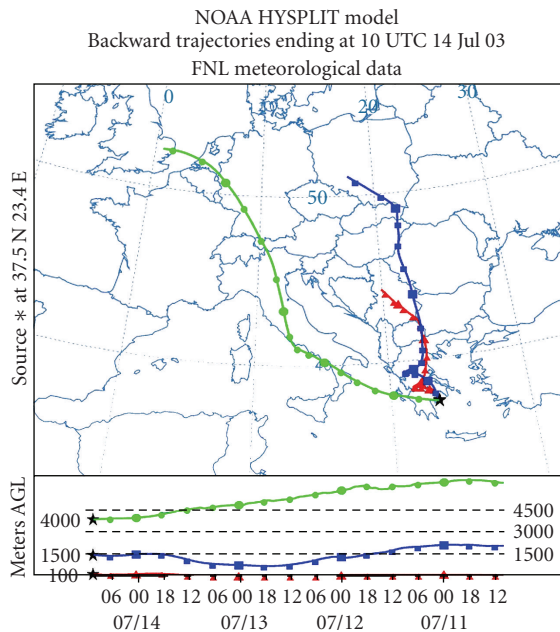
Job ID: 321297 Job start: Fri Feb 9 17:10:48 GMT 2007  
Source 1 lat: 37.5 Ion.: 23.4 hgts: 100, 1500, 4000 m AGL  
Trajectory direction: backward Duration: 96 hours Meteo data: FNL  
Vertical motion calculation method: model vertical velocity  
Produced with HYSPLIT from the NOAA ARL website (<http://www.arl.noaa.gov/ready/>)

(a)



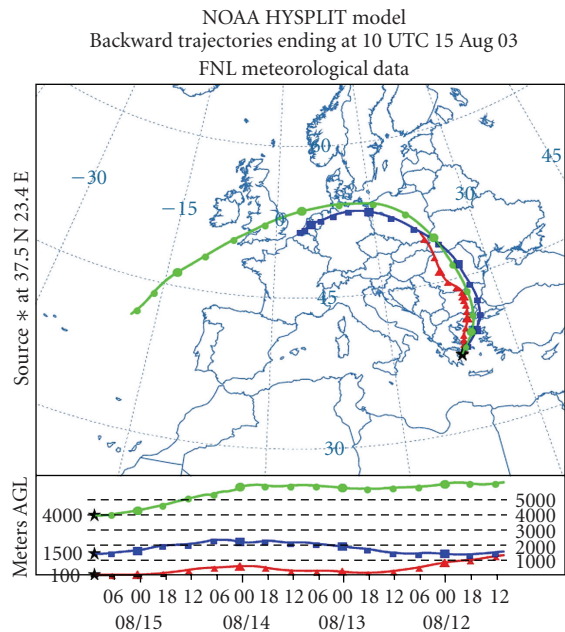
Job ID: 321323 Job start: Fri Feb 9 17:13:30 GMT 2007  
Source 1 lat: 37.5 Ion.: 23.4 hgts: 100, 1500, 4000 m AGL  
Trajectory direction: Backward duration: 96 hours Meteo data: FNL  
Vertical motion calculation method: model vertical velocity  
Produced with HYSPLIT from the NOAA ARL website (<http://www.arl.noaa.gov/ready/>)

(b)



Job ID: 321348 Job start: Fri Feb 9 17:15:30 GMT 2007  
Source 1 lat: 37.5 Ion.: 23.4 hgts: 100, 1500, 4000 m AGL  
Trajectory direction: Backward duration: 96 hours Meteo data: FNL  
Vertical motion calculation method: model vertical velocity  
Produced with HYSPLIT from the NOAA ARL website (<http://www.arl.noaa.gov/ready/>)

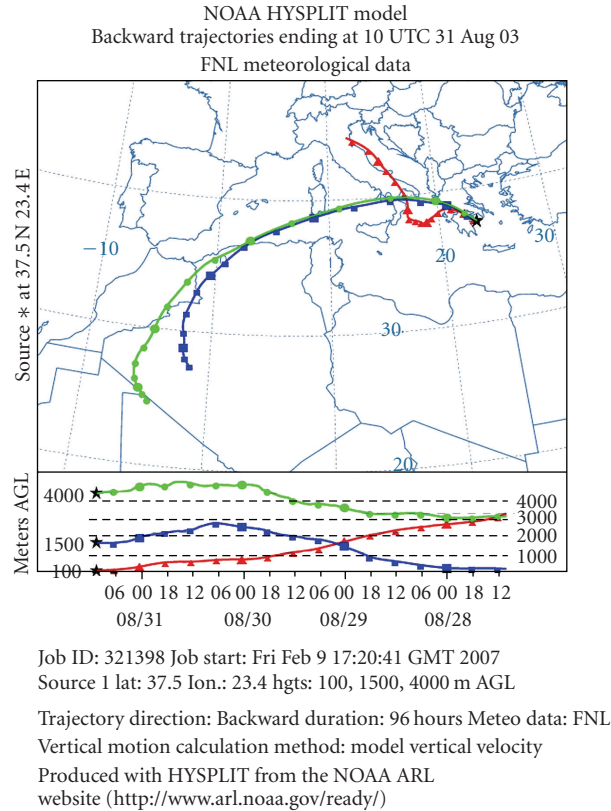
(c)



Job ID: 321365 Job start: Fri Feb 9 17:17:09 GMT 2007  
Source 1 lat: 37.5 Ion.: 23.4 hgts: 100, 1500, 4000 m AGL  
Trajectory direction: Backward duration: 96 hours Meteo data: FNL  
Vertical motion calculation method: model vertical velocity  
Produced with HYSPLIT from the NOAA ARL website (<http://www.arl.noaa.gov/ready/>)

(d)

FIGURE 2: Continued.



(e)

FIGURE 2: Air-mass back trajectories computed from NOAA-HYSPLIT model over AA (a) on 22/6/03, (b) on 4/7/03, (c) on 14/7/03, (d) on 15/8/03, and (e) on 31/8/03.

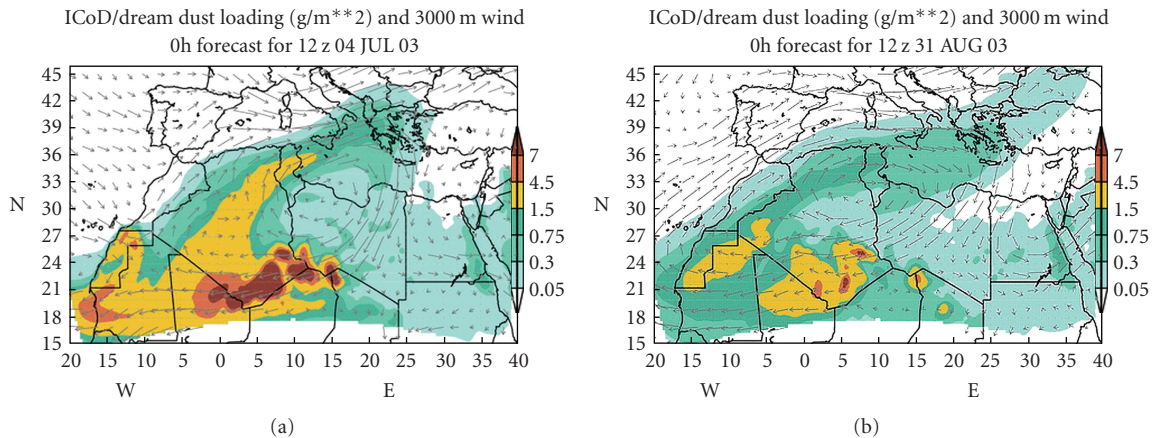


FIGURE 3: Dust loading (a) and dust dry deposition (b) forecasted by the DREAM model for the two dusty days (4/7/03 and 31/8/03).

$\text{AOD}_{550}$  was 0.195 and 0.175, respectively. As previously shown from back trajectories and DREAM applications, on two days (4 July 2003 and 31 August 2003), a Sahara dust plume affected GAA. These dust events further degraded air quality in the Athens urban environment, thus affecting mainly  $\text{PM}_{10}$  concentrations. Furthermore, on these days the TOMS AI values were high, thus indicating the presence of dust. In Mediterranean coastal urban areas, such as Athens,

which are close to North African arid regions, the effects of dust outbreaks play a key role in  $\text{PM}_{10}$  concentrations and further contribute to the urban air quality and human health. Many studies [36, 39–41] have established that dramatic  $\text{PM}_{10}$  enhancements in Southern Europe are with Sahara dust outbreaks. A  $\text{PM}_{10}$  concentration enhancement with simultaneous increase in columnar AOD is characteristic of convective dust transport over Greece [38]. Back trajectories

TABLE 2: Performance of DTA code on each of the available MERIS spectral bands expressed in terms of correlation between satellite-based AOD and ground-based aerosol ( $PM_{10}$ ) measurements.  $Y$ :  $PM_{10}$  ( $\mu\text{gr cm}^{-3}$ ),  $X$ :  $AOD(\times 10^3)$ .

Bands	Band center (nm)	$R^2$	$Y$
1	412.5	0.56	$0.12 x + 28.31$
2	442.5	0.54	$0.12 x + 30.48$
3	490	0.53	$0.12 x + 32.43$
4	510	0.53	$0.12 x + 33.57$
5	560	0.83	$0.19 x + 14.51$
6	620	0.48	$0.11 x + 39.39$
7	665	0.48	$0.10 x + 40.78$
8	681.25	0.48	$0.10 x + 41.02$
9	708.75	0.46	$0.10 x + 43.42$
10	753.75	0.32	$0.11 x + 46.19$
12	778.75	0.22	$0.09 x + 52.31$
13	865	0.19	$0.09 x + 51.74$
14	885	0.19	$0.09 x + 51.75$

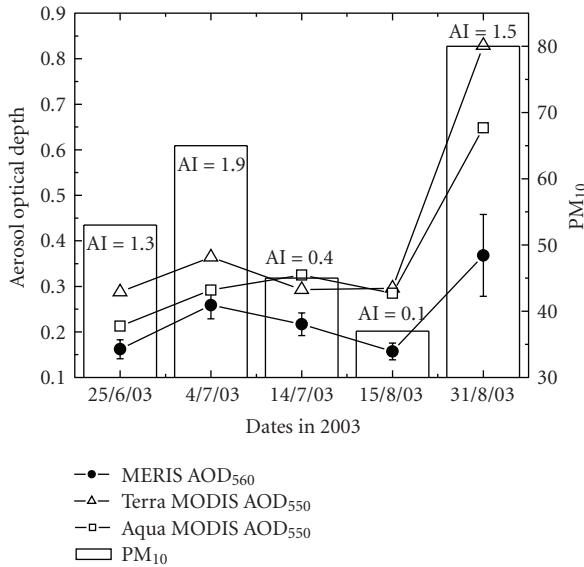


FIGURE 4: Mean daily values of AOD at 560 nm derived from MERIS at four sites with a  $260 \times 290 \text{ m}^2$  spatial resolution and spatially averaged over the Athens Basin. The daily Terra/Aqua MODIS  $AOD_{550}$  with  $10 \times 10 \text{ km}^2$  spatial resolution are also given. The  $PM_{10}$  concentrations are four-station averaged value at the time interval corresponding to MERIS pass time. AI values for each day are given while the vertical bars express one standard deviation from the spatially averaged MERIS AOD value.

at 4000 m and 1500 m on 4 July 2003 and 31 August 2003 verified this type of transport; so did DREAM simulations, which showed dry deposition of dust particles over Athens on these days.

Using the least-squares method the Ångström exponent  $\alpha$  was derived from MERIS-AOD values covering the spectral range 412.5–885 nm on each individual day. These values, associated with their standard deviations caused by averaging them over GAA, are presented in Figure 5. In the same

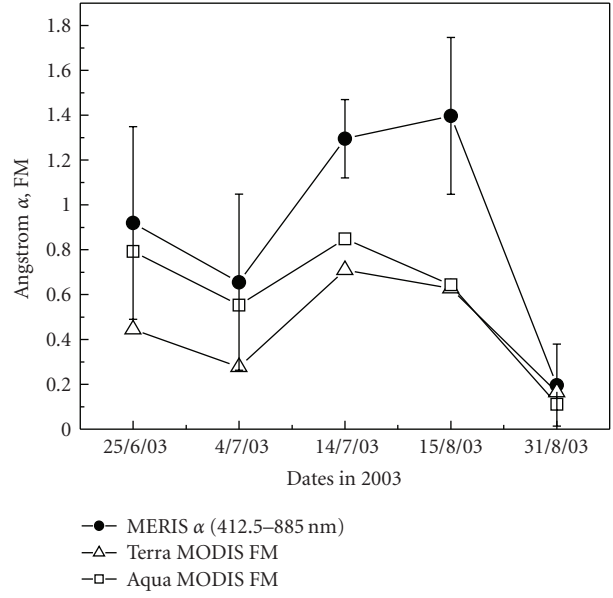


FIGURE 5: Mean daily Ångström exponent  $\alpha$  values derived from MERIS in the 412.5–885 spectral band. The vertical bars express one standard deviation from the spatially averaged MERIS  $\alpha$  value. The fine mode fraction values derived from both Terra/Aqua MODIS sensor over Athens are also shown.

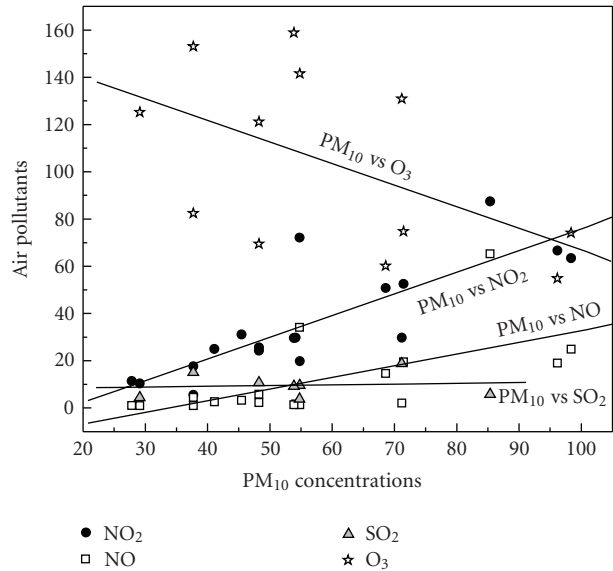


FIGURE 6: Correlation between daily mean  $PM_{10}$  concentrations with air pollutants at four air-pollution monitoring stations within the Athens Basin.

figure the FM values from both Terra- and Aqua-MODIS sensors are also plotted. Despite the limited number of days and difficulties encountered (i.e., different spatial resolution, significant typical error in  $\alpha$  computation) the analysis gave similar results with respect to  $\alpha$  and FM values. The only discrepancy was revealed on 15 August 2003 where the computed large mean  $\alpha$  value was not in accordance with respective FM values. On the other days, high  $\alpha$  values were associated with high FM values. The two dusty days (i.e.,

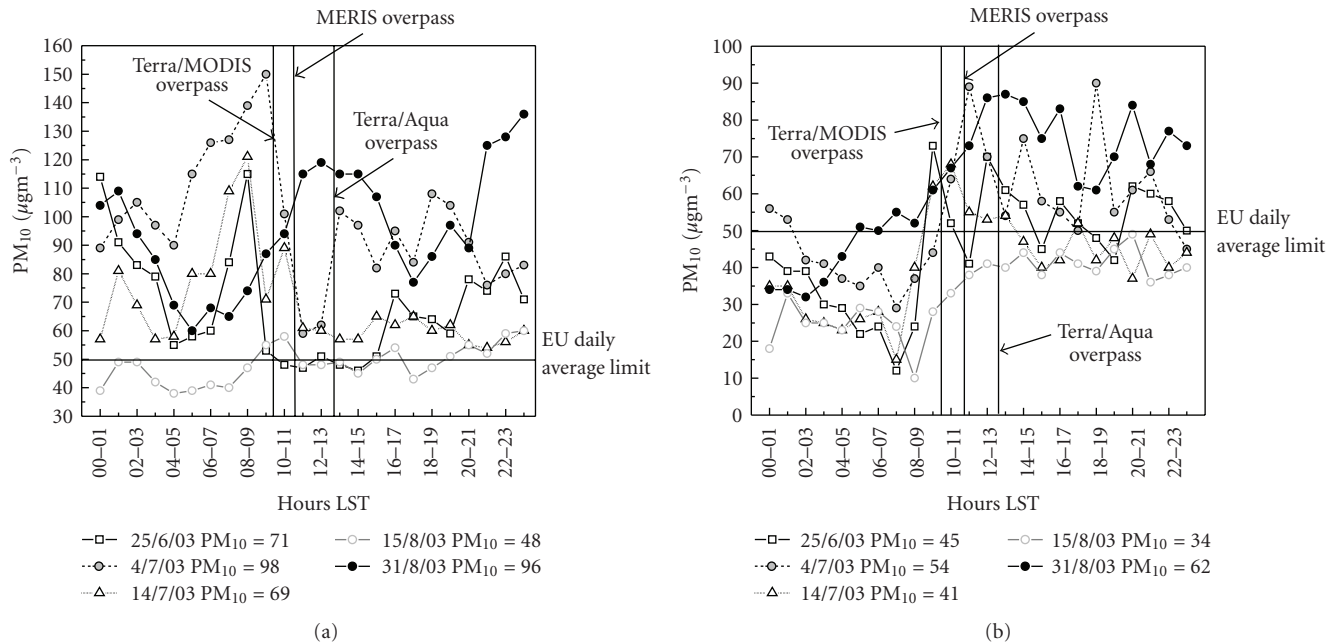


FIGURE 7: Diurnal variation of the PM<sub>10</sub> concentrations at (a) urban "Aristotelous" station, and (b) suburban "Zografou" station for the five days considered. The EU threshold daily mean value of 50  $\mu\text{gm}^{-3}$  is also shown.

4 July 2003, 31 August 2003) were characterized by low values in both  $\alpha$  and FM. The linear correlations between  $\alpha$  and FM values were significantly strong; their variance was 93% and 70% in the case of Terra- and Aqua-MODIS, respectively. This result clearly establishes the agreement between the two satellite sensors despite their different spatial resolution and the differences in product definition (i.e.,  $\alpha$  and FM). Terra-MODIS correlates better than Aqua-MODIS with MERIS retrievals due to proximity between their passes (approximately one hour lag). Unfortunately, there are no systematic measurements of fine particles (e.g., PM<sub>2.5</sub> or PM<sub>1.0</sub>) in GAA in order to compare with  $\alpha$  and FM values.

Figure 6 shows the correlations between daily mean PM<sub>10</sub> and air-pollutant concentrations for all the available data presented in Table 1. Particularly, the correlation between PM<sub>10</sub> and NO<sub>2</sub> ( $R^2 = 0.67$ ) is statistically significant ( $P < .001$ ) indicating that most of the aerosols that contribute to PM<sub>10</sub> have originated from vehicle exhausts, which are the main source for NO<sub>2</sub> production. NO<sub>2</sub> is a highly variable atmospheric constituent, which plays a key role in the complex ozone cycle, both in the stratosphere where it is naturally present, and the troposphere, where its concentration may be high due to pollution. The respective correlation (PM<sub>10</sub> versus NO) is positive but not statistically significant ( $R^2 = 0.39$ ), while no correlation between PM<sub>10</sub> and SO<sub>2</sub> seems to exist. Strong associations between particle-mass concentrations and primary gaseous pollutants have been previously reported in Birmingham, suggesting the importance of traffic-related emissions [42]. Gaseous pollutants (except ozone) are mostly associated with local sources, including exhaust emissions, domestic heating and industrial activities. These strong associations suggest that a

large fraction of particles are emitted locally. On the other hand, the tropospheric ozone, which is a photochemical pollutant, exhibits a decreasing trend when PM<sub>10</sub> concentration increases. Within the Athens Basin, primary air pollutants (such as NO) are mainly produced in downtown Athens ("Aristotelous" station), while the highest tropospheric O<sub>3</sub> concentrations take place at stations far from the city center, and mainly in the northern areas of the Basin ("Likovrisi" and "Agia Paraskevi" stations). This is attributed to the fact that tropospheric O<sub>3</sub> is a very reactive pollutant and, therefore, the highest concentrations of other pollutants in the center (like NO<sub>2</sub>, NO, SO<sub>2</sub>) contribute to its destruction.

In Figures 7(a) and 7(b) the diurnal variation of PM<sub>10</sub> at two stations within GAA is presented for the five days considered. The PM<sub>10</sub> values are the hourly average in the time intervals presented. The two stations selected are the urban "Aristotelous" (Figure 7(a)) and the suburban "Zografou" (Figure 7(b)), in order to establish the differences in PM<sub>10</sub> concentrations caused by local emissions. It should be noted that similar values at these stations have already been published by Chaloulakou et al. [3]. The main remarks from both figures is the inexistence of a clear diurnal pattern especially at "Aristotelous" station, while at "Zografou" the PM<sub>10</sub> concentrations exhibit an increasing trend from early morning to midday, remaining nearly constant in the rest of the day. It is also obvious that except of the local sources the dust deposition on the two dusty days significantly affected the PM<sub>10</sub> concentrations (see daily mean values in both figures). In both figures, the daily threshold value of 50  $\mu\text{gm}^{-3}$  suggested by EU is also shown in order to reveal the considerably higher PM<sub>10</sub> values over the Athens center. A full year monitoring of PM<sub>10</sub> concentrations in Athens [3]

gave a daily average of  $75 \mu\text{gm}^{-3}$  during the sampling period (1 June 1999 to 31 May 2000) at “Aristotelous” station. This annual mean is considerably higher than the EU annual  $\text{PM}_{10}$  standard of  $40 \mu\text{gm}^{-3}$ .

## 6. Conclusions

In this study, Envisat MERIS observations were used to retrieve urban aerosol concentrations in terms of AOD over Athens with the possibility of producing maps showing AOD's spatial distribution with approximately 300-m resolution. The extracted AOD values were relative to reference (i.e., pollution-free) satellite data. Additionally to MERIS data, AOD from Terra- and Aqua-MODIS sensors at 550 nm were also obtained over Athens with a 10-km spatial resolution.

Despite the different spatial resolutions and method inherent uncertainties compared to ground-based instruments, the satellite-based retrieval leads to satisfactory results in the majority of the cases; AOD derived by MERIS is in close agreement with AOD derived by MODIS even under different atmospheric conditions, such as dust or pollution. A high correlation was also found between MERIS AOD values, particularly those retrieved at 560 nm, and  $\text{PM}_{10}$  concentrations. These findings suggest that, at least for the Athens urban area, the application of the DTA code on MERIS imagery, whenever available and cloud-free, can be used to provide AOD values with air-quality associated information. Back-trajectory analysis and dust forecasts from the DREAM model completely verified these satellite outputs. The strong correlation of  $\text{PM}_{10}$  with AOD and  $\text{NO}_2$  indicates that (i) the majority of the aerosols are within the boundary layer and (ii) the most of the aerosol mass at ground level has originated from local emissions.

A more extended validation of the robustness of the method used in this study is foreseen in terms of further testing in other polluted urban areas and over a wider range of atmospheric conditions. The final objective is AOD mapping on an operational basis, which may be of interest to all metropolitan areas disposing ground-based pollution monitoring networks (including PM or gaseous concentration measurements), but which are few in number or spatially scarce.

## Acknowledgments

The authors acknowledge the NOAA Air Resources Laboratory (ARL) for the provision of HYSPLIT transport and dispersion model and READY website used in this publication. The scientific team for providing the DREAM model via <http://www.bsc.es/projects/earthscience/DREAM/> is also acknowledged.

## References

[1] C. A. Pope III and D. W. Dockery, “Acute health effects of  $\text{PM}_{10}$  pollution on symptomatic and asymptomatic children,” *American Review of Respiratory Disease*, vol. 145, no. 5, pp. 1123–1128, 1992.

[2] J. M. Samet, F. Dominici, F. C. Curriero, I. Coursac, and S. L. Zeger, “Fine particulate air pollution and mortality in 20 U.S. cities, 1987–1994,” *The New England Journal of Medicine*, vol. 343, no. 24, pp. 1742–1749, 2000.

[3] A. Chaloulakou, P. Kassomenos, N. Spyrellis, P. Demokritou, and P. Koutrakis, “Measurements of  $\text{PM}_{10}$  and  $\text{PM}_{2.5}$  particle concentrations in Athens, Greece,” *Atmospheric Environment*, vol. 37, no. 5, pp. 649–660, 2003.

[4] M. D. King, Y. J. Kaufman, D. Tanré, and T. Nakajima, “Remote sensing of tropospheric aerosols from space: past, present, and future,” *Bulletin of the American Meteorological Society*, vol. 80, no. 11, pp. 2229–2259, 1999.

[5] B. N. Holben, E. Vermote, Y. J. Kaufman, D. Tanré, and V. Kalb, “Aerosol retrieval overland from AVHRR data—application for atmospheric correction,” *IEEE Transaction on Geoscience and Remote Sensing*, vol. 30, no. 2, pp. 212–222, 1992.

[6] E. Vermote, N. Saleous, and B. N. Holben, “Aerosol retrieval and atmospheric correction,” in *Advances in the Use of NOAA AVHRR Data For Land Applications*, G. D’Souza, Ed., pp. 93–124, Kluwer Academic Publishers, Dordrecht, The Netherlands, 1996.

[7] A. Ignatov and L. Stowe, “Aerosol retrievals from individual AVHRR channels. Part I: retrieval algorithm and transition from Dave to 6S radiative transfer model,” *Journal of the Atmospheric Sciences*, vol. 59, no. 3, pp. 313–334, 2002.

[8] A. Retalis, N. Sifakis, N. Grosso, D. Paronis, and D. Sarigiannis, “Aerosol optical thickness retrieval from AVHRR images over the Athens urban area,” in *Proceedings of the International Geoscience & Remote Sensing Symposium (IGARSS '03)*, vol. 4, pp. 2182–2184, Toulouse, France, July 2003.

[9] J. Vidot, R. Santer, and D. Ramon, “Atmospheric particulate matter (PM) estimation from SeaWiFS imagery,” *Remote Sensing of Environment*, vol. 111, no. 1, pp. 1–10, 2007.

[10] N. Sifakis and P.-Y. Deschamps, “Mapping of air pollution using SPOT satellite data,” *Photogrammetric Engineering & Remote Sensing*, vol. 58, no. 10, pp. 1433–1437, 1992.

[11] N. I. Sifakis, N. A. Soulakellis, and D. K. Paronis, “Quantitative mapping of air pollution density using Earth observations: a new processing method and application to an urban area,” *International Journal of Remote Sensing*, vol. 19, no. 17, pp. 3289–3300, 1998.

[12] A. Retalis, C. Cartalis, and E. Athanassiou, “Assessment of the distribution of aerosols in the area of Athens with the use of Landsat Thematic Mapper data,” *International Journal of Remote Sensing*, vol. 20, no. 5, pp. 939–945, 1999.

[13] H. Yu, R. E. Dickinson, M. Chin, et al., “Annual cycle of global distributions of aerosol optical depth from integration of MODIS retrievals and GOCART model simulations,” *Journal of Geophysical Research D*, vol. 108, no. 3, Article ID 4128, 2003.

[14] C. Ichoku, Y. J. Kaufman, L. A. Remer, and R. Levy, “Global aerosol remote sensing from MODIS,” *Advances in Space Research*, vol. 34, no. 4, pp. 820–827, 2004.

[15] Y. J. Kaufman, D. Tanré, and O. Boucher, “A satellite view of aerosols in the climate system,” *Nature*, vol. 419, no. 6903, pp. 215–223, 2002.

[16] R. C. Levy, L. A. Remer, D. Tanré, et al., “Evaluation of the moderate-resolution imaging spectroradiometer (MODIS) retrievals of dust aerosol over the ocean during PRIDE,” *Journal of Geophysical Research*, vol. 108, no. 19, Article ID 8594, 2003.

[17] M. Chin, A. Chu, R. Levy, et al., “Aerosol distribution in the Northern Hemisphere during ACE-Asia: results from global model, satellite observations, and Sun photometer

- measurements,” *Journal of Geophysical Research*, vol. 109, no. 23, Article ID D23S90, 2004.
- [18] K. D. Hutchison, “Applications of MODIS satellite data and products for monitoring air quality in the state of Texas,” *Atmospheric Environment*, vol. 37, no. 17, pp. 2403–2412, 2003.
- [19] H. D. Kambezidis, R. Tulleken, G. T. Amanatidis, A. G. Paliatsos, and D. N. Asimakopoulos, “Statistical evaluation of selected air pollutants in Athens, Greece,” *Environmetrics*, vol. 6, no. 4, pp. 349–361, 1995.
- [20] A. D. Adamopoulos, H. D. Kambezidis, D. G. Kaskaoutis, and G. Giavis, “A study of aerosol particle sizes in the atmosphere of Athens, Greece, retrieved from solar spectral measurements,” *Atmospheric Research*, vol. 86, no. 3–4, pp. 194–206, 2007.
- [21] European Space Agency (ESA), *EnviSat MERIS Handbook; Issue 1.2e*, 2005, <http://envisat.esa.int/dataproducts/meris/>.
- [22] R. C. Levy, L. A. Remer, and O. Dubovik, “Global aerosol optical properties and application to Moderate Resolution Imaging Spectroradiometer aerosol retrieval over land,” *Journal of Geophysical Research D*, vol. 112, no. 13, Article ID D13210, 2007.
- [23] D. A. Chu, Y. J. Kaufman, C. Ichoku, L. A. Remer, D. Tanré, and B. N. Holben, “Validation of MODIS aerosol optical depth retrieval overland,” *Geophysical Research Letters*, vol. 29, no. 12, 2002.
- [24] L. A. Remer, D. Tanré, Y. J. Kaufman, et al., “Validation of MODIS aerosol retrieval over ocean,” *Geophysical Research Letters*, vol. 29, no. 12, Article ID 8008, 2002.
- [25] L. A. Remer, Y. J. Kaufman, D. Tanré, et al., “The MODIS aerosol algorithm, products, and validation,” *Journal of the Atmospheric Sciences*, vol. 62, no. 4, pp. 947–973, 2005.
- [26] D. Paronis and N. Sifakis, “Satellite aerosol optical thickness retrieval over land with contrast reduction analysis using a variable window size,” in *Proceedings of the IEEE International Geoscience and Remote Sensing Symposium (IGARSS '03)*, vol. 2, pp. 1276–1278, Toulouse, France, July 2003.
- [27] T. F. Eck, B. N. Holben, J. S. Reid, et al., “Wavelength dependence of the optical depth of biomass burning, urban, and desert dust aerosols,” *Journal of Geophysical Research D*, vol. 104, no. D24, pp. 31333–31349, 1999.
- [28] V. E. Cachorro, R. Vergaz, and A. M. de Frutos, “A quantitative comparison of  $\alpha$ -Ångström turbidity parameter retrieved in different spectral ranges based on spectroradiometer solar radiation measurements,” *Atmospheric Environment*, vol. 35, no. 30, pp. 5117–5124, 2001.
- [29] D. G. Kaskaoutis, H. D. Kambezidis, A. D. Adamopoulos, and P. A. Kassomenos, “Comparison between experimental data and modeling estimates of aerosol optical depth over Athens, Greece,” *Journal of Atmospheric and Solar-Terrestrial Physics*, vol. 68, no. 11, pp. 1167–1178, 2006.
- [30] R. R. Draxler and G. D. Rolph, *HYSPLIT (Hybrid single-particle Lagrangian Integrated Trajectory) Model*, NOAA Air Resources Laboratory, Silver Spring, Md, USA, 2003, <http://www.arl.noaa.gov/ready/hysplit4.html>.
- [31] D. Meloni, A. di Sarra, G. Biavati, et al., “Seasonal behavior of Saharan dust events at the Mediterranean island of Lampedusa in the period 1999–2005,” *Atmospheric Environment*, vol. 41, no. 14, pp. 3041–3056, 2007.
- [32] G. Pace, A. di Sarra, D. Meloni, S. Piacentino, and P. Chamard, “Aerosol optical properties at Lampedusa (Central Mediterranean). 1. Influence of transport and identification of different aerosol types,” *Atmospheric Chemistry and Physics*, vol. 6, no. 3, pp. 697–713, 2006.
- [33] A. Papayannis, D. Balis, V. Amiridis, et al., “Measurements of Saharan dust aerosols over the eastern Mediterranean using elastic backscatter-Raman lidar, spectrophotometric and satellite observations in the frame of the EARLINET project,” *Atmospheric Chemistry and Physics*, vol. 5, no. 8, pp. 2065–2079, 2005.
- [34] D. S. Balis, V. Amiridis, C. Zerefos, et al., “Raman lidar and sunphotometric measurements of aerosol optical properties over Thessaloniki, Greece during a biomass burning episode,” *Atmospheric Environment*, vol. 37, no. 32, pp. 4529–4538, 2003.
- [35] S. Nickovic, G. Kallos, A. Papadopoulos, and O. Kakaliagou, “A model for prediction of desert dust cycle in the atmosphere,” *Journal of Geophysical Research D*, vol. 106, no. D16, pp. 18113–18129, 2001.
- [36] M. Viana, C. Perez, X. Querol, A. Alastuey, S. Nickovic, and J. M. Baldasano, “Spatial and temporal variability of PM levels and composition in a complex summer atmospheric scenario in Barcelona (NE Spain),” *Atmospheric Environment*, vol. 39, no. 29, pp. 5343–5361, 2005.
- [37] C. Pérez, S. Nickovic, J. M. Baldasano, M. Sicard, F. Rocadenbosch, and V. E. Cachorro, “A long Saharan dust event over the western Mediterranean: Lidar, Sun photometer observations, and regional dust modeling,” *Journal of Geophysical Research D*, vol. 111, no. 15, Article ID D15214, 2006.
- [38] N. Kalivitis, E. Gerasopoulos, M. Vrekoussis, et al., “Dust transport over the eastern mediterranean derived from total ozone mapping spectrometer, aerosol robotic network, and surface measurements,” *Journal of Geophysical Research D*, vol. 112, no. 3, Article ID D03202, 2007.
- [39] E. Gerasopoulos, G. Kouvarakis, P. Babasakalis, M. Vrekoussis, J. P. Putaud, and N. Mihalopoulos, “Origin and variability of particulate matter (PM<sub>10</sub>) mass concentrations over the Eastern Mediterranean,” *Atmospheric Environment*, vol. 40, no. 25, pp. 4679–4690, 2006.
- [40] G. P. Gobbi, F. Barnaba, and L. Ammannato, “Estimating the impact of Saharan dust on the year 2001 PM<sub>10</sub> record of Rome, Italy,” *Atmospheric Environment*, vol. 41, no. 2, pp. 261–275, 2007.
- [41] D. G. Kaskaoutis, H. D. Kambezidis, P. T. Nastos, and P. G. Kosmopoulos, “Study on an intense dust storm over Greece,” *Atmospheric Environment*, vol. 42, no. 29, pp. 6884–6896, 2008.
- [42] R. M. Harrison, A. R. Deacon, M. R. Jones, and R. S. Appleby, “Sources and processes affection concentrations of PM<sub>10</sub> and PM<sub>2.5</sub> particulate matter in Birmingham (U.K.),” *Atmospheric Environment*, vol. 31, no. 24, pp. 4103–4117, 1997.

## Research Article

# Assessment of Aerosol Radiative Impact over Oceanic Regions Adjacent to Indian Subcontinent Using Multisatellite Analysis

S. K. Satheesh,<sup>1,2</sup> V. Vinoj,<sup>1,3</sup> and K. Krishnamoorthy<sup>4</sup>

<sup>1</sup>Indian Institute of Science, Bangalore 560012, India

<sup>2</sup>Divecha Centre for Climate Change, Indian Institute of Science, Bangalore 560012, India

<sup>3</sup>Pacific Northwest National Laboratory, 902 Battelle Boulevard, Richland, WA 99352, USA

<sup>4</sup>Space Physics Laboratory, Vikram Sarabhai Space Centre, Thiruvananthapuram 695022, India

Correspondence should be addressed to S. K. Satheesh, profsks@gmail.com

Received 5 April 2010; Revised 28 July 2010; Accepted 27 August 2010

Academic Editor: Vito Vitale

Copyright © 2010 S. K. Satheesh et al. This is an open access article distributed under the Creative Commons Attribution License, which permits unrestricted use, distribution, and reproduction in any medium, provided the original work is properly cited.

Using data from Ozone Monitoring Instrument (OMI) and Moderate Resolution Imaging Spectroradiometer (MODIS) instruments, we have retrieved regional distribution of aerosol column single scattering albedo (parameter indicative of the relative dominance of aerosol absorption and scattering effects), a most important, but least understood aerosol property in assessing its climate impact. Consequently we provide improved assessment of short wave aerosol radiative forcing (ARF) (on both regional and seasonal scales) estimates over this region. Large gradients in north-south ARF were observed as a consequence of gradients in single scattering albedo as well as aerosol optical depth. The highest ARF ( $-37 \text{ W m}^{-2}$  at the surface) was observed over the northern Arabian Sea during June to August period (JJA). In general, ARF was higher over northern Bay of Bengal (NBoB) during winter and premonsoon period, whereas the ARF was higher over northern Arabian Sea (NAS) during the monsoon and postmonsoon period. The largest forcing observed over NAS during JJA is the consequence of large amounts of desert dust transported from the west Asian dust sources. High as well as seasonally invariant aerosol single scattering albedos ( $\sim 0.98$ ) were observed over the southern Indian Ocean region far from continents. The ARF estimates based on direct measurements made at a remote island location, Minicoy ( $8.3^\circ \text{ N}$ ,  $73^\circ \text{ E}$ ) in the southern Arabian Sea are in good agreement with the estimates made following multisatellite analysis.

## 1. Introduction

The estimation of regional average aerosol radiative effect requires accurate information on the spatial pattern of aerosol optical depth (AOD) as well as aerosol single scattering albedo (SSA) [1]. The aerosol optical depth measurements using MODIS instrument over oceans have been found to be quite accurate [2, 3]. This has been confirmed based on several ship-based and island-based Sun photometer observations. A detailed knowledge of SSA, which is the fraction of intercepted radiation that is scattered, is one of the largest uncertainties in climate forcing assessments [4]. Depending on the surface albedo and vertical distribution of aerosols, a change (decrease) in single scattering albedo from 0.9 to 0.8 can even change the sign of forcing from negative to positive [5]. The modeling of

aerosol absorption is largely dependant on aerosol chemical composition, size distribution, and morphology which are highly uncertain especially over Asian regions. The carbonaceous aerosol compounds like black carbon emitted from both biomass and fossil fuel burning are some of the major uncertainty in the understanding of aerosol absorption [6–10]. Therefore, continuous measurements of single scattering albedo on a global basis could significantly reduce these uncertainties which hamper estimation of their radiative and hence climate effects. Till recently the spatial pattern of aerosol single scattering albedo was not available on the spatial scale required for climate model assimilation. The recent retrieval of aerosol absorption optical depth from OMI has made estimation of spatial pattern of aerosol SSA and hence radiative forcing possible. However, the accuracy of single scattering albedo derived by OMI depends on

the assumptions involved such as aerosol layer height [11]. Thus, there exists large uncertainty in these retrievals that impact the direct estimation of single scattering albedo. Therefore, estimation of aerosol radiative effect over the oceans using the single scattering albedo retrieved from OMI may be uncertain. Recently, Satheesh et al. [12] proposed a joint OMI-MODIS retrieval technique to make improved assessment of aerosol absorption. In this paper, we have retrieved regional distribution of aerosol single scattering albedo using OMI-MODIS joint retrieval following Satheesh et al. [12] over the oceanic regions adjacent to Indian subcontinent. Consequently, we provide improved assessment of short wave aerosol radiative forcing (ARF) (on both regional and seasonal scales) estimates over this region by utilizing the aerosol optical depth from MODIS and SSA from joint OMI-MODIS retrieval technique in conjunction with a radiative transfer model. The spatial pattern of aerosol absorption over oceans adjacent to Indian subcontinent and consequent radiative impact are discussed.

## 2. Data and Methodology

Earlier studies have shown that the MODIS-derived aerosol optical depth is quite accurate over oceans [2, 3]. The validation of MODIS aerosol optical depth over oceanic regions around India has been carried out using AOD measurements from ship-based and island-based measurements [13, 14]. The MODIS ocean algorithm makes use of its fine spatial resolution observations and wide spectral range to mask out suspended river sediments, clouds, and Sun-glint, then inverts the radiance at several wavelengths (550 to 2130 nm) to retrieve spectral aerosol optical depth (AOD) and particle size information [15, 16]. The broad spectral range from  $0.55\ \mu\text{m}$  to  $2.13\ \mu\text{m}$  provides sufficient information to retrieve the accurate spectral signature of the aerosol. The MODIS ocean aerosol retrieval is documented fully in the literature, [16–18] and hence is not repeated here.

The OMI near UV aerosol algorithm (OMAERUV) uses measurements made at two wavelengths in the UV region (354 and 388 nm). The large sensitivity of the upwelling radiances to aerosol absorption in this spectral region [19] is used to retrieve the aerosol absorption. The OMAERUV aerosol products are UV Aerosol Index (AI), and aerosol extinction and absorption optical depths at 388 nm. Aerosol extinction optical depth (AOD) and aerosol absorption optical depth (AAOD) at 388 nm are derived using an inversion algorithm that uses precomputed reflectance for a set of assumed aerosol models. Three major aerosol types are considered: desert dust, carbonaceous aerosols associated with biomass burning, and weakly absorbing sulfate-based aerosols. Each of these aerosol types are represented by seven aerosol models of varying single scattering albedo, for a total of twenty-one microphysical models. Given the large size ( $13\times 24\ \text{km}^2$  at nadir) of the OMI pixels, subpixel cloud contamination is one of the challenging issues resulting in the overestimation of the extinction optical depth and underestimation of the single scattering albedo in OMI [19]. However, in the calculation of the absorption optical depth a cancellation of errors takes place that allows the

AAOD retrieval even in the presence of small amounts of cloud contamination. Detailed description of the algorithm is given in an overview paper by Torres et al. [11].

The Aura-OMI and the Aqua-MODIS instruments fly on A-train platforms within 8 minutes of each other. The quasismultaneity of their observations makes these sensors suitable for the application of a combined retrieval approach. OMI retrieves both aerosol extinction optical depth (AOD) and absorption information reported as single scattering albedo, while MODIS retrieves AOD and particle size [11, 18]. The OMI-retrieved information on absorbing aerosols depends on the assumed aerosol layer height. The MODIS retrieval algorithm, on the other hand, is insensitive to the aerosol vertical distribution but it needs to assume a value of the single scattering albedo (in the form of aerosol models). OMI pixels at a spatial resolution of 13 km by 24 km are often cloud contaminated (owing to large pixel size) whereas MODIS pixels at a resolution of 500 m are significantly less affected by cloud contamination. Thus the combination of the observations from the two sensors offers the opportunity of taking advantage of their individual strengths: OMI's unique sensitivity to aerosol absorption and MODIS accurate retrievals of aerosol optical depth (see [12] for details). Please note that even though MODIS radiances (Level-1) are available at 500 m resolution for cloud screening, aerosol products are available only at 10 km resolution (Level-2 data).

MODIS's strength is the availability of several channels in the visible through short wave infrared bands that permit accurate retrieval of AOD across a wide spectral range, especially over ocean. OMI's strength is its sensitivity to aerosol absorption in the near UV. However, the accuracy of OMI's retrieval is limited by the fact that the standard aerosol algorithm is sensitive to assumptions of aerosol height, whereas, MODIS derived AOD is not sensitive to aerosol layer height. A joint OMI-MODIS methodology was recently proposed by Satheesh et al. [12] by utilizing the respective strengths of MODIS and OMI to derive aerosol absorption with a greater accuracy, which we follow in this study to obtain information on the regional distribution of aerosol absorption.

*2.1. OMI-MODIS Algorithm in Brief.* The approach used in this work consists on using the MODIS retrieved AOD as input to the OMI retrieval. A difficulty in this method is the need to extrapolate the MODIS-retrieved AOD (at visible wavelengths) to the near UV (388 nm) where OMI requires the AOD information for its retrieval. Satheesh et al. [12] have tested MODIS' ability to estimate AOD in the UV, by comparing the estimated UV AOD with high quality ground-based observations [Aerosol Robotics Network (AERONET)]. They demonstrated that it is possible to improve the linear extrapolation into the UV by including information on the AOD spectral curvature. The success of using the MODIS visible and near IR spectral AODs to estimate UV optical depth suggests that we can use MODIS-predicted AOD in the UV to constrain the OMI inversion, and leave OMI free to return information on aerosol height and most importantly, aerosol absorption. By utilizing this

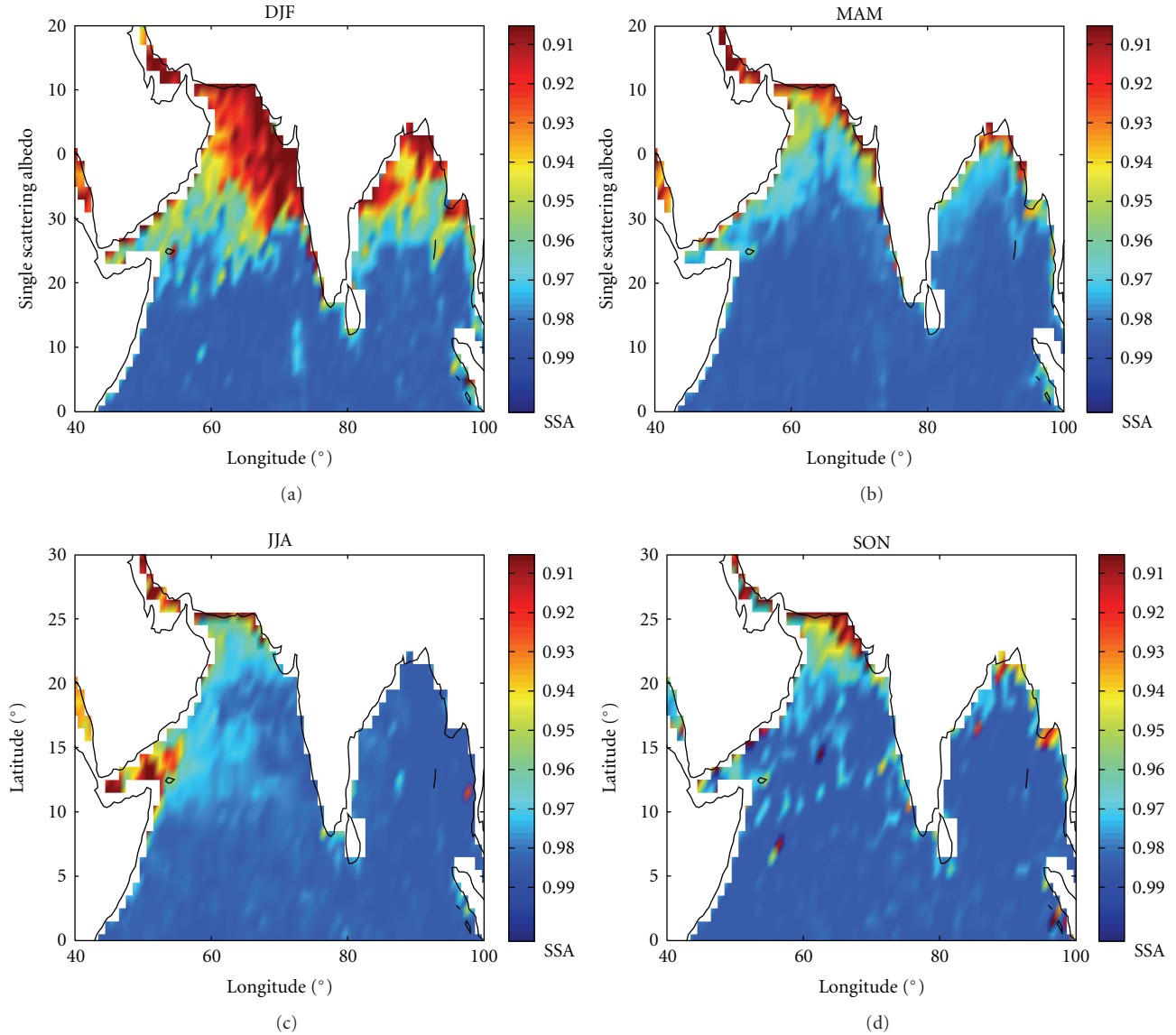


FIGURE 1: Seasonal and spatial distribution of aerosol single scattering albedo determined using the joint OMI/MODIS methodology.

observation, Satheesh et al. [12] followed a hybrid approach involving OMI and MODIS data in which MODIS can constrain the OMI retrieval by providing the AOD at  $0.38\ \mu\text{m}$ . Thus, joint OMI-MODIS retrieval can provide improved estimate of aerosol single scattering albedo. More details of this approach are available in Satheesh et al. [12] and hence are not repeated here.

### 3. Results and Discussion

**3.1. Single Scattering Albedo.** The regional distribution of aerosol single scattering albedo (SSA) derived using the joint OMI-MODIS methodology is shown in Figure 1. We find large spatial variation in SSA indicating a largely differing aerosol composition. We observe that the values of SSA over the vast open oceans are close to  $\sim 0.98$  which signifies largely scattering nature of aerosols possibly due to the dominance

of sea-salt aerosols. Close to the continents, the values are as low as  $\sim 0.88$  to  $0.91$  signifying moderately absorbing nature of the aerosols indicating the effect of anthropogenic black carbon. Such low values of SSA ( $\sim 0.9$ ) were reported during Indian Ocean Experiment (INDOEX) over north Indian Ocean based on measurements carried out over an island location [10]. Lowest SSA (highest absorption) was observed in the northern Arabian Sea ( $\sim 0.87$ ) during the winter (December-January-February). We find that the north-south gradient in SSA is largest during winter over the Arabian Sea as well as over the Bay of Bengal (Figure 2). It can be seen that during all the seasons, there exist a north-south gradient with higher SSA over the open oceans and decreasing as we move northwards (Figure 2). While comparing various SSA values reported in the past, it may be noted that the SSA reported here from satellite measurements is representative of the atmospheric column.

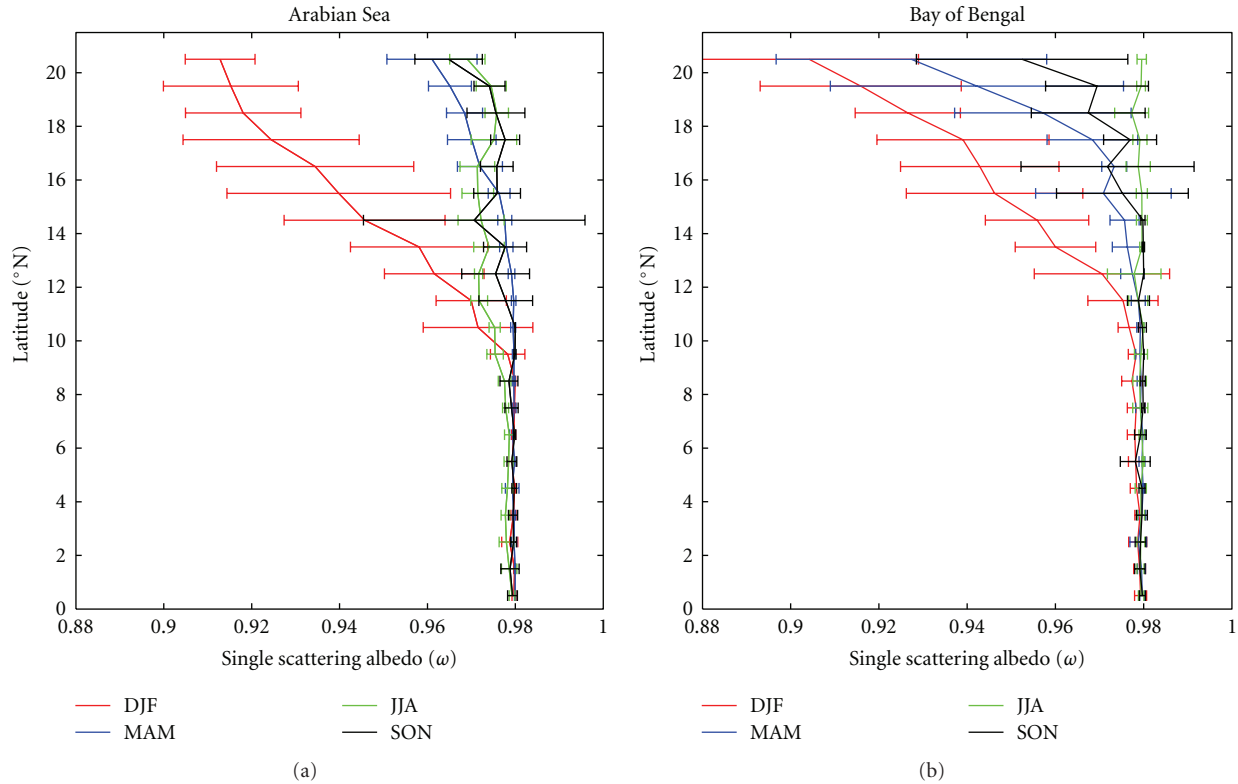


FIGURE 2: Latitudinal gradient of single scattering albedo over Arabian Sea and Bay of Bengal.

An SSA value of 0.89 to 0.93 at the mid-visible was inferred from airborne measurements during Tropospheric Aerosol Radiative Forcing Observational Experiment (TARFOX) in July 1996 over the eastern US and western Atlantic Ocean [20, 21]. Dubovik et al. [22] retrieved SSA from measurements made during Smoke Clouds and Radiation—Brazil (SCAR-B) campaign in August and September 1995 and found a value of 0.87 at 670 nm. The SSA retrieved from pyrheliometers and pyranometers in northern China during the period between 1993 and 2001 ranged from 0.80 to 0.85 at 550 nm [23]. However SSA from Qiu et al. [23] is most likely underestimated when compared with several later studies [24, 25]. Ganguly et al. [26] reported a value of  $\sim 0.7$  to 0.9 from a land-based campaign over the central part of India. But most of the low values of SSA reported are regions of high pollution or biomass burning. The lower value of SSA observed over the Indian region during winter as shown by Ganguly et al. [26] could be explained by seasonal biomass burning [27–29] and dust particles transported from Sahara (Figure 3 shows the prevailing wind pattern). In the present study, SSA retrievals were restricted to oceanic regions only due to the uncertainties involved in the retrieval of AOD from MODIS over land.

**3.2. Aerosol Optical Depth.** The seasonal and spatial pattern of aerosol optical depth from MODIS is shown in Figures 4 and 5. There are some important observations in the spatial patterns of aerosol optical depth. (a) High AODs close to the coast and a sharp gradient over the ocean. (b) Strong

north-south gradient. (c) Detached highs in the AODs over the ocean. (d) The highest AODs over both Arabian Sea and Bay of Bengal are observed during summer and the lowest during winter.

There have been several cruise-based measurements to understand the aerosol characteristics over the Arabian Sea, but most of them were either season or region specific. Though addressing important and specific scientific questions, they are not capable of providing the unprecedented spatial and temporal resolution that satellite observations offer. By integrating several independent island and ship-borne measurements Satheesh et al. [30] showed that there exists a latitudinal gradient in AODs over the Arabian Sea up to about  $12^{\circ}\text{N}$ . The gradient observed during the summer (JJA) continues almost exponentially ( $\sim 0.2$  at  $2^{\circ}\text{N}$  to  $\sim 0.8$  at  $20^{\circ}\text{N}$ ) unlike that during other seasons when gradient becomes shallower. The JJA season is characterized by heavy winds associated with south-west monsoon which leads to large production of sea-salt aerosols over the Arabian Sea. In spite of this fact, the AOD is decreasing towards the south indicating the dominating strength of desert dust from west Asia.

There were only a few aerosol measurements over northern AS during JJA due to the hostile weather conditions as well as persistent cloudiness [14] [13]. Ship-borne measurements have shown AOD of 0.4 to 0.7 over northern Arabian Sea [14]. The largest seasonality in AOD was observed over northern Arabian Sea, whereas their latitudinal gradient was similar during winter and pre-monsoon period (Figure 5).

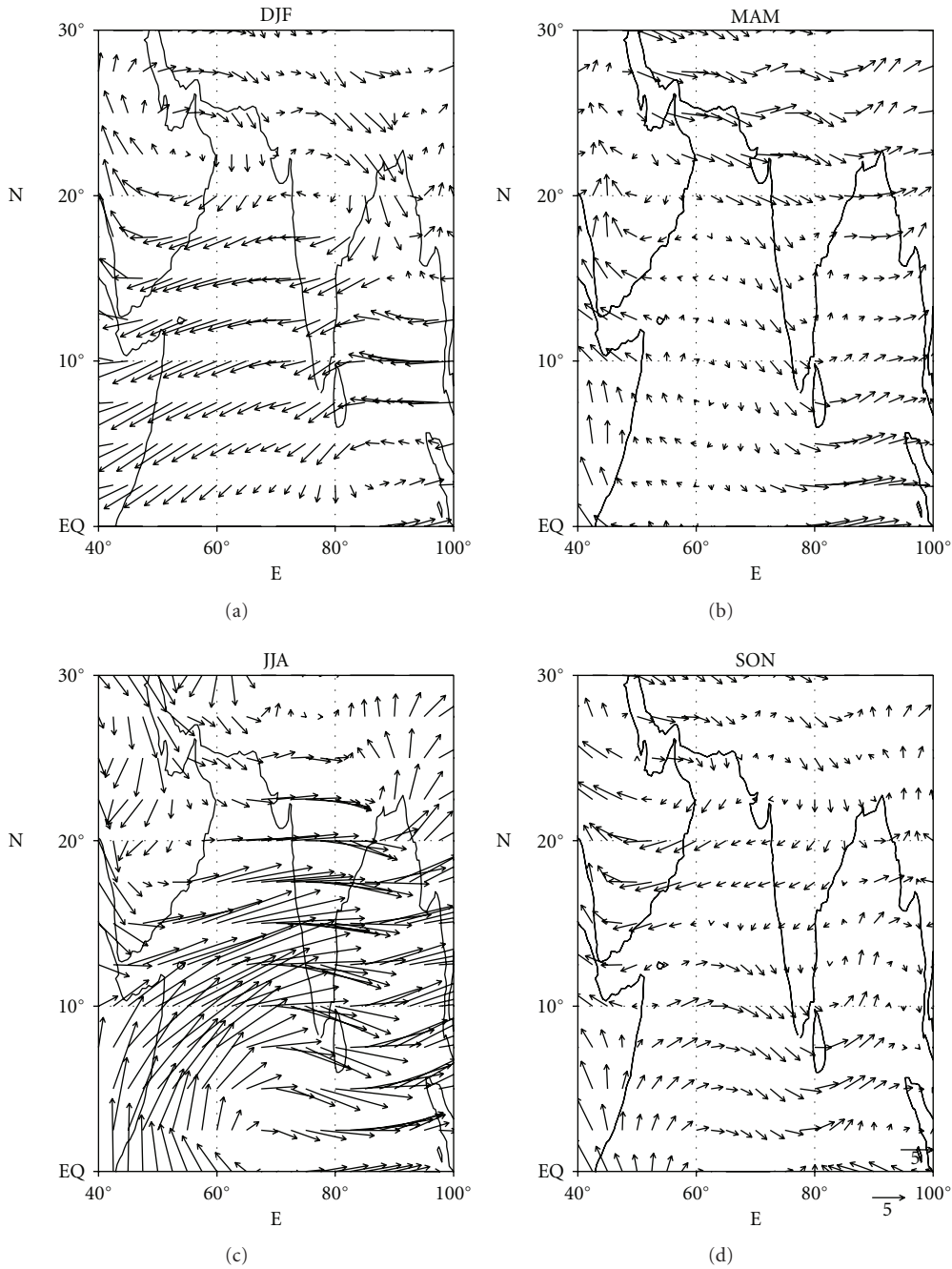


FIGURE 3: Observed wind pattern over the Indian region during different seasons (using NCEP Reanalysis).

Over the BoB, the highest AODs are more confined to the north BoB and close to the east coast of India. Therefore, there exists a large north-south latitudinal gradient, also a gradient over the east coast of India as well as the south coast of Bangladesh and west coast of Myanmar. Due to the land locked nature of BoB and its proximity to highly polluted regions, the AOD's are modulated by industrial pollution from various regions such as northern part of India and Bangladesh. Additional influence is the result of anthropogenic as well as natural biomass burning aerosols both

from the northern part of India and the west coast of Myanmar (Nair et al., [31]). This makes BoB highly dynamic as far as changes in aerosol properties are concerned. Similar to the AS, the largest gradient over the BoB is also observed during JJA. But the gradients are shallower during all seasons except during JJA. Recent measurements over BoB have shown that the head BoB is dominated by the biomass burning aerosols transported from over Myanmar, whereas the southern BoB is more or less dominated by fossil fuel burning transported from the east coast of India (Nair et al., [31]).

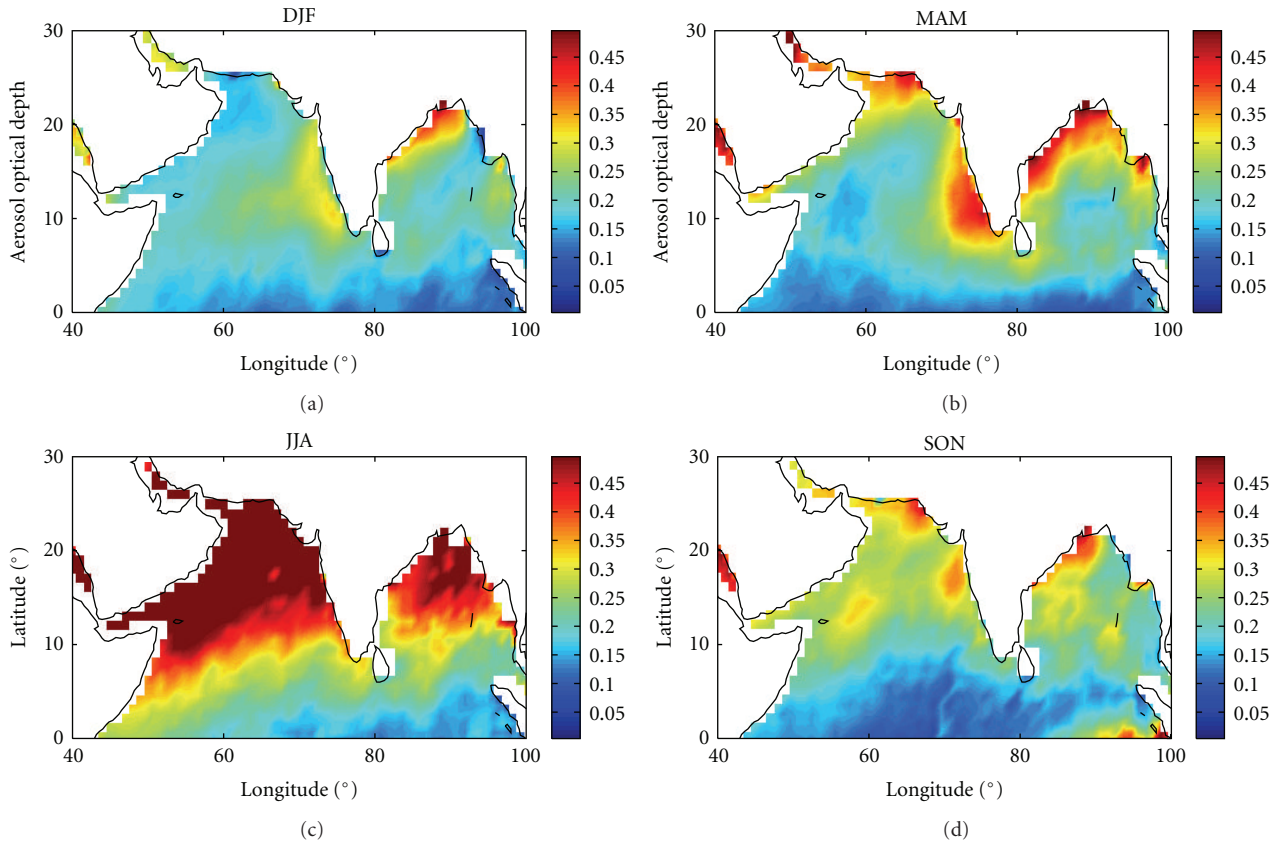


FIGURE 4: Seasonal and spatial distribution of aerosol optical depth over the oceanic regions around India.

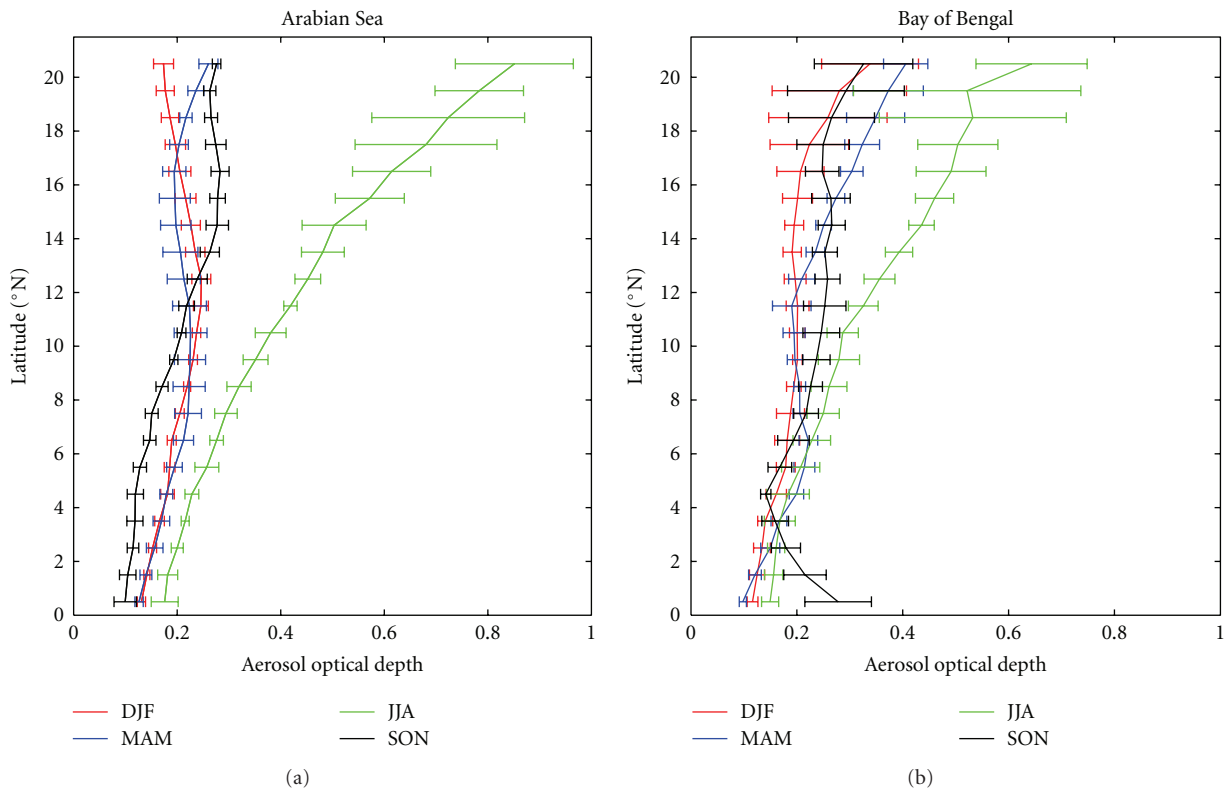


FIGURE 5: Latitudinal gradient of aerosol optical depth over Arabian Sea and Bay of Bengal.

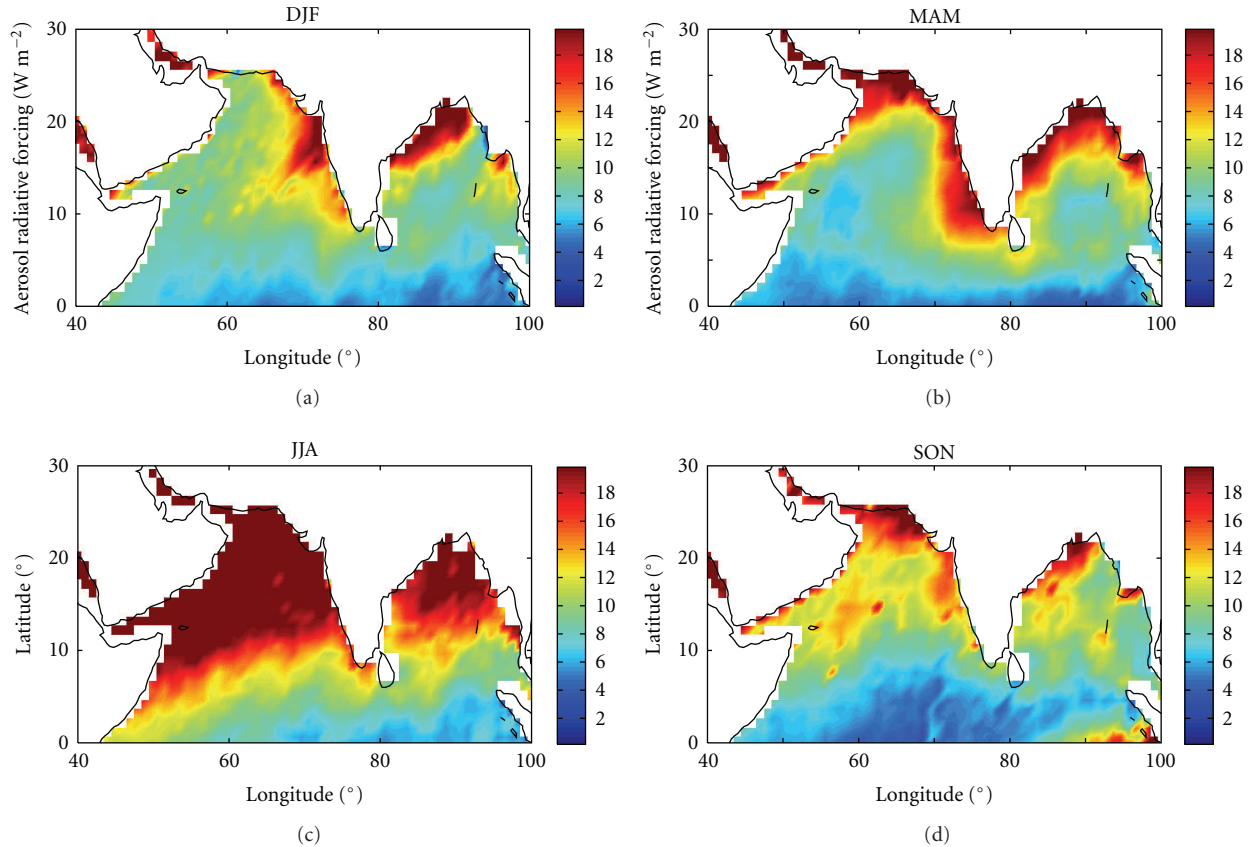


FIGURE 6: Seasonal and spatial distribution of surface aerosol radiative forcing over oceanic regions around India.

The large gradient in AOD (Figures 4 and 5) observed close to the coast can lead to large changes in the surface cooling within a very short distance (discussed in the next section). In Figure 4, the patterns shown are based on average AODs over each grid point over a three-month period and hence show the mean pattern during this period. As such, these features can be considered to be the average spatial pattern observed during the season irrespective of the day-to-day variations. Therefore, it is possible that such persistent north-south gradient in AOD can have large effect on the surface heat budget and hence change weather and climate regionally. In the present study, our main focus is to understand the spatial pattern of aerosol radiative impact, which is discussed in detail in the later sections. In the gradient pattern shown in Figure 5, the slight increase in AOD close to the equator over Bay of Bengal is due to the effect of aerosols from the Indonesian region during the post-monsoon period. The retrieved SSA using the joint OMI-MODIS methodology and AOD from MODIS were used to determine the aerosol radiative effect at surface as well as TOA.

**3.3. Regional Distribution of Aerosol Radiative Impact.** For estimating the regional distribution of aerosol radiative impact, we have used the values (maps) of SSA along with aerosol spectral optical depth as input to a Discrete Ordinate

Radiative Transfer model [Santa Barbara DISORT Atmospheric Radiative Transfer (SBDART) model] to estimate the short-wave clear sky aerosol radiative forcing at the surface and top of the atmosphere (TOA). This model is designed and developed by University of California, Santa Barbara [32] and is based on a collection of well-tested and reliable physical models, which were developed by the atmospheric science community over the past few decades. We have used tropical atmosphere model to describe atmospheric profiles and zenith angle-dependent ocean albedo [32]. Ocean albedo for overhead Sun was around 6%. We used eight streams in the radiative transfer calculation and computations were made for solar zenith angles at every  $5^\circ$  and thus estimated diurnally averaged radiative forcing. Radiation model requires aerosol scattering phase function as well in addition to the spectral optical depth and single scattering albedo. Since OMI-MODIS approach does not provide information about aerosol scattering phase function (and hence asymmetry factor), we used the “maritime tropical” model of Hess et al. [33]. It may be noted that radiative forcing maps we report in this paper corresponds to diurnally averaged values.

The seasonal and spatial pattern of aerosol radiative forcing at the Earth’s surface is shown in Figure 6. On a seasonal scale, the largest forcing at the surface was observed over the Arabian Sea during JJA (as large as  $-37 \text{ W m}^{-2}$ ).

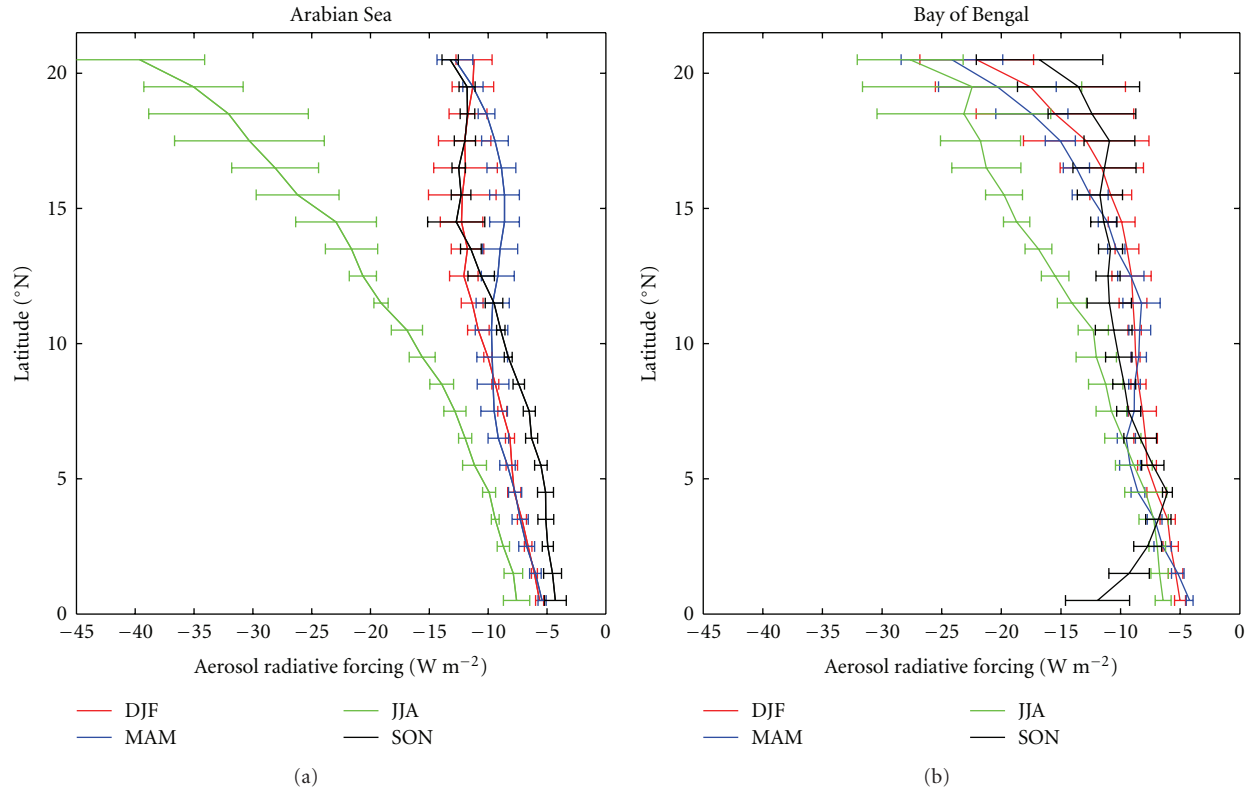


FIGURE 7: Latitudinal gradient of surface aerosol radiative forcing over Arabian Sea and Bay of Bengal.

In addition, a close examination of the gradient reveals that the gradient over Arabian Sea and Bay of Bengal at latitudes north of  $15^{\circ}\text{N}$  is weaker compared to that observed south of  $15^{\circ}\text{N}$  (Figures 7 and 8). Such observations have been reported for AOD earlier using measurements from several field campaigns (see [30]). The gradient of surface forcing during JJA is the largest with highest values of forcing is over the north of Arabian Sea (a six-fold increase compared to its value over southern Arabian Sea).

**3.4. Average over Subregions.** The large spatial as well as seasonal variation in aerosol radiative forcing (as a consequence of variability in aerosol properties like AOD and SSA over the Arabian Sea and Bay of Bengal) prompted us to look closer into this vast oceanic region by separating them into smaller subregions so as to understand the gradient and variability well. In this pursuit, we divided the whole oceanic regions around Indian subcontinent into 8 sub regions. They are North Arabian Sea (NAS,  $15$  to  $25^{\circ}\text{N}$ ,  $60$  to  $70^{\circ}\text{E}$ ), North Bay of Bengal (NBOB,  $15$  to  $25^{\circ}\text{N}$ ,  $85$  to  $95^{\circ}\text{E}$ ), Central Arabian Sea (CAS,  $10$  to  $20^{\circ}\text{N}$ ,  $57.5$  to  $72.5^{\circ}\text{E}$ ), Central Bay of Bengal (CBOB,  $10$  to  $20^{\circ}\text{N}$ ,  $82.5$  to  $97.5^{\circ}\text{E}$ ), Southern Arabian Sea (SAS) ( $5$  to  $15^{\circ}\text{N}$ ,  $60$  to  $70^{\circ}\text{E}$ ), Southern Bay of Bengal (SBOB,  $5$  to  $15^{\circ}\text{N}$ ,  $85$  to  $95^{\circ}\text{E}$ ), Northern part of Indian Ocean just south of the Indian subcontinent as North Indian Ocean (NIO,  $0$  to  $5^{\circ}\text{N}$ ,  $60$  to  $95^{\circ}\text{E}$ ), and the region just south of Equator as Equatorial Indian Ocean (EIO,  $5^{\circ}\text{S}$  to  $0$ ,  $60$  to  $95^{\circ}\text{E}$ ). The boundaries of these regions are shown in Figure 9.

The mean AOD and SSA for each of the sub regions are shown in Figures 10 and 11. Important feature observed is the clear seasonality in both AOD and SSA over both Arabian Sea and Bay of Bengal, amplitude of which falls off as we move away from the land (i.e, moving towards south). In each of these figures, it can be observed that the seasonality and its amplitude are highest in the northern most sub-regions which are NAS and NBOB. NAS exhibits the largest AOD ( $\sim 0.77$ ) during JJA which has already been discussed. The lowest SSA ( $0.92$  to  $0.97$ ) in all of the sub regions except for the NIO and EIO regions is during DJF. This clearly points to the highly absorbing nature of the aerosols as a result of transport (due to prevailing winds, see Figure 3) of the emission over the land which is expected to have large fraction of absorbing (e.g., BC) aerosols as a result of pollution. One of the most striking features is that of the low amplitude or nearly seasonally invariant SSA ( $\sim 0.98$ ) for sub regions like NIO and EIO, clearly showing the low influence of absorbing aerosols over this region. The aerosols over these regions are therefore expected to be purely marine in nature. The lowest mean SSA for any region was observed for NAS during JJA (SSA  $\sim 0.92$ ). It may be noted that the SSA values discussed are values averaged for the sub regions; individual grid point SSA's as low as  $0.88$  were also observed over this region.

The mean aerosol radiative forcing at surface, TOA and atmosphere for each of the sub regions are shown in Figure 12. It can be seen that the highest aerosol radiative forcing is observed during JJA over NAS, which has been

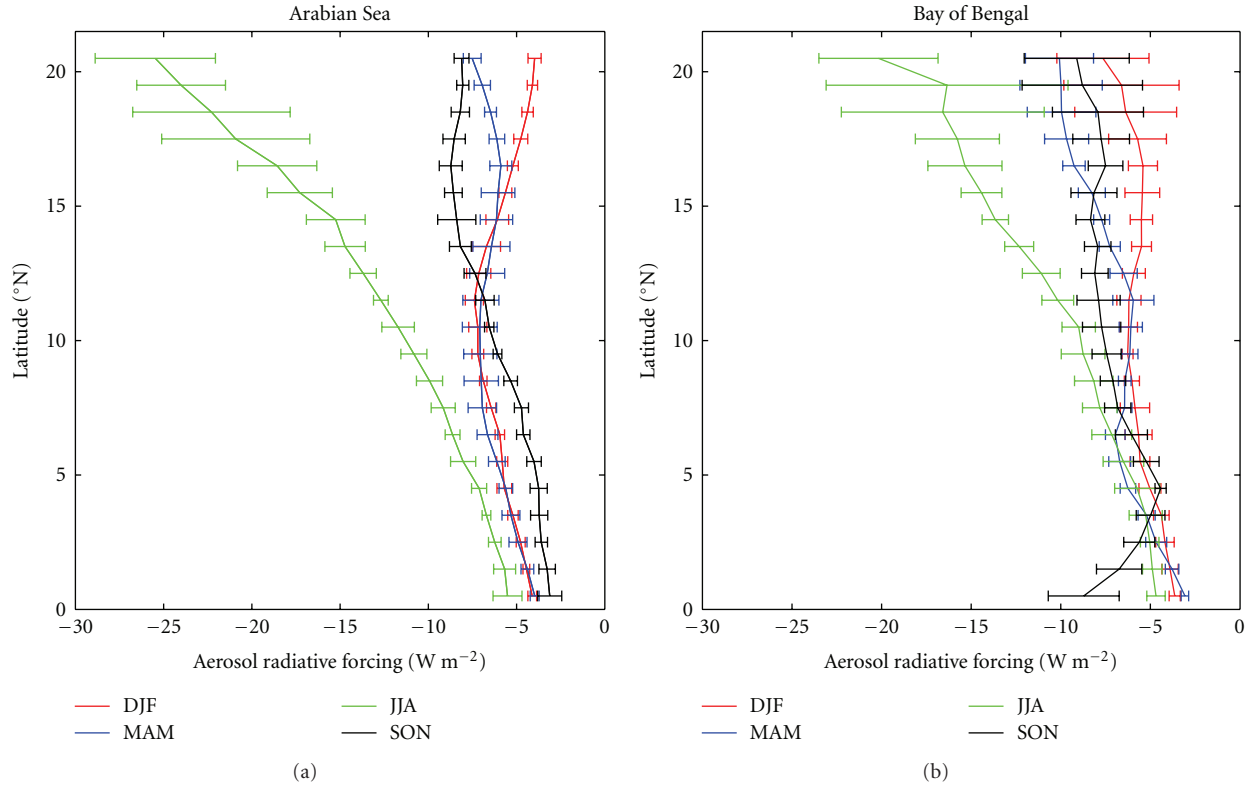


FIGURE 8: Latitudinal gradient of TOA aerosol radiative forcing over Arabian Sea and Bay of Bengal.

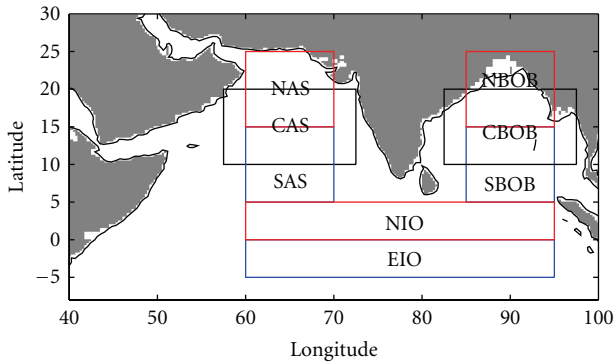


FIGURE 9: Details of the sub-regions selected over Arabian Sea, Bay of Bengal and North Indian Ocean.

shown as the region with the highest aerosol loading. The large transport of dust aerosols over to the northern Arabian Sea from the adjoining regions (NW India and West Asia) leads to this large forcing. Though NBOB also shows large forcing during JJA, it is much lower than the forcing estimated for NAS, which clearly shows the large impact of the dust transport. Previous investigations (or study) by Vinoj et al., [34] has shown that the forcing is maximum when the aerosol transport is from West Asia, the present result supplements those in situ findings made in southern Arabian Sea. It can be seen that the surface forcing in NAS are a factor of 6 to 7 more than that over SAS or NIO.

Moreover, the gradient in forcing (and consequent cooling) also is higher in Arabian Sea in comparison to BoB. Such large changes in surface forcing can have large effect on regional radiation budget and hence climate.

3.5. Comparison with Observations. The optical and micro-physical properties of aerosols were measured at a remote island location, Minicoy, in the southern Arabian Sea from February 2006 to March 2007. Aerosol optical depth was measured using a multiwavelength radiometer, black carbon using aethalometer (Magee Scientific, USA) and aerosol size distribution using an optical particle counter (GRIMM Inc) (see [34], for details). Using observations made at Minicoy, Vinoj et al. [34] have estimated aerosol radiative forcing, which provided us an opportunity to validate our estimates made using OMI-MODIS joint retrieval. The aerosol radiative forcing estimated using observations made at Minicoy over a year during 2006 has been used as a validation for the present study. It can be seen (from Figure 13) that the forcing estimates made at Minicoy from observations and using the joint OMI-MODIS methodology are comparable. The only other such estimate available over this region is INDOEX forcing estimates carried out during 1999. It can be seen that INDOEX estimates are much higher than those reported in this study. One possible explanation is that INDOEX is representative of aerosols during winter over this region while our estimates are annually averaged and are more representative of the entire year. In addition, aerosols optical depth during INDOEX intensive field campaign

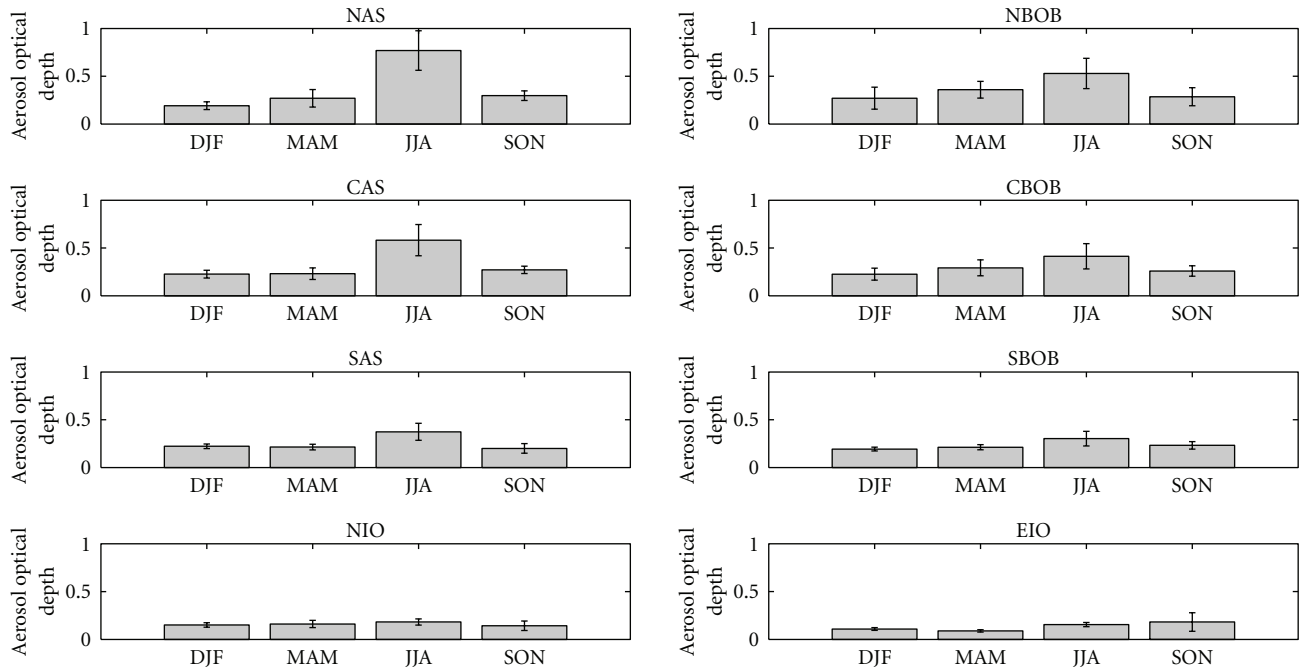


FIGURE 10: Average AOD for each sub-region region. The abbreviation over each sub-panel specifies the region.

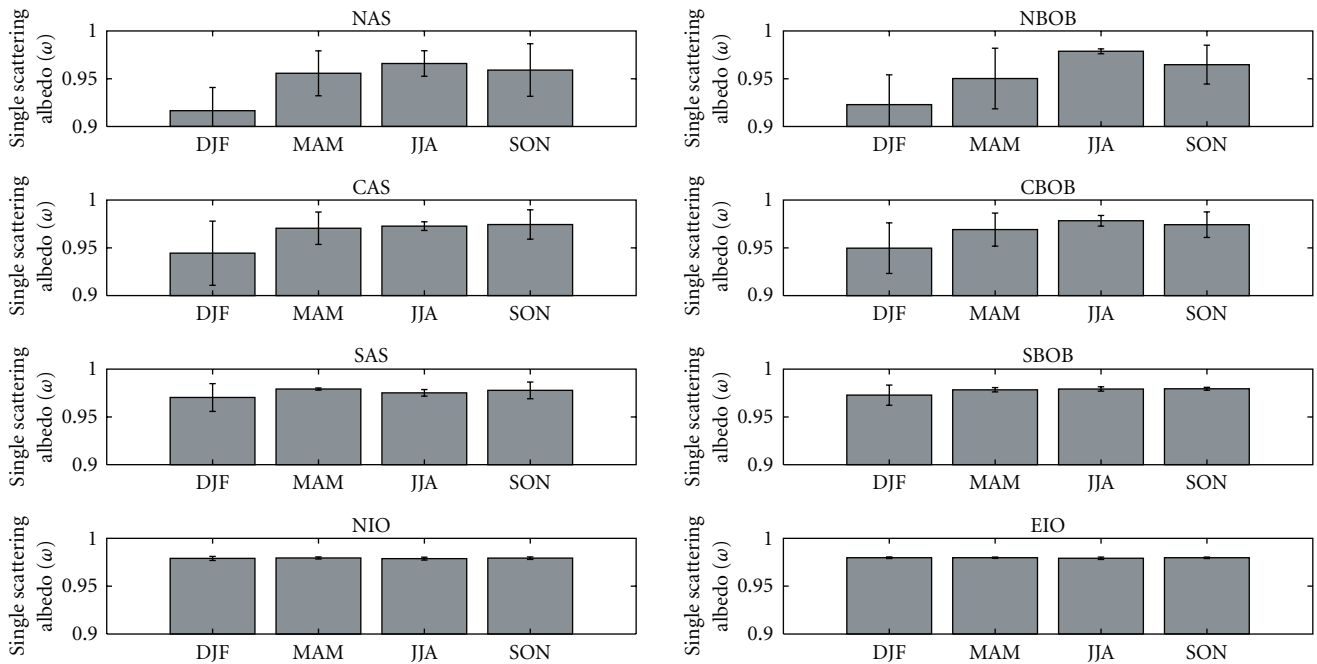


FIGURE 11: Mean single scattering albedo for each sub-region region.

period (1999) was larger compared to both 1998 and 2000. The present study, based on all season measurements made during 2006 at island location in Arabian Sea, has shown that the measured BC mass fraction were much lower than those observed in 1999. The annual mean aerosol radiative forcing estimated for the whole oceanic regions around India was  $-12$  and  $-7 \text{ W m}^{-2}$  at surface and TOA, respectively.

#### 4. Summary and Conclusions

We have retrieved regional distribution of aerosol column single scattering albedo using data from Ozone Monitoring Instrument (OMI) and Moderate Resolution Imaging Spectroradiometer (MODIS) instruments. Consequently, we provided improved assessment of short wave aerosol radiative forcing (ARF) (on both regional and seasonal scales)

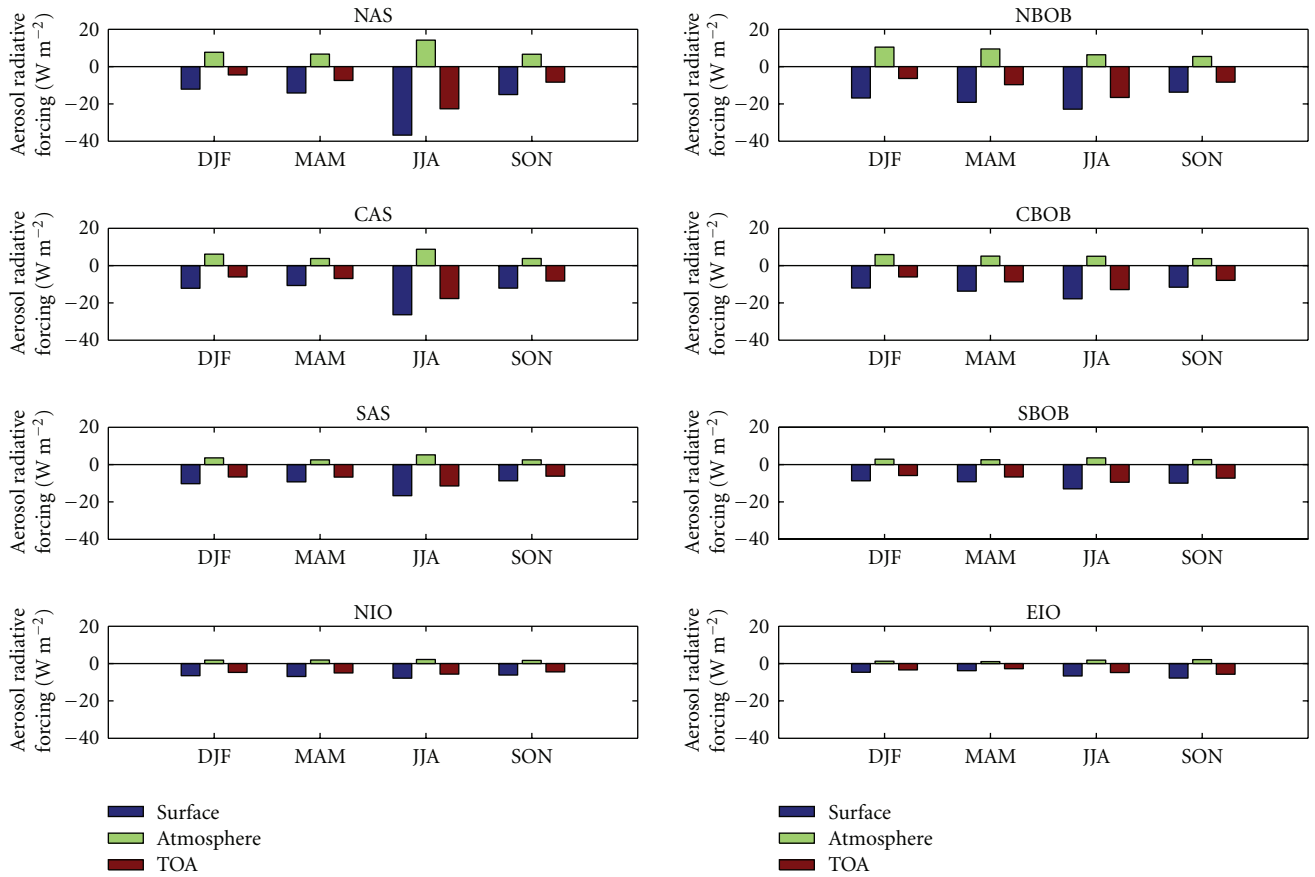


FIGURE 12: Mean aerosol radiative forcing for each sub-region region. The abbreviation over each subpanel specifies the region.

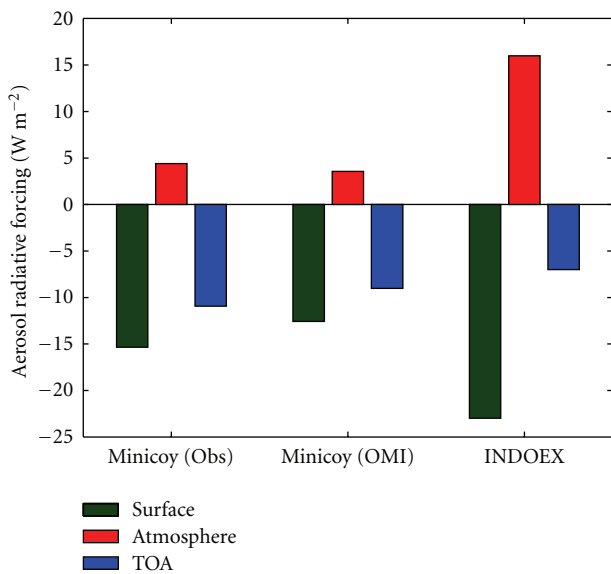


FIGURE 13: Comparison between the aerosol radiative forcing estimated at Minicoy from ground-based observation, satellite, and INDOEX.

estimates over this region. Major conclusions are listed as follows.

- (a) Large gradients in north-south ARF were observed as a consequence of gradients in single scattering albedo and aerosol optical depth.
- (b) The highest ARF ( $-37 W m^{-2}$  at the Earth's surface) was observed over the northern Arabian Sea during June to August period (JJA).
- (c) In general, ARF was higher over northern Bay of Bengal (NBoB) during winter and pre-monsoon period, whereas the ARF was higher over northern Arabian Sea (NAS) during the monsoon and post-monsoon period.
- (d) The largest forcing observed over NAS during JJA is the consequence of large amounts of desert dust transported from the west Asian dust sources.
- (e) High as well as seasonally invariant aerosol single scattering albedos ( $\sim 0.98$ ) were observed over the southern Indian Ocean region far from continents.
- (f) The ARF estimates based on direct measurements made at a remote island location, Minicoy ( $8.3^{\circ}N$ ,  $73^{\circ}E$ ) in the southern Arabian Sea are in good agreement with the estimates made following multi-satellite analysis.

## Acknowledgment

One of the authors (S. K. Satheesh) would like to thank Department of Science and Technology (DST), New Delhi for the Swarna Jayanti Fellowship.

## References

- [1] P. Forster, V. Ramaswamy, P. Artaxo et al., "Changes in atmospheric constituents and in radiative forcing," in *Climate Change 2007: The Physical Science Basis—Contribution of Working Group I to the Fourth Assessment Report of the Intergovernmental Panel on Climate Change*, S. Solomon, D. Qin, M. Manning et al., Eds., chapter 2, pp. 130–234, Cambridge University Press, New York, NY, USA, 2007.
- [2] L. A. Remer, D. Tanré, Y. J. Kaufman et al., "Validation of MODIS aerosol retrieval over ocean," *Geophysical Research Letters*, vol. 29, no. 12, pp. 1–4, 2002.
- [3] Z. Li, X. Zhao, R. Kahn et al., "Uncertainties in satellite remote sensing of aerosols and impact on monitoring its long-term trend: a review and perspective," *Annales Geophysicae*, vol. 27, no. 7, pp. 2755–2770, 2009.
- [4] J. T. Houghton, Y. Ding, D. J. Griggs et al., Eds., *Climate Change 2001: The Scientific Basis, Contribution of Working Group I to the Third Assessment Report of the Intergovernmental Panel on Climate Change*, Cambridge University Press, New York, NY, USA, 2001.
- [5] J. Hansen, M. Sato, and R. Ruedy, "Radiative forcing and climate response," *Journal of Geophysical Research D*, vol. 102, no. 6, pp. 6831–6864, 1997.
- [6] P. Chylek, G. Videen, D. Ngo, R. G. Pinnick, and J. D. Klett, "Effect of black carbon on the optical properties and climate forcing of sulfate aerosols," *Journal of Geophysical Research*, vol. 100, no. 8, pp. 16,325–16,332, 1995.
- [7] J. M. Haywood and K. P. Shine, "The effect of anthropogenic sulfate and soot aerosol on the clear sky planetary radiation budget," *Geophysical Research Letters*, vol. 22, no. 5, pp. 603–606, 1995.
- [8] J. E. Penner, C. C. Chuang, and K. Grant, "Climate forcing by carbonaceous and sulfate aerosols," *Climate Dynamics*, vol. 14, no. 12, pp. 839–851, 1998.
- [9] A. S. Ackerman, O. B. Toon, D. E. Stevens, A. J. Heymsfield, V. Ramanathan, and E. J. Welton, "Reduction of tropical cloudiness by soot," *Science*, vol. 288, no. 5468, pp. 1042–1047, 2000.
- [10] V. Ramanathan, P. J. Crutzen, J. Lelieveld et al., "Indian Ocean Experiment: an integrated analysis of the climate forcing and effects of the great Indo-Asian haze," *Journal of Geophysical Research D*, vol. 106, no. 22, pp. 28371–28398, 2001.
- [11] O. Torres, A. Tanskanen, B. Veihelmann et al., "Aerosols and surface UV products from Ozone Monitoring Instrument observations: an overview," *Journal of Geophysical Research D*, vol. 112, no. 24, Article ID D24S47, 2007.
- [12] S. K. Satheesh, O. Torres, L. A. Remer et al., "Improved assessment of aerosol absorption using OMI-MODIS joint retrieval," *Journal of Geophysical Research D*, vol. 114, no. 5, Article ID D05209, 2009.
- [13] V. Vinoj, S. S. Babu, S. K. Satheesh, K. K. Moorthy, and Y. J. Kaufman, "Radiative forcing by aerosols over the Bay of Bengal region derived from shipborne, island-based, and satellite (Moderate-Resolution Imaging Spectroradiometer) observations," *Journal of Geophysical Research D*, vol. 109, no. 5, Article ID D05203, 11 pages, 2004.
- [14] V. Vinoj, A. Anjan, M. Sudhakar, S. K. Satheesh, J. Srinivasan, and K. K. Moorthy, "Latitudinal variation of aerosol optical depths from Northern Arabian Sea to Antarctica," *Geophysical Research Letters*, vol. 34, no. 10, Article ID L10807, 2007.
- [15] D. Tanré, M. Herman, and Y. J. Kaufman, "Information on aerosol size distribution contained in solar reflected spectral radiances," *Journal of Geophysical Research D*, vol. 101, no. 14, pp. 19043–19060, 1996.
- [16] D. Tanré, Y. J. Kaufman, M. Herman, and S. Mattoo, "Remote sensing of aerosol properties over oceans using the MODIS/EOS spectral radiances," *Journal of Geophysical Research D*, vol. 102, no. 14, pp. 16971–16988, 1997.
- [17] R. C. Levy, L. A. Remer, D. Tanré et al., "Evaluation of the moderate-resolution imaging spectroradiometer (MODIS) retrievals of dust aerosol over the ocean during PRIDE," *Journal of Geophysical Research D*, vol. 108, no. 19, Article ID 8594, 13 pages, 2003.
- [18] L. A. Remer, Y. J. Kaufman, D. Tanré et al., "The MODIS aerosol algorithm, products, and validation," *Journal of the Atmospheric Sciences*, vol. 62, no. 4, pp. 947–973, 2005.
- [19] O. Torres, P. K. Bhartia, J. R. Herman, Z. Ahmad, and J. Gleason, "Derivation of aerosol properties from satellite measurements of backscattered ultraviolet radiation: theoretical basis," *Journal of Geophysical Research D*, vol. 103, no. 14, pp. 17099–17110, 1998.
- [20] P. B. Russell, P. V. Hobbs, and L. L. Stowe, "Aerosol properties and radiative effects in the United States East Coast haze plume: an overview of the tropospheric aerosol radiative forcing observational experiment (TARFOX)," *Journal of Geophysical Research D*, vol. 104, no. 2, pp. 2213–2222, 1999.
- [21] P. Hignett, J. P. Taylor, P. N. Francis, and M. D. Glew, "Comparison of observed and modeled direct aerosol forcing during TARFOX," *Journal of Geophysical Research D*, vol. 104, no. 2, pp. 2279–2287, 1999.
- [22] O. Dubovik, B. N. Holben, Y. J. Kaufman et al., "Single-scattering albedo of smoke retrieved from the sky radiance and solar transmittance measured from ground," *Journal of Geophysical Research D*, vol. 103, no. 24, pp. 31903–31923, 1998.
- [23] J. Qiu, L. Yang, and X. Zhang, "Characteristics of the imaginary part and single-scattering albedo of urban aerosols in northern China," *Tellus Series B*, vol. 56, no. 3, pp. 276–284, 2004.
- [24] K. H. Lee, Z. Li, M. S. Wong et al., "Aerosol single scattering albedo estimated across China from a combination of ground and satellite measurements," *Journal of Geophysical Research D*, vol. 112, no. 22, Article ID D22S15, 2007.
- [25] F. Zhao and Z. Li, "Estimation of aerosol single scattering albedo from solar direct spectral radiance and total broadband irradiances measured in China," *Journal of Geophysical Research D*, vol. 112, no. 22, Article ID D22S03, 2007.
- [26] D. Ganguly, H. Gadhavi, A. Jayaraman, T. A. Rajesh, and A. Misra, "Single scattering albedo of aerosols over the central India: implications for the regional aerosol radiative forcing," *Geophysical Research Letters*, vol. 32, no. 18, Article ID L18803, 4 pages, 2005.
- [27] B. N. Duncan, R. V. Martin, A. C. Staudt, R. Yevich, and J. A. Logan, "Interannual and seasonal variability of biomass burning emissions constrained by satellite observations," *Journal of Geophysical Research D*, vol. 108, no. 2, Article ID 4100, 22 pages, 2003.
- [28] S. Menon, J. Hansen, L. Nazarenko, and Y. Luo, "Climate effects of black carbon aerosols in China and India," *Science*, vol. 297, no. 5590, pp. 2250–2253, 2002.

- [29] D. G. Streets, T. C. Bond, G. R. Carmichael et al., "An inventory of gaseous and primary aerosol emissions in Asia in the year 2000," *Journal of Geophysical Research D*, vol. 108, no. 21, pp. 30–23, 2003.
- [30] S. K. Satheesh, K. K. Moorthy, Y. J. Kaufman, and T. Takemura, "Aerosol optical depth, physical properties and radiative forcing over the Arabian Sea," *Meteorology and Atmospheric Physics*, vol. 91, no. 1-4, pp. 45–62, 2006.
- [31] V. S. Nair, S. S. Babu, and K. K. Moorthy, "Aerosol characteristics in the marine atmospheric boundary layer over the bay of bengal and arabian sea during ICARB: spatial distribution and latitudinal and longitudinal gradients," *Journal of Geophysical Research D*, vol. 113, no. 15, Article ID D15208, 2008.
- [32] P. Ricchiuzzi, S. Yang, C. Gautier, and D. Sowle, "SBDART: a research and teaching software tool for plane-parallel radiative transfer in the earth's atmosphere," *Bulletin of the American Meteorological Society*, vol. 79, no. 10, pp. 2101–2114, 1998.
- [33] M. Hess, P. Koepke, and I. Schult, "Optical properties of aerosols and clouds: the software package OPAC," *Bulletin of the American Meteorological Society*, vol. 79, no. 5, pp. 831–844, 1998.
- [34] V. Vinoj, S. K. Satheesh, and K. K. Moorthy, "Optical, radiative, and source characteristics of aerosols at Minicoy, a remote island in the southern Arabian Sea," *Journal of Geophysical Research D*, vol. 115, no. 1, Article ID D01201, 2010.

## Research Article

# Vertical and Horizontal Gradients in Aerosol Black Carbon and Its Mass Fraction to Composite Aerosols over the East Coast of Peninsular India from Aircraft Measurements

S. Suresh Babu,<sup>1</sup> K. Krishna Moorthy,<sup>1</sup> and S. K. Satheesh<sup>2</sup>

<sup>1</sup> Space Physics Laboratory, Vikram Sarabhai Space Centre, Trivandrum 695022, India

<sup>2</sup> Centre for Atmospheric and Oceanic Sciences, Indian Institute of Science, Bangalore 560012, India

Correspondence should be addressed to S. Suresh Babu, s.sureshbabu@vssc.gov.in

Received 4 January 2010; Accepted 18 March 2010

Academic Editor: Victoria E. Cachorro

Copyright © 2010 S. Suresh Babu et al. This is an open access article distributed under the Creative Commons Attribution License, which permits unrestricted use, distribution, and reproduction in any medium, provided the original work is properly cited.

During the Integrated Campaign for Aerosols, gases and Radiation Budget (ICARB) experiment of ISRO-GBP, altitude profiles of mass concentrations of aerosol black carbon ( $M_B$ ) and total (composite) aerosols ( $M_T$ ) in the lower troposphere were made onboard an aircraft from an urban location, Chennai (13.04 °N, 80.17 °E). The profiling was carried out up to 3 km (AGL) in eight levels to obtain higher resolution in altitude. Besides, to explore the horizontal gradient in the vertical profiles, measurements were made at two levels [500 m (within ABL) and 1500 m (above ABL)] from ~10 °N to 16 °N and ~80 °E to 84 °E. The profiles showed a significant vertical extent of aerosols over coastal and offshore regions around Chennai with BC concentrations ( $\sim 2 \mu\text{g m}^{-3}$ ) and its contribution to composite aerosols remaining at the same level (between 8 to 10% for  $F_{BC}$ ) as at the surface. Even though the values are not unusually high as far as an urban location is concerned, but their constancy throughout the vertical column will have important implications to climate impact of aerosols.

## 1. Introduction

Direct radiative forcing due to black carbon (BC) aerosols crucially depends on the vertical profile of BC. Elevated BC layer over scattering aerosol/cloud layer will enhance the atmospheric forcing and can even reverse the “white house effect” [1]. Tripathi et al. [2] have reported that the difference in the short-wave, clear sky forcing between the steadily decreasing and increasing BC aloft is as much as a factor of 1.3. Lubin et al. [3] have shown that this difference can be as much as a factor of two in the case of long wave. Haywood and Ramaswamy [4] have reported from GCM simulation that the direct radiative forcing of a BC aerosol layer increases approximately by a factor of 5, as the layer is moved between the surface and 20 km. Based on model simulation and observation during INDOEX, Ackerman et al. [5] reported that enhanced layer of BC aerosols reduces the cloud cover by BC-induced atmospheric heating and hence offsets the aerosol-induced radiative cooling at the top

of the atmosphere on a regional scale. Thus information on the altitude variation of BC and its mass fraction to total composite aerosols is very important in estimating its radiative forcing.

Even though LIDAR can give information on the vertical distribution of scattering aerosol, it cannot give any information on the altitude distribution of absorbing aerosols. Thus, in situ measurement of absorbing aerosol such as BC from aircraft is very important. Such measurements are very limited worldwide, especially over India except for Moorthy et al. [6], Tripathi et al. [2], and Babu et al. [7]. Nevertheless, these measurements were restricted only to BC mass concentration and were over inland locations. As part of the air segment of Integrated Campaign for Aerosols gases and Radiation Budget (ICARB) field experiment [8], altitude profiles of the mass concentrations of BC ( $M_B$ ) and total ( $M_T$ ) aerosols were made over coastal areas of the urban centre of Chennai (13.04 °N, 80.17 °E) in the east coast of India.

## 2. Experimental Details and Data Base

Measurements were made onboard an aircraft (beach craft 20, propeller aircraft) of the National Remote Sensing Centre (NRSC) from the base at Chennai (13.04°N, 80.17°E), a large urban centre situated on the eastern coast of India. Besides being a city with over 5 million population and the associate urban activities, automobiles and so forth, the city also has sound industries, very large port, and a thermal power station at its periphery. The instruments used were an Aethalometer; (model AE-42 of Magee Scientific, USA, [9]) for measuring mass concentrations ( $M_B$ ) of BC and an Optical Particle Counter (OPC) spectrometer (model 1.108 of Grimm Aerosol Technique, Germany, [10]) operated in its mass mode for measuring the mass concentration ( $M_T$ ) of total (composite) aerosols. Aethalometer, a simple rugged instrument for field experiments, estimated  $M_B$  by measuring the change in the transmittance of its quartz filter tape onto which the particles impinge [9]. The OPC is designed to measure particle size distribution and particulate mass based on the light scattering measurement of individual particles in the sampled air. The design and operation of the instrument are described in [10]. The instantaneous position of the aircraft at every second was recorded using a global positioning system (GPS).

The details of the sampling technique and configuring the above instruments in an aircraft are available elsewhere [2, 6]. The instruments were mounted inside the cabin of the aircraft, which was kept unpressurised. The ambient air was aspirated through a stainless steel pipe, fitted to the body of the aircraft under its nose, such that the inlet opens into the incoming air as the aircraft flies. The inlets of the instruments were connected to the pipe using a Teflon tube, ~1.5 m long.

The aethalometer estimated  $M_B$  by measuring the change in the transmittance of its quartz filter tape onto which the particles impinge. The flow rate was determined by its internal pump operated under standard mass flow condition and the time base is programmable. The measured concentrations were corrected for the change in pumping speed caused by the change in the ambient pressure as the aircraft climbs to different height levels following the principle outlined in [6]. Reports are available in the recent literature on uncertainties in the aethalometer estimated BC [11–14] with several suggestions to account for it and these were followed in analyzing the data.

During the flight, the aethalometer was operated at a time base of 2 minutes and a flow rate of 6.5 standard liters per minute (under standard temperature ( $T_0$ , 293 K) and pressure ( $P_0$ , 1017 hPa)). However, because the ambient pressure decreases while the aircraft climbs higher, the pumping speed increases to maintain the set mass flow rate, and as such, more volume of air is aspirated. The actual volume  $V$  of air aspirated at an ambient pressure  $P$  and temperature  $T$  is thus

$$V = V_0 \cdot \frac{P_0}{P} \cdot \frac{T}{T_0}. \quad (1)$$

Since the measured BC concentrations ( $M_B^*$ ) are calculated based on standard flow rate  $V_0$ , the actual BC concentration  $M_B$ , after correcting for the change in flow rate, is

$$M_B = M_B^* \left[ \frac{P_0 T}{P T_0} \right]^{-1}. \quad (2)$$

Following the above equation each measurement of  $M_B^*$  was converted to the true BC concentration  $M_B$ . Using the simultaneous measurements of  $M_B$  and  $M_T$ , the BC mass fraction to total ( $F_{BC} = M_B/M_T$ ) was also estimated

*2.1. Flight Details.* The measurements were made between 1st April and 8th April 2006, during this period the aircraft made 6 sorties from Chennai towards the Bay of Bengal (BoB). The ground traces of the vertical profiling are shown in Figure 1(a). Each flight was configured distinctly to address different requirements of the experiment, so that a three-dimensional distribution of aerosols is obtained around the region. These included

- (i) a high resolution vertical profiling (termed as spiral sortie) during which the aircraft made a nearly spiral ascent (about 50 km offshore from Chennai over the BoB), making profile measurements at 8 levels within the altitude region 500 m to 3000 m above ground level. At each level, it flew for about 12 minutes horizontally, maintaining the same height as much as possible. The flight path of this profiling is shown in Figure 1(b). This sortie is made during the forenoon hours, after the local boundary layer has evolved well and gives a high-resolution profile in the lower atmosphere where the species concentration is very high;
- (ii) a “latitudinal profiling” in which the aircraft covered a large latitudinal extent over coastal BoB, where concentrations are measured at two altitudes, one within the ABL (500 m) and one above it (1500 m), along a long horizontal track;
- (iii) a “longitudinal profiling” in which the aircraft covered a large longitudinal extent, along particular latitude, similar to that done for latitudinal profiling.

## 3. Prevailing Meteorology and Air Mass Back Trajectories

The prevailing meteorology during the study period over off Chennai coast over Bay of Bengal was composed predominantly of calm synoptic conditions with weak winds, clear skies and absence of precipitation. No major weather systems or cyclonic depressions were encountered in the study area during the experiment. Aerosol properties over coastal oceanic regions would be significantly modified by the advection of aerosols from adjoining land masses under favourable wind conditions. With a view to examine the effect of air mass trajectories, which act as potential conduits for aerosol transport, using HYSPLIT (Hybrid Single Particle Lagrangian Integrated Trajectory) model

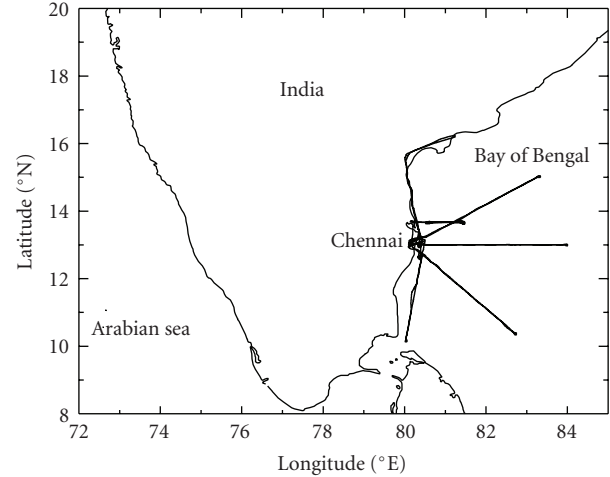
of NOAA (<http://www.arl.noaa.gov/ready/hysplit4.html>), seven-day back trajectories for all days during the period of study were computed. Clusters of 7-day back trajectories arriving off Chennai for 500 m, 1500 m, and 3000 m height levels are shown in Figure 2. It shows that the study region over BoB is influenced mainly by the advection from the peninsular India at 3000 m (free troposphere), whereas at lower levels, (500 m and 1500 m) advection is mainly from coastal India or coastal oceanic region with very few trajectories extending up to Indo-Gangetic plain.

## 4. Results and Discussion

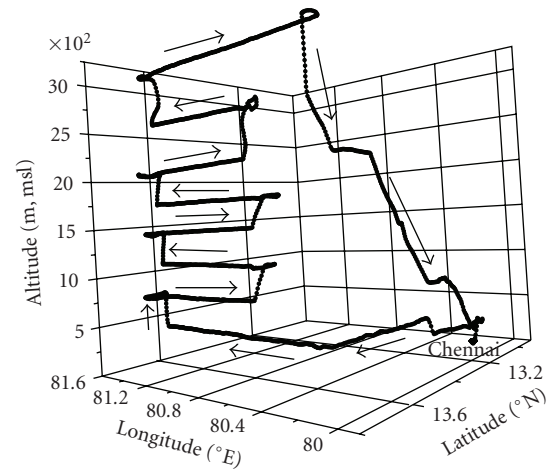
**4.1. Altitude Distribution.** The altitude profile of  $M_B$ ,  $M_T$ , and  $F_{BC}$  are shown in Figures 3(a), 3(b), and 3(c), respectively. As, during the same period, the measurements of  $M_B$  were also made onboard the ship ORV Sagar Kanya over the coastal oceanic region near to Chennai as a part of the ocean segment of ICARB [15] using a similar aethalometer, which is intercompared with the one onboard the aircraft, the data points corresponding to the surface are obtained as average of the shipboard measurements conducted in the same region. It is important and interesting to see that the vertical profiles of  $M_B$ ,  $M_T$ , and  $F_{BC}$  showed two peaks: one between 800 and 1000 m (which is bit broad) and a sharp peak at  $\sim 1700$  m. At these peaks,  $M_B$  values are in the range  $2.5$  to  $3 \mu\text{g m}^{-3}$ . Very high values of  $M_B$  up to  $12 \mu\text{g m}^{-3}$  were reported at altitudes  $2.5$  km from aircraft measurements during TRACE A experiment over Brazilian forests [16]. In addition to the common feature,  $M_T$  showed an increasing trend with altitude from surface to  $3$  km, with a positive gradient of  $2.5 \pm 1.16 \mu\text{g m}^{-3} \text{ km}^{-1}$ , which lead to a weak decreasing trend in  $F_{BC}$ . Novakov et al. [17] reported an increasing trend in  $F_{BC}$  with altitude during the aircraft measurements in the eastern coast of United States. Nevertheless, it was surprising to notice the large BC fraction as high as  $8\%$  even at  $3$  km above the surface.

At this juncture it is also interesting to compare the  $M_B$  profile with a profile obtained (in February 2004) over the inland stations, Hyderabad ( $17.75^\circ\text{N}$ ,  $78.73^\circ\text{E}$ ,  $557$  m amsl, [6] and Kanpur ( $26.43^\circ\text{N}$ ,  $80.33^\circ\text{E}$ ,  $142$  m amsl, [2]), which are shown by hollow circles connected by dotted line and triangles connected by dashed line, respectively, in Figure 3(a). Over both Hyderabad and Kanpur,  $M_B$  showed a sharp decrease from surface to  $500$  m and above  $500$  m the values are more or less steady. However, over Kanpur a weak increase in  $M_B$  at  $\sim 900$  m is seen. Over Chennai  $M_B$  showed a nearly steady profile from surface to  $3$  km with a distinctive and broad peak with a layer thickness of  $\sim 1$  km from  $\sim 750$  m to  $\sim 1750$  m.

Based on model calculations Haywood and Ramaswamy [4] have shown that the aerosol radiative forcing becomes higher when the BC is placed at high altitudes, especially above cloud layers. Keil and Haywood [18] have shown that a partially absorbing aerosol, such as biomass burning aerosol displaying a single scattering albedo in the range of  $0.86$  to  $0.93$ , overlying a sheet of stratocumulus causes a significant positive (warming) radiative effect as opposed to a negative



(a)



(b)

FIGURE 1: The flight paths of the aircraft from Chennai (a). The red line corresponds to the ground trace of the aircraft flight track during the multilevel sortie and the blue line corresponds to the ground trace of the sorties used for examining latitudinal gradient at two altitudes. (b) The track in which the high resolution vertical profiling was done at 8 levels.

(cooling) effect that would occur if the cloud was absent. Thus, the vertical positioning of aerosol and cloud layers can be crucial to both the sign and magnitude of local and regional radiative forcing. In the present study, we have visually observed a cloud layer from the aircraft between  $500$  and  $800$  m. Above this cloud layer, both  $M_B$  and  $M_T$  showed a significant increase from the surface values.  $M_B$  increases from  $\sim 1.7 \mu\text{g m}^{-3}$  to  $\sim 2.7 \mu\text{g m}^{-3}$  and  $M_T$  increases from  $\sim 18 \mu\text{g m}^{-3}$  to  $\sim 25 \mu\text{g m}^{-3}$ . However, the  $F_{BC}$  values are found to be more or less same as that of the surface values except for the two peaks at  $800$  and  $1700$  m. It is important to note that even though these values are not unusually high as far as an urban location is concerned, but their constancy throughout the vertical column will have important implications to climate impact assessment.

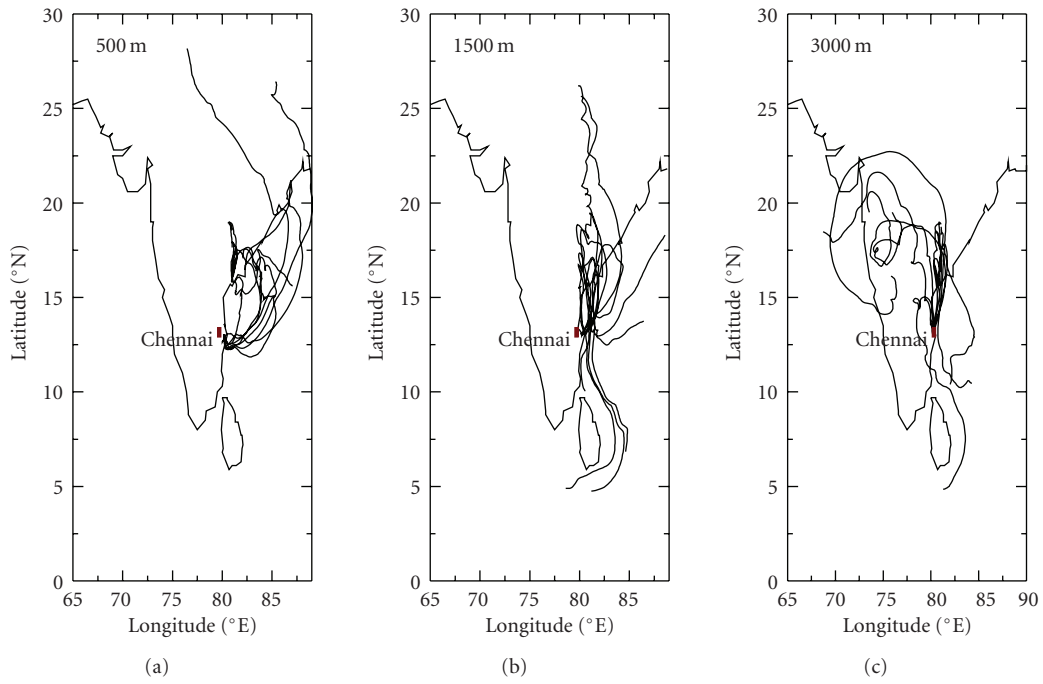


FIGURE 2: Air mass back trajectories arriving off Chennai coast at three different heights, 500, 1500, and 3000 m amsl, respectively.

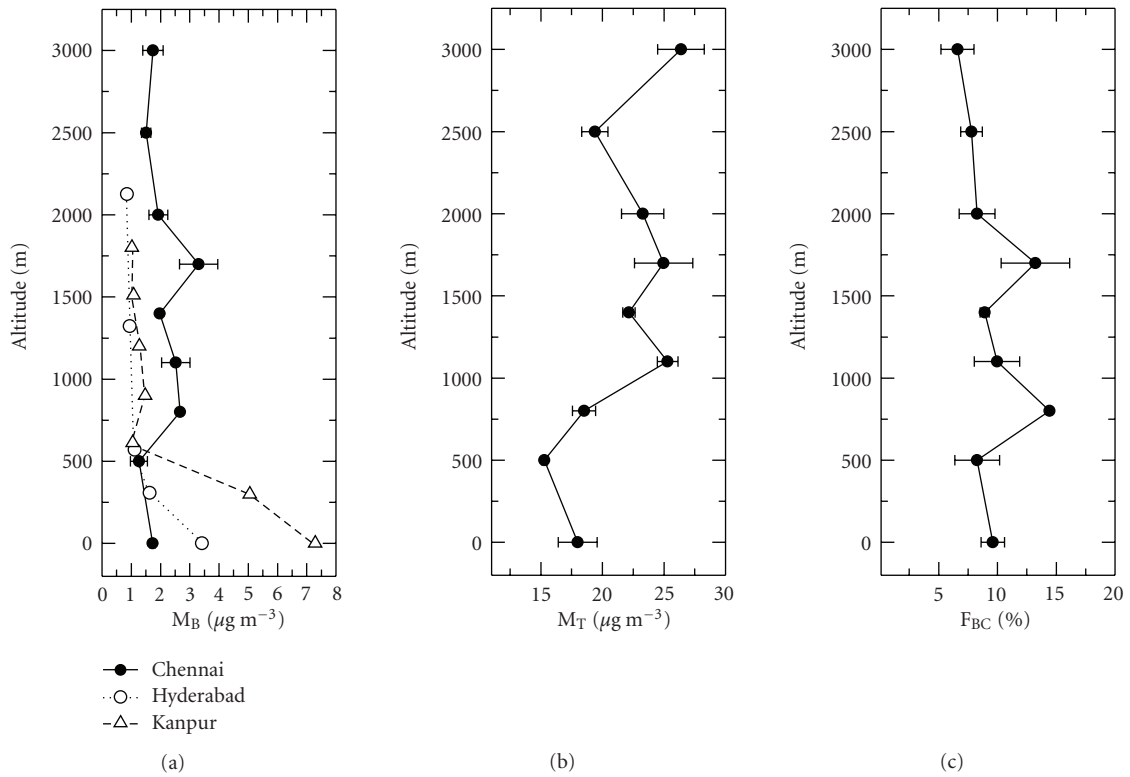


FIGURE 3: Altitude profiles of  $M_B$ ,  $M_T$ , and  $F_{BC}$  over the coastal oceanic region off Chennai. Altitude profile of  $M_B$  over Hyderabad (circles with dotted line) and Kanpur (triangles with dashed line) are also shown in panel (a) for comparison.

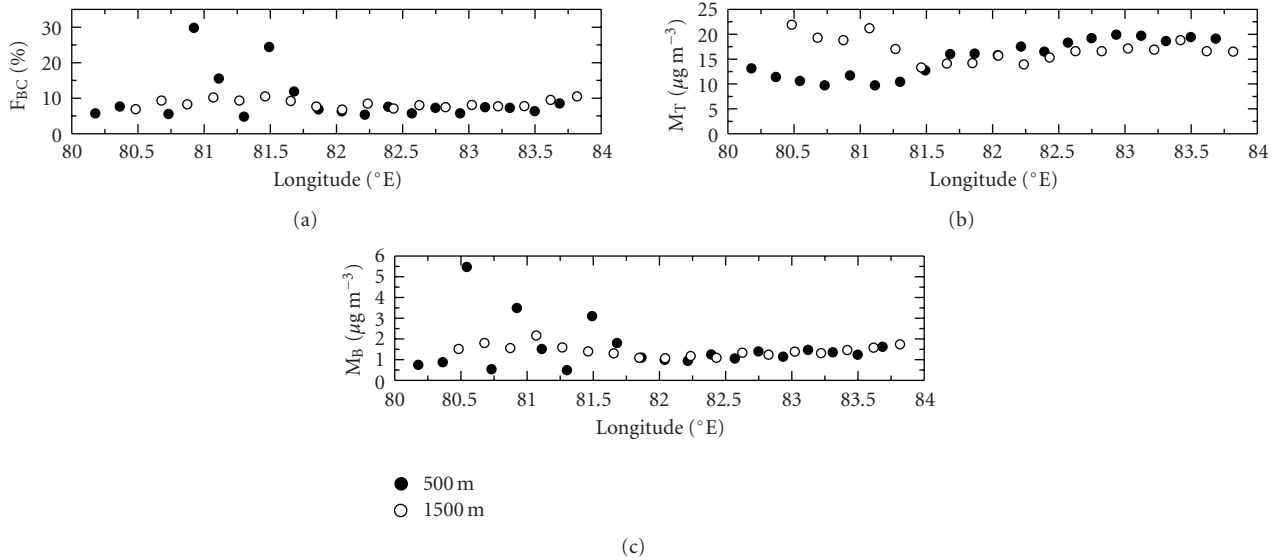


FIGURE 4: Longitudinal variation of  $M_B$ ,  $M_T$ , and  $F_{BC}$  at 500 m and 1500 m.

**4.2. Longitudinal Variations Normal to the Coastline.** Advection of continental aerosols over to oceans is a strong input to marine aerosol system and has been drawing the attention of scientists and environmentalists. All the recent field experiments (ACE I & II, TARFOX, INDOEX, ACE-Asia) have been extensively addressed to this problem. In the coastal region, this is accelerated by the mesoscale meteorological process such as land-sea breeze circulations. Based on a cruise experiment over the Arabian Sea, Subrahmanyam et al. [19] reported that the vertical extent of the sea breeze circulation cell can be up to 1.2 km, and this can have an offshore extend of  $\sim 100$  km. Based on model simulation Rani et al. [20] reported that the horizontal extend of land/sea breeze circulation over ocean can be up to 130 km away from the coast during pre-monsoon season. Keeping these in mind, we examined the longitudinal sortie, which was conducted at two levels, 500 m (within the marine boundary layer) and 1500 m (just above the marine boundary layer). These height levels are selected based on [21] from Chennai normal to the coastline as shown in Figure 1(a). The sortie covered a longitudinal span of  $4^\circ$  into the ocean.

The longitudinal variation at 500 m and 1500 m are shown in Figure 4 for  $M_B$  (c),  $M_T$  (b) and  $F_{BC}$  (a). In the figure, the filled circles correspond to the values at 500 m and the open circles correspond to the values at 1500 m. Up to  $\sim 81.5^\circ\text{E}$  ( $\sim 130$  km from the coast),  $M_B$  at 500 m (within MABL) showed large fluctuations with values as low as  $0.5 \mu\text{g m}^{-3}$  and as high as  $5.5 \mu\text{g m}^{-3}$  with a mean value of  $2 \pm 0.6 \mu\text{g m}^{-3}$ , where as  $M_B$  values at 1500 m in the same region was more or less steady with a mean value of  $1.6 \pm 0.1 \mu\text{g m}^{-3}$ . Beyond  $81.5^\circ\text{E}$ , the  $M_B$  values appeared to be nearly steady at both 500 m and 1500 m. The mean values of  $M_B$  beyond  $81.5^\circ\text{E}$  were  $1.23 \pm 0.06 \mu\text{g m}^{-3}$  and  $1.31 \pm 0.06 \mu\text{g m}^{-3}$ , respectively, at 500 m and 1500 m levels.

Compared to  $M_B$ ,  $M_T$  showed a rather smooth variation at 500 m throughout the sortie varying between  $\sim 10 \mu\text{g m}^{-3}$

and  $\sim 20 \mu\text{g m}^{-3}$  with higher values farther from the coast (beyond  $81.5^\circ\text{E}$ ). More interestingly,  $M_T$  values were higher at 1500 m than at 500 m in the near coastal region, up to  $81.5^\circ\text{E}$  and vice versa beyond  $81.5^\circ\text{E}$ . However,  $F_{BC}$  at both 500 and 1500 m showed longitudinal variations similar to that of  $M_B$  with large variations in  $M_B$  at 500 m up to  $81.5^\circ\text{E}$  (varies between  $\sim 5\%$  to  $30\%$ ) and almost steady beyond  $81.5^\circ\text{E}$ .  $F_{BC}$  at 1500 m shows more or less steady values throughout the sortie, varies between  $7\%$  and  $10\%$ , with slightly higher values up to  $81.5^\circ\text{E}$ . This, combined with Figure 3, indicates that  $\sim 8$  to  $10\%$  of  $F_{BC}$  prevails not only at the surface but extends up to  $\sim 3$  km vertically and  $400$  km ( $\sim 4^\circ$ ) longitudinally across the coast into the deep oceanic regions. However, within the sea breeze circulation cell both  $M_B$  and  $F_{BC}$  (at 500 m) showed large variations.

**4.3. Latitudinal Variation along the Coast.** Two sorties were made along the coast from Chennai to down south up to  $\sim 10^\circ\text{N}$  and to north up to  $\sim 16^\circ\text{N}$  again at the same two different levels, 500 m and 1500 m (on 2nd April and 6th April, 2006), and these data were used to examine the North-South variation of  $M_B$ ,  $M_T$ , and  $F_{BC}$  along the coast. The results are shown in Figure 5. Both  $M_B$  and  $M_T$  showed an increasing trend at 500 m towards north, except the high values observed above Chennai due to the city impact. This was quite understandable as similar trends were seen in the latitudinal variation within MABL from the ship borne measurements also [15]. However, at 1500 m, this trend reverses and high  $M_B$  values were observed over the south of Chennai than that of the north. The variations are rather smooth and a steady decrease in  $M_B$  with latitude is observed at 1500 m level. A linear regression analysis yielded  $\sim 197 \text{ ng m}^{-3}$  decrease in  $M_B$  for every degree increase in the latitude, with a correlation coefficient of 0.64. In the case

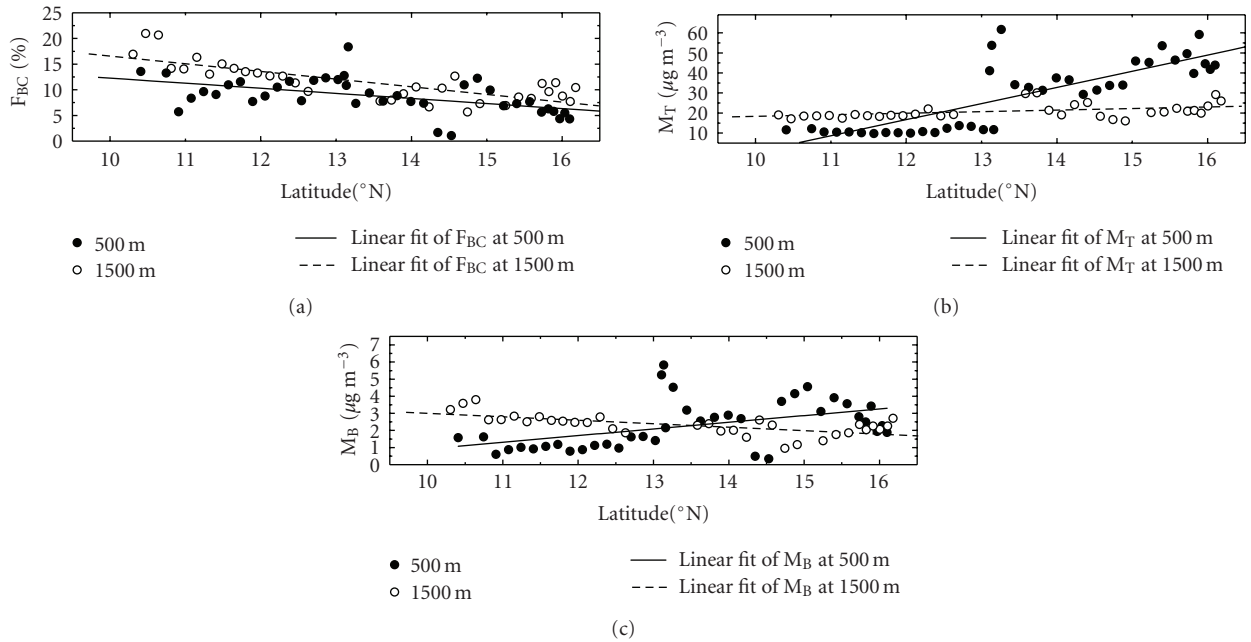


FIGURE 5: Latitudinal variation of  $M_B$ ,  $M_T$ , and  $F_{BC}$  at 500 m and 1500 m.

of  $M_T$ , the correlation coefficient estimated at 500 m (0.81) is quite significant ( $P < .0001$ ) and is higher than that at 1500 m (0.45) where the  $P = .01$ . At 500 m the regression slope gives an increase of  $\sim 8 \mu\text{g m}^{-3}$  in  $M_T$  for every degree increase in latitude where as at 1500 m the regression slope gives a much smaller value of  $\sim 0.84 \mu\text{g m}^{-3}$  for every degree increase in the latitude. At this juncture, it is interesting to note that based on a road campaign over peninsular India in 2004, Moorthy et al. [22] have observed a similar latitudinal variation in  $M_B$  at the surface level during the winter season along the west coast of peninsular India.

The most interesting feature is the higher  $F_{BC}$  values over the south of Chennai than that over north, even though the industrial and anthropogenic sources are distributed more to the north of Chennai. A consistent decrease in  $F_{BC}$  was also observed from the south to north at 500 and 1500 m altitudes, irrespective of the latitudinal trends in  $M_B$  and  $M_T$ . The fraction of BC in the aerosol system decreased northward above the MABL. This could be probably because of the large decrease in coarse mode particles aloft, leading to a sharper decrease in the mass concentration of composite aerosols than that of the MABL. It is interesting to note that, measurements onboard ship over the same region also indicated a steady  $F_{BC}$  values ( $\sim 3.0\%$ ) over the entire BoB [15].

## 5. Conclusions

During the Integrated Campaign for Aerosols, gases and Radiation Budget (ICARB) studies of ISRO-GBP, altitude profiles of mass concentrations of aerosol black carbon ( $M_B$ ) and total (composite) aerosols ( $M_T$ ) in the lower troposphere were made onboard an aircraft from an urban location,

Chennai. From the simultaneous measurements of  $M_B$  and  $M_T$ , BC mass fraction ( $F_{BC}$ ) is derived. The profiles showed;

- (i) a significant vertical extent of aerosols over coastal and offshore regions around Chennai with BC concentrations remaining at the same level as at the surface,
- (ii) two distinct peaks, first one between 800 m and 1000 m and the second at around 1700 m where the concentrations are higher than that near the surface,
- (iii) a near steady value (between 8 to 10%) for  $F_{BC}$  from ground to 3 km with two peaks at  $\sim 800$  m and 1700 m where  $F_{BC}$  goes as high as 15% and a weak still significant increasing trend in  $M_T$  from surface to 3 km with a positive gradient of  $2.5 \pm 1.16 \mu\text{g m}^{-3} \text{ km}^{-1}$ .
- (iv) Even though the values are not unusually high as far as an urban location is concerned, their constancy throughout the vertical column will have important implications to climate impact assessment.

## Acknowledgments

This work formed as part of the ICARB experiment under ARFI project of ISRO-GBP. The authors wish to thank the crew of the aircraft for their help throughout the field campaign and wholehearted support of the NRSC aircraft team headed by Dr. K. Kalyanaraman and Mr. Raghu Venkataraman. They acknowledge the NOAA Air Resources Laboratory for the provision of the HYSPLIT transport and dispersion model and READY website (<http://www.arl.noaa.gov/ready.html>) used in this publication.

## References

- [1] S. K. Satheesh, "Aerosol radiative forcing over land: effect of surface and cloud reflection," *Annales Geophysicae*, vol. 20, no. 12, pp. 2105–2109, 2002.
- [2] S. N. Tripathi, S. Dey, V. Tare, S. K. Satheesh, S. Lal, and S. Venkataramani, "Enhanced layer of black carbon in a north Indian industrial city," *Geophysical Research Letters*, vol. 32, no. 12, Article ID L12802, 4 pages, 2005.
- [3] D. Lubin, S. K. Satheesh, G. McFarquar, and A. J. Heymsfield, "Longwave radiative forcing of Indian Ocean tropospheric aerosol," *Journal of Geophysical Research*, vol. 107, article 8004, 13 pages, 2002.
- [4] J. M. Haywood and V. Ramaswamy, "Global sensitivity studies of the direct radiative forcing due to anthropogenic sulfate and black carbon aerosols," *Journal of Geophysical Research*, vol. 103, no. D6, pp. 6043–6058, 1998.
- [5] A. S. Ackerman, O. B. Toon, D. E. Stevens, A. J. Heymsfield, V. Ramanathan, and E. J. Welton, "Reduction of tropical cloudiness by soot," *Science*, vol. 288, no. 5468, pp. 1042–1047, 2000.
- [6] K. K. Moorthy, S. S. Babu, S. V. Sunilkumar, P. K. Gupta, and B. S. Gera, "Altitude profiles of aerosol BC, derived from aircraft measurements over an inland urban location in India," *Geophysical Research Letters*, vol. 31, no. 22, Article ID L22103, 4 pages, 2004.
- [7] S. S. Babu, S. K. Satheesh, K. K. Moorthy, et al., "Aircraft measurements of aerosol black carbon from a coastal location in the north-east part of peninsular India during ICARB," *Journal of Earth System Science*, vol. 117, supplement 1, pp. 263–271, 2008.
- [8] K. K. Moorthy, S. K. Satheesh, S. S. Babu, and C. B. S. Dutt, "Integrated campaign for aerosols, gases and radiation budget (ICARB): an overview," *Journal of Earth System*, vol. 117, pp. 243–262, 2008.
- [9] A. D. A. Hansen, H. Rosen, and T. Novakov, "The aethalometer, an instrument for the real-time measurement of optical absorption by aerosol particles," *Science of the Total Environment*, vol. 36, pp. 191–196, 1984.
- [10] H. Grimm and D. J. Eatough, "Aerosol measurement: the use of optical light scattering for the determination of particulate size distribution, and particulate mass, including the semi-volatile fraction," *Journal of the Air and Waste Management Association*, vol. 59, no. 1, pp. 101–107, 2009.
- [11] E. Weingartner, H. Saathoff, M. Schnaiter, N. Streit, B. Bitnar, and U. Baltensperger, "Absorption of light by soot particles: determination of the absorption coefficient by means of aethalometers," *Journal of Aerosol Science*, vol. 34, no. 10, pp. 1445–1463, 2003.
- [12] W. P. Arnott, K. Hamasha, H. Moosmüller, P. J. Sheridan, and J. A. Ogren, "Towards aerosol light-absorption measurements with a 7-wavelength aethalometer: evaluation with a photoacoustic instrument and 3-wavelength nephelometer," *Aerosol Science and Technology*, vol. 39, no. 1, pp. 17–29, 2005.
- [13] P. J. Sheridan, W. Patrick Arnott, J. A. Ogren, et al., "The reno aerosol optics study: an evaluation of aerosol absorption measurement methods," *Aerosol Science and Technology*, vol. 39, no. 1, pp. 1–16, 2005.
- [14] C. E. Corrigan, V. Ramanathan, and J. J. Schauer, "Impact of monsoon transitions on the physical and optical properties of aerosols," *Journal of Geophysical Research*, vol. 111, no. 18, Article ID D18208, 2006.
- [15] V. S. Nair, S. S. Babu, and K. K. Moorthy, "Aerosol characteristics in the marine atmospheric boundary layer over the Bay of Bengal and Arabian Sea during ICARB: spatial distribution and latitudinal and longitudinal gradients," *Journal of Geophysical Research*, vol. 113, no. 15, Article ID D15208, 2008.
- [16] E. B. Pereira, A. W. Setzer, F. Gerab, P. E. Artaxo, M. C. Pereira, and G. Monroe, "Airborne measurements of aerosols from burning biomass in Brazil related to the TRACE A experiment," *Journal of Geophysical Research*, vol. 101, no. 19, pp. 23983–23992, 1996.
- [17] T. Novakov, D. A. Hegg, and P. V. Hobbs, "Airborne measurements of carbonaceous aerosols on the East Coast of the United States," *Journal of Geophysical Research*, vol. 102, no. 25, pp. 30023–30030, 1997.
- [18] A. Keil and J. M. Haywood, "Solar radiative forcing by biomass burning aerosol particles during SAFARI 2000: a case study based on measured aerosol and cloud properties," *Journal of Geophysical Research*, vol. 108, no. D13, article 8467, 2003.
- [19] D. B. Subrahmanyam, K. Sen Gupta, S. Ravindran, and P. Krishnan, "Study of sea breeze and land breeze along the west coast of Indian sub-continent over the latitude range 15°N to 8°N during INDOEX IFP-99 (SK-141) cruise," *Current Science*, vol. 80, pp. 85–88, 2001.
- [20] S. I. Rani, R. Ramachandran, D. B. Subrahmanyam, D. P. Alappattu, and P. K. Kunhikrishnan, "Characterization of sea/land breeze circulation along the west coast of Indian sub-continent during pre-monsoon season," *Atmospheric Research*, vol. 95, no. 4, pp. 367–378, 2010.
- [21] V. Manghnani, S. Raman, D. S. Niyogi, et al., "Marine boundary-layer variability over the Indian Ocean during INDOEX (1998)," *Boundary-Layer Meteorology*, vol. 97, no. 3, pp. 411–430, 2000.
- [22] K. K. Moorthy, S. S. Babu, K. V. Badarinath, S. V. Sunilkumar, T. R. Kiranchand, and Y. N. Ahmed, "Latitudinal distribution of aerosol black carbon and its mass fraction to composite aerosols over peninsular India during winter season," *Geophysical Research Letters*, vol. 34, no. 8, Article ID L08802, 2007.

## Research Article

# Urban Surface Temperature Reduction via the Urban Aerosol Direct Effect: A Remote Sensing and WRF Model Sensitivity Study

Menglin Jin,<sup>1</sup> J. Marshall Shepherd,<sup>2</sup> and Weizhong Zheng<sup>3</sup>

<sup>1</sup>Department of Meteorology and Climate Science, San José State University, 1 Washington Square, San José, CA 95192-0104, USA

<sup>2</sup>Department of Geography, University of Georgia, Athens, GA 30602, USA

<sup>3</sup>IMSG at Environmental Modeling Center, NOAA/NCEP, Camp Springs, MD 20746, USA

Correspondence should be addressed to Menglin Jin, jin@met.sjsu.edu

Received 9 April 2010; Revised 13 October 2010; Accepted 24 November 2010

Academic Editor: Krishnaswamy Krishnamoorthy

Copyright © 2010 Menglin Jin et al. This is an open access article distributed under the Creative Commons Attribution License, which permits unrestricted use, distribution, and reproduction in any medium, provided the original work is properly cited.

The aerosol direct effect, namely, scattering and absorption of sunlight in the atmosphere, can lower surface temperature by reducing surface insolation. By combining National Aeronautics and Space Administration (NASA) AERONET (AErosol RObotic NETwork) observations in large cities with Weather Research and Forecasting (WRF) model simulations, we find that the aerosol direct reduction of surface insolation ranges from 40–100Wm<sup>-2</sup>, depending on aerosol loading and land-atmosphere conditions. To elucidate the maximum possible effect, values are calculated using a radiative transfer model based on the top quartile of the multiyear instantaneous aerosol data observed by AERONET sites. As a result, surface skin temperature can be reduced by 1°C–2°C while 2-m surface air temperature reductions are generally on the order of 0.5°C–1°C.

## 1. Introduction

The Urban Heat Island (UHI) is an anthropogenic climate change signal described when urban skin surface, canopy, or 2-m air temperatures are higher than the temperatures in surrounding nonurban regions [1–5]. Studies spanning many decades [3, 5–8] have shown that urban regions are warmer than their surroundings, using both traditional *in-situ* measurements of surface air temperature ( $T_{\text{air}}$ ) [1] as well as satellite remotely sensed skin temperature ( $T_{\text{skin}}$ , [4, 9]). This so-called urban heat island effect, though reported extensively in the literature, still is an ad hoc research topic since details of the mechanisms responsible for warm urban surface are still not clear. Specifically, the interactions between urban temperature and aerosol effects are only now being studied with greater detail.

Extreme high temperatures have been reported over many urban regions in the warm season. Meehl et al. [10] recently found that record high temperatures in the United States have outpaced record low temperatures over the period 2000–2009. Record-breaking high temperatures were reported from China and India in the summer 2009, causing

hundreds of deaths ([http://www.thaindian.com/newsportal/eniornment/heat-wave-death-toll-rises-to-three-in-orissa\\_100185481.html](http://www.thaindian.com/newsportal/eniornment/heat-wave-death-toll-rises-to-three-in-orissa_100185481.html)). Sterl et al. [11] found that extreme temperatures would increase more rapidly than mean global temperatures in the future. Further, heat-wave events in urban areas caused significant loss of life in the Midwestern United States [12] and Europe [13, 14]. Cheval et al. [15] described Bucharest's urban heat island conditions during extreme heat conditions in 2007. They found evidence that the UHI could be enlarged or shifted under certain conditions. Zhou and Shepherd [8] found that the UHI between Atlanta and a surrounding rural station was larger during heat-waves. The research community must understand important physical processes related to the urban surface temperature in order to accurately simulate and predict it [16–19].

Aerosols affect the surface temperature mainly via two mechanisms. The first mechanism involves altering surface insolation through scattering and absorption by atmospheric aerosol layers (namely, the aerosol direct effect, [20]). In general, aerosols reduce surface insolation and consequently reduce surface temperature. Since sulphate aerosols typically

are most abundant over urban regions, it is often argued that aerosols have a net cooling effect (it was reported that black carbon has significant absorption on shortwave and longwave radiation [21]. Nevertheless, sulphate aerosols strongly scatter solar radiation and thus reduce surface insolation) [21]. The second mechanism involves changing cloud properties through aerosol microphysical and radiative pathways (the so-called “indirect effect”), which in turn influences the surface energy balance. The latter (aerosol-cloud-interaction), although widely studied, is still far from understood due to complex microphysical processes [22–25]. Our paper focuses on the aerosol direct effect to assess how much urban surface temperatures are reduced by that mechanism.

Previous research by Jin et al. [4], among others, reported that urban aerosols over New York City reduce surface insolation by  $20 \text{ Wm}^{-2}$ . But that study only used one random day of aerosol observations in September, and then employed a radiative transfer model [26] to calculate the change in surface insolation induced by urban aerosol scattering. Two key remaining issues that we address herein are (1) how exactly is surface temperature, rather than the surface insolation, reduced in the urban system? (2) Is there any seasonal variation in surface insolation reduction since urban aerosol loading has seasonality? This paper aims to shed light on these two questions using both remotely sensed aerosol observations and a regional climate model.

Specifically, the approach of this study is to assess aerosol load and microphysical properties over Beijing, New York City, Mexico City and Moscow using ground observation sites of the National Aeronautics and Space Administration (NASA) AERONET (AErosol RObotic NETwork, [27]). Next, the aerosol properties are input into a radiative transfer model [26] to quantify reductions in surface insolation ( $\delta S$ ) as a function of urban aerosols. The final step is to calculate skin and 2-m air temperature reduction induced by  $\delta S$  through an atmosphere and land surface model governed by the land surface energy balance.

Key parameters for determining the aerosol direct effect on surface insolation are the microphysical properties of aerosols, in particular, the single scattering albedo, the asymmetry factor, and aerosol amount in the atmospheric column. These parameters can be directly measured or retrieved from the AERONET ground-based sites. With these properties and certain assumptions, including that surface and vertical distributions of aerosol are uniform, the radiative transfer model can be used to calculate  $\delta S$ . After determining  $\delta S$ , the temperature can be derived from surface insolation, surface properties, and soil moisture using the most recent version of the Weather Research and Forecasting (WRF) Model.

Urbanization is an extreme case of land cover change characterized by transformation of original vegetation-covered surface to impervious surfaces like water-proof roads, buildings, and parking lots. Such land cover change reduces soil moisture (Running et al. 2006), albedo and emissivity [9], and vegetation coverage, and consequently, alters various subcomponents of Earth systems, particularly the water, carbon, and nitrogen cycle [28].

Land cover is described by a land surface model using a set of thermal and dynamic parameters, following the first-generation land models circa 1980s [29]. The most critical parameters are albedo, leaf area index, vegetation fraction cover, thermal and moisture conductivity. Satellite-observed albedo, emissivity, and vegetation index, can be directly used in the land surface models to represent the urban system [17].

Two types of surface temperature measurements are examined in this study: 2-m screen temperatures ( $T_{\text{air}}$ : surface air temperature at 2-m reference level. This screen-level temperature is the thermodynamic temperature obtained by thermometers that are sheltered in water-permeable wooden boxes located at 1.5–2 m above flat grass.  $T_{\text{air}}$  is conventionally used in climate studies to detect global temperature variations (Jones et al. 1999, Karl et al. 1993) and urban heat-waves) (i.e.,  $T_{\text{air}}$ ), and land surface skin temperature ( $T_{\text{skin}}$ , land surface skin temperature, is the radiometric temperature derived from surface emission. This temperature is closely related to land surface radiative properties (Jin et al. 1997). The  $T_{\text{skin}}$  data used herein are developed from MODIS infrared channels. See Section 2 Data Sets for details) ( $T_{\text{skin}}$ ) [4, 9]. Both temperatures are critical because  $T_{\text{skin}}$  is directly related to the surface energy balance and  $T_{\text{air}}$  is the traditional variable used in UHI studies [1]. More importantly, because  $T_{\text{skin}}$  and  $T_{\text{air}}$  have different physical meanings and responses to radiative forcing at different rates and magnitude (Jin and Dickinson 2002), we expect different responses of  $T_{\text{skin}}$  and  $T_{\text{air}}$  due to the aerosol direct effect. Examining urban  $T_{\text{skin}}$  changes and mechanisms that govern the  $T_{\text{skin}}$  changes is critical to realistically predicting the spatial-temporal variations of urban surface temperature.

This study focuses only on assessing the direct effect of aerosols on surface temperatures ( $T_{\text{skin}}$  and  $T_{\text{air}}$ ).  $T_{\text{skin}}$  changes can be connected not only to changes in greenhouse gases (we fully understand the critical role of greenhouse gases (GHG) in global warming. Since many others have been working on GHG effect, our project is designed to study how other facets such as aerosol change may contribute to surface warming) but also to changes in land use (i.e., urbanization, desertification, agricultural practice, etc.), cloud cover, rainfall patterns, or aerosols. It is essential to identify urban aerosol effect on  $T_{\text{skin}}$ , which is relatively new in urban research. Section 2 discusses the data sets used in this study, followed by Results and Discussions (Section 3). Final discussion is given in Section 4.

## 2. Data and Model

**2.1. Land Surface Skin Temperature.** The Moderate Resolution Imaging Spectroradiometer (MODIS) instrument is carried on NASA’s Terra satellite, launched in December 1999, and NASA’s Aqua satellite, launched in May 2002. Skin temperatures were retrieved using 7 solar and 3 thermal spectral bands [30] at 10:30 LT and 22:30 LT daily (Terra) and 13:30 LT and 1:30 LT (Aqua). Each pixel has a 1 km resolution at nadir [31]. The measurements used in this study have been scaled up to a 5 km resolution and averaged

to monthly values by the MODIS land team [32]. Since only skin temperature under clear skies can be measured, only the values with quality flags attesting to the absence of clouds are used.

**2.2. AERONET Observations.** Ground-based, continuous aerosol observations conducted by the NASA AEROSOL ROBOTIC NETWORK program are used. AERONET has sites over Beijing (site name Beijing, 39°58'N, 116°22'E), New York City (site name CCNY, 40°49'N, 73°56'W), Mexico City (19°20'N, 99°10'W), and Moscow (55°42'N, 37°30'E). Level 2 data, which are quality assured and include single scattering albedo, aerosol optical thickness, and the asymmetry factor are examined in the analysis of monthly local aerosol loading [33, 34]. Two limits related to AERONET observations that must be acknowledged for this investigation and future studies are that AERONET sites can only measure aerosols under clear-sky condition, and for certain sites, the observation time is not long enough or the data quality is not as robust as other sites. For example, year 2005 data for New York City is of questionable quality and thus is removed from this analysis. Level 2 data is available for AOD and high single scattering albedo and refractive indices cases. There are only a few cases in March, April, and October in New York City (NYC) and very few cases in February, March, April, and October for Moscow in which measurements reveal such high AOD. Nevertheless, Level 2 data may still shed light on the relative pollution condition of a city.

**2.2.1. Weather Research and Forecasting (WRF) Model Sensitivity Study.** Governed by the land surface energy balance, urban surface temperature varies as a function of surface insolation, heat redistribution, soil moisture, wind speed, albedo, emissivity, and other factors. It is impossible to know exactly how surface temperature would change without considering the complex interactions among soil, vegetation, and atmosphere [29]. Therefore, a numerical simulation approach is appropriate to investigate the land surface temperature change following the surface insolation reduction ( $\delta S$ ) induced by the direct effect of urban aerosols.

In order to assess the surface responses to the aerosol-induced  $\delta S$ , the Weather Research and Forecasting (WRF) model version 3 [35] is used in this study. WRF is a community-developed mesoscale weather prediction system which has demonstrated capability to simulate or predict mesoscale atmospheric circulation. We use a two-way interactive, nested-grid technique and the configuration consists of an 18-km outer domain with horizontal grid spacing of  $201 \times 200$  grid points, and a 6-km fine domain with a horizontal grid spacing of  $154 \times 151$  grid points, at the center of domain of 40.0°N, 116.0°E. A total of 27 full  $\sigma$  levels in the vertical are used with the model top at 50 hPa. We also employ a stretched vertical grid to improve resolution near the surface. In this study, the primary model physics activated in WRF include the Rapid Radiative Transfer Model (RRTM) longwave radiation; Dudhia shortwave radiation; Yonsei University (YSU) planetary boundary layer scheme; WRF Single-Moment 3-Class (WSM) cloud microphysics;

Kain-Fritsch (new Eta) convective parameterization; Monin-Obukhov surface-layer scheme; and unified Noah land-surface model [36, 37]. The urban canopy model (UCM, [38]) can represent the thermal and dynamical effects of urban regions but is not used due to the lack of urban morphological parameters for the study region. Instead, the urban effects are parameterized via the Noah land surface model. The digital elevation is attained using 30-second United States Geological Survey (USGS) topography data. The USGS 24-category data set is used to represent surface characteristics in the model, and Category 1 denotes urban and builtup land. For Category 1, the albedo is 0.15 and momentum roughness length is 0.80 m. Beijing city is located at 39°56'N and 116°20'N. According to the recent distribution of building height data in Beijing, we assign the domain of 39.7–40.1°N and 116.1–116.7°E as the Beijing area in the model. The outermost coarse-mesh lateral boundary conditions are specified by linearly interpolating the National Centers for Environment Prediction (NCEP) 6-hourly Final Analyses (FNL) at a resolution of  $1^\circ \times 1^\circ$  degree.

Two 48-hour simulations starting from 00Z July 26, 2008 to 00Z July 28, 2008 were conducted as control and sensitivity runs, respectively. The sensitivity run differs from the control run only in the reduction of surface insolation of  $100 \text{ Wm}^{-2}$  in daylight hours within the domain of 39.7–40.1°N and 116.1–116.7°E. While this is a simplified experiment, it does provide insight on how the skin and 2-m air temperatures change. A sensitivity study over other periods of time has also been conducted (not shown), but the results presented herein are typical.

It should be noted that in this experiment reducing aerosol-induced surface insolation over urban region should not be interpreted to mean that aerosols have no such effect over nonurban region. In fact, aerosol effects on solar radiation exist wherever aerosols are present. Nevertheless, these numerical experiments are designed to simplify a complicated set of processes to examine the pertinent physical processes. The focus of this study is on how much urban aerosols reduce surface temperature over urban region, not aerosol effect on urban heat island effect (i.e., the difference in temperature between urban and surrounding regions).

### 3. Results and Discussions

**3.1. Observed Urban Heat Island Effects.** The urban region is shown in the land cover maps (Figures 1(c) and 1(d)) for Beijing and New York City, respectively. The Beijing region's (center 39°50'N, 116°40'E) monthly skin temperatures in July 2008 are as high as 308–314 K (Figure 1(a)), while the exception is for arid and mountainous regions in the NW part of the region where the temperatures exceed 303 K. Similarly, New York City (NYC) has a temperature range of 300–310 K (Figure 1(b)), while NYC's surrounding regions have skin temperatures near 298–304 K. These results are based on monthly averages from Terra (10:30 AM). At the instantaneous scale, the UHI signal could be much stronger than the average value [4]. Urban pixels can be identified using MODIS land cover data (see [39, 40]).

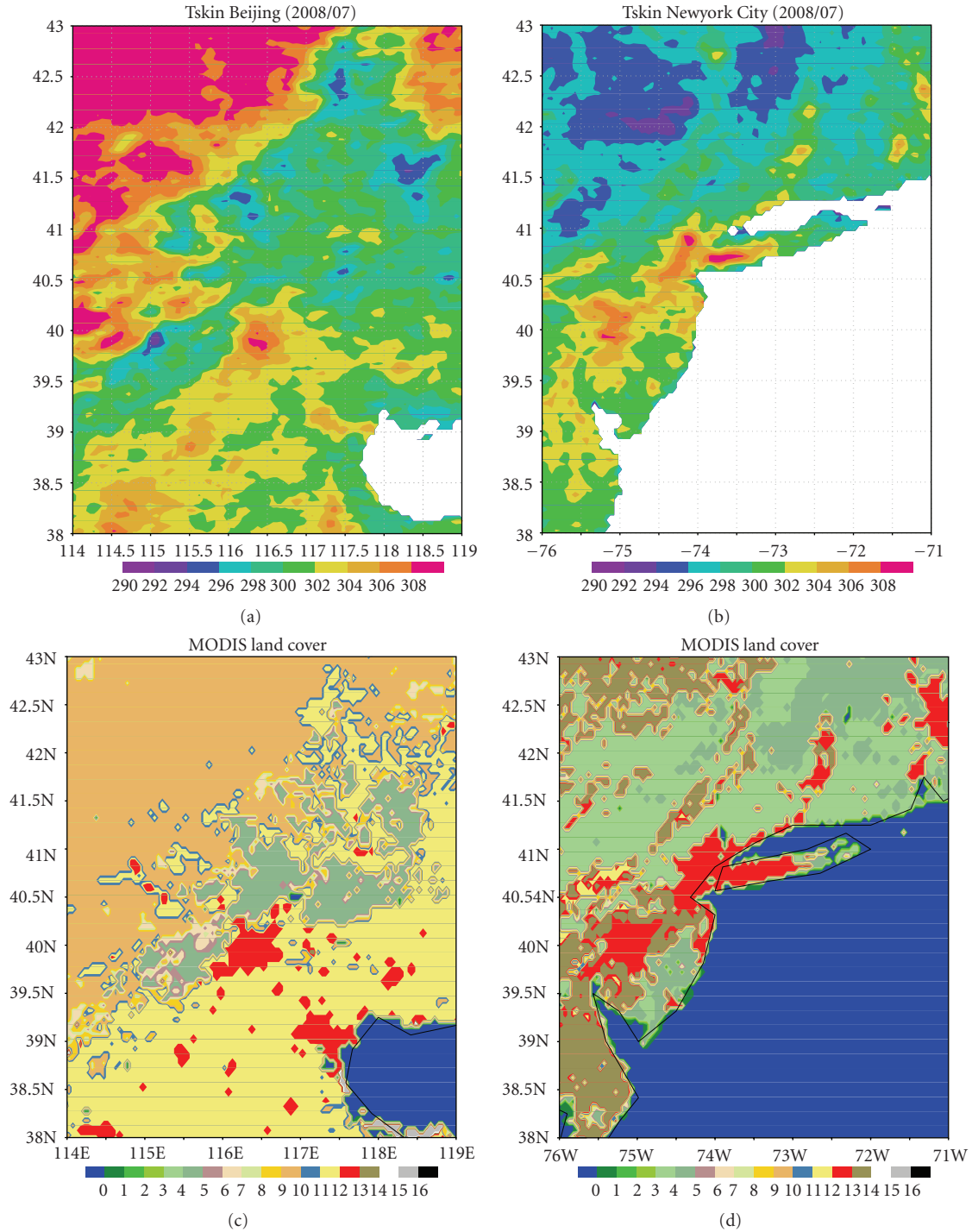


FIGURE 1: MODIS observed monthly mean land surface skin temperature starting from July 2000. (a) Beijing and (b) New York City (NYC). (c) is land cover map for Beijing region and (d) is land cover for New York City region. The land cover is defined by MODIS as (1) evergreen needleleaf forest, (2) evergreen broadleaf forest, (3) deciduous needleleaf forest, (4) deciduous broadleaf forest, (5) mixed forest, (6) closed shrubland, (7) open shrubland, (8) woody savannas, (9) savannas, (10) grassland, (11) permanent wetland, (12) cropland, (13) urban and builtup, (14) cropland/natural vegetation mosaic, (15) snow and ice, (16) barren or sparsely vegetated. In addition, 0 is water.

The advantage of the satellite observations is that there is one  $T_{skin}$  observation for each pixel, therefore we can examine all urban pixels within an area to reveal its  $T_{skin}$  relationship compared with surrounding nonurban regions. For example, the area-averaged, skin-level UHIs are observed

at Beijing and NYC (Figure 2). For July 2008, within a  $0.6^\circ \times 0.6^\circ$  box centered on Beijing ( $39.7\text{--}40.3^\circ\text{N}$ ,  $116.1\text{--}116.7^\circ\text{E}$ ), the urban-pixel-averaged  $T_{skin}$  is higher than other-land-cover-averaged  $T_{skin}$  present in the 0.6 by 0.6 degree box. In this box, 60.4% of pixels are urban cover (LC = 13),

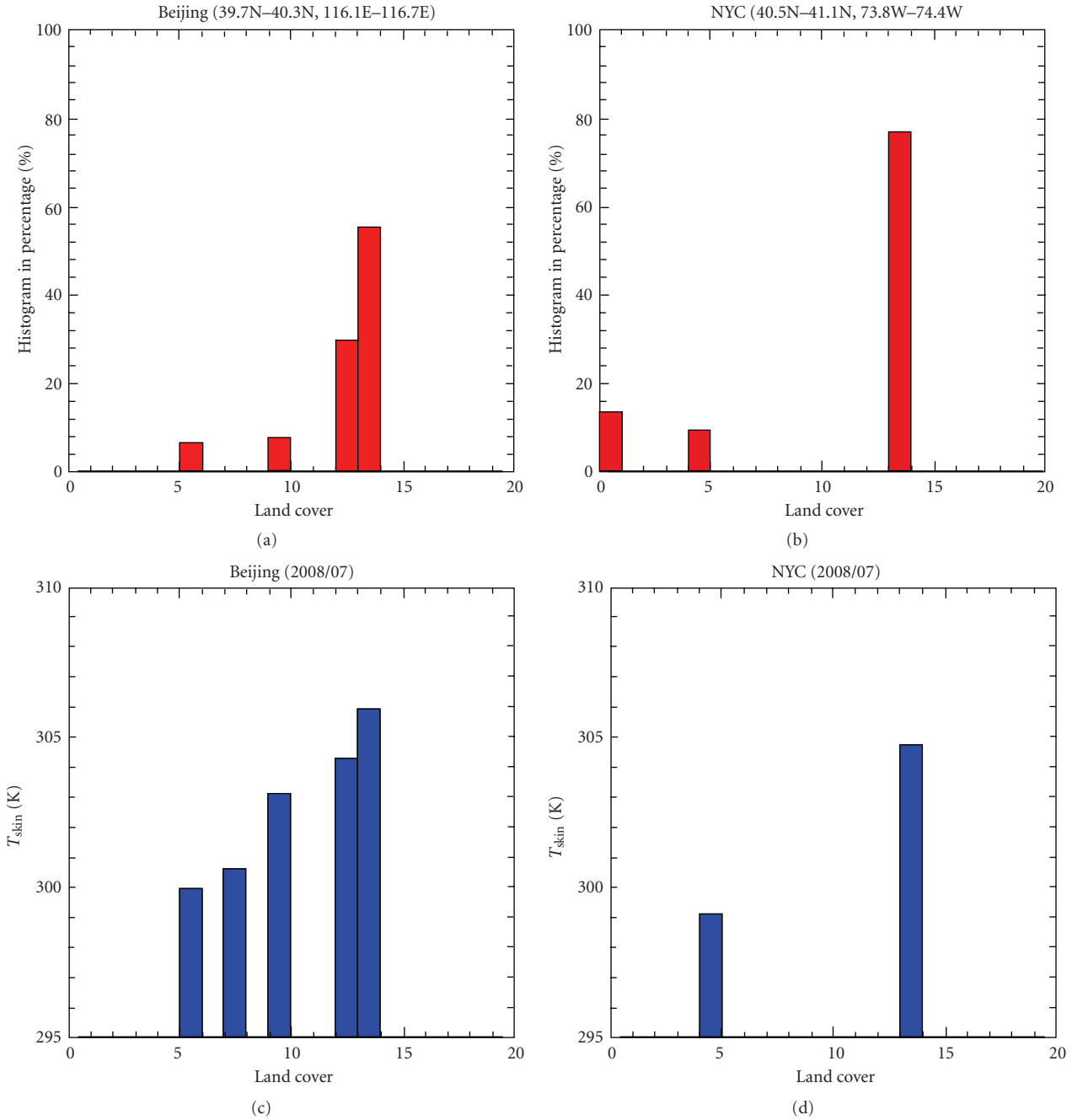


FIGURE 2: Land-cover averaged skin temperature for Beijing and New York City. (a) and (b) are land cover percentages for  $0.6 \times 0.6$  box for Beijing ( $39.7^{\circ}$ – $40.3^{\circ}$ N,  $116.1^{\circ}$ – $116.7^{\circ}$ E) and New York City ( $40.5^{\circ}$ – $41.1^{\circ}$ N,  $73.3^{\circ}$ – $74.4^{\circ}$ W). Land cover type is defined in MODIS as (1) evergreen needleleaf forest, (2) evergreen broadleaf forest, (3) deciduous needleleaf forest, (4) deciduous broadleaf forest, (5) mixed forest, (6) closed shrubland, (7) open shrubland, (8) woody savannas, (9) savannas, (10) grassland, (11) permanent wetland, (12) croplands, (13) urban and built-up, (14) cropland/natural vegetation mosaic, (15) snow and ice, (16) barren or sparsely vegetated. (c) and (d) are skin temperature versus land cover in the  $0.6 \times 0.6^{\circ}$  boxes for Beijing and new york city, respectively.

approximately 32.1% are cropland (LC = 12), 8.2% are Savannas (LC = 9), and 7.3% are mixed forest. Correspondingly,  $T_{skin}$  values include all-urban-pixel-averaged Beijing area (306 K), cropland (304 K), Savanna (303 K), and mixed forest (300 K). Other land covers near the Beijing area are too small to be apparent in the land cover figure (Figure 2(a)). However, their  $T_{skin}$  values are all lower than urban  $T_{skin}$ .

Similarly, a 0.6 by 0.6 degree box is selected over the NYC area ( $40.5$ – $41.1^{\circ}$ N,  $73.8$ – $74.4^{\circ}$ W). Over this box, 78% of pixels are urban (LC = 13), and  $T_{skin}$  is 304.8 K, while 15.4% are water (LC = 0) (no  $T_{skin}$  is presented since this specific research only studies land cover  $T_{skin}$ ) and 12.2% are mixed forest (LC = 5) with  $T_{skin}$  of 299.2 K. The UHI is evident in the satellite  $T_{skin}$  field. It is also apparent that

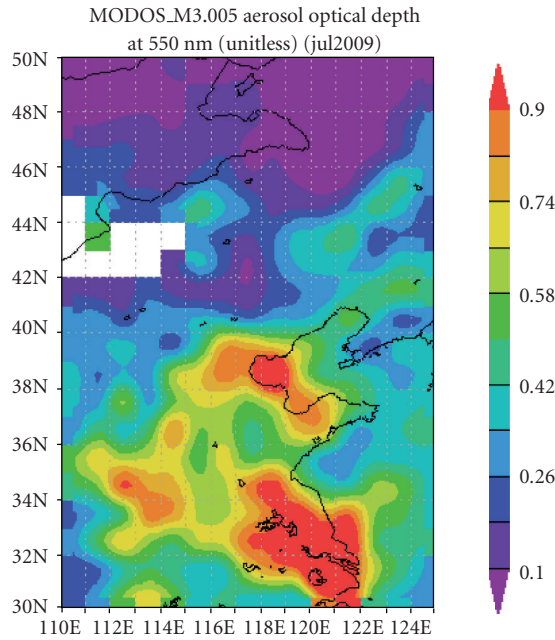


FIGURE 3: Monthly aerosol optical thickness for August 2008. Observation is from MODIS Terra daytime pass (10:30 AM) via 0.55 micrometer. The image is plotted via [http://gdata1.sci.gsfc.nasa.gov/daac-bin/G3/gui.cgi?instance\\_id=neespi](http://gdata1.sci.gsfc.nasa.gov/daac-bin/G3/gui.cgi?instance_id=neespi).

a skin temperature UHI is observed during the daytime. Traditionally, the air temperature UHI is maximized at night or in the very early morning hours [5]. We will say more on this in later sections. For comparison, relatively larger boxes are selected and the same UHI signal is observed, namely, urban  $T_{skin}$  is higher than those over other land covers.

**3.2. Observed Urban Aerosols.** Figure 3 shows the spatial distribution of aerosol optical thickness, a parameter indicating aerosol loading within the total atmospheric column. The Beijing region has heavy aerosols due to urban construction, traffic, and air conditioning. In the nearby nonurban regions, aerosol load is generally less. If nonurban regions have relatively less aerosols, the aerosol direct effect on  $T_{skin}$  would not be as significant as that over urban regions. Nevertheless, since MODIS aerosol data have coarse resolution and problems with the land surface in the retrievals [41], we have to be cautious when applying MODIS data to assess urban and nonurban aerosol concentration.

Based on aerosol optical thickness, we divide the cities into two types: (a) heavily polluted and (b) normally polluted. Although the threshold to distinguish one from another is still a research topic, Beijing is considered heavily polluted because of its much higher aerosol concentration compared to NYC, Mexico City, and Moscow. This is revealed in the aerosol optical thickness parameters (AOT, Figure 4(a)) that were observed from AERONET. Urban aerosols are defined herein as aerosols over local urban regions including those transported from remote regions as well as produced by urban regions. Beijing's AOT at

wavelength of  $0.675 \mu\text{m}$  peaks during the summer months with a maximum value of 0.8. For comparison, the NYC AOT peaks in July at 0.2 while Moscow's value peaks in September at 0.18. Mexico City has a bimodal peak in May and September around 0.22. The Beijing urban aerosol amount is significantly higher than other cities, and thus we selected Beijing as the focus of our research in the next three steps. In addition, the Beijing and NYC distributions exhibit seasonality, with maxima in summer and minima in winter. Moscow is less sensitive to seasonality. Moscow has peaks, which may be related to biomass burning and harvesting of agricultural crops. More importantly, Beijing has a higher annual AOT range than NYC and other cities. The seasonal range of NYC is only 0.15 (minimum is 0.05 in January and maximum is 0.2 in July) while the Beijing minimum (maximum) is in December (June) at 0.32 (0.8). These measurements indicate that Beijing is more polluted than NYC and other cities; therefore it is reasonable to use Beijing as an extreme urban case to demonstrate how urban aerosols affect surface insolation and temperature.

The AERONET aerosol single scattering albedo plot of monthly means shows some unexpected features. Since AERONET Level 2 single scattering albedo (SSA) retrievals are only made for moderate-to-high AOD (AOD(440 nm) > 0.4), there are very few cases for March, April and October in NYC and very few in Feb, Mar, Apr, and Oct in Moscow. These are not robust samples for these months and therefore should not be implied as representative. Removing SSA data for months with less than 10–15 days of observations is suggested by AERONET investigators, although it seems unlikely that there would be more than 10 different days with SSA retrievals in March for NYC.

The single scattering albedo is the ratio of scattering to extinction, and it approaches unity for purely scattering particles, decreasing as the degree of absorption increases (increasing concentrations of carbon soot or absorbing minerals like hematite). In most months of the year (May–December), Beijing has a higher single scattering albedo than NYC, Moscow, and Mexico City (Figure 4(b)). For Beijing, the single scattering albedo ranges from 0.87 to 0.94, with low values in winter and high values in summer. Although a few months of data are missing, both Moscow and Mexico City also exhibit seasonality in single scattering albedo with high values in summer and low values in winter. The seasonality of NYC's single scattering albedo, however, is not evident. Further research is required to determine why NYC has different features in aerosol single scattering albedo. Additionally, the high values for NYC in March are questionable.

Smaller asymmetry factors (Figure 4(c)) are related to smaller aerosol particles. Asymmetry factor is defined as the cosine weighting of the phase function and is a measure of how forward the scattering is. A zero is symmetric between forward and backscattering, such as Rayleigh scattering or isotropic scattering, in which the probability is just as great that the scattering is in the forward hemisphere as in the backscattering hemisphere. A value of 1 denotes complete forward scattering and  $-1$  denotes complete backscattering in the  $180^\circ$  direction. Aerosol particles typically have values

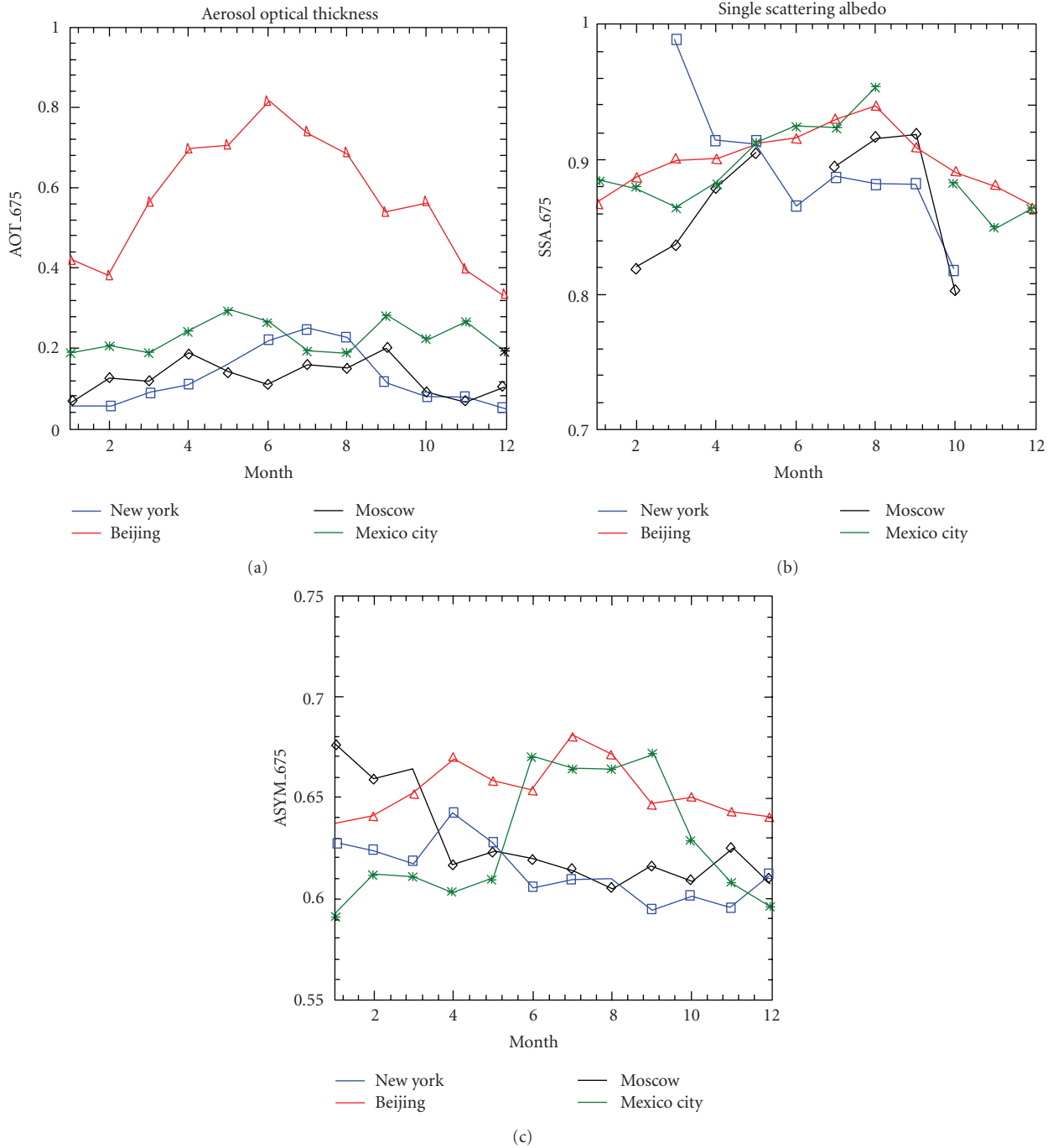


FIGURE 4: Monthly observations for (a) aerosol optical thickness, (b) single scattering albedo, and (c) the asymmetry factor from NASA AERONET sites for four cities (Beijing, New York City, Mexico City, and Moscow). Data are sampled from multiyear averages.

in the 0.7 range and cloud drops that are larger, compared to the wavelength, are more typically 0.85. Together with AOT and single scattering albedo, this parameter is useful for obtaining the basic radiative properties of aerosols. In the summer, Beijing and Mexico City have higher asymmetry factors than NYC and Moscow, which means that aerosol particles over Beijing and Mexico City are larger than those over NYC.

3.3. *Aerosol Reduction on Surface Insolation.* Since Beijing represents an extremely-polluted city and New York City represents a normally polluted city, this section focuses on how the surface insolation changes in these two cities as a result of aerosol loads. We do not discuss rural aerosols here because of the unavailability of the observations. However, this should not be interpreted as suggesting that rural regions have no aerosols and aerosol effect.

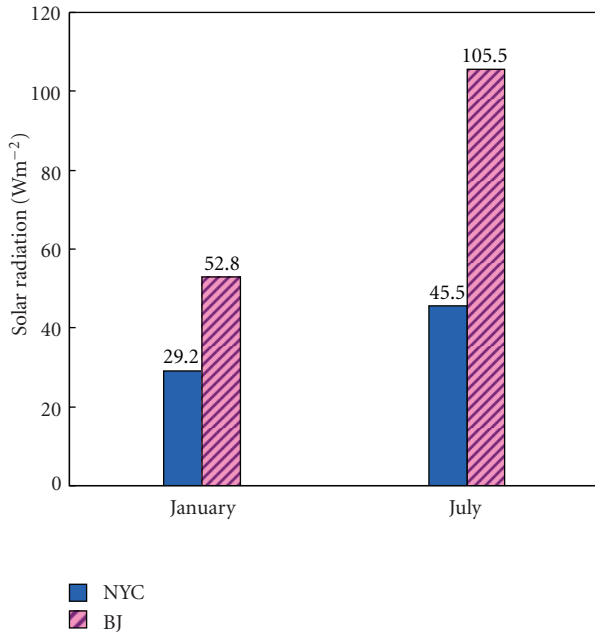


FIGURE 5: Aerosol reduction on surface insolation calculated from the radiative transfer model for Beijing and New York City in January and July, respectively.

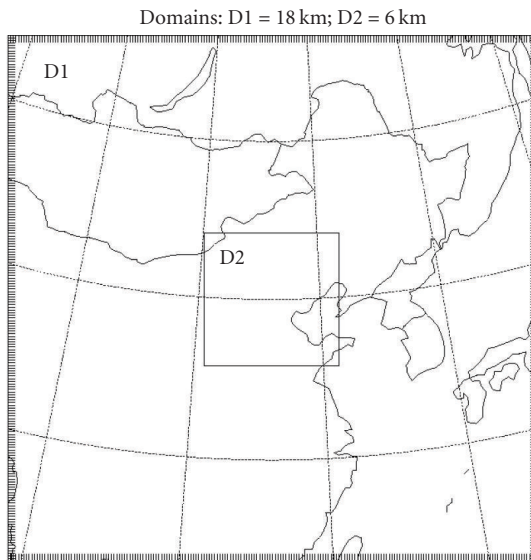


FIGURE 6: The domain size and location of the study. D1 resolution is 18 km and D2 resolution is 6 km.

A radiative transfer model [26, 42] is used to simulate urban aerosol-induced changes in surface insolation based on the AERONET-observed aerosol optical properties for both Beijing and NYC (Figure 5). Top quartile, 6-year, instantaneous-averaged AOT, single scattering albedo, and asymmetry factor observed from NASA AERONET were input into the radiative transfer model to calculate how much surface insolation is reduced due to the direct effect. The vertical distribution of aerosols near the surface is assumed to be uniform. The vertical distribution of aerosols has

a relatively minor effect on reduction of solar radiation at the surface. The sky is cloudy-free. In addition, the atmospheric conditions and surface albedo were predefined in the radiative transfer model to represent the surface [26]. The reduction of surface insolation ( $\delta S$ ) is a function of solar zenith angle as well as aerosol amount, and therefore, varies with seasons. The reduction of surface insolation ( $\delta S$ ) for NYC is less significant than in Beijing due to moderate AOT in this city (Figure 3). Specifically, for NYC,  $\delta S$  is as low as  $20 \text{ Wm}^{-2}$  in winter and as high as  $40 \text{ Wm}^{-2}$  in summer. By more strongly scattering and absorbing solar radiation, the aerosols reduce surface insolation by about  $105.5 \text{ Wm}^{-2}$  for Beijing during the summer and  $50.5 \text{ Wm}^{-2}$  during the winter (January).

The  $\delta S$  depends on atmospheric conditions of clouds and aerosols. Using different radiative transfer models or assumptions may result in slightly different values of  $\delta S$ . The Chou and Suarez radiative transfer model [26] was employed because WRF's aerosol scheme is under development with unknown capability (Qian, personal communication 2009), and because Chou and Suarez' [26] model has been adapted to calculate aerosols in various studies [4, 9, 42].

**3.4. Aerosol Reduction on Surface Skin Temperature ( $T_{\text{skin}}$ )—Model Simulations.** Surface skin temperature ( $T_{\text{skin}}$ ) is a diagnostic variable in the land surface model of WRF. WRF-NOAH, similar to most land surface models developed since the middle 1980s [29], simulates energy redistribution within the land surface-biosphere system in terms of upward longwave radiation, sensible heat flux, latent heat flux and ground heat flux.  $T_{\text{skin}}$ , one of the key variables that determines sensible and latent heat flux via the differences between the skin layer and air surface layer, is determined by both surface insolation as well as surface-biosphere conditions. The sensitivity simulations are conducted over the domain in Figure 6 for 27 July 2008, where Beijing is in domain 2 (D2). On this day, AERONET-observed AOD is 1.66 at 0.675 nm, which is very high. Domain 1 (Figure 6) shows the area over which the WRF model conducts the overall regional sensitivity simulations. Domain 2 is at 6 km resolution representing the dense Beijing urban regions where surface insolation reduction ( $\delta S$ ) is reduced by  $100 \text{ Wm}^{-2}$ . Therefore,  $T_{\text{skin}}$  is expected to decrease via the reduction of surface insolation. Nevertheless, our goal is to assess how much  $T_{\text{skin}}$  is affected by aerosols and whether  $T_{\text{skin}}$  responds to the aerosol direct effect in the same manner as  $T_{\text{air}}$ , in terms of magnitude and diurnal change.

Although the sensitivity study studies urban region, it should not imply that aerosols have no effect on rural regions. In fact, as long as aerosols are present, it would change solar radiation as function of aerosol properties in that region. In this paper, urban surface temperature change is our interest and thus we design our numerical experiments over urban regions.

The surface response to aerosol loading is largely determined by the surface and atmosphere conditions [23]. Therefore, Figure 7 presents the land conditions for the runs. Specifically, the soil category for Beijing is set (Figure 7(a)) to sand clay loam. Terrain height (Figure 7(b)) shows that

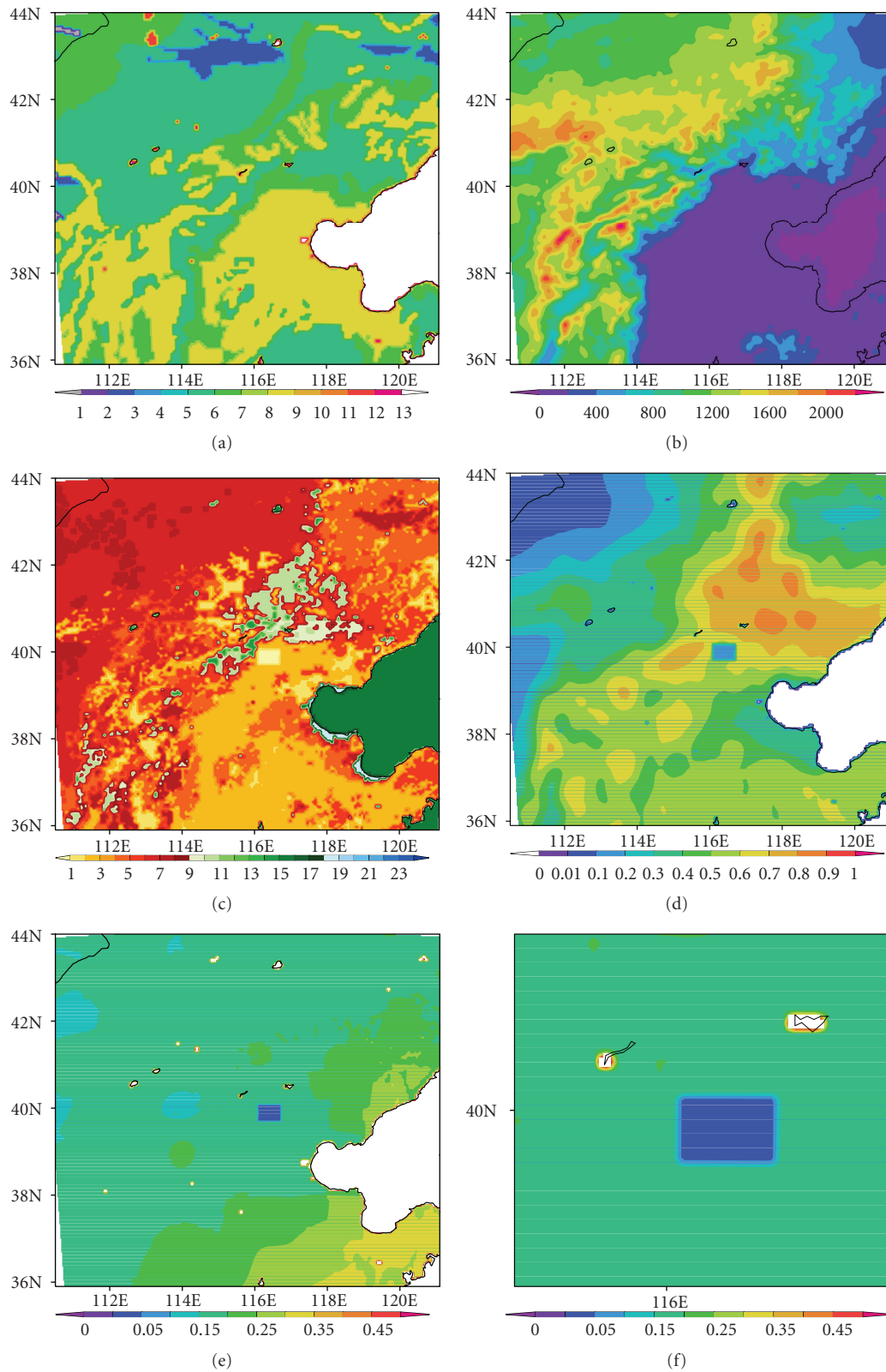


FIGURE 7: The land surface properties of the study domain in WRF: (a) soil category, (b) terrain height, (c) land use category, (d) green vegetation fraction (GVF), (e) soil moisture at the first soil layer (5 cm) for domain 2, and (f) the same as (e) but for analysis area.

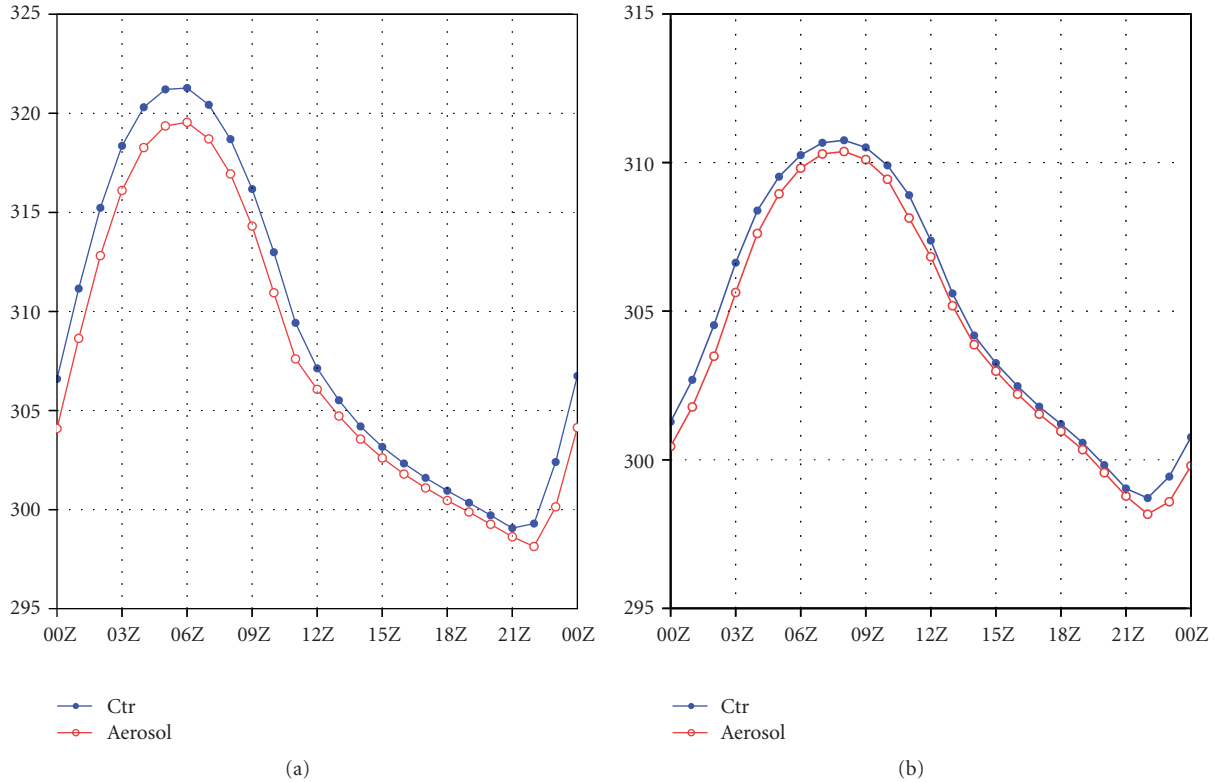


FIGURE 8: Aerosol effects on (a) land surface skin temperature, and (b) land surface 2 m air temperature. Model output for July 27, 2008. Averaged over Beijing (39.7–40.1°N, 116.1–116.7°E).

Beijing is less than 200 m with much higher values in Northwestern surrounding regions and lower values in Southeastern regions. The land use in Beijing is categorized in the USGS 24-category as “urban and builtup land-1” (Figure 7(c)). Green vegetation fraction (Figure 7(d)) in Beijing is about 0.5 from the NCEP reanalysis data, which is obviously too high. Thus, in our runs we set this value as 0.2 as previous model development suggested [18]. Soil moisture in the first model soil layer in Beijing is 0.2–0.3  $\text{m}^3 \cdot \text{m}^{-3}$ , but we reset it as a smaller value (Figures 7(e) and 7(f)).

The magnitude of  $T_{\text{skin}}$  reduction (Figure 8(a)), up to 2.1°C, is greatest during the period 6–9 AM (LST) for 27 July 2008. Such reduction occurs during the entire day, but the minimum is around 5–7 PM (LST). It should be noted that the only difference between these two runs (control versus sensitivity run) is  $\delta S$  during daylight hours. Clearly, the aerosol direct effect propagates into the nocturnal hours because of the memory of land surface to energy changes in the daytime. By comparison,  $T_{\text{air}}$  at 2 m (Figure 8(b)) shows a reduction due to the daytime aerosol direct effect. Nevertheless, the overall  $T_{\text{air}}$  reduction is smaller than  $T_{\text{skin}}$ . For example, the maximum  $T_{\text{air}}$  reduction is only 0.9°C at 9 AM and minimum reduction is only 0.45°C at 1 PM.

Figure 9 shows the spatial distribution of the  $T_{\text{skin}}$  (Figure 9(a)),  $T_{\text{air}}$  (Figure 9(b)) and  $\delta T_{\text{skin}}$  and  $\delta T_{\text{air}}$  (the sensitivity run minus the control run) at 12Z 27 July 2008, respectively (Figures 9(c) and 9(d)).  $T_{\text{skin}}$  (Figure 9(c)) changes more than  $T_{\text{air}}$  (Figure 9(d)) at this time. For comparison, the

spatial distribution of  $T_{\text{skin}}$  and  $T_{\text{air}}$  reveals the heat gradient over the simulated regions. Corresponding to height (Figure 9(b)), the high mountains regions have low  $T_{\text{skin}}$  and  $T_{\text{air}}$ , only the middle Beijing and southern region have higher temperatures. This geographical distribution also affects the surface temperature reduction due to the aerosol direct effect.

Figure 10 shows the  $\delta T_{\text{skin}}$  and  $\delta T_{\text{air}}$  at 18Z 27 July 2008. Clearly, at midnight, the aerosol effect on  $T_{\text{air}}$  (Figure 10(b)) is now no longer noticeable. Namely,  $\delta T_{\text{air}}$  is 0 for Beijing regions. On the contrary,  $\delta T_{\text{skin}}$  is still evident, but the magnitude is only about 0.5–1°C. This may imply that  $T_{\text{air}}$  has a shorter memory than  $T_{\text{skin}}$  to the aerosol direct effect.

#### 3.4.1. Sensitivity Studies with Albedo and Soil Moisture.

Further sensitivity experiments were designed to examine the albedo effect on surface temperature. In the albedo experiment, albedo is designated as 0.15 and 0.10, respectively.  $T_{\text{skin}}$  values were compared from 00Z 27 July 2008 to 00Z 28 July 2008. Figure 11 illustrates that with lower albedo (alb = 0.10),  $T_{\text{skin}}$  is always higher than in the high albedo case (alb = 0.15). The largest differences, with 1.7 K peak difference, occur at 06Z 27 July 2008, which corresponds to local noon. Although the albedo effect is low during the night because of lack of insolation,  $T_{\text{skin}}$  of the low albedo case is still higher than that of the high albedo case. This means that heat accumulated during the daytime can propagate to change the nighttime surface temperature.

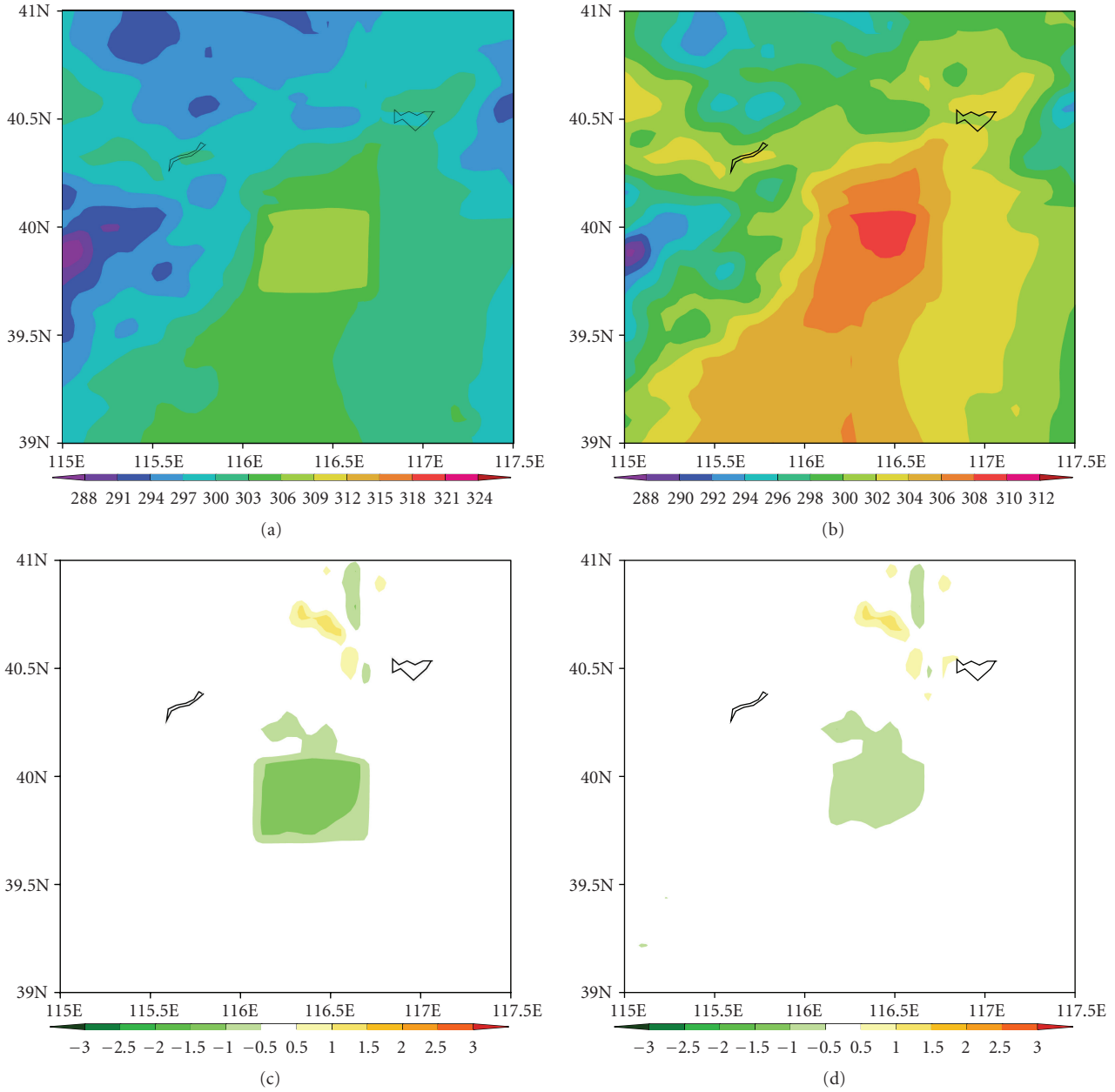


FIGURE 9: (a) the model output for the control run on skin temperature, (b) Model output for 2 m surface air temperature, (c) sensitivity run minus control run on skin temperature, and (d) sensitivity run minus control run on 2 m surface air temperature. The outputs are on 12Z, July 27, 2008.

Another sensitivity experiment is designed to examine the model’s soil moisture effect on  $T_{skin}$ . The Control run sets soil moisture as  $0.15 \text{ m}^3/\text{m}^3$  interpolated from the NCEP reanalysis, and the sensitivity run sets the soil moisture as 0.001 (i.e., dry case). Figure 12 clearly reveals that with less soil moisture, the surface is warmer by 1.6K during the daytime. This is because with less soil moisture, more of the absorbed surface insolation is redistributed to sensible heat flux and ground heat flux to warm the surface and underlying soil. Nevertheless, at night, the less-soil moisture case shows that the surface is cooler. This is mainly due to the stronger longwave radiative cooling of the dryer surface.

#### 4. Discussion

Urban aerosols reduce both  $T_{skin}$  and  $T_{air}$  (2-m). This is a potential competing mechanism with land cover change for the urban warm surface. Namely, although significant changes in vegetation, land cover, and soil moisture over urban regions lead to a warmer surface, aerosols may offset such heating, partly, by reducing surface insolation. Nevertheless, the magnitude of aerosol-induced surface cooling is only  $0.5\text{--}2^\circ\text{C}$ , and thus cannot fully offset the urban heat island effect, which is about  $2\text{--}10^\circ\text{C}$  warmer than surrounding regions in summer. It is important to note

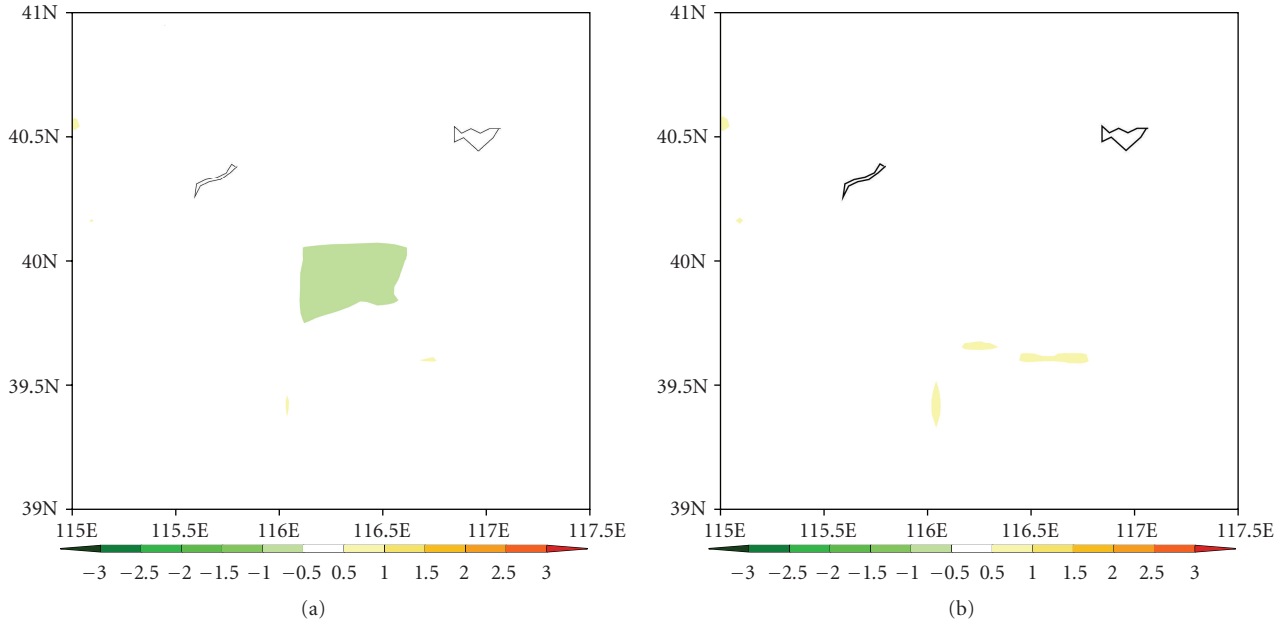


FIGURE 10: Same as Figures 9(c) and 9(d) except for 18Z, July 27, 2008. (a) The difference of  $T_{skin}$  between sensitivity run and the control run, and (b) same as (a) except for  $T_{air}$ .

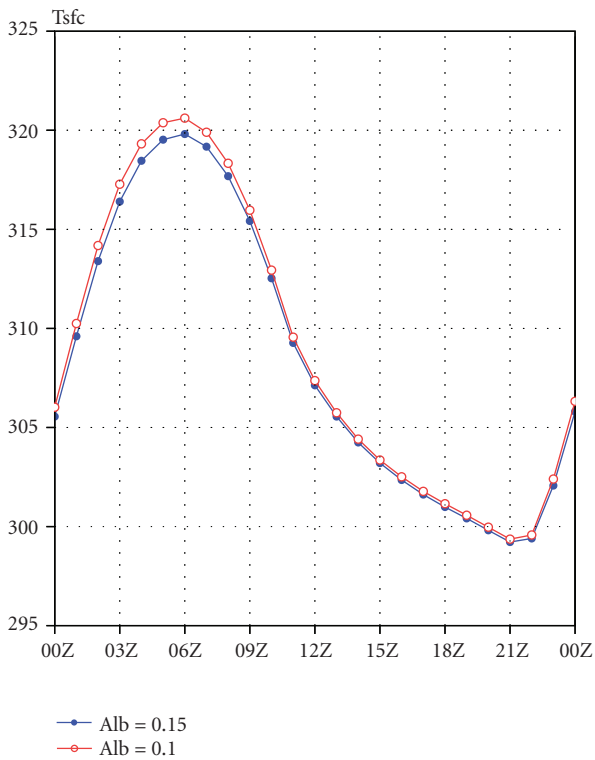


FIGURE 11: Sensitivity study for surface albedo effect on surface skin temperature. Alb = 0.15 is the high albedo case when surface albedo is set as 0.15, and alb = 0.10 is the low albedo case when the surface albedo is set as 0.10. The experiment area is over Beijing (39.7–40.1°N, 116.1–116.7°E). The unit of the  $y$ -axis is Kelvin (K).

that only the direct effect of aerosols is considered here. The indirect effect related to cloud formation and aerosol longwave emission is not discussed and is the subject of ongoing research.

The slightly different responses from  $T_{skin}$  and  $T_{air}$  are particularly important. Traditionally, urban temperature studies use 2-m shelter-based  $T_{air}$  measurements, and it has been reported to be a more nocturnal phenomena [7]. However,  $T_{skin}$  responds to heat more significantly during daytime than at night. This is consistent with recent findings by Shepherd et al. [43] who tried to examine why Houston's UHI could generate a mesoscale circulation during daytime hours. Through land cover change, urban surface albedo and emissivity are reduced [4, 9] and thus  $T_{skin}$  is increased. The heated surface stores extra energy and at night, such heat is emitted to warm the air layer closest to the skin surface layer. Therefore,  $T_{air}$  is also found to be warmer than the urban surrounding regions at night.

The sensitivity study approach is an entryway to more robust analysis in the future. We applied an offline radiative transfer model to calculate aerosol directly reduction on surface insolation to avoid using WRF model inbuilt aerosol scheme, which is under development and is linked with cloud formation but has not been fully examined by the users. We did not study aerosol-cloud interaction in this work. In addition, the WRF approach can show how aerosols affect  $T_{skin}$  and how that leads to a change in local mesoscale circulations, and further changes  $T_{skin}$ , by using a 4-D (space-time) atmosphere-land surface coupled model. For example, wind is indeed altered due to the change of  $T_{skin}$  (result is not shown).

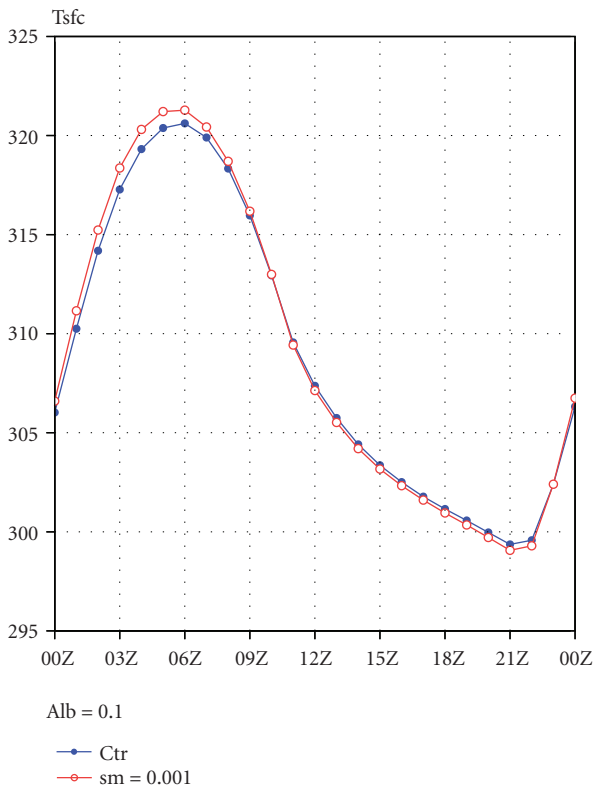


FIGURE 12: Sensitivity study for soil moisture on surface skin temperature. In the control run, initial soil moisture is interpolated from NCEP FNL analysis, and in the sensitivity run, soil moisture in Beijing is set as a small value ( $0.001 \text{ m}^3/\text{m}^3$ ). The surface albedo is set as 0.10. The experiment area is over Beijing ( $39.7\text{--}40.1^\circ\text{N}$ ,  $116.1\text{--}116.7^\circ\text{E}$ ). The unit of the y-axis is Kelvin (K).

Sensitivity experiments on albedo and soil moisture suggest that these land cover related physical processes are as important to  $T_{\text{skin}}$  change as aerosol direct effect. The aerosol direct effect appears to reduce surface temperature while albedo and soil moisture reduction increases it. Therefore, in order to predict urban  $T_{\text{skin}}$  or UHI, one needs to include all these comparable processes in the model.

The implications of this research are far reaching. At the local to regional scales, proper representation of urban aerosol loading could be critical for diagnosing or forecasting the UHI hazard described by Zhou and Shepherd [8]. In terms of climate analysis, Menon et al. [44] suggested that aerosols, both direct and indirect effects, have a significant impact on many aspects of climate. It is also likely that aerosol variability could explain global brightening/dimming trends in recent decades. Further, the interplay between urban land cover and aerosols is not trivial and must be accounted for in the next generation of global climate models.

## Acknowledgments

This work was funded by NSF Climate Dynamics Program (ATM CDP) (Award no. 0701440), NASA PMM Program

(Award no. NNX07AF39G), and by the Defense Threat Reduction Agency (PI Steve Burian). The authors thank AERONET PIs Hong-Bin Chen and Philippe Goloub for making the measurements public accessible via AERONET site. Thanks for Michael D. King, Tom Eck, and Brent Holben for helpful discussions on AERONET measurements.

## References

- [1] H. E. Landsberg, "Man-made climate change," *Science*, vol. 170, pp. 1265–1274, 1970.
- [2] A. J. Arnfield, "An approach to the estimation of the surface radiative properties and radiation budgets of cities," *Physical Geography*, vol. 3, no. 2, pp. 97–122, 1982.
- [3] C. S. B. Grimmond and T. R. Oke, "Heat storage in urban areas: local-scale observations and evaluation of a simple model," *Journal of Applied Meteorology*, vol. 38, no. 7, pp. 922–940, 1999.
- [4] M. Jin, R. E. Dickinson, and D. A. L. Zhang, "The footprint of urban areas on global climate as characterized by MODIS," *Journal of Climate*, vol. 18, no. 10, pp. 1551–1565, 2005.
- [5] D. M. Yow, "Urban heat islands: observations, impacts, and adaptation," *Geography Compass*, vol. 1, no. 6, pp. 1227–1251, 2007.
- [6] T. R. Oke, "Canyon geometry and the nocturnal urban heat island: comparison of scale model and field observations," *Journal of Climatology*, vol. 1, no. 3, pp. 237–254, 1981.
- [7] T. R. Oke, "The energetic basis of the urban heat island (Symons Memorial Lecture, 20 May 1980)," *Quarterly Journal, Royal Meteorological Society*, vol. 108, no. 455, pp. 1–24, 1982.
- [8] Y. Zhou and J. M. Shepherd, "Atlanta's urban heat island under extreme heat conditions and potential mitigation strategies," *Natural Hazards*, vol. 52, no. 3, pp. 639–668, 2010.
- [9] M. Jin, J. M. Shepherd, and M. D. King, "Urban aerosols and their interaction with clouds and rainfall: a case study for New York and Houston," *Journal of Geophysical Research*, vol. 110, Article ID D10S20, 12 pages, 2005.
- [10] G. A. Meehl, C. Tebaldi, G. Walton, D. Easterling, and L. McDaniel, "Relative increase of record high maximum temperatures compared to record low minimum temperatures in the U.S.," *Geophysical Research Letters*, vol. 36, no. 23, Article ID L23701, 2009.
- [11] A. Sterl, C. Severijns, H. Dijkstra et al., "When can we expect extremely high surface temperatures?" *Geophysical Research Letters*, vol. 35, no. 14, Article ID L14703, 2008.
- [12] S. A. Changnon, K. E. Kunkel, and B. C. Reinke, "Impacts and responses to the 1995 heat wave: a call to action," *Bulletin of the American Meteorological Society*, vol. 77, no. 7, pp. 1497–1506, 1996.
- [13] B. Menne, "The health impacts of 2003 summer heat-waves. Briefing note for the delegations of the fifty third session of the WHO regional Committee for Europe," WHO Europe, 12pp.
- [14] M. Beniston, "The 2003 heat wave in Europe: a shape of things to come? An analysis based on Swiss climatological data and model simulations," *Geophysical Research Letters*, vol. 31, no. 2, pp. L02202–4, 2004.
- [15] S. Cheval, A. Dumitrescu, and A. Bell, "The urban heat island of Bucharest during the extreme high temperatures of July 2007," *Theoretical and Applied Climatology*, vol. 97, no. 3–4, pp. 391–401, 2009.
- [16] J. M. Shepherd, R. Showstack, and M. Jin, "Linkages between the built urban environment and earth's climate system," *Eos*, vol. 85, no. 23, pp. 227–228, 2004.

- [17] M. Jin and J. M. Shepherd, "On including urban landscape in land surface model—how can satellite data help?" *Bulletin of the AMS*, vol. 86, no. 5, pp. 681–689, 2005.
- [18] M. Jin, J. M. Shepherd, and C. Peters-Lidard, "Development of a parameterization for simulating the urban temperature hazard using satellite observations in climate model," *Natural Hazards*, vol. 43, no. 2, pp. 257–271, 2007.
- [19] B. Lampte, "An analytical framework for estimating the urban effect on climate," *International Journal of Climatology*, vol. 30, no. 1, pp. 72–88, 2010.
- [20] Y. J. Kaufman and I. Koren, "Smoke and pollution aerosol effect on cloud cover," *Science*, vol. 313, no. 5787, pp. 655–658, 2006.
- [21] IPCC, "The Fourth Assessment Report of the Intergovernmental Panel on Climate Change. WG1: Climate Change," The Physical Science Basis. Cambridge University Press, pp.996, 2007.
- [22] D. Rosenfeld, "Suppression of rain and snow by urban and industrial air pollution," *Science*, vol. 287, no. 5459, pp. 1793–1796, 2000.
- [23] M. Jin and J. M. Shepherd, "Aerosol relationships to warm season clouds and rainfall at monthly scales over east China: urban land versus ocean," *Journal of Geophysical Research D*, vol. 113, no. 24, Article ID D24S90, 2008.
- [24] T. L. Bell and D. Rosenfeld, "Comment on "Weekly precipitation cycles? Lack of evidence from United States surface stations" by D. M. Schultz et al," *Geophysical Research Letters*, vol. 35, no. 9, Article ID L09803, 2008.
- [25] M. K. Kim, . , M. Chin, K. M. Kim, Y. C. Sud, and . , "Atmospheric teleconnection over Eurasia induced by aerosol radiative forcing during boreal spring," *Journal of Climate*, vol. 19, no. 18, pp. 4700–4718, 2006.
- [26] M. Chou and M. J. Suarez, "A solar radiation parameterization for atmosphere studies," Technical Memorandum 104606, NASA, Greenbelt, Md, USA, 1999, vol. 12, 40pages.
- [27] B. N. Holben, T. F. Eck, I. Slutsker et al., "AERONET—a federated instrument network and data archive for aerosol characterization," *Remote Sensing of Environment*, vol. 66, no. 1, pp. 1–16, 1998.
- [28] K. C. Seto and J. M. Shepherd, "Global urban land-use trends and climate impacts," *Current Opinion in Environmental Sustainability*, vol. 1, no. 1, pp. 89–95, 2009.
- [29] R. Dickinson, "BATS," Tech. Rep., NCAR, 1986.
- [30] Z. Wan, "A generalized split-window algorithm for retrieving land-surface temperature from space," *IEEE Transactions on Geoscience and Remote Sensing*, vol. 34, no. 4, pp. 892–905, 1996.
- [31] K. Wang, Z. Wan, P. Wang, M. Sparrow, J. Liu, and S. Haginoya, "Evaluation and improvement of the MODIS land surface temperature/emissivity products using ground-based measurements at a semi-desert site on the western Tibetan Plateau," *International Journal of Remote Sensing*, vol. 28, no. 11, pp. 2549–2565, 2007.
- [32] Z. Wan and Z.-L. Li, "Radiance-based validation of the V5 MODIS land-surface temperature product," *International Journal of Remote Sensing*, vol. 29, pp. 5373–5395, 2008.
- [33] T. F. Eck, B. N. Holben, J. S. Reid et al., "Wavelength dependence of the optical depth of biomass burning, urban, and desert dust aerosols," *Journal of Geophysical Research D*, vol. 104, no. 24, pp. 31333–31349, 1999.
- [34] O. Dubovik and M. D. King, "A flexible inversion algorithm for retrieval of aerosol optical properties from Sun and sky radiance measurements," *Journal of Geophysical Research D*, vol. 105, no. 16, pp. 20673–20696, 2000.
- [35] W. C. Skamarock, J. B. Klemp, J. Dudhia et al., "A description of the Advanced Re-search WRF Version 3," NCAR Tech Notes 475+STR, 2008.
- [36] F. Chen and J. Dudhia, "Coupling and advanced land surface-hydrology model with the Penn State-NCAR MM5 modeling system. Part I: model implementation and sensitivity," *Monthly Weather Review*, vol. 129, no. 4, pp. 569–585, 2001.
- [37] M. B. Ek, K. E. Mitchell, Y. Lin et al., "Implementation of Noah land surface model advances in the National Centers for Environmental Prediction operational mesoscale Eta model," *Journal of Geophysical Research D*, vol. 108, no. 22, pp. 1–16, 2003.
- [38] H. Kusaka, H. Kondo, Y. Kikegawa, and F. Kimura, "A simple single-layer urban canopy model for atmospheric models: comparison with multi-layer and slab models," *Boundary-Layer Meteorology*, vol. 101, no. 3, pp. 329–358, 2001.
- [39] M. A. Friedl, D. K. McIver, J. C. F. Hodges et al., "Global land cover mapping from MODIS: algorithms and early results," *Remote Sensing of Environment*, vol. 83, no. 1-2, pp. 287–302, 2002.
- [40] M. Jin, "MODIS observed seasonal and interannual variations of atmospheric conditions associated with hydrological cycle over Tibetan Plateau," *Geophysical Research Letters*, vol. 33, no. 19, Article ID L19707, 2006.
- [41] H. Jethva, S. K. Satheesh, J. Srinivasan, and K. K. Moorthy, "How good is the assumption about visible surface reflectance in MODIS aerosol retrieval over Land? A comparison with aircraft measurements over an urban site in India," *IEEE Transactions on Geoscience and Remote Sensing*, vol. 47, no. 7, part 1, Article ID 4812038, pp. 1990–1998, 2009.
- [42] L. Oreopoulos, M. D. Chou, M. Khairoutdinov, H. W. Barker, and R. F. Cahalan, "Performance of Goddard earth observing system GCM column radiation models under heterogeneous cloud conditions," *Atmospheric Research*, vol. 72, no. 1-4, pp. 365–382, 2004.
- [43] J. M. Shepherd, W. M. Carter, M. Manyin, D. Messen, and S. Burian, "The impact of urbanization on current and future coastal convection: a case study for Houston," *Environment And Planning B*, vol. 37, no. 2, pp. 284–304, 2010.
- [44] S. Menon, N. Unger, D. Koch et al., "Aerosol climate effects and air quality impacts from 1980 to 2030," *Environmental Research Letters*, vol. 3, no. 2, Article ID 024004, 12 pages, 2008.